10th Numerical Towing Tank Symposium

23-25 September 2007

Hamburg/Germany

Volker Bertram (Ed.)

ENSIETA
ÉCOLE NATIONALE SUPÉRIEURE D'INGÉNIEURS
FORMATION INITIALE - FORMATION CONTINUE - RECHERCHE

TuTech
TUHH Technologie GmbH
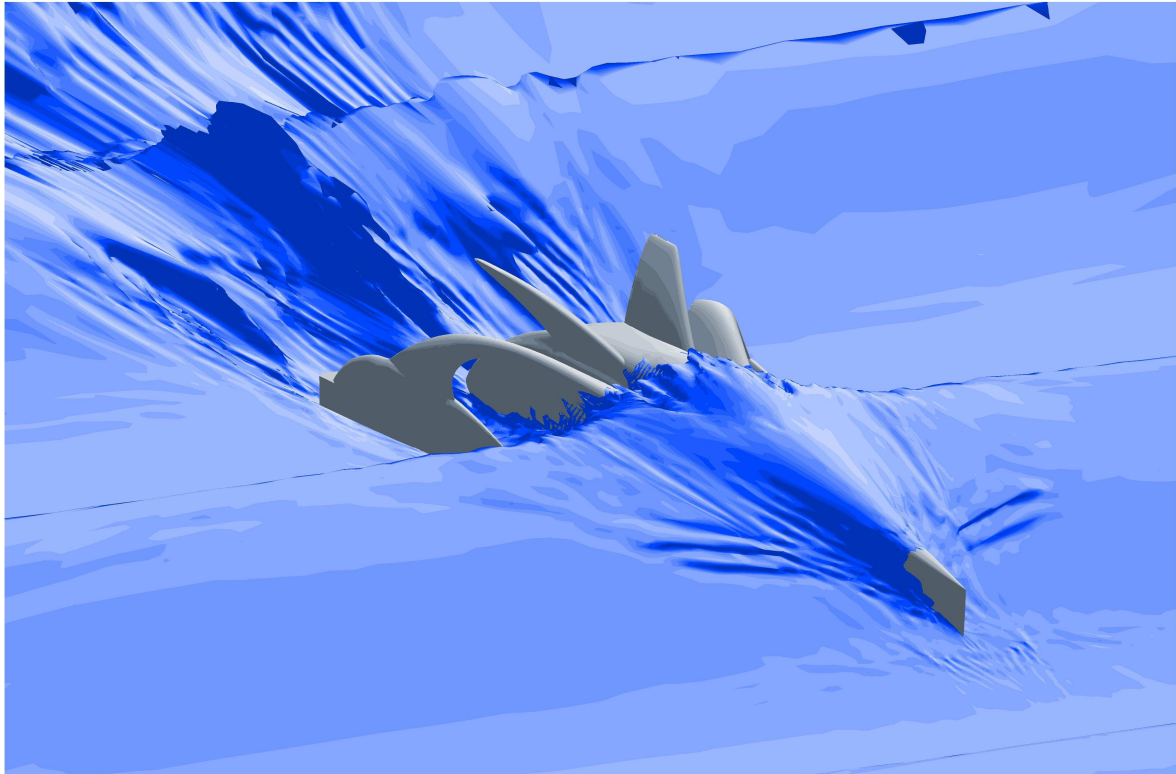
Sponsored by

Office of Naval Research Global
www.onrglobal.navy.mil

NUMECA
www.numeca.com

CD-Adapco
www.cd-adapco.com

Fr. Lürssen Werft
www.lurssen.com

Blohm & Voss GmbH
www.tk-marinesystems.de

Voith Turbo Marine GmbH & Co
www.voith.com

Schottel GmbH & Co KG
www.schottel.de

Germanischer Lloyd
www.gl-group.org

Looking back in pleasure

Ten years ago, preparation started for the first NuTTS Symposium. I had participated as a young PhD student in the International Workshop on Water Waves and Floating Bodies, initiated by Prof John Nicolas Newman and Prof David Evans, who turned out to be Nick and Dave and very human, and who helped me a lot in establishing a network of scientific contacts at an early stage of my scientific career. The Workshop was unique, newcomers like me met the established experts in our field, and prices were kept incredibly low. I slept in a bunk bed in Woodshole in the first Workshop I attended, but so what. I met people like Newman, Wehausen, Miloh, Faltinsen… and the PhD student who worked on the same problem as me, only at MIT. Ten years later, the Workshop continued, but kept its focus on mathematics and offshore applications. I drifted into CFD for ships, which at that time was generally without free surface, and anyway the Workshop was just not the right forum for number crunchers.

The solution seemed clear. We, the number crunchers, should have something akin to the Workshop in format, albeit with a different focus. Encouraged by my friend Maurizio Landrini, who passed away tragically, I went ahead despite assorted skepticism voiced by most colleagues. For the first NuTTS in 1998, we had 15 papers presented, and about as many participants. While it was a modest start, it was fun and the intimate atmosphere of the workshop and some glasses of wine were enough to convince Maurizio Landrini to co-organize the next NuTTS in Rome. That year, we had had already 23 papers, enough critical mass to establish NuTTS. By the 3rd NuTTS (held in Sweden with the help of Lars Larsson), we had established the Symposium at its present level of some 30 papers presented.

Whatever hair I have left has turned a mellow shade of grey and I seem to be more active now in administrative tasks than spending time programming as I did as a PhD student. I have 'graduated' and our science is dynamically advanced by the many young PhD students and post-docs which have found their forum at NuTTS. The apple tree planted 10 years ago bears fruit now year after year. CFD applications have advanced a lot in 10 years, as shown in the invited presentations of Takanori Hino and Milovan Peric, and industry has widely accepted CFD as a valuable and trusted engineering tool for a multitude of applications.

Looking back, I feel pleasure and gratitude. Gratitude for the colleagues, who pushed NuTTS ahead, Prof Söding, Maurizio Landrini, Gerard Delhommeau, Emilio Campana, and Stefan Kyulevcheliev. Gratitude also for our assorted sponsors who allowed keeping the prices so low for everybody, most of all the PhD students. Of the many sponsors, I would like to mention particularly Germanischer Lloyd who was the only sponsor of the very first NuTTS and has faithfully continued its support every time we have been at Haus Rissen.

I hope you enjoy the 10th NuTTS as much as we enjoyed the previous ones. And many happy returns.

Volker Bertram

Content

Large Eddy Simulation of Viscous Flow around a Submarine During Maneuver

R.E. Bensow[1] and C. Fureby[1,2]

[1] Dept. of Shipping and Marine Technology, Chalmers University of Technology, Sweden,

[2] Defense Security Systems,The Swedish Defense Research Agency – FOI, Sweden,

rickard.bensow@chalmers.se, fureby@foi.se

Understanding the fluid dynamics of three-dimensional (3D) unsteady turbulent separating flows around maneuvering submarines is important to ensure the operational safety of the submarines and their crews and to reduce the passive acoustic signatures. Separating flows past the hull, sail, and control surfaces may be responsible for unsteady forces and moments that are not well understood, detrimental to boat performance, and may be unexpected. The desire to design novel configurations or conduct new types of operations, for example such as those involving launch and recovery of UUV's, for which little or no empirical knowledge exists, makes the task more urgent. Even if model test data exists, it is recognized that usual stability derivatives from tests, incorporated into empirical equations of motion, fail to predict the unsteady dynamics associated with transient maneuvers involving sail-hull junction vorticity and sail and body crossflow separation. Thus the interest in maneuvering simulations is increasing and for reasons of reliability together with the potential of more accurately predicting noise and vibrations, the use of LES is attractive, in spite of its higher cost compared with RANS. Since the particular demands for a successful LES are high with respect to grid generation, resolution and wall treatment, interpretation of unsteady flow data, and the access of high performance computer facilities, the present availability of this technique is limited. In the present study, the DARPA SubOFF model, (Huang et al., 1992; Liu et al., 1998), is used to gain experience in the performance of LES in maneuvering test. For validation, the experiments performed at Virginia Polytechnic and State University, (Hosder and Simpson, 2001; Granlund and Simpson, 2001), is used, where skin-friction, separation topology and the associated unsteady forces and moments have been measured during steady and unsteady maneuvers consisting of a sail-on-side pitch-up

maneuver. To perform this maneuvering test, we perform fully unsteady, three-dimensional (3D) simulations. Moving the hull through the maneuver incrementally, and computing or measuring the flow at a sequence of angles of attack is a quasi-steady approach and insufficient to capture the time-evolution of the forces and moments on the hull. The approach taken here and in (Alin et al., 2007) to perform the maneuver is to use an Arbitrary Lagrangian Eulerian (ALE) formulation, in which the motion of the hull, or the mesh, is incorporated into the equations of motion through a mesh or boundary velocity. A mixed subgrid model is used in combination with a wall model. Detailed comparison with measured skin-friction is made and we briefly discuss the validation problem arising when comparing one, or few, realizations of the maneuver with an ensemble averaged experimental dataset.

Before describing the maneuvering simulations, we emphasize that we have previously, (Wikström et al., 2004; Alin et al., 2004; Bensow et al., 2006), demonstrated the capability for accurate computations using LES of flows past submarines at zero pitch and yaw, as well as crossflow separation topology, forces and moments about submarine-like bodies at fixed angles of attack. Furthermore, validation of simpler flow, including comparisons with RANS and DES, are reported in, e.g. (Bensow et al., 2006; Fureby, 2007; Grinstein et al. (eds.), 2007). Concerning incompressible flow, being of importance to submarine maneuvering, we emphasize the validation studies of fully developed turbulent channel flows at Re-numbers, from Re $=395$ to 1800 (Wei and Willmarth, 1989; Moser et al., 1999), flow over a surface mounted hill at Re=$1.3 \cdot 105$ (Byun and Simpson, 2006) and flow around an inclined 6:1 prolate spheroid at Re$\approx 4.0 \cdot 106$ (Chesnakas and Simpson, 1996).

The selected validation test consists of the experimental study of Hosder (2001) and Hosder and Simpson (2001) using the DARPA AFF2 configuration with sail

but no rudders. Measurements of C_f using hot-wire sensors were performed in the Virginia Tech Stability Wind tunnel using the Dynamic Plunge, Pitch and Roll actuator (DyPPiR). The hull was placed in a slotted section of the tunnel in order to reduce blocking, a problem that otherwise may become important during maneuvering experiments with a large model. The velocity during the experiments was v_0=42.7 m/s and the hull length was L=2.24 m, resulting in a Re-number of Re_L=5.5·10^6. The maneuver consists of a 1° to 28° pitch-up motion in 0.33 s with a pitch rate that, except in the beginning and the end of the maneuver, was 78°/s. Since the model was mounted with the sail on side, this is equivalent to a yaw maneuver. The center of rotation was at x_{cg}/L=0.24. To acquire data for all azimuthal angles, the model was rotated between repetitions of the measurements, thus all C_f values are not obtained during the same pitch-up operation. The size of the sensors was about 2° of the circumferential, and data can thus be considered as averaged over the sensor. The random uncertainties in C_f was estimated to 8% between adjacent pitch-up runs, which in turn gives an error in the location of the separation of 2°. For absolute values of the skin friction, C_f, other error sources would need to be considered leading to higher uncertainty, which however do not affect the separation line predictions. In the experiments, ensemble averages over a set of repeated yaw motions were formed to reduce the noise. Based on the standard deviation, it is claimed that the repeatability of the flow is high and ten repetitions of the motion was used to form this ensemble averages. To determine the minima in C_f, LOESS smoothing (linear weighted average) was performed to reduce the variations in the measured profile whereas preserving the primary features of these.

When setting up the computational model, the slotted wind tunnel wall, utilized to emulate the freestream conditions in the experiments, was neglected and instead a large domain was used. A block-structured grid with 4.3·10^6 hexahedral cells was used. The grid is graded towards the hull to better capture the boundary layer, which however occurs at the expense of the resolution of the sail wake and far field. The resulting cell sizes in axial, normal and azimuthal directions, expressed in non-dimensional units, are $\Delta x^+ \approx$1100, $\Delta y^+ \approx$30, and $\Delta z^+ \approx$300-900, respectively, at the hull midsection with the lower Δz^+ values behind the sail and on the lower opposite side of the body. The outer boundary consists of a cylinder with a length of 4L and a diameter of 3L. In order to ensure a constant mass flow through the computational domain during the entire maneuver, the freestream velocity was prescribed on the upstream end of the cylinder as well as on the outer cylinder surface. No slip conditions were applied on the model hull and an outlet condition with prescribed pressure and homogeneous Neumann condition for the velocity was used on the downstream cylinder end. A more advanced treatment of the actual outflow, i.e. where fluid leaves the domain, was discussed, but tests indicated that the described set up was satisfactory for all angles-of-attacks considered. The LES was run from quiescient conditions at 0° angle-of-attack, until a developed flow had evolved before the maneuver was initiated. The yaw motion was here specified as a linear ramp from 0° to 28° with a pitch rate of 78°/s. The low start angle was chosen since measurements below 1° are presented despite reporting this as starting angle. This lag due to the different starting angle for the LES is estimated to have only a marginal effect. Two runs have been performed in order to compare the unsteadiness of the flow, in relation to the ensemble average for the experiments, where on the second run the maneuver is started from a later simulation time at 0° angle-of-attack. Another set-up detail that affects the comparison between the experiments and the LES is the presence of boundary layer trips on the model. Studs to fix the turbulent transition point are placed on the forebody and along the sides of the sail in the experiments, but in the computations no attempts were made to emulate the effects of these tripping de-

(a)   (b)
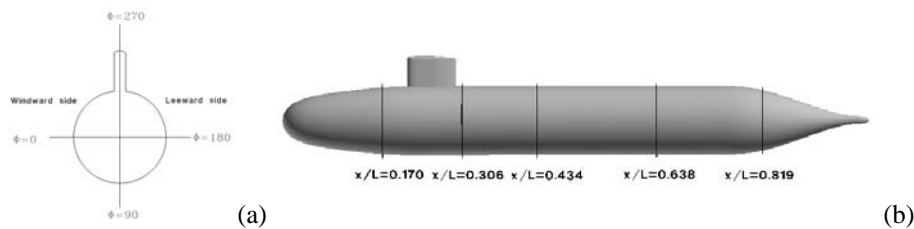
Figure 1. Definition of angles and cuts for the C_f plots in figures 7-18.

vices. This is likely to affect the boundary layer along the hull, but it is difficult to parameterize such a tripping device.

In the figures below we present perspective views of the flow around the hull, from the LES, in terms of streamlines, axial velocity contours and skin-friction contours on the hull, as well as comparisons between measured and predicted skin-friction coefficients at different locations along the hull at different angle-of-attack. The definition of the angle and the location of the presented skin-friction data is shown in figure 1. Experiments have been performed both for the full yaw motion and for a sequence of angles-of-attacks corresponding to a quasi-stationary motion. These datasets will from now on be referred to as the unsteady and the steady data. It is interesting to notice the differences between these two data sets. Part of this difference is due to the data collection and handling, but there is also a difference in the flow between unsteady and quasi-steady flow. As mentioned above, no uncertainty analysis for the skin-friction coefficient, C_f, as been presented but error bars of 20% are superimposed to the data to facilitate the comparison and validation of the LES.

For 0.0° yaw, the main flow features are the horseshoe vortex, originating from the roll-up of the boundary layer in front of the sail as well as the sail-wake. As the horseshoe vortex is transported aft, it partly loses its coherence and flattens out towards the hull. while interacting with the curved thickening hull-boundary layer to create a complex near-wall flow field with embedded vortices approaching the tapered stern. On the tapered part of the stern we find a region of intermittent separation with an unsteady shedding of hairpin-like vortex structures. For more details of this flow, see Persson *et al.* (2004).

When the yaw motion begins, the leeward leg of the horseshoe vortices becomes directly diverted towards the leeward-side of the hull (figure 4). Also the separation pattern on the stern begins to change with somewhat larger structures developing on the leeward side. At around 9° yaw angle, the leeward vortex leg interacts with the crossflow vortex that has begun to develop due to the angle of attack (figure 5). The horseshoe vortex is deflected further aft in the windward direction and at later times during the maneuver, the crossflow vortex detaches from the hull creating a very complex system of weak vortex separations between this vortex and the hull surface. The windward horseshoe vortex leg is not affected by the
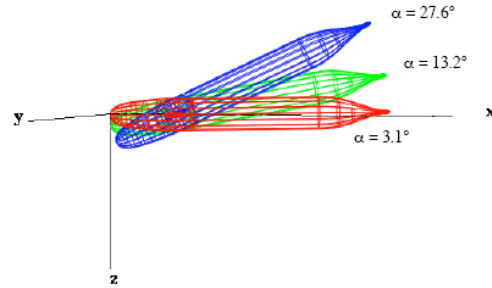
Figure 2. Schematic illustrating the yaw motion.

cross-flow in the early stages of the maneuver but starts to interact with the sail wake at 9° angle of attack and for higher angles, these structures merge. When 13° is reached, this vortex is swept of the hull and a second vortex is generated below the horseshoe vortex (figure 6). Approaching 20°, this second vortex merges with the leeward vortex system described above. On the lower side of the hull, the flow pattern is not as complicated, and differs from a steady crossflow only by a time lag. Between 7° and 9° the flow from beneath the hull causes the unsteady boundary layer to roll-up, from the stern, to form a longitudinal vortex on the lower leeward side of the hull that starts to detach at around 11°. A secondary vortex is found to develop for angles of attack over 20° (figure 7). The flow pattern in the stern and in the wake changes constantly, depending on the developing and detaching vortices created upstream. In general, on the windward side of the stern, smaller structures are created in the boundary layer and separate from the hull, while on the leeward side larger structures from the vortices dominates. The sail-tip vortex detaches from the sail wake earlier and earlier as the yaw angle is increased and at around 15°, two vortices start to appear on the sail tip, one on the trailing edge of the sail and one detaching on the leeward side, that however directly merges again. Also at this stage of the maneuver, separation starts to occur on the leeward side of the sail. Thus, in general terms, the separation pattern on the hull changes continuously as the yaw angle increases, and it is expected that hereditary effects will influence the near-wall flow and the entire separation pattern. This is indicated also by the experiments.

The sequence of figures 4b to 7b compares the time evolution of C_f between the steady and unsteady measurements and the LES results. Considerable differences are found between the steady and unsteady measurement data, but the loss of structures in the presented unsteady C_f profiles are however, at least partly, due to a higher amount of data smoothing applied in the unsteady case. Another reason might be that the vortices

detected in the steady experiments do not have time to fully evolve during the unsteady maneuver. When it comes to the CFD data, we conclude that the LES are reasonably capable of reproducing the measured C_f, in particular in the light of the possible uncertainties in the experimental data, but there are some clear differences. The major trends and structures are predicted although in some aspects the results seem to be more similar to the steady measurements than the unsteady: the amplitude of the peaks and the general variation of a profile are similar to the steady data, but the location of minima in C_f is close to the unsteady data. The two different LES are very similar in most profiles, but it is apparent that the location of the structures can vary considerable from one run to another, see e.g. figure 5. Also details in small-scale topology may differ between the two runs. Furthermore, the C_f profiles lies between the steady and the unsteady data. On the leeward side for lower angles of yaw, the LES underpredicts C_f, a behavior similar to defects caused by the blocking effect, examined by Hosder (2001) using solid walls instead of the slotted walls. This discrepancy between the LES and data might thus be due to the boundary conditions used. Studying the effect of data smoothing, we see that applying a similar smoothing to the LES data as was done to the measured data creates equally smooth profiles with a risk of eliminating some of the smaller structures in the sail wake region. For example, the secondary separation in the non-sail region developing at 20° yaw angle would disappear if smoothing was applied to the CFD data, cf. figure 3. This loss of structures would be even more pronounced if an averaging of several runs is made, making the appearance of the simulations agree even better with the experiments.

To conclude the experiences of this study, there are several items to discuss when using LES for maneuvering simulations. The issues of geometry representation and grid construction remain impediment to the widespread use of all CFD, and this is even worse for LES than for RANS, since the mesh quality needed is higher and the resolution needs to be high not only in wall normal direction but also in stream- and spanwise directions, especially the latter one. However here, where the experimental data focus on skin-friction and separation, the wall model seems to do a good job in predicting these quantities with a reasonable resolution. Turbulence modeling is another issue, whose impact is small normally. In maneuvering simulations however, this might be different. If the

discrepancies in variation between the LES and the unsteady data is due to differences in how fully evolved the different vortices are, the subgrid model may play an important role, but is otherwise likely to be less important than the inflow/outflow boundary condition issue or the issue relating to how to handle the near wall flow. When comparing results from LES with experimental data for such complicated situations as the maneuvering considered here, the data handling needs to be considered. One LES gives only one realization of the flow, while the experiments are repeated to generate averages, even during an unsteady maneuver, and the comparison will depend on the variability of the flow. The two runs performed in this study show that large variation may occur in this flow, while some features appear almost identical. Even more simulations will be necessary to say whether these large variations can occur in other locations than displayed here. For the same reason, different noise reduction techniques will also have a larger impact. In a steady LES, mean flow features are extracted by averaging over a time period and this effect is heavily reduced. Thus, even though the present results are encouraging with respect to the predicted skin-friction, some issues need to be studied further, such as the influence of the varying inflow/outflow regions and boundary conditions and the effect of boundary layer tripping. The reasons behind the observation that the unsteady flow predicted by the LES is in some aspects somewhat closer to the steady measurements than the unsteady, also merits further consideration.
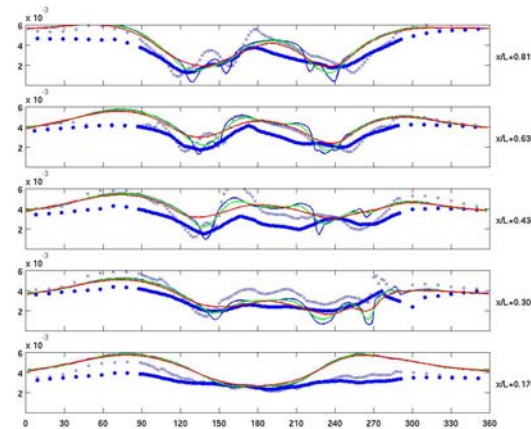
Figure 3. Effect of data smoothing examplified by the C_f-plots at 19.4 ° yaw. Legend (—) LES, (—) LES with smoothing as in the steady experiments, (—) LES with smoothing as in the unsteady experiments, (O) steady experimental data, and (•) unsteady experimental data.
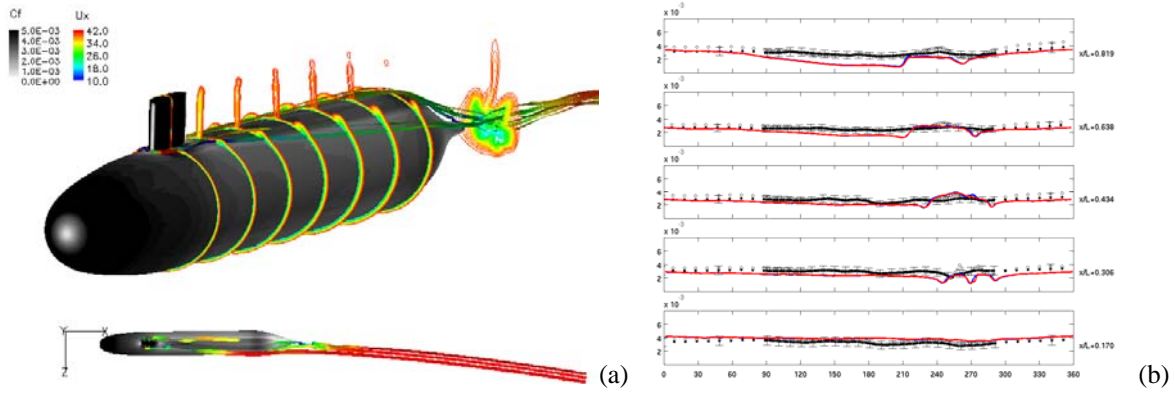
Figure 4. Turning DARPA AFF2 Suboff model at 0.9° yaw. (a) perspective view in terms of axial velocity contours, streamlines and C_f on the hull, and (b) measured and predicted C_f at different cross sections. Legend (—/—) LES, (•) unsteady, and (○) steady experimental data.
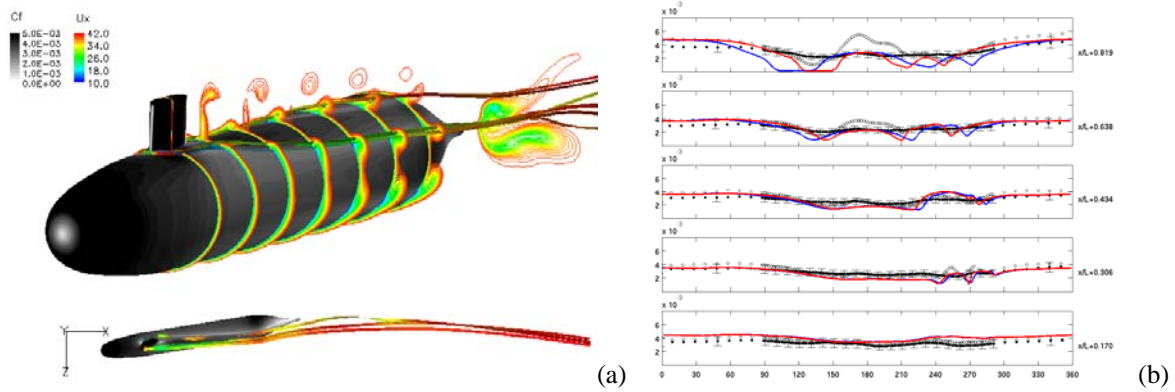
Figure 5. Turning DARPA AFF2 Suboff model at 9.3° yaw. (a) perspective view in terms of axial velocity contours, streamlines and C_f on the hull, and (b) measured and predicted C_f at different cross sections. Legend (—/—) LES, (•) unsteady, and (○) steady experimental data.
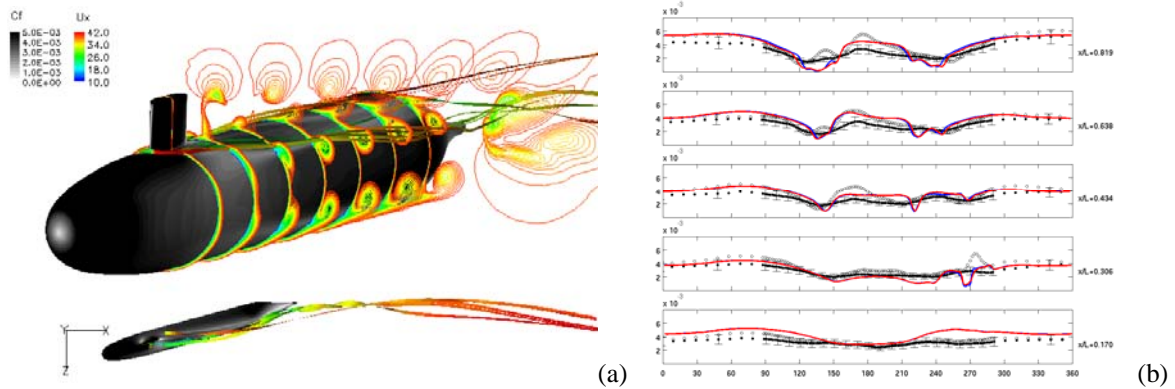
Figure 6. Turning DARPA AFF2 Suboff model at 15.3° yaw. (a) perspective view in terms of axial velocity contours, streamlines and C_f on the hull, and (b) measured and predicted C_f at different cross sections. Legend (—/—) LES, (•) unsteady, and (○) steady experimental data.
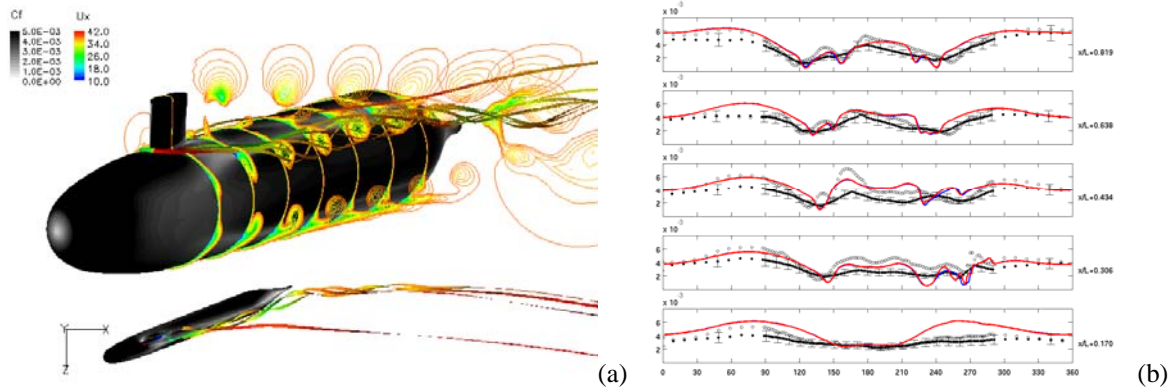
Figure 7. Turning DARPA AFF2 Suboff model at 21.4° yaw. (a) perspective view in terms of axial velocity contours, streamlines and C_f on the hull, and (b) measured and predicted C_f at different cross sections. Legend (—/—) LES, (●) unsteady, and (○) steady experimental data.

REFERENCES

Alin N., Bensow R.E., Fureby C., Persson T., Ramamurti R., AIAA Paper 2005-1104, 2004.

Alin N., Fureby C., Svennberg U., Sandberg W.C., Ramamurti R. and Bensow R.E., AIAA Paper 2007-1454, 2007.

Bensow. R., Fureby C., Liefvendahl M. and Persson T., 26th Symp. on Naval Hydrodynamics, Rome, Italy, Vol 1, p 117, 2006.

Byun G and Simpson R.L., AIAA J., Vol 44, p 999, 2006.

Chesnakas C.J. and Simpson R.L., J. Fluids Eng., Vol 118, p 268, 1996.

Fureby C., Ercoftac Bulletin, March issue, 2007.

Fureby C., "ILES and LES of Complex Engineering Flows," To appear in ASME J. Fluids Engng., 2007.

Granlund K. and Simpson R., AIAA Paper 2004-729, 2001.

Grinstein F. F., Margolin, L. G. and Rider W. J. (Eds), Implicit Large Eddy Simulation; Computing Turbulent Fluid Dynamics, Cambridge University Press, 2007.

Hosder S., VaTech, Aerospace Engineering, June 15, 2001.

Hosder S. and Simpson R.J., AIAA Paper 2001-1000, 2001.

Huang T.T., Liu H-L., Groves N.C., Forlini T.J., Blanton J. and Gowing S., Proceedings of 19th Symp. on Naval Hydrodynamics, Seoul, Korea, 1992.

Liu H. and Huang T., Naval Surface Warfare Center Carderock Division Technical Report, CRDKNSWC/HD-1298-11, 1998.

Moser R.D., Kim J. and Mansour N.N., Phys. Fluids, Vol 11, p 943, 1999.

Persson T., Bensow R., Fureby C., Alin N., Svennberg U., 25th Symp. on Naval Hydrodynamics, St. John's, Canada, Vol 2, p 261, 2004.

Wikström N., Svennberg U., Alin N. and Fureby C., J. Turbulence, Vol 5, p 29, 2004.

Numerical Error and Uncertainty Analysis for a Propeller in Open Water

Nabila Berchiche and Carl-Erik Janson

nabila.berchiche@chalmers.se, carl-erik.janson@chalmers.se

Chalmers University of Technology, Department of Shipping and Marine Technology, SE-41296 Gothenburg

The complex geometry of a propeller and the complex flow around the propeller introduce local requirements of the grid distribution in order to resolve the boundary layer on the blade, the detailed flow around the leading edge, the trailing edge and in the tip region where the vortex is generated. Of particular interest is also the grid distribution along the vortex core behind the propeller blade. It is extremely difficult to meet all the requirements on the grid distribution. The final grid will therefore be a compromise and this will of course influence the accuracy of the solution in the different parts of the computational model.
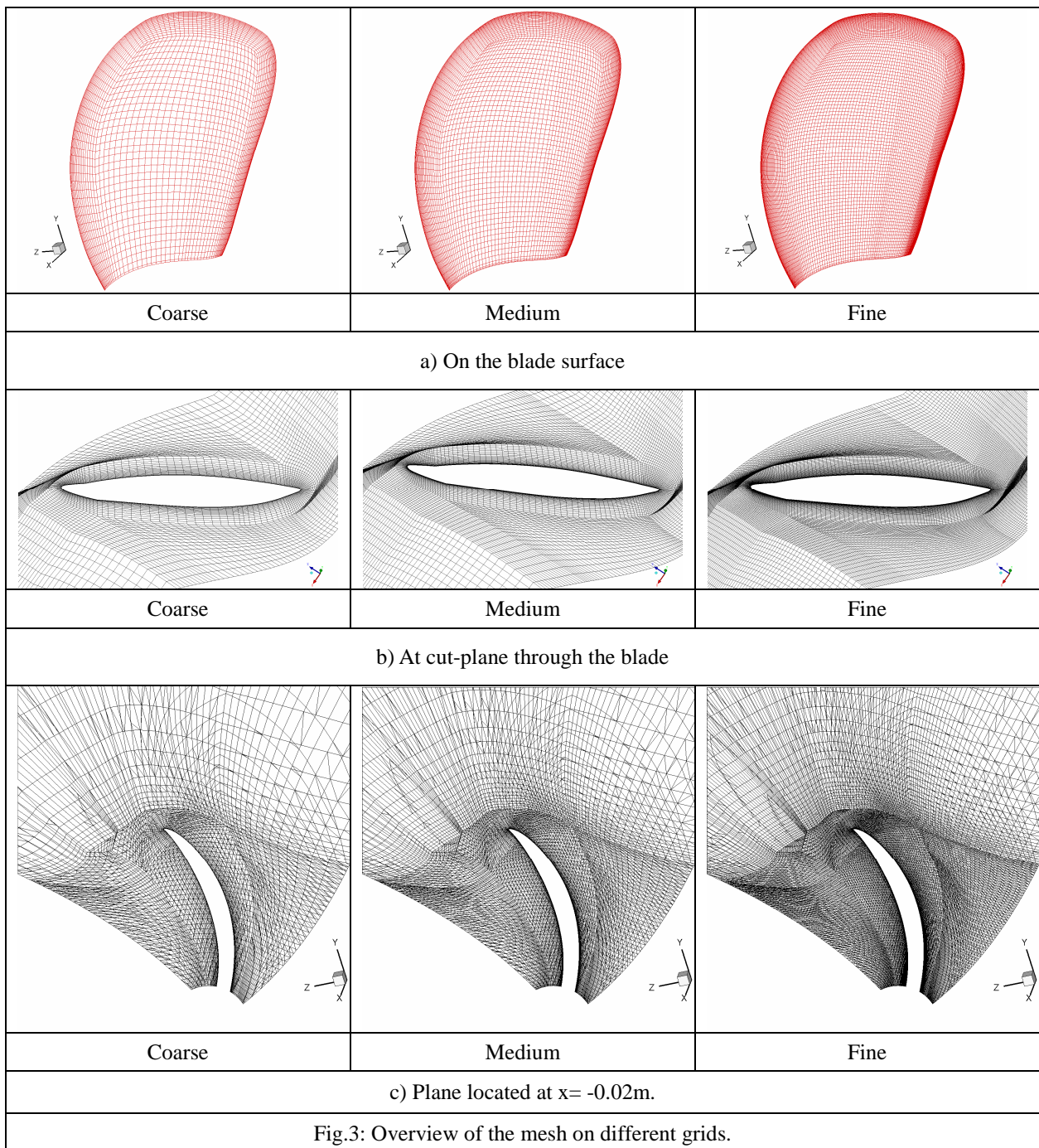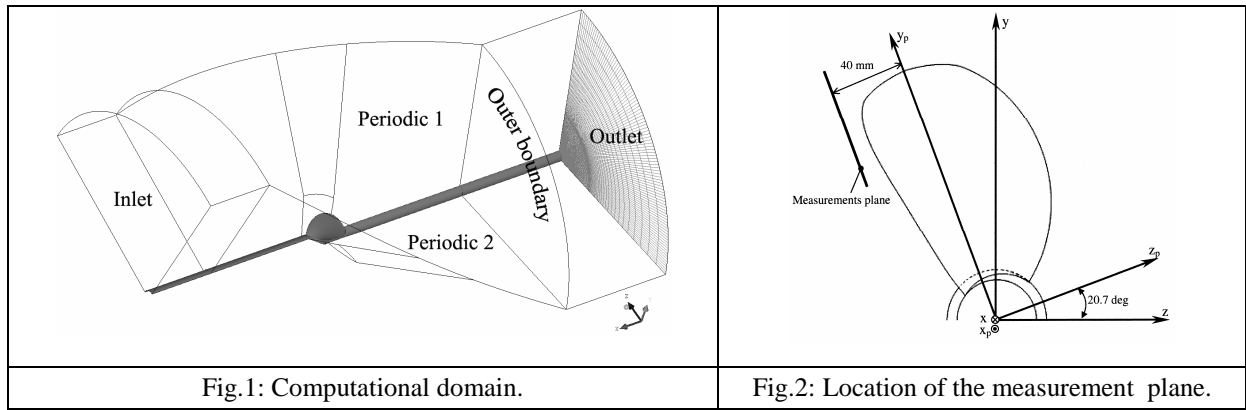
The present work concerns a grid dependence study for a conventional propeller in open water using three grid refinement levels. On the average the grid resolution was increased by a factor square root of 2 in each direction between the refinement levels. The number of cells for the three levels was 0.5, 1.4 and 3.9 millions respectively.

A four-bladed, fixed-pitch propeller of conventional shape, *MARIN report (2003)*, was investigated in the present work. The diameter, D, of the model scale propeller is 0.281m, the boss/diameter ratio is 0.181, the chord/diameter ratio at 0.7R is 0.315 and the blade area ratio is 0.586. Computations were carried out for the model scale propeller. Since the flow in the actual propeller configuration is periodical and stationary, only one blade was modelled. The computational domain, Fig.1, was thus reduced to one blade. The inlet boundary was located at 2D upstream from the propeller centre, the outlet 3D downstream, the outer boundary at 2D from the hub axis and two periodic boundaries on each side of the blade. The hub section was extended in both upstream and downstream boundaries. The grid was generated in ICEM CFD using Hexa mesh. The computational domain, Fig.1, consists of 28 blocks, 9 blocks were used to capture the blade geometry. An O-type grid topology was applied around the propeller blade to achieve a good quality mesh and resolve the boundary layer on the solid surface. In the rest of the domain around the propeller, an H-type grid was applied. The $y+$ was below 1 for all grids. Fig 3a shows the surface mesh on the blade surface for each grid. The grid was refined on the blade near the zones of strong gradients in particular close to the leading edge and the trailing edge. A view of the mesh at a cut-plane through the blade and at a plane located at x= -0.02 are also shown in Fig. 3.

Steady incompressible RANS equations were solved in a single rotating reference frame fixed to the propeller using the CFD software Fluent. A segregated solver with absolute velocity formulation was used. The SIMPLE scheme was used for the pressure-velocity coupling and the pressure was discretized with a second order scheme. The momentum, turbulence kinetic energy and dissipation rate were discretized using a second order upwind scheme. The shear stress transport SST k-ω model, *Menter (1994),* was used to compute the turbulence quantities.

A uniform velocity inlet was assigned at the upstream boundary; a pressure outlet at the downstream boundary; a no-slip solid wall condition was applied on the blade and hub surface, and rotational periodicity was specified on the periodic boundaries. For the outer radial boundary, a slip condition was imposed. The flow condition investigated in this study was based on the experimental condition at an advance coefficient J= 0.4, which was also the design condition of the propeller. The axial inflow velocity V and the number of revolutions of the propeller n were equal to 0.89m/s and 8 rps respectively. The Reynolds number Re = 0.44 10^6 is defined by the rotational velocity at 0.7 non-dimensional radius of the propeller blade and the chord length at that radius. The convergence was assessed by monitoring the history of the residuals of all equations and forces acting on the propeller blade.

The computed thrust and torque coefficients of the three grids are compared to the experimental values in Table 1. The total thrust and torque forces were obtained by integration over the blade surface. The error in K_T seems to decrease as the grid is refined whereas no significant variation is observed for the prediction of K_Q. K_T displays a monotonic convergence but not K_Q.

| Fig.1: Computational domain. | Fig.2: Location of the measurement plane. |

| Coarse | Medium | Fine |

a) On the blade surface

| Coarse | Medium | Fine |

b) At cut-plane through the blade

| Coarse | Medium | Fine |

c) Plane located at x= -0.02m.

Fig.3: Overview of the mesh on different grids.

The difference of K_T is about 3% between the fine and the coarse grid and only 0.14% for K_Q. This might be due to the fact that the number of cells used within the boundary layer was sufficient for all grids and the y+ values were below 1 for all cases. The results obtained with the fine grid show that the prediction of K_T is rather good but not K_Q which is over-predicted by about 8 %. This can be associated to an error in the prediction of the radial distribution of the blade force which might be due to the lack of a proper transition model but this need to be further investigated. This over-prediction of the torque has been also attributed to an over-estimation of the total drag force due to an error in the evaluation of the pressure at the stagnation point, *Bulten and Oprea (2005)*.

The pressure distribution on the blade is similar for all grids and the value of the minimum pressure coefficient, Cp_{min}, is found near the leading edge of the blade close to section 0.95R. However, the value of Cp_{min} varies with the grid resolution. The difference of Cp_{min} between the fine and the coarse grids is about 13.6% which is greater than the difference of K_T and K_Q estimated for same grids. Since Cp_{min} is usually compared to the local cavitation number to asses the risk of cavitation inception, it is therefore important to ensure high grid resolution for a better prediction of Cp_{min}. In his paper, *Li-Da Qing (2006)* conducted a grid study on a highly skewed propeller using six geometrically similar grids and observed same tendencies that the variation of local variables as Cp_{min} with the grid resolution is more significant compared to the variation of the forces on the propeller blades.

An experimental investigation of the vortical flow downstream the propeller model was performed by Marin using Particle Image Velocimetry system (PIV) which measured the three components of the velocity vector in the measurement plane, Fig 2. In the present study, only the axial velocity is used for comparison with the numerical predictions. A comparison of all components with the measured data can be found in *Berchiche and Janson (2006)*. The axial velocity is parallel to the inflow and positive in the main flow direction. Fig. 4 shows a comparison of the non-dimensional axial velocity between the numerical results obtained with all grids and the PIV data at the measurements plane downstream of the propeller. The computed and measured values of the velocities were made non-dimensional by the tip speed πnD and the inflow velocity is subtracted from the axial velocity. The general pattern of the tip vortex in the measurements plane is captured by all grids. However, the velocity magnitudes increased significantly with the grid refinement. The computed maximum and minimum velocities were under-predicted by about 46 % and 41% respectively with the coarse grid, and by about 19% and 6.5% with the fine grid.
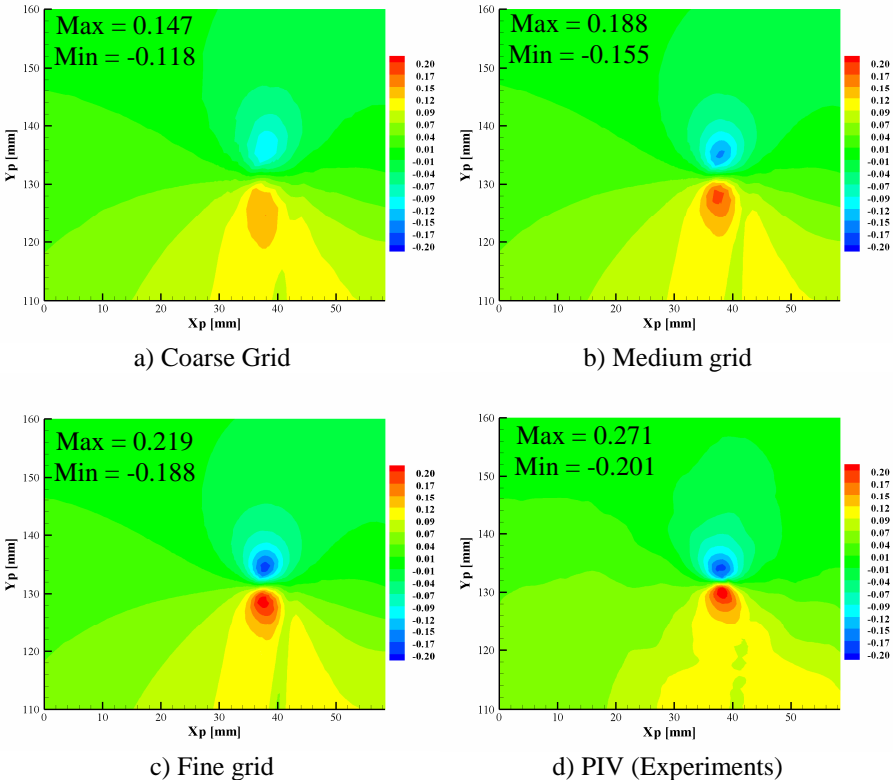
Fig. 4: Comparison of the non-dimensional axial in-plane velocity.

A more formal investigation of the numerical error was also conducted. The error was estimated by Richardson extrapolation as:

$$\delta_{RE} = \phi_i - \phi_0 = \alpha h_i^p$$

Where ϕ_i is the numerical solution of any local or integral scalar quantity on a given grid, ϕ_0 is the exact solution, α is a constant, h_i is the representative grid cell size and p is the observed order of accuracy. ϕ_0, α and p are the three unknown in equation, therefore three grids are required. If the grid refinement ratios h_2/h_1 and h_3/h_2 are equal, the order of accuracy can be obtained from:

$$p = \frac{\log\left(\dfrac{\phi_3 - \phi_2}{\phi_2 - \phi_1}\right)}{\log\left(\dfrac{h_2}{h_1}\right)}$$

And the error $\delta_{RE} = \phi_1 - \phi_0$ from:

$$\delta_{RE} = \frac{\phi_2 - \phi_1}{\left(\dfrac{h_2}{h_1}\right)^p - 1}$$

The convergence condition for three grids is defined by the convergence ratio R:

$$R = \frac{\phi_2 - \phi_1}{\phi_3 - \phi_2}$$

Where ϕ_1 is the solution of the finest grid, ϕ_2 solution of the medium grid and ϕ_3 is the coarse grid solution. Four convergence conditions are possible, *Roache (2003)*:

$0 < R < 1$ $\Rightarrow$ Monotonic convergence
$-1 < R < 0$ $\Rightarrow$ Oscillatory convergence
$R > 1$ $\Rightarrow$ Monotonic divergence
$R < -1$ $\Rightarrow$ Oscillatory divergence

In a grid convergence study with three grids, the solution is convergent if $(\phi_2 - \phi_1)*(\phi_3 - \phi_2)$ is positive and the order of accuracy p is also positive. This means that the solution varies monotonically and has a finite value for a grid cell size equal to zero. The discretization uncertainty U for any local or integral variable is estimated by the procedure proposed by *Eca and Hoekstra (2006)*, which based on the standard Grid Convergence Index, *Roache (1998)*:

- For monotonic convergence, three alternatives for uncertainty estimation are defined depending on the range of the order of accuracy p:

  - For $0.95 \leq p < 2.05$, $U = 1.25\delta_{RE} + U_s$, U_s is the standard deviation of the fit, in our case since only three grids are available, U_s is equal to zero.

  - For $0 < p < 0.95$, $U = \min(1.25\delta_{RE} + U_S, 1.25\Delta_M)$.
  - For $p \geq 2.05$, $U = \max\left(1.25\delta_{RE}^* + U_S, 1.25\Delta_M\right)$, δ_{RE}^* is the error estimate calculated with $p = 2$.

- If monotonic convergence is not observed, $U = 3\Delta_M$, where Δ_M is the maximum difference between all solutions.

Four variables were selected for the grid study: the integral variables K_T and K_Q and two local variables; the pressure coefficient Cp and the axial velocity u at four points (location 1: x=-0.035, y=0.123, z=-0.068, location 2: x=-0.047, y=0.0956, z=-0.08637, location3: x=-0.0377, y=0.1088, z=-0.08285 and location4: x=-0.0376, y=0.1285, z=-0.08285), Table 1. The convergence ratio R, order of accuracy p, extrapolated solution S_c ($S_c = \phi_1 - \delta_{RE}$) and uncertainty for all variables are shown in Table 2. The first point is chosen close to the blade surface in the tip region, the second point is close to the trailing edge of the blade and the last two points are located in the vortex region of the reference plane shown in Fig 2.

Most variables display a monotonic grid convergence except K_Q and Cp at locations 2 and 3 that exhibit an oscillatory convergence and divergence respectively. Therefore, the extrapolated values of K_Q and C_p at locations 2 and 3 could not be estimated, but the uncertainty was determined by multiplying Δ_M by a factor of 3. For the thrust coefficient K_T, p is found higher than the theoretical order used by the solver; the numerical error was thus estimated by replacing p with its theoretical value in Richardson extrapolation. According to *Eca and Hoekstra (2006)*, this super-convergence is not realistic and is an indication that the data are outside the asymptotic range. At location 1, the variable Cp exhibits the theoretical order of accuracy but for the axial velocity, p is smaller than 1. In other locations, p is slightly lower than 2. The different values of the observed order of accuracy p suggest that the data are not in the asymptotic range. This variation of p might be also influenced by the fact that the three grids are not geometrically similar. Furthermore, the propeller geometry is rather complex which makes the convergence of the solutions to a limiting value as the grid is refined very difficult and it is not as smooth as for simple geometries. Using more than three grids, would allow the analysis of different grids triplets and would probably result in a better estimation of the order of accuracy.

Table 1: Values of K_T, $10K_Q$, Cp and u for all grids.

Variable	Fine (grid1)	Medium (grid2)	Coarse (grid3)	Data
K_T	0.1648	0.1662	0.1698	0.165
$10K_Q$	0.2105	0.2114	0.2102	0.195
Cp (1)	-1.85	-1.81	-1.73	-
Cp (2)	0.0536	0.145	0.1185	-
Cp (3)	-1.63	-1.17	-0.77	-
Cp(4)	-0.565	-0.389	-0.502	-
u (1)	-2.012	-1.736	-1.383	-
u (2)	0.684	0.657	0.607	-
u (3)	0.136	0.129	0.118	-
u (4)	1.473	1.252	0.872	-

Table 2: Verification of K_T, $10K_Q$, Cp and u.

Variable	R	p	Sc	U
K_T	0.39	2.7	0.1639	6.25×10^{-3}
$10K_Q$	-0.75	-	-	3.6×10^{-3}
Cp (1)	0.5	2	-1.89	0.05
Cp (2)	-3.4 divergence	-	-	0.274
Cp (3)	1.15 divergence	<0	-	2.58
Cp (4)	0.56	1.66	-0.647	0.1024
u (1)	0.78	0.72	-2.979	0.785
u (2)	0.54	1.76	0.716	0.04
u (3)	0.53	1.83	0.143	9×10^{-3}
u (4)	0.58	1.57	1.778	0.382

The results show that the integrated quantities K_T and K_Q are rather insensitive to the grid resolution while the local quantities such as pressure coefficient and velocity do exhibit a significant change as the grid is refined.
A visual comparison to PIV measurements of the axial velocity components at a plane behind the propeller plane indicates that the computational results of the fine grid are close to the measurements. One may therefore draw the conclusion that the solution using the fine grid is close to grid convergence. The more formal uncertainty analysis of selected integral and local flow quantities showed that the data are not in the asymptotic range and that grid convergence can only be demonstrated in certain parts of the computational domain. A general conclusion is therefore that more grid points are needed together with a better control over the local distribution of the grid points. This will however be a difficult task to realize for a complex case like the flow around a propeller.

References

BERCHICHE, N.; JANSON, C-E. (2006), Numerical computations and comparison to experiments for a propeller in open-water Condition, Ship Technology Research, Vol.53.

BULTEN, N.W.H.; OPREA, I.A. (2005), Consideration on deviations in torque prediction for propellers and waterjets with RANS codes, Marine CFD 2005, Southampton, UK.

ECA, L.; HOEKSTRA, M. (2006), Discrestization Uncertainty Estimation based on a Least Squares version of the Grid Convergence Index, 2nd Workshop on CFD Uncertainty Analysis, Lisbon.

LI, D.-Q. (2006), "Validation of RANS Predictions of Open Water Performance of a Highly Skewed Propeller with Experiments", Conference of Global Chinese Scholars on Hydrodynamics, Shanghai, China.

MARIN report (2003) "Data of Selected Propellers" Report No. 16206-2-RD

MENTER, F.R. (1994), Two-Equation Eddy-Viscosity Turbulence Models for Engineering Applications, AIAA Journal, 32/8, pp.1598-1605.

ROACHE, P.J. (2003), Error bars for CFD, AIAA-2003-048, 41th Aerospace Sciences Meeting, Reno.

ROACHE, P.J. (1998), Verification and validation in Computational Science and Engineering, Hermosa Publishers.

Verification of the PDSTRIP 2-d Radiation Problem Module

Volker Bertram, ENSIETA, volker.bertram@ensieta.fr
Heinrich Söding, TU Hamburg-Harburg, h.soeding@tu-harburg.de

Strip methods for rigid body seakeeping and vertical bending vibrations of ships need a module to compute the two-dimensional hydrodynamic characteristics of a cross section oscillating harmonically and with infinitesimally small amplitude near the free surface (radiation problem). This module needs to handle typical cross sections and typical frequencies. Sutulo and Guedes Soares present a modern Rankine panel method for the 2-d radiation problem, comparing results to assorted classical methods with good agreement. Bertram et al. (2006) describe the public-domain strip method PDSTRIP.

The theory behind the PDSTRIP 2-d module is described in detail in *Bertram et al. (2006), Bertram and Söding (2007)*. The module computes the 2-d potential flow of an incompressible fluid to determine the added mass and damping of ship cross sections. The flow is assumed to be excited alone by sinusoidal translations of the body in y (positive to port) and z (positive down) direction, and by a sinusoidal rotation about the coordinate origin. The motions are assumed to be small.

The problem is formulated as a boundary value problem, with the Laplace equation as fundamental field equation, subject to boundary conditions:

1. Decay of disturbance far away from the cross section

2. At the undisturbed free surface, a condition combining the conditions of constant pressure and no flow through the real (wavy) surface, linearized with respect to wave steepness.

3. There is no flow through the (submerged part of the) hull contour:

4. Waves created by the hull propagate away from the hull. To formulate this as a boundary condition, the formula for linear (Airy) waves is applied.

The numerical solution follows a patch method, which computes the forces more accurately than a traditional panel method. The patch method approximates the potential as a superposition of point sources. These sources are located within the section contour or above the line $z = 0$, i.e. outside the fluid domain of interest. For symmetrical sections, mirror images of sources on both sides of the symmetry plane $y = 0$ are used.

The section contour is defined by given offset points. For each contour segment between adjacent offset points, one source is generated near to the midpoint between the two offset points, however shifted from the midpoint to the interior of the section by 1/20 of the segment length. Along the average water surface $z = 0$ grid points are generated automatically. Near to the body, their distance is equal to 1.5 of the offset point distance on the contour at the waterline. Farther to the sides, the distance increases by a factor of 1.5 from one segment to the next, until a maximum distance of 1/12 of a wavelength (of the waves generated by the body oscillations) is attained. Source points are again located above the mid-points of each free-surface segment, here however at a distance of one segment length. The number of free-surface grid points used is 55 for a symmetrical body of which only one half needs to be discretized, and $2 \cdot 55$ for asymmetrical bodies where the water surface to both sides of the section must be discretized.

Whereas in the panel method the boundary conditions are, usually, satisfied at a 'collocation point' in the middle of each segment, in the patch method the integral of the boundary condition over each segment has to be used. For the body boundary condition, the flux induced by a source at S through a segment between points A and B is equal to the source strength times

the angle ASB divided by 2π. The total flux is the sum of the fluxes coming from all sources. This method is used also for one term in the free-surface condition which – after integration over a segment – is also the flux through that segment. The integral over the other term is evaluated by a simple approximation which gives the correct result if the source is located near to the midpoint of the segment AB. For sources farther off from the segment the errors are small anyway.

The bottom condition is satisfied automatically by the superposition of Rankine sources; however, for vertical motion the accuracy is improved by adding another source and specifying the additional condition that the sum of all source strengths is zero. The location of the additional source is at $y = 0$ at a distance above the waterline of $1/2$ the distance to the farthest free-surface grid point.

The radiation condition is integrated over a panel between points A (nearer to the body) and B (farther out). Using the same approximation as for the free-surface condition results in simple condition, requiring only the evaluation of the potentials at four points. This condition is applied in the outer range of the free surface, for asymmetrical bodies on both sides. The details of satisfying the radiation condition are important for the accuracy of the method and for the necessary length of the discretized part of the free surface. This length, in turn, influences the required computer time. Therefore a number of improvements have been made in the treatment of the radiation condition, e.g. a new approach to implement numerical wave damping in the outer region involving a shift in points where the potential is evaluated. See *Bertram and Söding (2007)* for details.

The linear equation system resulting from the boundary conditions is solved for the complex amplitudes of all source strengths. The flow potential follows then from a superposition of all sources. The linearized Bernoulli's equation couples pressures to the time derivative of the potential only, easily evaluated for the harmonically oscillating potential. The complex pressure amplitude is integrated over the section contour to give the complex amplitudes of horizontal force, vertical force and x (roll) moment, each for horizontal, vertical and rolling motion of the section with unit amplitude.

Considering one of the three force terms $\hat{f}$ due to one of the three motion amplitudes $\hat{u}$, where $\hat{\ }$ denotes the complex amplitude, we can then write the proportionality

$$\hat{f} = -m(-\omega^2\hat{u}) - d(i\omega\hat{u}) \qquad (1)$$

m is the added mass, d the damping, ω the frequency. The 3 forces due to 3 motions yield 3×3 matrices for m and d, which depend on the motion frequency.

The first test case is a half-submerged circle at the free surface. The contour oscillated at different frequencies as expressed by the nondimensional frequency $\omega' = \omega^2 r/g$, where r is the radius of the circle, $g = 9.81$ m/s^2. The added mass and damping coefficients are for unit motion. The added mass for sway and heave is made non-dimensional with the displaced mass of the submerged cross section, i.e. for example for sway $m'_{22} = m_{22}/(\frac{1}{2}\rho \cdot \pi r^2)$, where ρ is the density. The corresponding damping coefficients were nondimensionalized similarly, but also divided by ω. Sutulo and Guedes Soares (2004) ensured in their work that results a sufficient number of elements was used on free surface and body contour to avoid significant discretization errors. Test computations with 4, 8, 16 and 32 equidistant elements over the circumference of the semi-circle showed rapid convergence, Fig.1. The results for 16 and 32 elements coincided within plotting accuracy. Results for the grid with 32 elements were then taken as grid independent and used for comparison with other computations. Fig.2 and Fig.3 show very good agreement with Sutulo and Guedes Soares. The default frequencies used in PDSTRIP were used to compute our results, but the plots were cut off at $\omega' = 2.5$, as the plots of Sutulo and Guedes Soares.
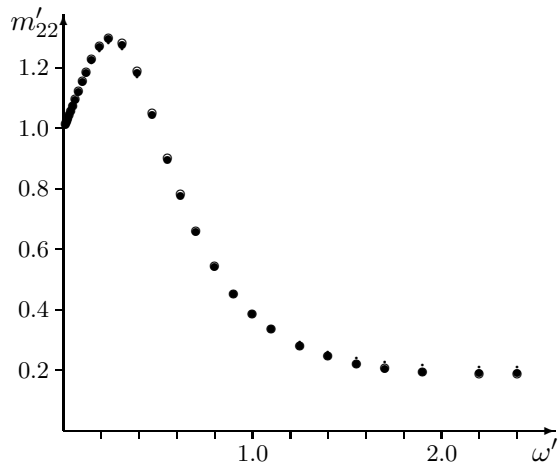
Fig.1: Semi-circle: Added mass coefficients for sway; present method
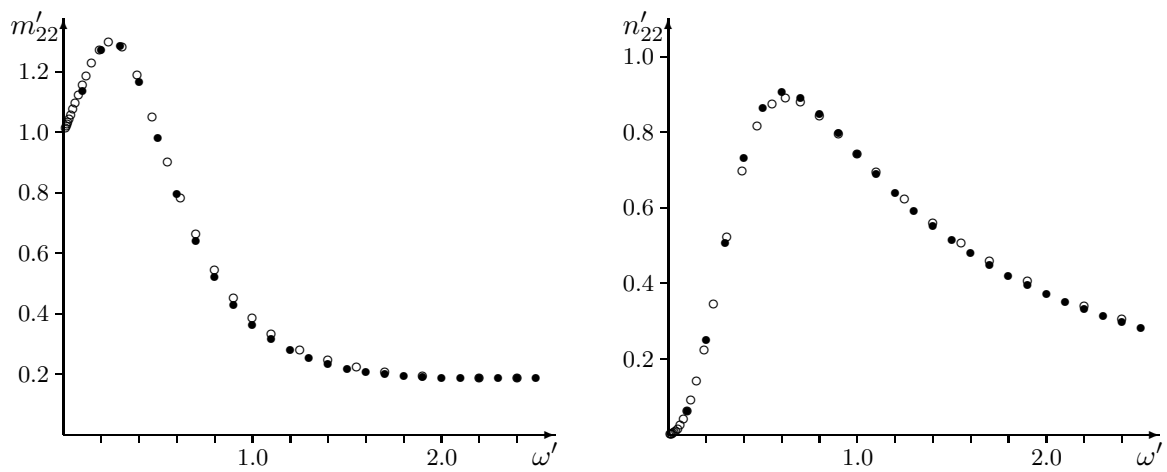· 4 elements, • 8 elements, ○ 16 and 32 elements

Fig.2: Semi-circle: Added mass (left) and damping coefficients (right) for sway;
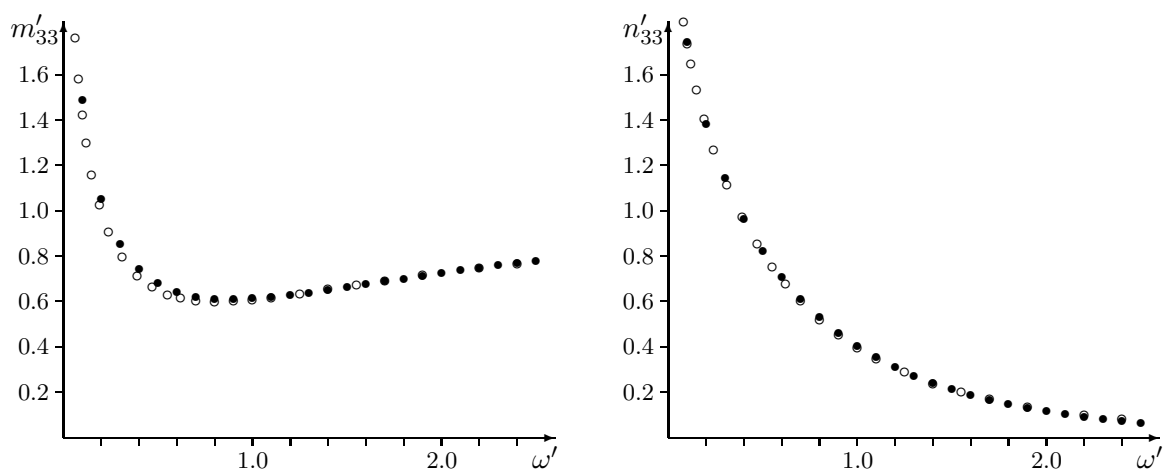• Sutulo and Guedes Soares, ○ present method

Fig.3: Semi-circle: Added mass (left) and damping coefficients (right) for heave;
• Sutulo and Guedes Soares, ○ present method

The next test case is a flat rectangle with breadth-to-draft ratio $B/T = 10$, Fig.4. The added mass and damping were non-dimensionalized as follows:

$$m'_{22} = \frac{m_{22}}{\rho\pi T^2}; \qquad m'_{24} = \frac{m_{24}}{\rho\pi(B/2)^3}; \qquad m'_{44} = \frac{m_{44}}{\rho\pi(B/2)^4}; \qquad m'_{33} = \frac{m_{33}}{\rho\pi(B/2)^2} \qquad (2)$$

The corresponding damping coefficients were nondimensionalized similarly but also divided by ω. Results are plotted over the nondimensional parameter $kB/2$, with $k = \omega^2/g$. The agreement between the two methods is generally excellent, Fig.5. Only for damping involving roll motion (n_{24} and n_{44}), the patch method in PDSTRIP yields slightly lower values near the peak.
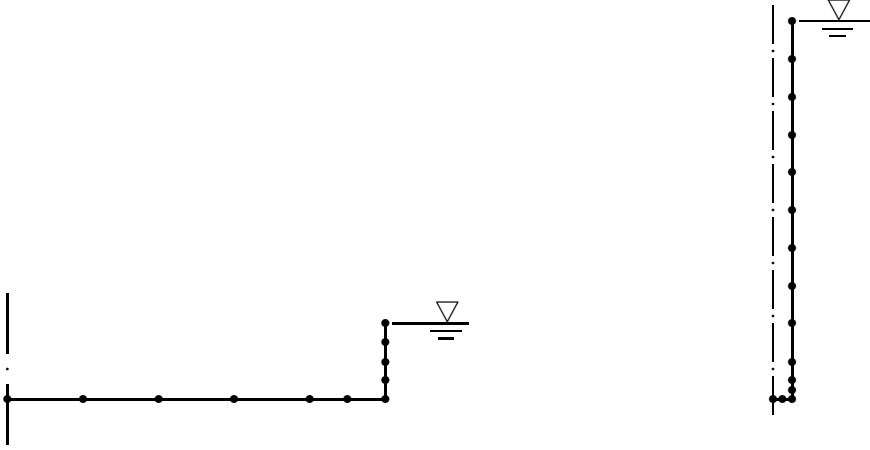
Fig.4: Grid for flat (left) and the thin (right) rectangle; points indicate patch vertices

The third test case is a rectangle with breadth-to-draft ratio $B/T = 1/10$, Fig.4. The added mass and damping were non-dimensionalized as follows:

$$m'_{22} = \frac{m_{22}}{\rho\pi T^2}; \qquad m'_{24} = \frac{m_{24}}{\rho\pi T^3}; \qquad m'_{44} = \frac{m_{44}}{\rho\pi T^4}; \qquad m'_{33} = \frac{m_{33}}{\rho\pi(B/2)^2} \qquad (3)$$

The corresponding damping coefficients were nondimensionalized similarly but also divided by ω. Results are plotted over the nondimensional parameter $kB/2$, with $k = \omega^2/g$. The agreement between the two methods is again very good, Figs.6 and 7.

In conclusion, the results verify the correct implementation of the radiation problem module. The results agree well with other modern methods for a variety of geometries. The source code in Fortran 90X is available from the authors upon request.

References

BERTRAM, V.; SÖDING, H. (2007), *A patch method to computate added mass and damping for a harmonically oscillating cross section at a free surface*, J. South-African Mechanical Engineers (submitted)

BERTRAM, V.; VEELO, B.; SÖDING, H.; GRAF, K. (2006), *Development of a freely available strip method for seakeeping*, 5th Conf. Computer and IT Applications in the Maritime Industries (COMPIT'06), Leiden, pp.356-368

SUTULO, S.; GUEDES SOARES, C. (2004), *A boundary integral equations method for computing inertial and damping characteristics of arbitrary contours in deep fluid*, Ship Technology Research 51, pp.69-93

Fig.5: Flat rectangle: Added mass (left) and damping coefficients (right) from top to bottom: sway, heave, sway-heave cross term, roll; • Sutulo and Guedes Soares, ∘ present method

Fig.6: Thin rectangle: Added mass (left) and damping coefficients (right) from top to bottom: sway, heave, sway-heave cross term, roll; ● Sutulo and Guedes Soares, ○ present method

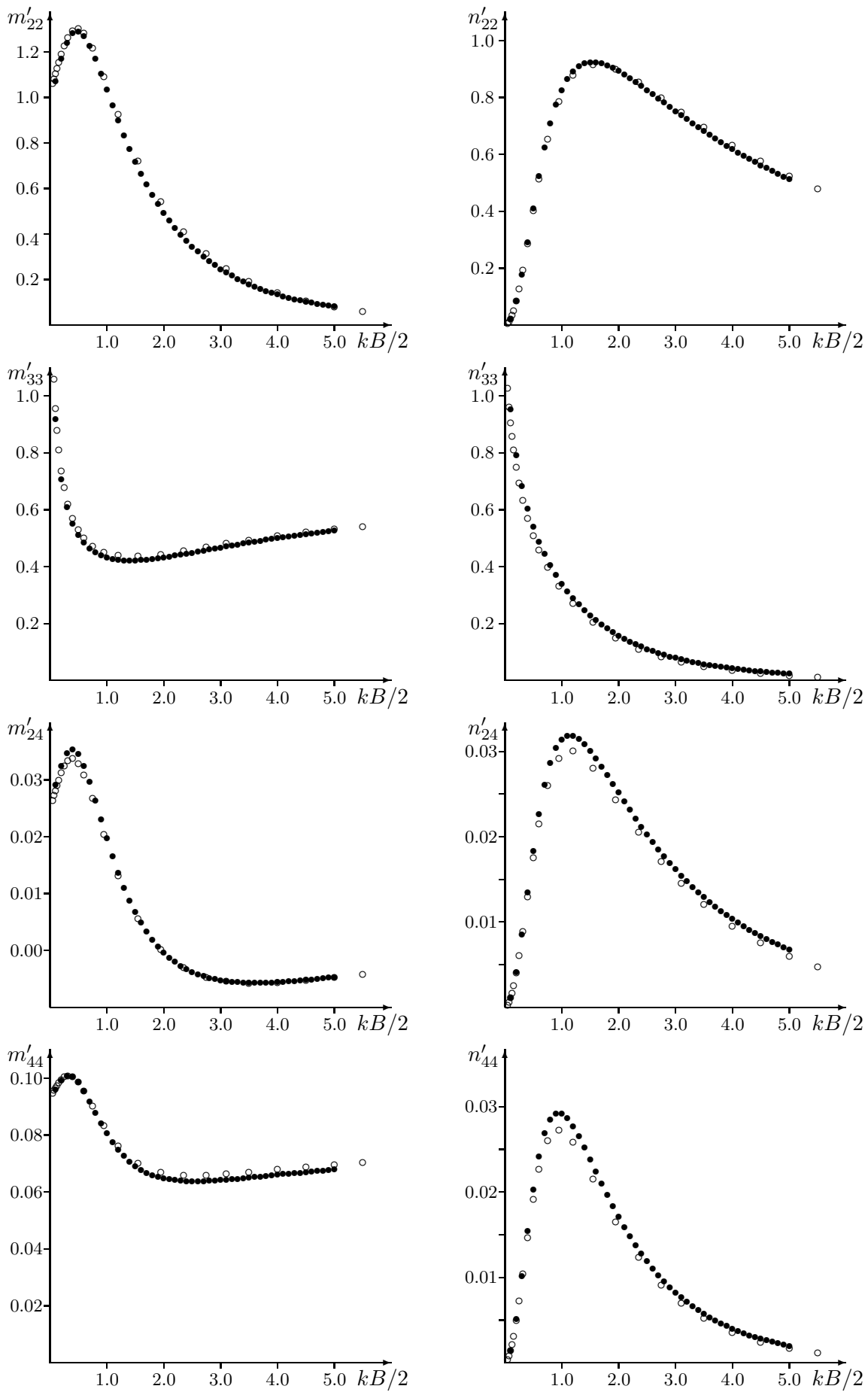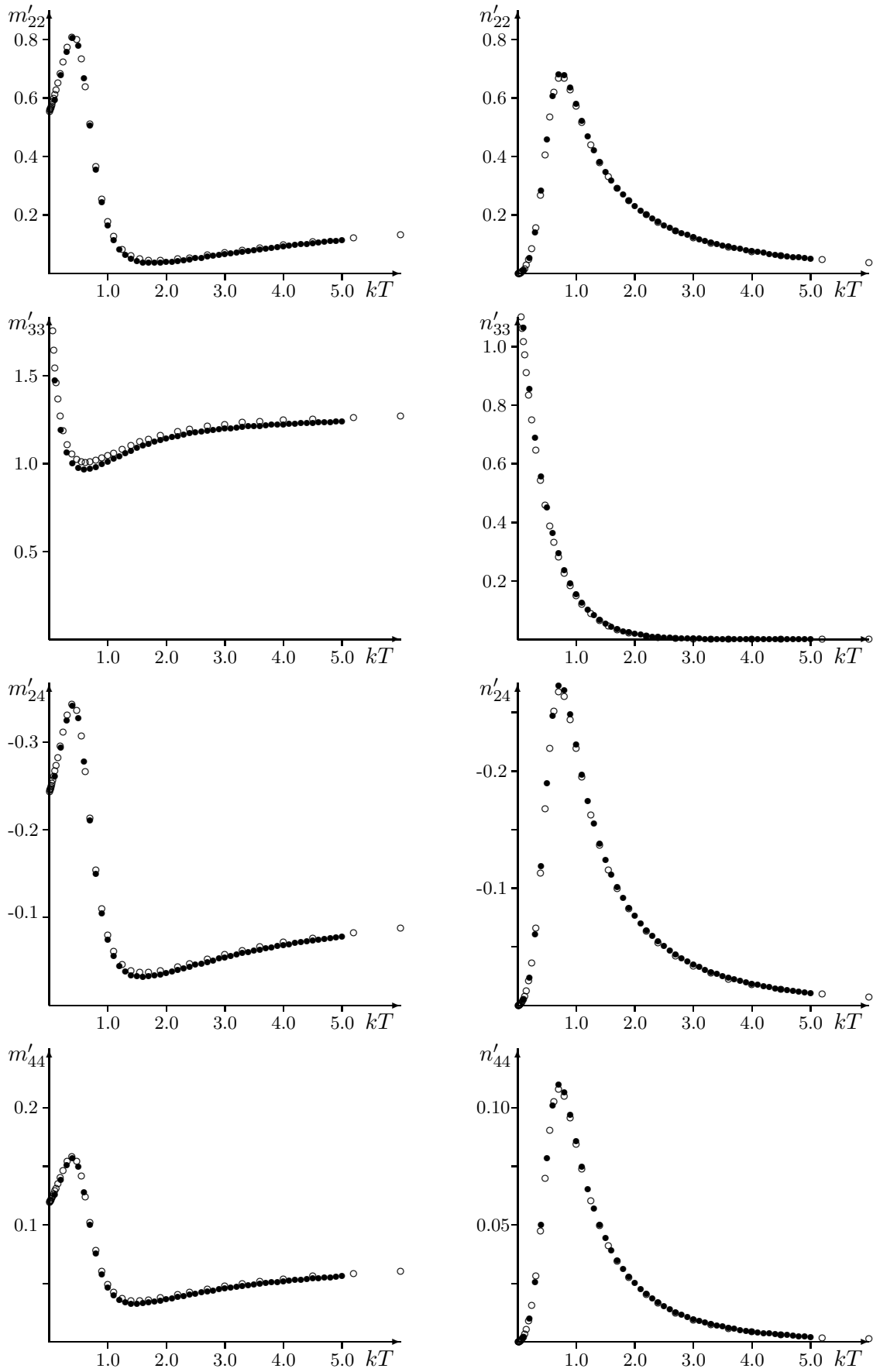# Numerical and experimental investigation of sloshing phenomena in conditions of low filling ratios.

B.Bouscasse[1], A.Colagrossi[1,2], G.Colicchio[1,2], C.Lugni[1,2]

1. INSEAN, Italian Ship Model Basin, Rome
2. CESOS: Centre of Excellence for Ship and Ocean Structures, NTNU, Trondheim, Norway.

Introduction

A numerical model and experiments have been used to study some features of the flow developing in tanks forced to move with harmonic motion. Attention has been focused on the conditions of low filling ratios. In this cases, non-linearities are easily developed, and their features are strongly dependent on the following parameters: amplitude and frequency of oscillation and filling height. Here the parameter are chosen so to cause the occurrence of bore (according to [8]. Ondular bore and, critical cases, breaking bores will be shown. The modelling of these features requires a robust and accurate numerical solver, and the Smoothed Particle Hydrodynamics (SPH) has proved its ability to model them in the direct comparison with the experiments. In [6], the same solver has also shown the ability to model other, strongly non linear events as the dam-break flows, sloshing flows, ship flows and wave breaking process.

Experimental set up

A global sketch of the experimental setup is shown in left plot of figure 1: the tank is $L = 1$ m long, $b = 0.1$ m wide and is filled with water up to a height h. To ensure a purely sinusoidal motion $A sin(2\pi t/T)$ along the longitudinal direction, an *ad hoc* mechanical system has been used. Here A is the displacement amplitude and T is the period of the prescribed motion. The geometry of the tank, *i.e.* $b/L = 0.1$, ensures an almost-2D flow in the main tank plane.

Two capacitance wave probes are placed at the sides of the tank. The first one η_1 is positioned at a distance of 1 cm from one side, the second one η_2 at distance of 5 cm. During the tests, flow visualizations were performed through low- and high-speed digital video cameras. In particular, a low-speed camera (JAI CV-M2) with spatial resolution 1600x1200 pixels and frequency rate equal to 15 Hz was placed in front of the tank and sufficiently far from it to record the global behavior of the wave propagating. Further, a high-speed camera was placed closer to the front wall. Finally, a wire potentiometer was used for a direct measurement of the position of the tank. Particular care has been devoted to the synchronization of the several acquisition systems with different sampling rates, used for the recording of the signals. A suitable synchronizer has been used to trigger the start of the several acquisition systems at the selected time instants.

Numerical methods

Governing Field Equations The fluid evolution is governed by the Navier-Stokes equation in the domain Ω

$$\frac{\mathrm{D}\boldsymbol{u}}{\mathrm{D}t} = -\frac{\nabla p}{\rho} + \boldsymbol{f_v}(\boldsymbol{x}, t) + \boldsymbol{f}(\boldsymbol{x}, t) \tag{1}$$

where $\boldsymbol{f_v}(\boldsymbol{x}, t)$ is the viscous force and $\boldsymbol{f}(\boldsymbol{x}, t)$ are the external non inertial forces (see [3]).

Two strategies can then be adopted for the solution of the water domain. The first one is to consider the flow incompressible, implying that its velocity $\boldsymbol{u}$ is divergence free. Inserting this constraint into the Navier-Stokes equation leads to a Poisson equation for the pressure field p (this approach is usually used for the incompressible Navier-Stokes solvers). The second strategy (used in the SPH method) considers the flow as weakly-compressible, meaning that the pressure field is linked directly to the density field through an equation of state for example the equation $p = c_0^2 (\rho - \rho_0)$ can be used. The weakly-compressible assumption implies that the speed of sound c_0 must be at least one order of magnitude greater than the maximum flow velocity.

CSPH (Corrected Smoothed Particles Hydrodynamic) The corrected Smoothed Particle Hydrodynamics (cSPH) mathematical model was developed into a join collaboration between INSEAN and Ecole Centrale de Nantes. The main details of the method are described in [3] and [4].

The basic idea is to consider a set of N particles distributed over the fluid domain Ω. Each particle is associated with a *kernel* (or *smoothing*) function W, and moves in the force field generated by the entire particles system. The mass conservation is intrinsically enforced since each particle has a constant mass all along the simulation. The SPH is a meshless method and all the variables are represented through interpolation integrals with suitable kernel functions W, (see *i.e.* [7] for a discussion of meshless methods). The essential features of the resulting algorithm are the complete absence of a computational grid and a fully Lagrangian character.

In discrete form $W_j(\boldsymbol{x}_i)$ indicates the kernel function centered on the particle j and evaluated in the generic point $\boldsymbol{x}_i$. In the following, the particle function $c_i = \sum_{k=1}^{N} W_k(\boldsymbol{x}_i)\, dV_k$ will be used; the summation is on the whole set of particle while dV_k indicates the volume of the generic particle k. Inserting the discrete formulation of the spatial derivatives, obtained through the integral interpolation, into the continuity and momentum equations, two systems of evolution equations for the ith particle are derived:

$$
A) \begin{cases}
\dfrac{\mathrm{D}ln\mathcal{J}_i}{\mathrm{D}t} = \displaystyle\sum_{j=1}^{N} \boldsymbol{u}_j \cdot \nabla W_j^{MLS}(\boldsymbol{x}_i)\, dV_j \\[2ex]
\dfrac{\mathrm{D}\boldsymbol{u}_i}{\mathrm{D}t} = \displaystyle\sum_{j=1}^{N} p_j \nabla W_j^{MLS}(\boldsymbol{x}_i)\, dV_j + \\[2ex]
\qquad \boldsymbol{f_v}(\boldsymbol{x}_i, t) + \boldsymbol{f}(\boldsymbol{x}_i, t)
\end{cases}
\quad
B) \begin{cases}
\dfrac{\mathrm{D}ln\mathcal{J}_i}{\mathrm{D}t} = \displaystyle\sum_{j=1}^{N} (\boldsymbol{u}_j - \boldsymbol{u}_i) \cdot \nabla W_j(\boldsymbol{x}_i)/\, c_i\, dV_j \\[2ex]
\dfrac{\mathrm{D}\boldsymbol{u}_i}{\mathrm{D}t} = \displaystyle\sum_{j=1}^{N} \left[\dfrac{p_j}{c_j} + \dfrac{p_i}{c_i} \right] \nabla W_j(\boldsymbol{x}_i)\, dV_j + \\[2ex]
\qquad \boldsymbol{f_v}(\boldsymbol{x}_i, t) + \boldsymbol{f}(\boldsymbol{x}_i, t)
\end{cases}
\tag{2}
$$

where $\mathcal{J}_i(t)$ is the ratio $dV_i(t)/dV_i(t=0)$ and W^{MLS} is the moving least square kernel defined in [7]. The set A of the evolution equations is used when the matrix which defines the W^{MLS} kernel is well-conditioned while the set B is used in the other cases (see [3]).

The evolution equations B are quite close to the standard SPH equations and present the same characteristics of robustness which are relevant to follow complex free surface dynamics. On the other hand the set of equation A permits a more accurate evaluation inside the bulk of the fluid, because of the MLS kernel.

Once $\mathcal{J}_i$ is evaluated, it is possible to calculate the volume distribution of the generic i-th particle: $dV_i(t) = \mathcal{J}_i\, dV_i(t=0)$. The density field is derived through the use of the MLS kernel:

$$
\rho(\boldsymbol{x}_i) = \sum_j m_j\, W_j^{MLS}(\boldsymbol{x}_i)\, dV_j
\tag{3}
$$

where m_j is the mass of the generic j-th particle. The mass distribution has to be set in the beginning of the simulation, and the mass of each particle does not change during the time evolution. In equation (3), the MLS kernel is used only if the matrix, which defines this type of kernel, is well conditioned, otherwise the Shepard kernel W^S is adopted.

The free-surface boundary conditions are easily handled by the SPH method. More in detail, due to the Lagrangian character of the solver, the kinematic condition is intrinsically satisfied while the dynamic condition must be enforced as described in [4]. The solid boundaries are modeled through a 'ghost particles' technique. It consists in the local mirroring of the fluid with respect to the solid boundary for a length $3h$ inside the wall.

The viscous term $\boldsymbol{f_v}$ is modelled as described in [1], while the boundary layer effect is neglected because a free-slip condition is assumed on the tank walls.

The discrete divergence operator, on the right hand side of equations (2), has to be filtered in space at each time step. This permits to avoid unphysical high-frequency oscillations of the particle's volume, but causes numerical noise on the pressure field, and therefore on local loads on the tank wall. The numerical aspects of this correction are still under investigations.

The evolution equations can be stepped forward in time by any ODE integrator. In the present implementation a forth-order Runge Kutta is adopted with a dynamic choice of the time step
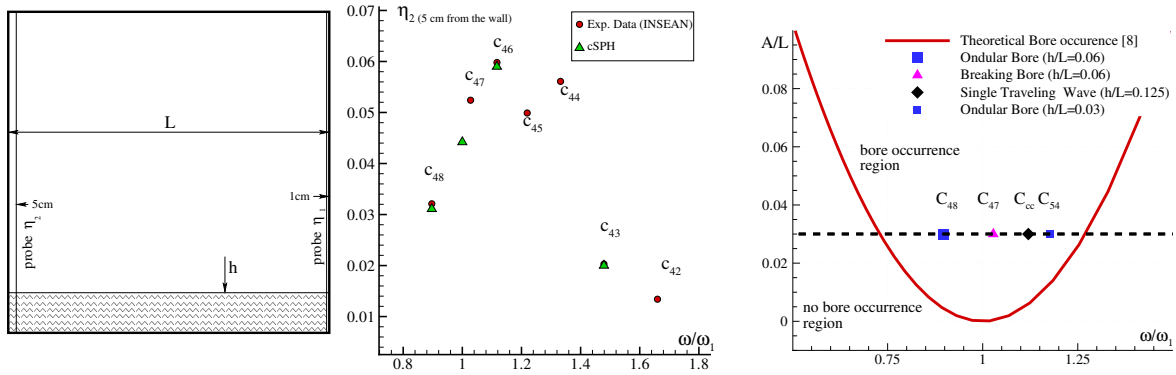
δt according to stability constraints.

Analysis

Figure 1: Left: sketch of the problem. Center: Maximum wave elevation for the sway excitation ($A = 0.03L$, $h = 0.06L$). Right: Occurrence diagram of bore type propagation.

case	h/L	ω/ω_1	case	h/L	ω/ω_1
C_{54}	0.030	1.178	C_{47}	0.060	1.028
C_{48}	0.060	0.897	C_{cc}	0.125	1.120

Table 1: Parameters of the analyzed test cases. For each case $A/L = 0.03$.

Identification of sloshing regimes   This study is focused on the analysis of swaying tanks in conditions of filling ratios $h/L < 0.337$ and with frequency of oscillations in the range $[0.8, 1.8]\omega_1$, where ω_1 is the first natural sloshing period. These conditions imply that a *hard spring type* regime [5] realizes, that is the most energetic sloshing motions develop for frequencies of oscillation slightly higher than the natural frequency. Here, only $A = 0.03L$ will be analyzed.

The center plot in figure 1 shows the numerical and experimental average maximum wave height measured at $5cm$ from the wall (see left plot of the same figure). The behaviour corresponds to the one described in [5]. The circles in the plots correspond to the experimental data collected at INSEAN, while the triangles correspond to the numerical data obtained through the cSPH simulations. The labels shown in the plots are inherited from the experimental campaign and they will be used in the following to identify the different runs.

The range of frequency that will be analyzed in the following is wide and we aim to highlight the features of the flow developing. The response amplitude operator in figure 1 refers to an amplitude of oscillation $A = 0.03L$ and filling height $h = 0.06L$ (center plot). The maximum wave height doubles the initial water height. Once a critical frequency is overcome, say $\omega > 1.4\omega_1$, the amplitude of motion decays abruptly. The analysis of the experimental images and of the numerical simulations shows an almost linear behaviour of the free surface, *i.e.* it is the results of the superposition of sinusoidal standing waves.

The response operator shows that for $\omega/\omega_1 \in (0.8, 1.2)$ the strong non-linear effects take place. From the theory in [8] (see right plot of figure 1) indicates that, there, the waves always propagate in a bore form.

Propagation of ondular bores   The left experimental pictures of figure 2 show the flow developing for the test C_{54} (see table 1). It is an ondular bore propagation. The comparison with the numerical solution left-bottom plot of figure 2 shows that the general behaviour is well captured. In cSPH simulation, the front of the bore breaks with a plunging jet with characteristic length of about 1cm. The surface tension (not modelled in the present numerical solver) prevents this phenomenon in experiments. Figure 3 shows the records of numerical
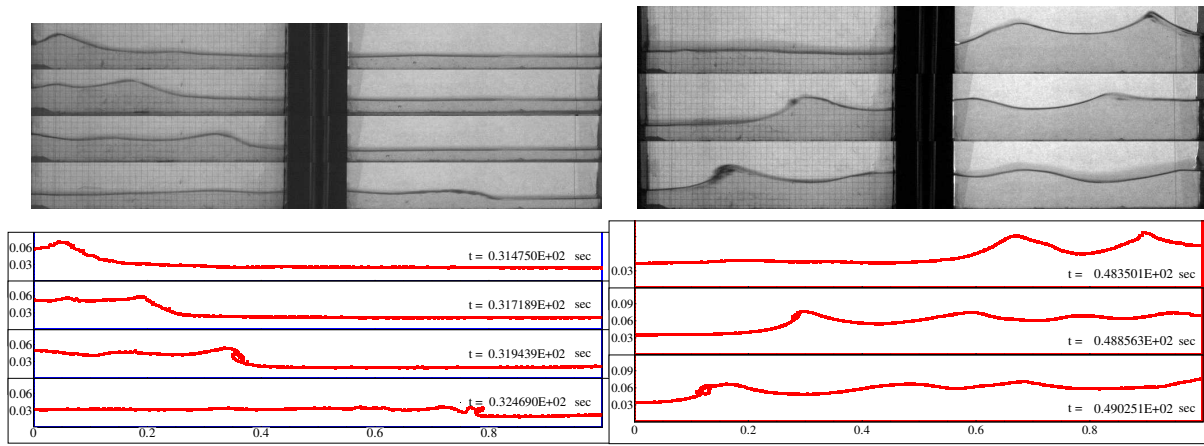
Figure 2: Experimental (top) and numerical (bottom) evolution of the free surface for the cases C_{54} (left) and C_{48} (right) (see table 1).

and experimental wave elevation at 5cm from the wall. The comparison is satisfactory, but for the maximum amplitude, which is higher in the numerical data, because of the breaking phenomenon. Moreover, the experimental data present successive local maxima related to the wave train following the bore front. They are hidden in the numerical solution by the presence of the breaking reflected by the wall and interacting with the following waves. This is more clearly visible in left plot of figure 4, where the contour plots of the numerical wave heights are plotted in the time-space plane. At $t/T = -0.2$ the breaking front is reflected by the wall and interacts with the two secondary waves. In this figure the celerity of the bore front is approximated by $\sqrt{gh}$ when it leaves the wall and increases to $2\sqrt{gh}$ before impacting the opposite side. Case
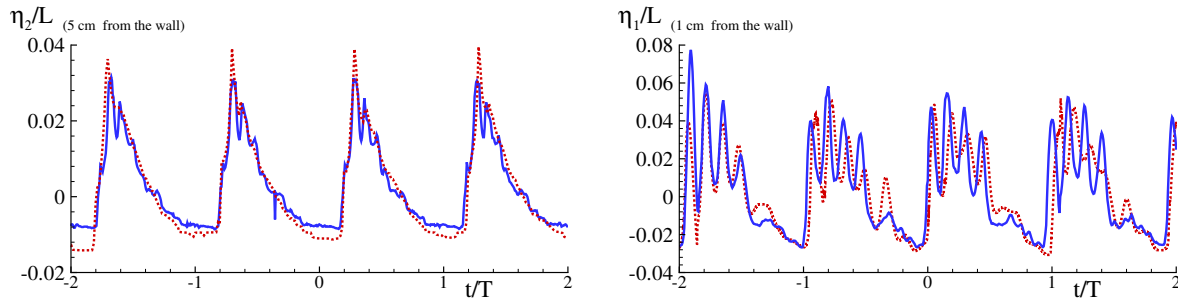
Figure 3: Wave height close to the wall for the cases C_{54} (left) and C_{48} (right) (see table 1. The solid line represents the experimental measurements, the dashed line stands for the numerical solution.
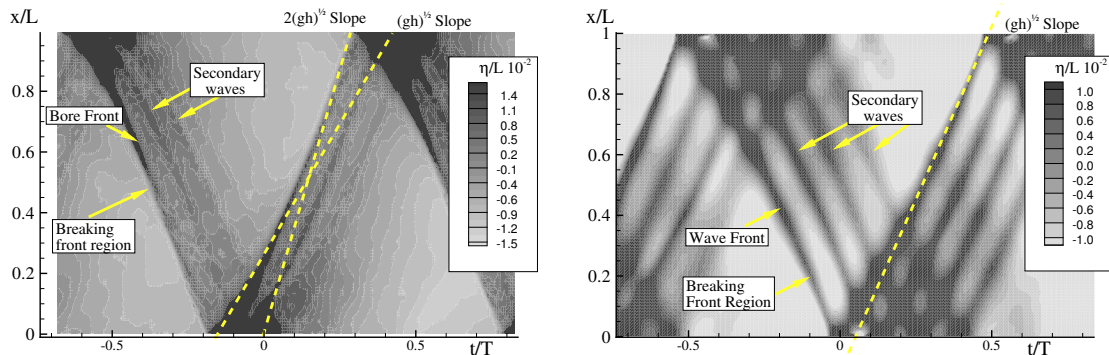
Figure 4: Evolution of the wave height in the cases C_{54} and C_{48} respectively from left to right.

C_{48} refers to a smaller excitation frequency, and double filling height. These parameters cause a more intense ondular bore with respect to the previous case. It is also characterized by a higher wave train and by a breaking stage realizing closer to the tank wall. The latter prevents

the development of a proper breaking front. These features are present both in the experiments and in the numerical simulations as shown by the right plots of figure 2. Such a similar good agreement is present in figure 3, where the wave heights η_1 (see figure 1 for definition) on the wall are compared. Both the tools of analysis show the presence of four peak of the η_1 time record. They are due to the presence of three waves following the bore front in the wave train as made evident in the right of figure 4. The same plot shows that the bore front travels with a celerity close to $\sqrt{gh}$.
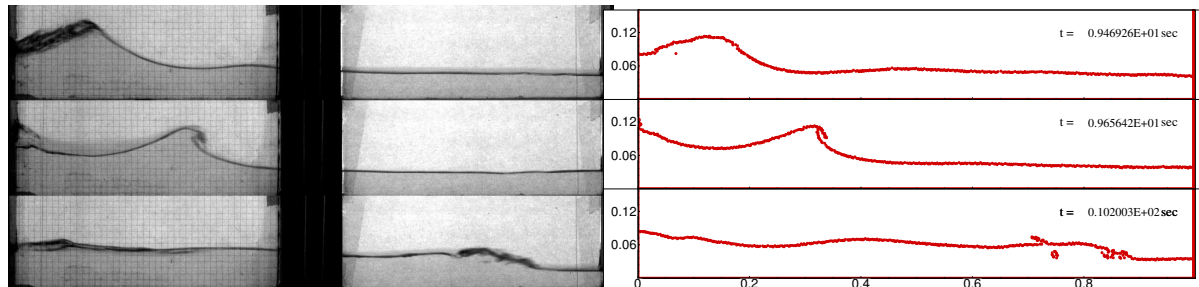

Figure 5: Experimental (left) and numerical (right) evolution of the free surface for the case C_{47} (see table 1).
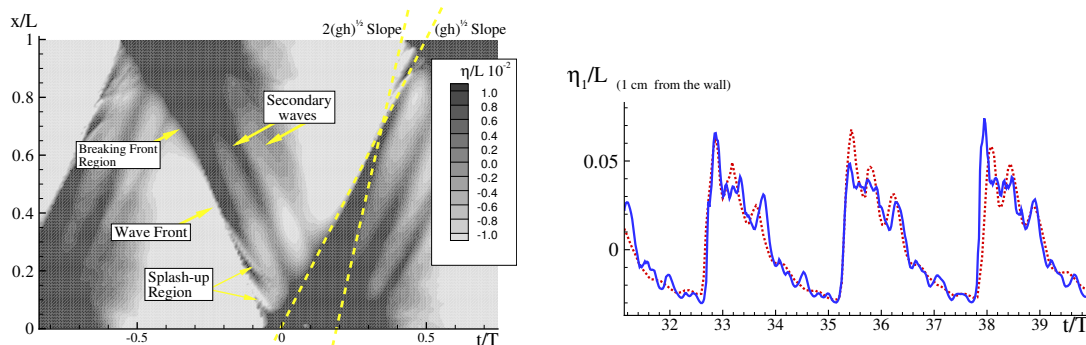

Figure 6: Evolution of the wave height in time-space plane (left) and wave height close to the wall versus time (right) for the case C_{47}

Propagation of breaking bores   In the previous paragraphs, the evolution of the free surface has been analyzed for frequencies both in the higher and lower neighbourhood of the first natural one. In the test case C_{47} (see table 1 the ratio $\omega/\omega_1 \simeq 1$ and, as show for the case C_{54}, the free surface is characterized by the presence of an ondular bore (see figure 5). Differently from what noticed before, here both the numerical data and the experimental images present a breaking front already developing before the mid of the tank. This means that a breaking bore develops. Its trace is highlighted on the time-space plane of figure 6. The same figure shows the presence of two secondary waves as in case C_{54}, confirmed by the three peaks of the wave height, recorded close to the wall (right side of figure 6). Another feature of the breaking bore is the presence of the splash-up region, whose trace are visible in the time-space plane, when the bore front approaches the opposite wall. When the splash-up appears, the bore front changes its celerity from $\sqrt{gh}$ to $2\sqrt{gh}$.

Sloshing steep wave impacting against walls   Further increasing the filling ratio up to 0.125, while ω is slightly higher than the natural frequency ω_1, the ondular bore disappears for a single wave-front that moves with a celerity $2\sqrt{gh}$. When approaching the opposite wall, it becomes very steep and, eventually, breaks against the wall. This is the critical condition studied in [3], because of the violent and localized impacts on the tank wall. Left figure 7 shows the evolution of the free-surface up to the impact, while the right side gives the wave evolution on the time-space plane. Here the propagation of the wave front is highlighted as well as the effect of the impact on the wall. This one causes a high run-up, whose maximum value is reached
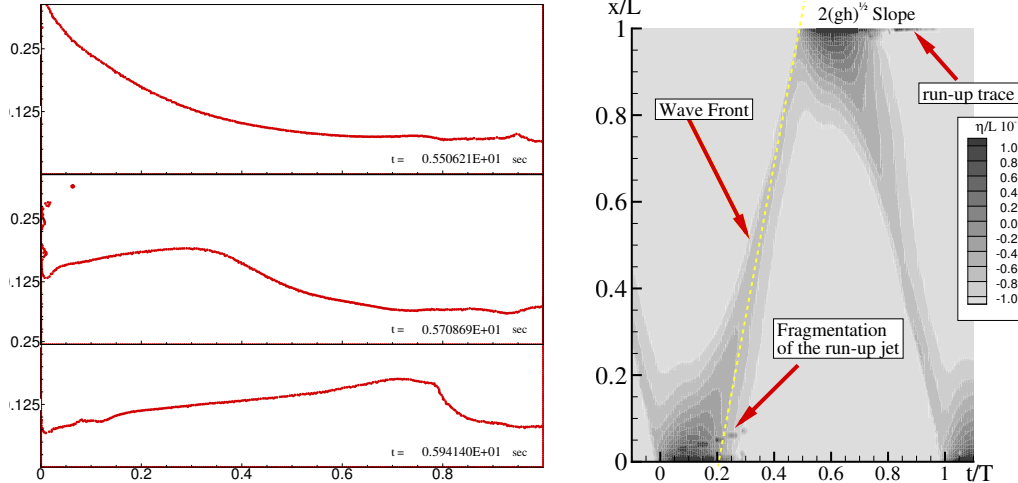
Figure 7: Numerical evolution of the free surface (left) and evolution of the wave height in time-space plane (right) for the case $A = 0.03L$, $h = 0.125L$, $\omega/\omega_1 \simeq 1.12$.

in about 1/6 of the excitation period. At that time the wave starts to propagate in the other direction, while the gravity collapse takes another 1/6 of excitation period.

References

[1] MONAGHAN, J.J. 2005 Smoothed Particle Hydrodynamics. *Reports on Progress in Physics*. Institute of Physics Publishing, **68**, 1703-1759.

[2] COLAGROSSI, A., & LANDRINI, M. 2003 Numerical simulation of interfacial flows by Smoothed Particle Hydrodynamics. *Journal of Computational Physics*. **191**, 448-475.

[3] COLICCHIO, G., COLAGROSSI, A., LUGNI, C., BROCCHINI, M. & FALTINSEN O.M. 2007 Challenges in the numerical investigation of the flip-through *Proc. 9th Int. Conf. in numer. ship hydr., Michigan*. **2**, 95-104.

[4] LANDRINI, M., COLAGROSSI, A., GRECO, M. & TULIN, M.P. 2007 Gridless simulations of splashing processes and near-shore bore propagation *to be published on Journal of Fluid Mechanics*.

[5] FALTINSEN, O.M. & ROGNEBAKKE, O.F. 2000 Sloshing. *Proc. Int. Conf. on Ship and Shipping Research*. Venezia, Italy.

[6] COLAGROSSI, A. 2005 Meshless Lagrangian Method for Free–Surface and Inter-face Flows with Fragmentation, *PhD Thesis University of Rome*, La Sapienza *Italy (http://padis.uniroma1.it)*

[7] FRIES, T.P. & MATTHIES, H.G. 2004 Classification and Overview of Meshfree Methods. *Informatikbericht 2003-03, Institute of Scientific Computing, Technical University Braunschweig, Brunswick, Germany*.

[8] VERHAGEN, J.H.G. & VAN WIJNGAARDEN,L. 1965 Non linear oscillation of fluid in a container. *J. of Fluid Mechanics* **22**.

Study on Numerical Prediction of Effective Wake Field

Tomasz Bugalski

Ship Design and Research Centre S.A., Poland
Tomasz.Bugalski@cto.gda.pl

The number of ship hydrodynamics problems which can be solved with the help of computational fluid dynamics (CFD) methods is constantly increasing. Practically all research institutions that perform ship model tests employ computer systems for estimation of the flow around the ship hull. Many research centres make a great effort in order to use commercial or home-developed computer systems that take into account the effects of viscosity and are more accurate and suitable in hull design process. Recently the efforts were also oriented towards the possibility of the numerical analysis of propulsion characteristics of the ship and propeller. CFD Tokyo workshop (Hino 2005) suggested self –propulsion case as a one of the main bench –marking test cases.

The simulation methods of self –propelled conditions using different level of CFD systems were developed by Ship Design and Research Centre S.A. (CTO S.A.) –(Bugalski 1997, Koronowicz et al. 2003). This paper presents a current proposal of method for simplified modelling of flow around ship stern with the propeller operation taken into account. The major features of the proposed method are as follows:

- The propeller is modelled with body forces (actuator disc).
- Non-uniform distribution of the body force and the propeller rotation are taken into account.
- The body force distribution is based on the pressure distribution on the propeller blades, computed with the use of the lifting-surface-based code.
- The free surface is neglected.
- The mesh of high density is generated for aft part of the hull only, and the inlet boundary condition is taken from the RANSE computations for entire hull.
- FLUENT solver, extended with appropriate user coding (written in C) is used for the computations.

The program for transforming the results from the lifting-surface code is not ready yet, but the preliminary code enabling the non-uniform, rotating actuator disc, based on the simple formulae for the distribution of body forces was already implemented in FLUENT. The principles of this code are described here, the results for the test case are also presented.

The simplest approximation of the propeller action is the distribution of angular axial and tangential body forces according to the following formulae:

The axial body force distribution, modeling the propeller thrust, is calculated as follows:

$$F_X = A r^* \sqrt{1 - r^*}$$

where: $r^* = \dfrac{r' - r_h'}{1 - r_h'}$, $\qquad r_h' = \dfrac{R_h}{R_0}$, $\qquad r' = \dfrac{r}{R_0}$

R_0 is the propeller diameter, and R_h is the hub diameter.

The coefficient A is determined as follows:

$$A = \frac{2T}{\pi R_0^2 \Delta} \frac{105}{16} \frac{1}{(4 + 3r_h')(1 - r_h')},$$

where T is the thrust and Δ is the thickness of the propeller disc.

The tangential body force distribution is calculated as follows:

$$F_\theta = B \frac{r^* \sqrt{1 - r^*}}{r^*(1 - r_h') + r_h'}$$

where:

$$B = K_Q \frac{\rho U_{ref}^2}{\Delta} \frac{105}{\pi J^2} \frac{1}{(4 + 3r_h')(1 - r_h')},$$

K_Q is the torque coefficient, J is the advance coefficient.

(formulae given by MichaelVisonneau in the report of the EFFORT project - Visonneau et al. 2005).
The distribution of body forces according to these formulae is a function of radius only. In our code, the body forces distribution is also angle-dependent and time-dependent, which is realized as follows:

- The projected leading and trailing edge of the propeller blade is approximated by polynomials, rotating at the propeller's angular velocity (angle as a function of radius and time, $\varphi_L(r,t)$, $\varphi_T(r,t)$.

- For the cells located in the propeller disc, between the leading and trailing edge of one of the blades, the body forces are distributed according to the bilinear function, with zero values on the edges and maximum value located in the distance of $0.2c$ from the leading edge, where c is the blade chord on the specified radius.

An example of computations carried out with the use of the described code is presented below. The test case is B500/2 "Ajama" container ship, built in Gdańsk Shipyard in the 90's.

The computational mesh was generated with HEXPRESS, allowing for generating hexahedral, unstructured meshes, which can be refined in the region of interest. Details of the mesh are presented in the figure below. The number of cells is about 350 000.

Surface mesh on the hull

Horizontal section of the mesh
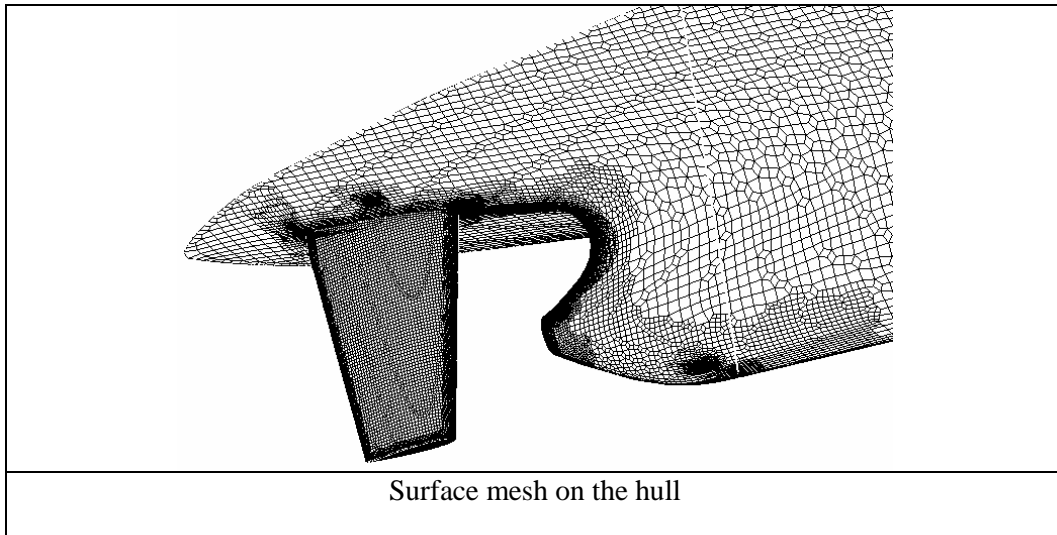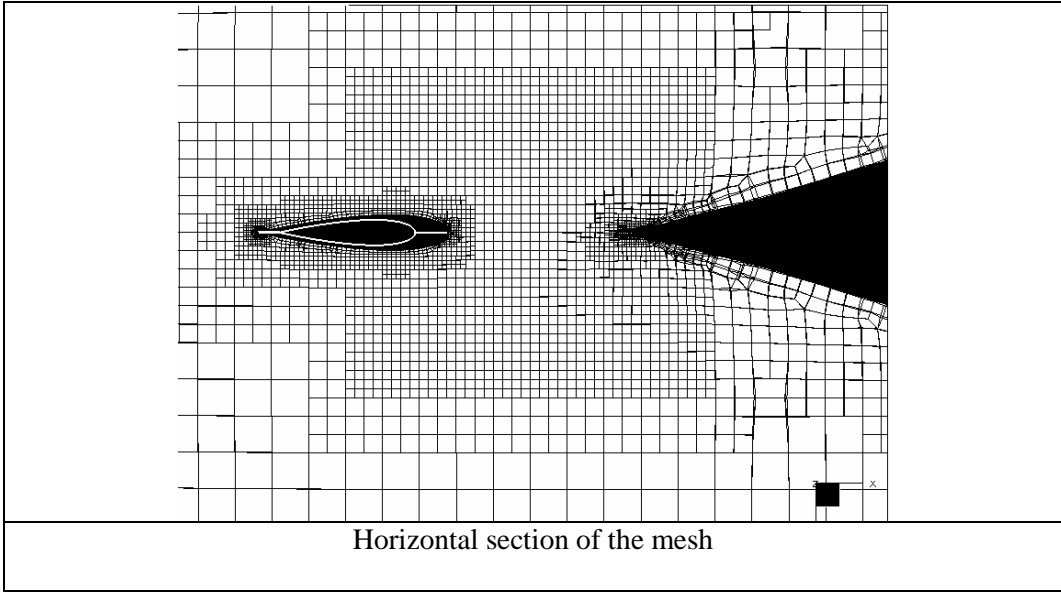
The following figure presents sample results.

| 1.54e+00 |
| 1.46e+00 |
| 1.37e+00 |
| 1.29e+00 |
| 1.20e+00 |
| 1.12e+00 |
| 1.04e+00 |
| 9.51e-01 |
| 8.67e-01 |
| 7.82e-01 |
| 6.98e-01 |
| 6.14e-01 |
| 5.29e-01 |
| 4.45e-01 |
| 3.61e-01 |
| 2.76e-01 |
| 1.92e-01 |
| 1.08e-01 |
| 2.35e-02 |
| -6.08e-02 |
| -1.45e-01 |

Axial velocity field in propeller plane (view from stern)

Axial velocity field in propeller plane in other point of time

Pressure distribution on starboard of ship hull with presence of working propeller

1.20e+03	
1.08e+03	
9.60e+02	
8.40e+02	
7.20e+02	
6.00e+02	
4.80e+02	
3.60e+02	
2.40e+02	
1.20e+02	
0.00e+00	
-1.20e+02	
-2.40e+02	
-3.60e+02	
-4.80e+02	
-6.00e+02	
-7.20e+02	
-8.40e+02	
-9.60e+02	
-1.08e+03	
-1.20e+03	

Pressure distribution on portside of ship hull with presence of working propeller

Conclusions

As a future work a computational method of joint RANS solver and effects of propeller work behind ship stern would be devised in order to analyze the complete unsteady flow about hull and propeller system. This is necessary to investigate the improvement of the cavitation and propeller exciting forces in the design stage of propeller and hull of ship.

References

Bugalski T., Modern Methods for Investigation of Hull -Propeller Interaction Phenomena using CFD, NAV 1997 International Conference on Ship and Marine Research , HSMV 1997 Symposium on High Speed Marine Vehicles, Sorrento –Italy, 1997.

Hino, T., Proceedings of CFD Workshop Tokyo 2005, Tokyo –Japan, 2005.

Kim J., Kim K.S., Kim G.D., Park I.R., Van S.H., Hybrid RANS and Potential Based Numerical Simulation of Self –Propulsion test for a Practical Ship, 7th International Conference on Hydrodynamics, Ischia –Italy, ICHD 2006.

Kimura K., Taketani T., Yamasaki E., Fujii A., Study on Interaction between Ship Hull and Propeller using RANS Method with VLM, 7th International Conference on Hydrodynamics, Ischia –Italy, ICHD 2006.

Koronowicz T., Miller W., Bugalski T., The Influence of the Scale and Propeller Operation on the Velocity Field Behind a Ship Hull, 15th International Conference on Hydrodynamics in Ship Design, Safety and Operation, , Gdansk, HYDRONAV'2003.

Visonneau M., Queutey P., Deng G.B., EFFORT Work Package 4- ECN-CNRS Report, Internal report of EU project: G3RD-CT-2002-00810 -European Full-Scale Flow Research & Technology, under the 5th Framework Program, Nantes –France, 2005.

Predictions of the Open Water Propeller Cavitation

Using the SOLAGA solver

Paweł Dymarski

Ship Design and Research Centre S.A. (CTO S.A.), Poland

padym@cto.gda.pl

Introduction

The main target of the paper is to show state of development of computer program SOLAGA, especially its ability to solve problems connected with viscous flow around ship propeller with the use of periodic boundary conditions as well as to present the results of computations of cavitation. Program SOLAGA has been developed in the framework of research project supported by Polish Committee of Science. It has been also the main subject of the author's PhD thesis.

Governing Equations

The closed system of motion equations, derived for incompressible fluid, is based on the momentum and mass conservation laws. An integral form of mass conservation equation formulated for control volume Ω with a surface S reads

$$\int_S \rho \mathbf{v} \cdot \mathbf{n} \mathrm{d}S = 0 \tag{1}$$

and the conservation equation of i-th momentum component has the following form:

$$\frac{\partial}{\partial t} \int_\Omega \rho u_i \mathrm{d}\Omega + \int_S \rho u_i \mathbf{v} \cdot \mathbf{n} \mathrm{d}S = \int_S \left(\tau_{ij} \mathbf{i}_j - p \mathbf{i}_i \right) \cdot \mathbf{n} \mathrm{d}S \ , \tag{2}$$

where $\mathbf{v}$ is velocity vector, u_i - i-th velocity component, p - pressure, ρ - density, $\mathbf{n}$ - unit vector normal to S surface, i_i - i-th component of Cartesian unit vector and τ_{ij} is a viscous stress tensor.

When the flow is turbulent, $\mathbf{v}$ and u_i refer to mean velocity vector and mean i-th velocity component, p is a mean value of pressure. The word "mean" denotes average in a time period, which is long compared to the period of turbulent oscillations [5].

The viscous stress tensor τ_{ij} is specified by Boussinesq approximation [1],[5]:

$$\tau_{ij} = 2\left(\mu + \mu_t\right)S_{ij} \ , \tag{3}$$

where μ is a molecular viscosity, μ_t is the turbulent viscosity and S_{ij} is the mean strain-rate tensor. The turbulent viscosity is calculated with the use of Spalart-Allmaras turbulence model [1],[5].

Cavitation

The cavitation model is based on travelling bubble method [4]. It is assumed in the model, that a large number of micro gas nuclei is present in the liquid. When pressure value decreases below a specified critical level, the radius of nucleus starts to grow rapidly and – according to the model – this is the inception of cavitation.

To determine behaviour of a single bubble the pressure field, velocity field (or bubble trajectory) and initial size of nucleus have to be given.

The single bubble dynamic is described by Rayleigh-Plasset equation [4]:

$$R\frac{d^2 R}{dt^2}+\frac{3}{2}\left(\frac{dR}{dt}\right)^2+\frac{\mu}{\rho R}\frac{dR}{dt}=\frac{-p+\dfrac{2A}{R}-p_v-p_g}{\rho} \ , \tag{4}$$

where R is a radius of the bubble, t is time, p is pressure far from the bubble, p_v - vapour pressure, p_g - pressure of the gas in the bubble, A denotes the surface tension coefficient.

Let us consider a control volume V of water which is large enough, so that the number of nuclei inside it is of the order of 100 or more. When spectrum of nuclei is given (i.e. number of nuclei in a given range of radius), it is possible to calculate the number of nuclei of given size inside the volume V of water:

$$N_{Vi} = n_i V \ , \tag{5}$$

n_i number of nuclei with initial size R_{0i} per unit volume.

The total volume of gas phase inside V can be calculated as:

$$V_g = \sum_i \frac{4}{3}\pi R_i^3 N_{Vi} \ , \tag{6}$$

The volume fraction of gas phase α inside the volume V is given by following formula:

$$\alpha = \frac{V_g}{V} = \frac{1}{V}\sum_i \frac{4}{3}\pi R_i^3 n_i V = \sum_i \frac{4}{3}\pi R_i^3 n_i \ , \tag{7}$$

where $\alpha = 0$ - when the volume V is filled with water,

$\alpha = 1$ - when the volume V is filled with gas.

The use of α coefficient is proper, when the considered volume of fluid is large enough. However when the evaluation of the fluid phase at specified point is required, it is more suitable to use the concept of probability of gas phase occurrence (at given point).

The probability of gas occurrence at specified point may be calculated with the use of the formula similar to (7). During solving the equation (4) for bubble radius, the influence of neighbouring bubbles is neglected. This simplified approach may result in a solution with P_{CAV} greater than 1. To avoid this unnatural effect, simple trick has been applied:

$$P_{CAV} = \mathrm{cut}\left(\sum_i \frac{4}{3}\pi R_i^3 n_i\right) \ , \text{ where } \mathrm{cut}(x)=\begin{cases} x; x \le 1 \\ 1; x > 1 \end{cases} \tag{8}$$

Numerical Methods

The solution algorithm for solving the viscous flow is based on Finite Volume Method. The Finite Volume Method is based on integral form of conservation equations. The solution domain is subdivided into a finite

number of control volumes, and the conservation equations are applied to each of them. The computational node at which the values of field functions are to be calculated lies at the centroid of each control volume (CV).

To express the value of each field quantity on CV surface S, suitable interpolation methods are used. In the presented program two methods are applied: upwind UDS (first order) and linear interpolation CDS (second order). Surface and volume integrals are approximated using midpoint quadrature [3]. As a result of FV discretization approach, one obtains an algebraic equation for each CV. The system of equations (after linearization) is solved using an iterative method. Two algorithms for solving the systems of algebraic equations are used: ICCG for symmetric systems and Bi-CGSTAB for non-symmetric systems [3] .

When the issue of flow around a propeller is solved with the use of rotating grid, the problem becomes unsteady. The time integral in the Navier-Stokes equation is solved with the use of implicit Euler method.

Rotating grid

Computation of flow around ship propeller requires the use of rotating grid or rotating coordinate system. In the first method, the conservations equations have to be modified in order to take into account a relative velocity between grid (control volumes) and coordinate system. The mass conservation of equation for single rotating control volume in integral form reads

$$\int_S \rho(\mathbf{v} - \mathbf{v}_b) \cdot \mathbf{n} \mathrm{d}S \ , \tag{9}$$

where $\mathbf{v}_b = \boldsymbol{\omega} \times \mathbf{r}_b$ is a velocity of CV boundary, $\boldsymbol{\omega}$ - rotational velocity of the grid, $\mathbf{r}_b$ - position vector of a point at S.

The momentum conservation equation for i-th momentum component takes the following form:

$$\frac{\mathrm{d}}{\mathrm{d}t} \int_\Omega \rho u_i \mathrm{d}\Omega + \int_S \rho u_i (\mathbf{v} - \mathbf{v}_b) \cdot \mathbf{n} \mathrm{d}S = \int_S (\tau_{ij} \mathbf{i}_j - p \mathbf{i}_i) \cdot \mathbf{n} \mathrm{d}S \ . \tag{10}$$

Periodic boundary conditions

In case of computation of open water characteristic of a propeller, it is possible to use periodic boundary conditions. This approach reduces the size of domain z - times (where z is a number of propeller blades).

At the periodic boundaries we have the following conditions:

$$p_L = p_R, \quad \varphi_L = \varphi_R, \quad \mathbf{v}_L = \mathbf{Q}_{RL} \mathbf{v}_R \ , \tag{11}$$

where φ is a scalar quantity (i.e.: turbulent viscosity), $\mathbf{Q}_{RL}$ is a transformation matrix from "right" R to "left" L periodic boundary.

Non-matching interfaces

From the numerical point of view periodic boundary condition is an interface between two subdomains. In SOLAGA solver, the grid at periodic interface may be non-matching, it allows to build almost orthogonal grids with better fitted structure than "matching" grids.

Test case: Flow around skewed propeller

Geometry of the propeller model. Computational conditions

Table 1. Geometry of Propeller model B:

Type:	Controllable pitch
No of blades:	5
Diameter:	265.73 mm
Pitch ratio at 0.7 radius:	1.4281
Expanded area ratio:	0.820
Hub ratio:	0.3026

Table 2. Computational conditions

Propeller velocity v_p:	2.0 m/s
Propeller revolutions n_p:	11.0 1/s
Advance coefficient J:	0.684
Reference pressure (at inflow) p_0:	0.04; 0.06; 0.08; 0.10 bar
Number of nuclei (at inflow) n_0:	$0.1*10^6$ 1/m3
Radius of nuclei (at inflow) R_0:	$10.0*10^{-6}$ m

The domain size and grid structure

Size of the domain: the inlet is located 1.9 D upstream from the propeller, the outlet is 1.9 D downstream, the diameter of the domain is 2.4 D. The boundary faces of the domain are presented in Fig 1 a.

The grid was generated with the use of program ANSYS ICEM CFD Hexa. The grid is hexahedral and block-structured, number of CV's (per one blade) is 1 086 176. The grid structure on blade, hub and periodic surface is shown in Fig. 1 b.
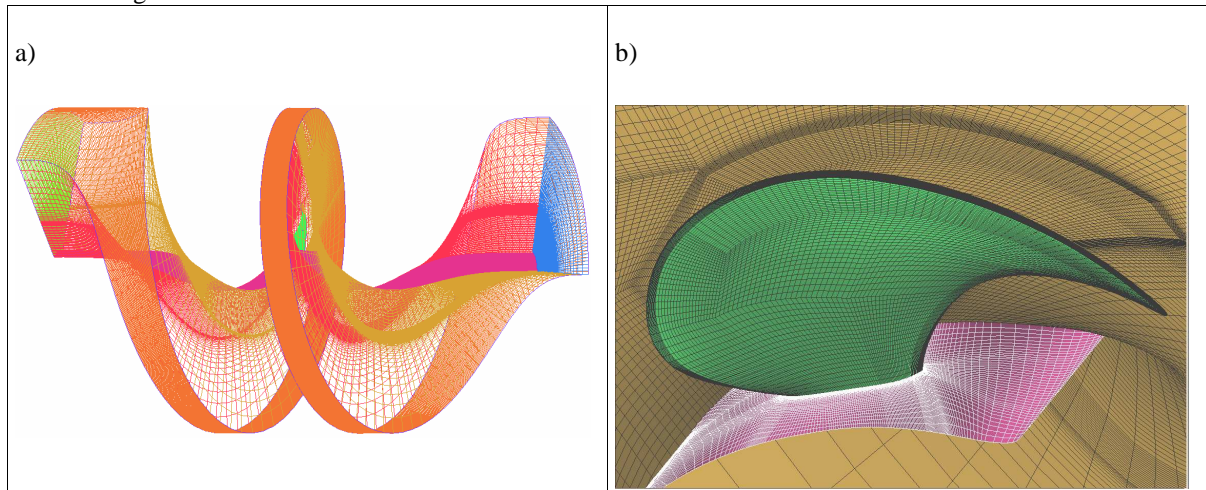

Fig. 1. a) Model B: domain of computations, b) grid structure on the propeller blade, hub and periodic surface

Results of computations

Pressure distribution over the suction and pressure side of the propeller blade is shown in Fig a,b, however picture 2 c shows pressure distribution inside the domain. The low pressure area which is stretched behind a blade tip is caused by a strong vorticity of tip vortex. The tip vortex is visible even far than 180 degrees behind the blade.

Figure 3 presents distribution of probability of cavitation P_{CAV} at blade surface as well as the shape of isosurface $P_{CAV} = 0.5$ which can be treated as a face of large scale cavitation structures, e.g.: laminar cavitation, tip vortex cavitation or large bubbles. Bubble cavitation can be expected in regions where function of probability takes a value between about 0.1 and 0.5. The presented model does not predict secondary form of cavitation, e.g.: cloud cavitation.

Open water cavitation tests for the propeller are planned to be carried out in the near future. Up to now, the presented cavitation model has been validated on an example of rectangular hydrofoil [2]. Figure 4 shows the comparison of cavitation modelling results obtained from SOLAGA solver for rectangular hydrofoil with the results of cavitation tests which were carried out in cavitation tunnel in CTO S.A.
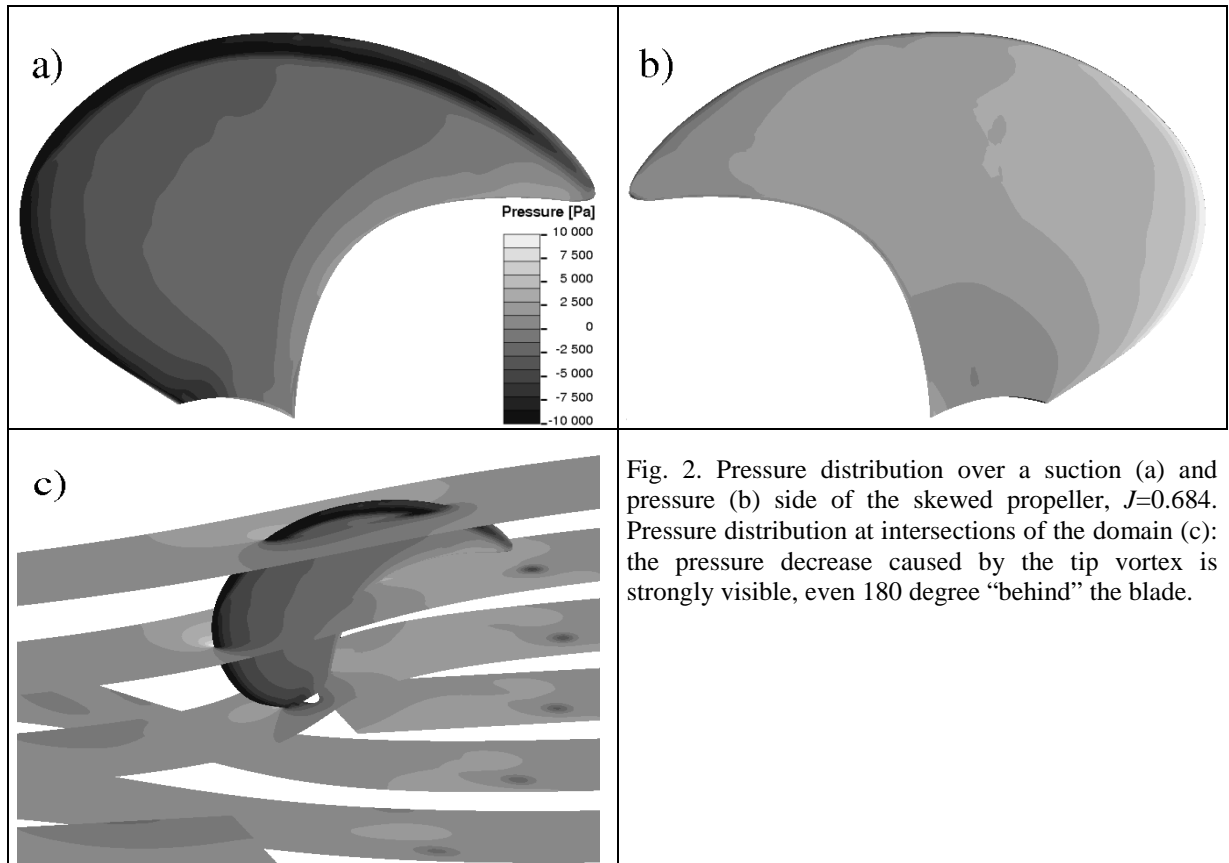
Fig. 2. Pressure distribution over a suction (a) and pressure (b) side of the skewed propeller, J=0.684. Pressure distribution at intersections of the domain (c): the pressure decrease caused by the tip vortex is strongly visible, even 180 degree "behind" the blade.

Fig. 3. Computational predictions of cavitation phenomenon on propeller blade for advance coefficient J=0.684 and various values of reference pressure. The pictures shows probability of cavitation P_{CAV} on blade surface as well as isosurface $P_{CAV} = 0.5$.

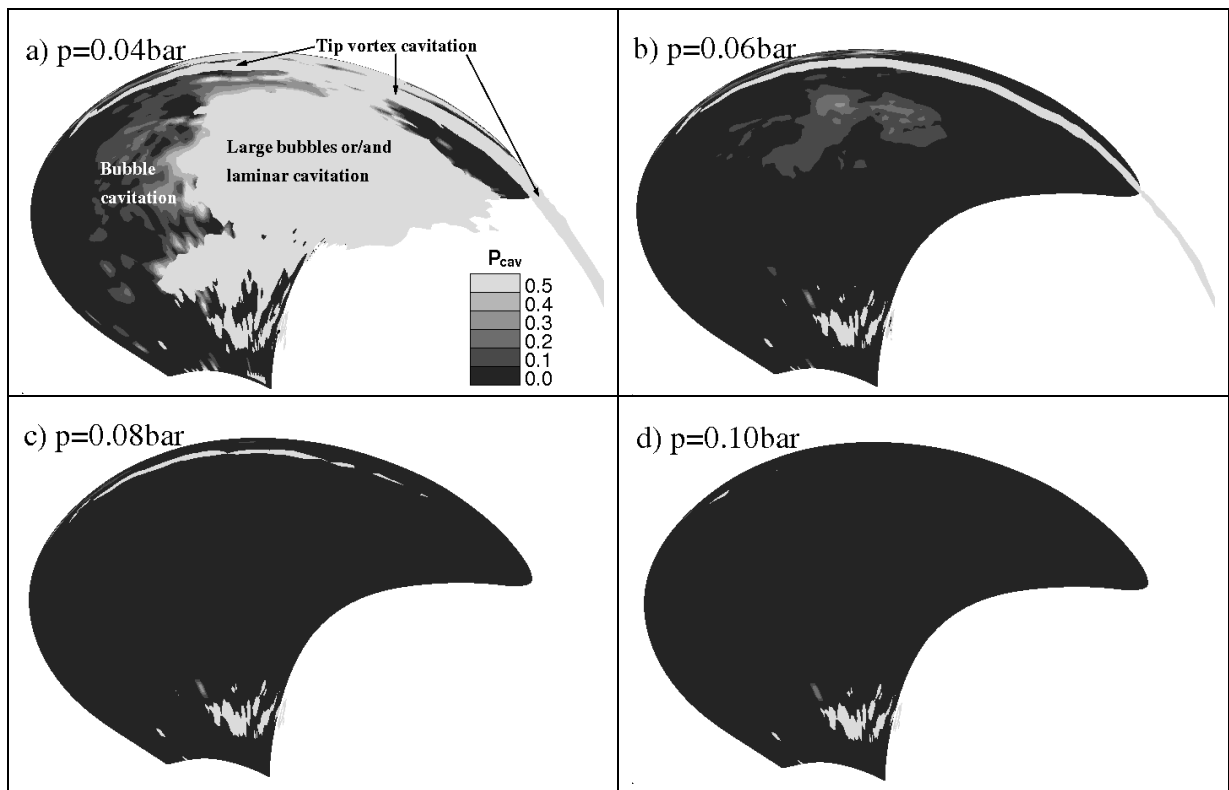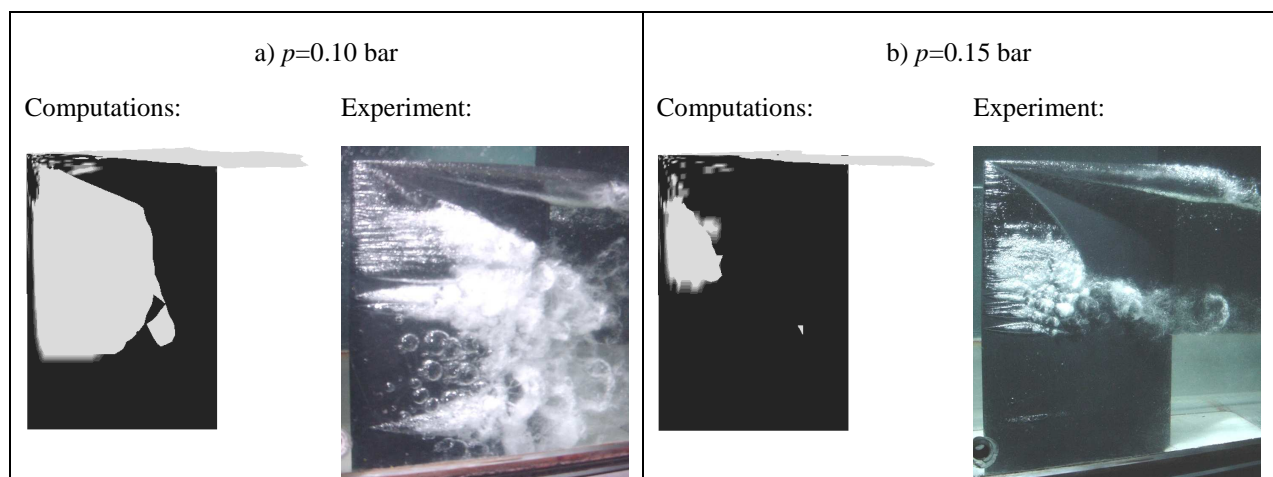| a) *p*=0.10 bar | b) *p*=0.15 bar |
| Computations: Experiment: | Computations: Experiment: |

Fig 4. Comparison of computational predictions of cavitation phenomenon with the test results. The model is a rectangular hydrofoil based on NACA16 profile. The computational grid consists of about 1 600 000 control volumes.

Conclusions

1. The calculated pressure distribution over the blades of the propellers is smooth, without numerical oscillations, also there are no pressure oscillations near periodic, non-matching boundaries.

2. Program SOLAGA can be a good tool for the tip vortex modelling. The low pressure area caused by vorticity is clearly visible far behind the propeller blade (Fig. 2 c). Close examination of his figure shows the core of the vortex created by the next blade.

3. Figure 3, in which the probability of cavitation is presented, shows the structures of cavitation like those observed on similar propeller models in cavitation tunnel. One can distinguish the elongated structure of tip vortex cavitation which spreads from leading edge, through the tip, to the slipstream (Fig. 3 a,b,c). The regions are also visible where bubble cavitation may appear, where P_{CAV} ranges from about 0.1 to 0.5 (Fig. 3 a,b) as well as large area where laminar or/and developed bubble cavitation can be expected (Fig. 3 a).

References

[1]   Blazek J.: *Computational Fluid Dynamics: Principles and Applications*, ELSEVIER 2001

[2]   Dymarski P.: *Numerical computation of hydrodynamic forces on hydrofoil. Prediction of cavitation phenomenon*. 8th Numerical Towing Tank Symposium, 2-4 Oct. 2005, Varna

[3]   Ferziger J.H, Peric M.: *Computational Methods for Fluid Dynamics*, 2nd ed., Berlin, Springer 1999

[4]   Lecoffre Y.: *Cavitation. Bubble Trackers*, A.A. Balkema/Rotterdam/Brookfield 1999

[5]   Wilcox D.C.: *Turbulence Modeling for CFD*, DCW Industries 2002

Free Surface Flow Simulations with a Coupled Algebraic Multigrid Algorithm

Stephan Eder, ANSYS Fluent Deutschland GmbH
Birkenweg 14a, 64295 Darmstadt
stephan.eder@ansys.com

INTRODUCTION

For marine and offshore applications as well as liquid sloshing in containers, CFD provides a useful tool to model free-surface flows. But for a successful application of free-surface CFD modelling there are two main requirements, accuracy and efficiency.

To solve accuracy of free surface flows, there are a number of modelling approaches, like surface-adaptive methods, interface capturing methods and interface-tracking methods. For special classes of free surface flows the surface-adaptive methods (e.g.: Zwart, 1999; Raithby et al., 1995) are useful, but not for complex flows.

Interface-capturing and interface-tracking methods, often called Volume-of-Fluid methods (VOF), solve an additional equation for the volume fraction for the phases and can be used with complex geometries. Continuum advection discretisation used by interface capturing methods often leads to cloudy free surface interfaces. Using compressive advection schemes, such as donor-acceptor (Hirt and Nichols, 1981) or CICSAM (Ubbink and Issa, 1999) minimizes the smearing of the interface, but these methods are controlled down-winding, and due to that, they need small time steps. The need of small time steps is contrary to the requirement of efficiency. Usual solution algorithms need such small time steps or large underrelaxation factors. Hence, a long time for a converged solution is needed.

In the following, a new coupled-implicit VOF algorithm is described, which removes the need for small time steps.

NUMERICAL MODEL

In CFX meshes can consist of tetrahedral, hexahedral, pyramid or prismatic elements. The solver automatically constructs a polyhedral element around each mesh node, as illustrated in figure 1. From now on V is the volume of the polyhedral control volume, A^i_{ip} is the area vector of a surface corresponding to an integration point, δt is the time step an the superscripts (n+1) an n corresponds to the new and the old time step, respectively.

Figure 1. Element-based finite volume discretisation of the spatial domain. Grey lines define element boundaries and black lines divide elements into sectors. Solution unknowns are collocated at the vertices • and surface fluxes are evaluated at the integration points **x**. A polyhedral contour volume is constructed around each vertex
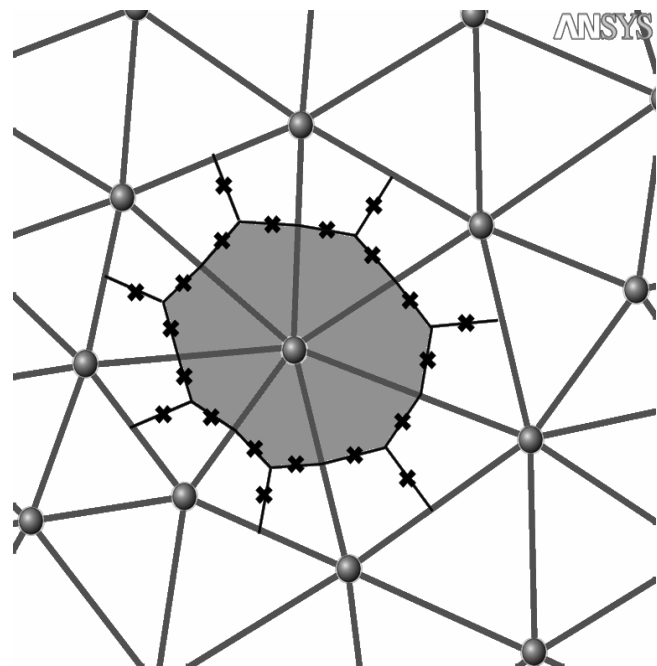
With these definitions the three main equations are:

$$\frac{V}{\delta t}\left((\rho_\alpha r_\alpha)^{n+1} - (\rho_\alpha r_\alpha)^n\right) + \sum_{ip}\left(\rho_\alpha u^i A^i\right)^{n+1}_{ip}\left(r_{\alpha,ip}\right)^{n+1} = 0 \tag{1}$$

$$\frac{\rho_m V}{\delta t}\left((u^i)^{n+1} - (u^i)^n\right) + \sum_{ip}\left(\rho_m u^j A^j\right)^{n+1}(u^i)^{n+1} = -\sum_{ip}P^{n+1}_{ip}A^i + \rho^{n+1}_m g^i V + \sum_{ip}\left((\tau^{ji})^{n+1}A^j\right)_{ip} \tag{2}$$

$$\sum_{\alpha=1}^{N} r_\alpha^{n+1} = 1 \tag{3}$$

With these three algebraic equations the volume fraction, the velocity and the pressure field can be calculated. These equations form a 6x6 coupled system at each control volume for a two phase flow and are solved simultaneously with the new coupled volume fraction algorithm. In comparison with the old semi-coupled algorithm, where pressure and velocity are coupled, but not the volume fraction, the new fully coupled algorithm is scalable. That means, with mesh size the solution cost increases linearly.

The solution strategy proceeds as follows:

a) Solve equations (1), (2) and (3) in a coupled manner and update the velocity, pressure and volume fraction fields accordingly.
b) Assemble and solve other relevant equations (e.g. turbulence)
c) Return to step 1 until the solution converges

EXAMPLES

Flow over a Ramp

The flow over a ramp is a first small example for the capability of the new coupled volume fraction algorithm. A two-dimensional hexahedral mesh with 48608 nodes was built. At the inlet a bulk mass flow rate and a zero gradient for volume fraction were used and at the outlet a hydrostatic pressure profile. In figure 2 the geometry of the test case and a plot of the water volume fraction are shown.

Figure 2. Water volume fraction with the coupled VOF algorithm

One sees, that the coupled volume fraction algorithm provides a sharp free surface.

Figure 3 and 4 show the residual plots of the calculations with the segregated and the coupled algorithm, respectively. The calculation with the segregated volume fraction algorithm is
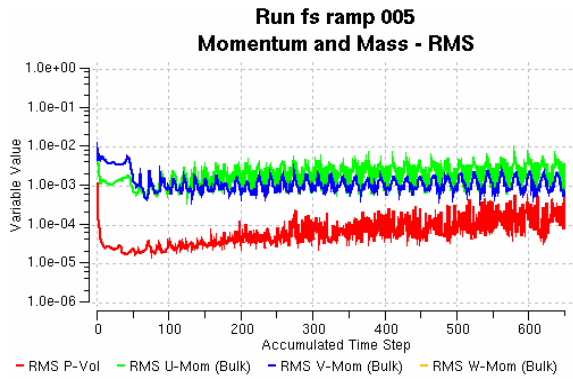
Figure 3. Convergence behaviour with the segregated volume fraction algorithm
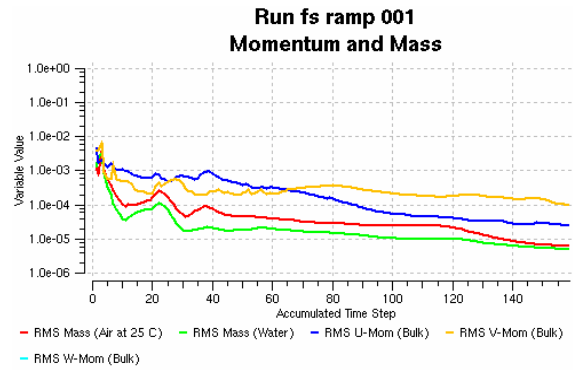

Figure 4. Convergence behaviour with the coupled volume fraction algorithm

unstable, whereas the calculation with the coupled algorithm shows good convergence behaviour and converges within 160 iteration steps.

Ocean Waves

As a test for the new coupled algorithm deep water waves were simulated. For the calculation a 2d hexahedral grid (depth 1 cell) was created with a length of 480 m in x-direction and a height of 200 m in z-direction. The water surface is in the mid-plane at z = 0 m. The resolution of the grid in the vicinity of the free surface was change in five steps. The five grid sequences for "wave amplitude x wave length" are: 8x8 cells, 16x16 cells, 32x32 cells, 64x64 cells and 128x128 cells with a total cell count of 1,536, 4,224, 12,288, 38,784 and 129,792, respectively. Additionally, five different time step sizes based on the wave motion were used: 8 time steps per period (tspp), 16 tspp, 32 tspp, 64 tspp and 128 tspp. Hence, a 5x5 matrix of different time and grid resolutions is calculated. In a physical scale 8 tssp are approximately 0.63 s and 128 tssp are approximately 0.04 s.

The inlet velocity is 16 ms^{-1} plus the time dependent velocity profile derived from the linear wave theory (deep water assumption). The wave is 160 m long and has an amplitude of 3.2 m and a periodic time of T = 10.126 s. The velocity of propagation is 15.8 ms^{-1}. Hence, the Doppler periodic time is 5.063 s. At the outlet
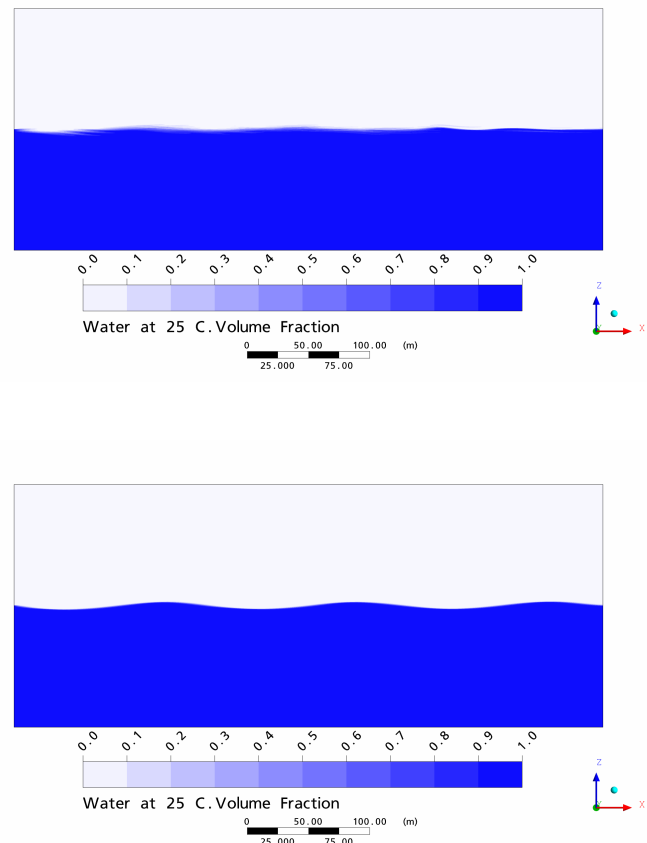

Figure 5. Water volume fraction; top : 8 time steps per period; cloudy surface, high damping; bottom : 32 time steps per period, sharp surface, no damping

a hydrostatic pressure profile was used. The top and the bottom boundary conditions are opening and free-slip wall, respectively.

The tests were performed to provide a guideline for mesh and time step resolution to simulate free surface water waves in an adequate way.

The results show an independency of the time step size between 64 tssp and 128 tssp. There are no differences in the free surface level. But with an adequate mesh resolution 32 tssp are sufficient to resolve the free surface.
Also the results show, that at least a mesh resolution of 32 x 32 cells for "wave amplitude x wave length" is needed, because with a coarser mesh the numerical damping is too high. Additionally, from the results we get the information, that for a fine mesh and a big time step, we need more inner iteration loops. With a fine mesh and a coarse time step size, the free surface is somewhat cloudy. If the number if inner loops is increased, the cloudy surface vanished and a sharp free surface level is obtained. But the main wave pattern remains the same. Figure 5 shows an example of the free surface with two different time step sizes. In the upper picture with 8 tspp one sees a cloudy water surface and a high damping in the flow direction from left to right (inlet to outlet). In the lower picture with 32 tspp a sharp free surface and almost no damping occurred.

At least it can be said, that with the new coupled VOF algorithm a time step size of 32 time steps per period (here : 0.16 s) and a mesh resolution of 32 x 32 for "wave amplitude x wave length" (here : 0.1m x 5 m) is needed.

Wigley Hull

The wigley hull is an academic hull shape which is commonly used as a benchmark for free surface flows. For the testing of the new coupled VOF algorithm two hexahedral meshes were built. A coarse mesh with 100,000 nodes and fine mesh with 500,000 nodes. The calculations were performed by Zwart, 2007.
At the inlet the fluid velocity is 1.452 ms^{-1} for air and water. At the outlet a hydrostatic pressure profile is specified, whereas at the side and the bottom free slip walls are defined. Symmetry boundary conditions and an entrainment opening are specified at the symmetry plane and the top, respectively. The hull surface is a no-slip wall.
Based on the hull length and the inlet velocity the Froude number is 0.267 and the Reynolds number is 4.9×10^6.
For turbulence modelling a k-ε turbulence model is used. A steady state calculation is performed and with a RSM residual drop below 10^{-5} convergence is declared.
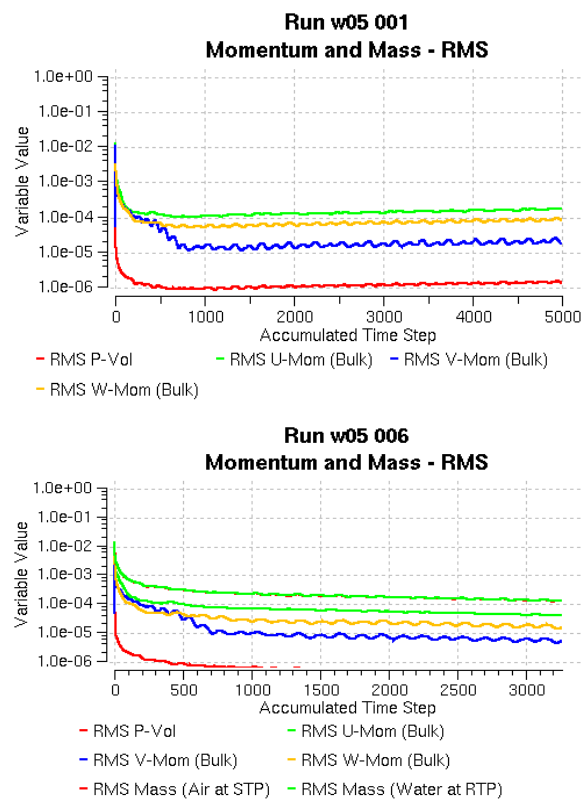

Figure 6. Convergence plots for wigley hull test case; top : segregated volume fraction; bottom : coupled volume fraction

In figure 6 a comparison between the calculation with the segregated and the coupled algorithm is shown. The segregated algorithm shows poor convergence, in contrast to the calculations with the coarse mesh and the coupled algorithm, which converges.

In the next step the physical time step size with the coupled algorithm is changed. Although this is a steady-flow simulation, a physical time step is still used as a means of providing underrelaxation as the solution approaches steady-state.

In this second step for the first twenty time steps a time step size of 0.1 s is used and afterwards switched to 0.2 s. The residuals of that second calculation are shown in Figure 7. In comparison with figure 6 the residuals show much faster convergence behaviour.

In a third step the so called "false time step linearization" was switched off after the first twenty time steps. Figure 6 shows the new rms residual plots of that third calculation. It shows that with the new coupled VOF algorithm we can achieve convergence for the wigley hull test case within 200 iteration steps.
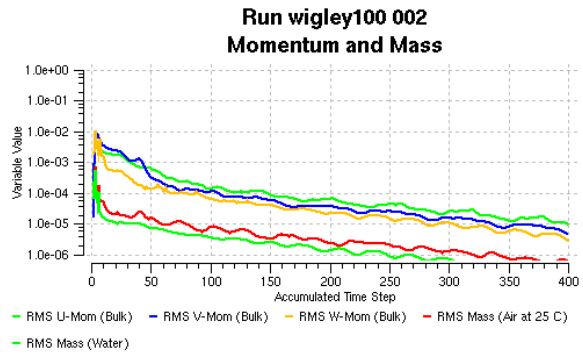
Figure 7. Convergence plots for wigley hull test case 2
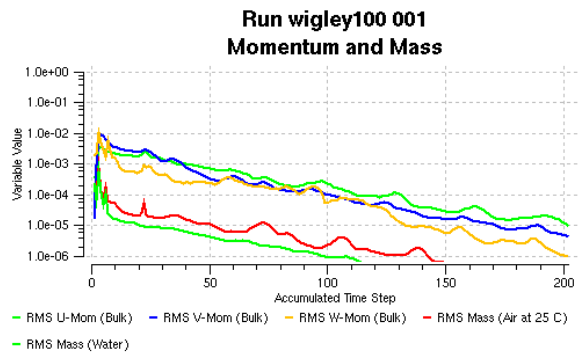
Figure 8. Convergence plots for wigley hull test case 3

In figure 9 the water level on the hull surface of the coarse and the fine meshes are plotted and compared with the experimental data. Figure 10 shows a plot of the elevation contours of the free surface level with the coarse and the fine mesh.
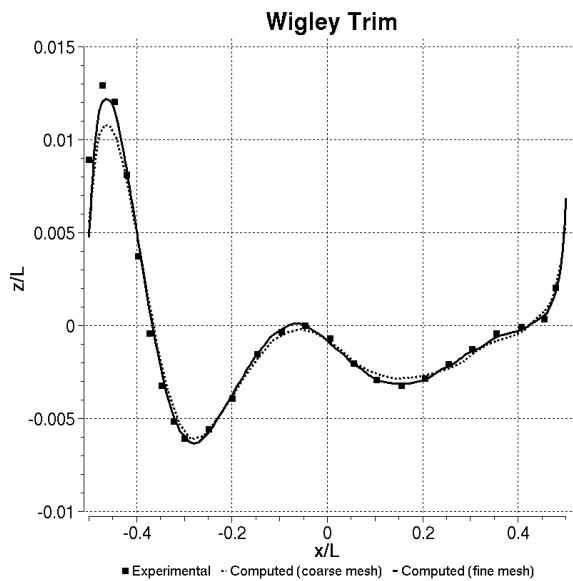
Figure 9. Water Level on hull surface: experimental ■; coarse mesh …; fine mesh —
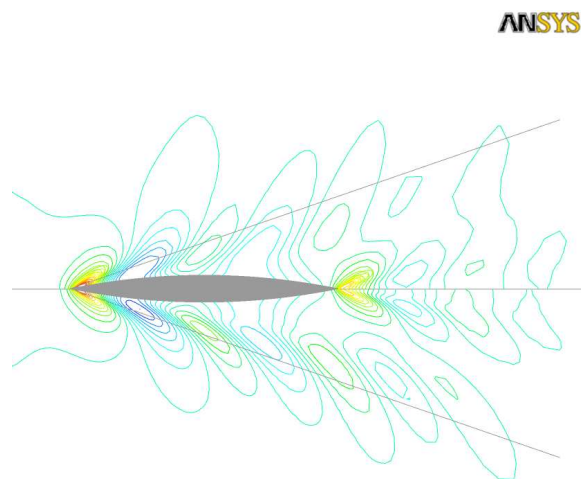
Figure 10. Contour lines of water surface elevation; top : coarse mesh; bottom : fine mesh

CONCLUSION

An efficient and accurate model to predict buoyant free surface flows had been developed. Several examples have shown that this new coupled algorithm performs a more stable calculation. The surface stays sharper as with the segregated algorithm and the convergence of the calculation is much better and faster.

ACKNOWLDGEMENTS

REFERENCES

ANSYS CFX 11.0 Users Guide

C.W. Hirt and B.D. Nichols (1981), *Volume of Fluid (VOF) method for dynamics of free boundaries*, Journal of Computational Physics

G.D. Raithby, W.-X. Xu, G.D. Subely (1995), *Prediction of incompressible free surface flows with an element-based finite volume method*, Computational Fluid Dynamics

O.Ubbink, R.I. Issa (1999), *A method for capturing sharp fluid interfaces on arbitrary meshes*, Journal of Computational Physics

P.Zwart (1999), *The integrated space-time finite volume method, PhD Thesis*, University Waterloo

P. Zwart, A.D. Burns, P.F. Galpin (2007), Coupled Algebraic Multigrid for free surface flow simulations, OMEA 2007-29080

Grid Resolution for the Simulation of Sloshing using CFD

Bernhard Godderidge*, Mingyi Tan*, Chris Earl** & Stephen Turnock*

*Fluid-Structures Interaction Research Group, School of Engineering Sciences, University of Southampton, Highfield, Southampton SO17 1BJ, UK
**BMT SeaTech, Grove House, 7 Ocean Way, Southampton SO14 3TJ, UK

Corresponding author's email: bg401@soton.ac.uk

Introduction

Sloshing occurs when a tank is partially filled with a liquid and subjected to an external excitation force [1]. Ships with large ballast tanks and liquid bulk cargo carriers, such as very large crude carriers (VLCCs), are at risk of exposure to sloshing loads during their operational life [2]. The inclusion of structural members within the tanks dampens the sloshing liquid sufficiently in all but the most severe cases. However, this approach is not used for Liquefied Natural Gas (LNG) carriers and the accurate calculation of the sloshing loads is an essential element of the LNG tank design process [3, 4].

The increase in global demand for LNG has resulted in a new generation of LNG tankers with a capacity in excess of 250,000 m^3, compared to 140,000 m^3 today. A prerequisite for the safe operation of these LNG tankers is an accurate calculation of the sloshing loads experienced by the containment system [5, 6].

The work of Abramson [7] summarizes the methods available in modern sloshing analysis, and Ibrahim [8] gives an up-to-date survey of analytical and computational sloshing modeling techniques. A more general modeling technique is the solution of the Navier-Stokes equations using Computational Fluid Dynamics (CFD). Some recent examples of CFD sloshing simulation include Hadzic *et al.* [9], Aliabadi *et al.* [10], Standing *et al.* [11], Kim *et al.* [12], Rhee [13] and El Moctar [14].

Sloshing flows are treated as a transient problem in CFD. While the number of sloshing oscillations can vary, a large number of time steps, usually $O(10^2)$ to $O(10^3)$ per oscillation are required. Design optimization or the use of a numerical wave tank to gather statistical sloshing pressure data [15] requires long simulation times or multiple runs. Parameters such as time step size, grid spacing and model choice directly influence the complexity and computational cost of a CFD model.

A sway-induced resonant sloshing flow in a 1.2 m x 0.6 m rectangular container is investigated using a commercial Navier-Stokes CFD code. The selected computational model was validated using experimental pressure data from Hinatsu [16] by Godderidge *et al.* [17, 18]. The effect of grid spacing when capturing impact pressure caused by an enclosed air bubble is investigated. It is found that local flow features are best suited to indicate that the flow is sufficiently well resolved. These findings are further investigated using larger, geometrically similar sloshing tanks. The initial grid geometry is used to simulate the scaled sloshing flow at two and four times the initial grid size. Then, the grid is refined to give the same mesh spacing as in the first problem.

Sloshing Problem

Sloshing in rectangular container, induced by pure sway motion, is investigated in the present study. Figure 1 shows the tank dimensions, locations of pressure monitor points and axis system orientation. The CFD model was validated using the experimental steady state sloshing pressures given by Hinatsu [16]. The tank displacement is given by

$$x = A \sin\left(\frac{2\pi}{T} t\right),\qquad(1)$$

where A is the displacement amplitude, T the sloshing period and t the elapsed time. In the current case, the tank motion is in the x-direction only, as indicated in Figure 1. The first part of the investigation is focused on a resonant sloshing flow at 20% filling level, where $A = 0.06$ m and $T = 1.74$ sec. Subsequently, a near-resonant sloshing flow with $A = 0.015$ m and $T = 1.404$ sec is considered.
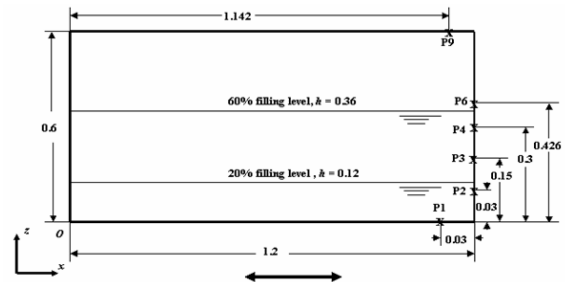

Figure 1: The sloshing problem used for CFD validation (all dimensions in m)

The fluid interaction models for the numerical simulation of sloshing can be implemented using the volume fraction of each fluid to determine the fluid mixture properties. This is a *homogeneous* multiphase model. It is analogous to the volume of fluid (VOF) method developed by Hirt and Nichols [19], but it includes a simplification as the free surface pressure boundary condition is neglected. A more general but computationally more expensive approach is an *inhomogeneous* multiphase model, where the solution of separate velocity fields for each fluid is matched at the fluid interfaces using mass and momentum transfer models [20]. An inhomogeneous viscous compressible multiphase flow with two phases α and β is governed by the conservation of mass for the compressible phase α

$$\frac{\partial}{\partial t}\left(r\rho\right) + \frac{\partial}{\partial x_i}\left(r\rho u_i\right) = m + \Gamma^{\alpha\beta},\qquad(2)$$

where $\Gamma^{\alpha\beta}$ is mass transfer between the phases and m mass sources, ρ density, r volume fraction and u_i velocity of phase α. The conservation of momentum for phase α is given as

$$\frac{\partial}{\partial t}\left(r\rho u_i\right) + \frac{\partial}{\partial x_j}\left(r\rho u_i u_j\right) = -r\frac{\partial p}{\partial x_i} +$$
$$+ \frac{\partial}{\partial x_j}\left[r\mu\left(\frac{\partial u_i}{\partial x_j} + \frac{\partial u_j}{\partial x_i}\right)\right] + M^\Gamma + M^\alpha + b_i,\qquad(3)$$

where b_i are body forces, M^α forces on the interface caused by the presence of phase β, μ the dynamic viscosity and the term $M^\Gamma\left(= \Gamma^{\alpha\beta}u_i^\beta - \Gamma^{\beta\alpha}u_i\right)$ interphase momentum transfer caused by mass transfer. If the fluid is compressible, Equations (2) and (3) are closed using an energy equation, or an equation of state if the compressible fluid can be treated as an ideal gas [21]. A discussion of the fluid interface forces is given by Godderidge *et al.* [22].

As a full set of conservation equations has to be solved for each phase, the computational effort required for the inhomogeneous model has been found to be 2.3 times greater[1] than for the homogeneous model [22]. However, Brennen [23] finds that if two conditions derived from particle size parameter, mass parameter and particle Reynolds number are violated, the inhomogeneous multiphase model (Equations 2 and 3) should be used. It is observed that for the current problem, the particle Reynolds number condition is not satisfied. This suggests that the use of an inhomogeneous multiphase model is required for the analysis of the current problem.

The computational models used in the sloshing studies are summarised in Table 1. The selection is based on the sensitivity study by Godderidge *et al.* [17]. It was found that the pressure histories of the current fluid model combination differed by less than 0.1% from the fully compressible model but required 20% less computational time. Kim *et al.* [12] showed that the sloshing pressure is not influenced by the inclusion of a turbulence model, but the use of a standard $k - \varepsilon$ turbulence model with a scalable

---

wall function aided convergence when using a viscous flow model [17]. The high resolution scheme for spatial discretization varies between a first and second order upwind scheme depending on the gradient [21]. The grids used for the various studies are detailed in the sections describing the respective results.

Table 1: Computational models used for sloshing simulations

Parameter	Setting
Water	Incompressible fluid
Air	Ideal gas
Multiphase model	inhomogeneous
Sloshing motion	Body force
Turbulence model	Standard $k - \varepsilon$ with scalable wall function
Spatial discretization	High resolution
Time discretization	Second order backward Euler
Timestep control	Root-mean-square (RMS) Courant number=0.1
Convergence control	RMS residual $< 10^{-5}$

The investigation of sloshing in geometrically similar containers required the calculation of an appropriate sloshing excitation. The nature of the excitation, given in Equation (1), is maintained but the amplitude and frequency are adjusted. The sloshing period is 95% of the resonant period which depends on the tank size. The resonant frequency for each case is calculated from potential theory as

$$\omega_n^2 = \frac{\pi g}{a}\tanh\left(\pi\frac{h}{a}\right),\qquad(4)$$

where a is the tank length, g gravity and h the filling level. The amplitude of the sloshing excitation is adjusted using the sloshing velocity, which may be obtained by differentiating Equation (1). Taking the excitation velocity as a characteristic velocity, the following non-dimensional scaling parameter based on the Froude number [7] can be used

$$\frac{\dot{x}_l}{\dot{x}_L} = \frac{\sqrt{gD_l}}{\sqrt{gD_L}},\qquad(5)$$

where D_l and D_L are characteristic length scales.

Impact bubble

The fluid motion caused by sloshing results in static and dynamic pressure loads. The dynamic pressures are usually confined to small regions, but cause large localised loads on the structure. Sloshing pressure loads can be categorised as pure fluid impact, impact air bubble formation and the impact of an air-water mixture formed during a previous fluid impact. Pure fluid impact has been studied experimentally by Peregrine [24] and impact pressures in excess of 100 times the static fluid pressures were observed. The resonant sloshing flow results in a jet impacting the tank wall and subsequent air bubble entrainment. This tends to result in a longer, oscillating pressure history when compared to a pure fluid impact.
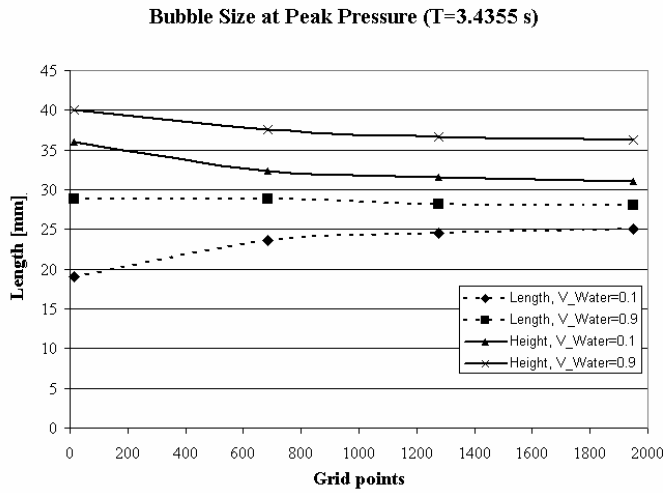
2(a): Bubble size dependence on grid
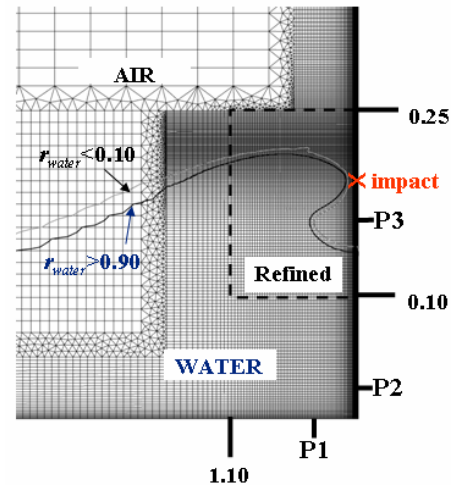
2(b): Air bubble formation

Figure 2: Air entrainment bubble formed during sloshing impact

3(a): P2

3(b): P3

Figure 3: Pressure history at P2 (left) and P3 (right)

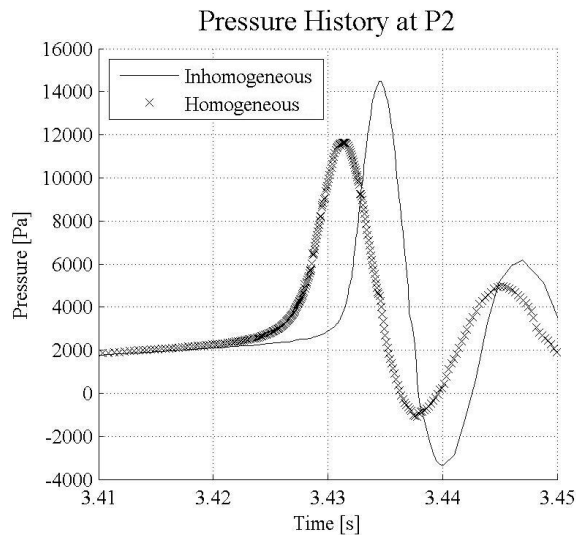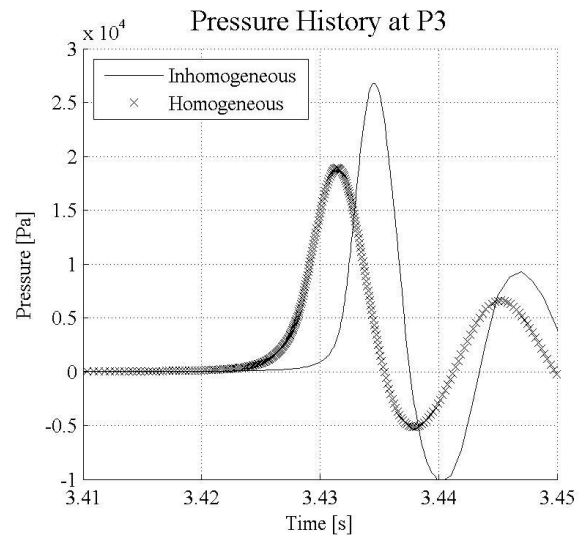The sloshing flow is simulated on a hybrid grid with a refined region indicated in Figure 2. Table 2 gives the grid particulars in the refined region. Figure 2(a) shows the grid dependence of the air bubble dimensions and the formation of the air bubble is illustrated in Figure 2(b).

Table 2: Grid refinement for sloshing impact

Grid	Hex.	horizontal (first node) (mm)	vertical (mm)
Grid a	408	0.30	12
Grid b	2552	0.10	3.5
Grid c	4602	0.05	2.0
Grid d	16284	0.02	0.5

Figure 3 shows the pressure history during fluid impact at P2 and P3 for the 20% filling level. In both cases, the homogeneous multiphase model gives, for the identical fluid model and initialisation, a significantly lower pressure than the inhomogeneous model. Figure 4 shows that the direction of the water prior to impact depends on the selected multiphase model. The inhomogeneous flow predicted water velocity is inclined $14.0°$ from the horizontal, while the homogeneous model estimated the velocity vector inclination at $40.3°$.

The grid dependence of the calculated pressures is shown in Figure 5. The characteristic length scales are the length and depth for P1 and P2 are taken where the water surface is above its initial position The length and height of the bubble are the characteristic scales for P3 . Figure 5(a) shows the plot for the grid spacing perpendicular to the bottom wall for P1 and P2 and the side wall for P3. The grid spacing parallel to the wall is shown in Figure 5(b).
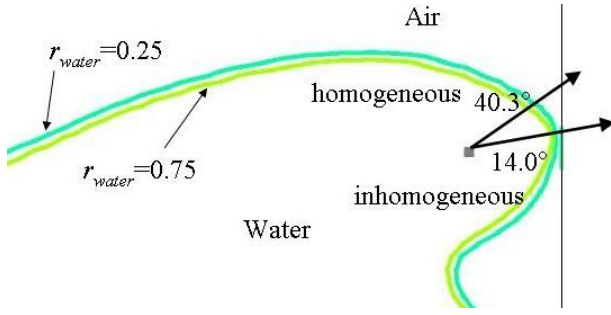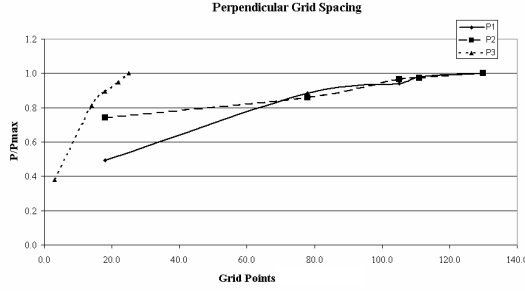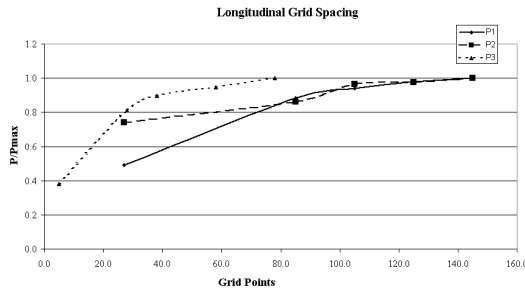
Figure 4: Water flow 0.5 mm before impact

5(a): Perpendicular grid spacing

5(b): Longitudinal grid spacing

Figure 5: Pressure dependence on local perpendicular (top) and longitudinal (bottom) flow feature resolution

Tank Size Variation

Equation (1), which describes the sloshing excitation, can be rewritten as

$$x = \alpha A \sin\left(\frac{2\pi}{T}\, t\right), \qquad (6)$$

where α is a constant. Using Equation (4) and (5), the sloshing excitation can be adjusted for kinematic similitude corresponding to the tank size. The computed values are given in Table 3.

The grid used for Case 1 which consists of 9360 elements is shown in Figure 6. Grid size and time discretisation parameters were determined from Ref [25]. This grid is then resized using the appropriate size factors for cases 2 and 3. The number of grid cells remains constant but the size of each element increases accordingly. A second set of grids (grid 2 and 3) is constructed for cases 2 and 3 respectively. They contain 38,319 and 153,273 elements respectively and they have the same cell size as the grid used for

Table 3: Systematic tank size variations

Parameter	Case 1	Case 2	Case 3
Sloshing Tank			
Size factor	1	2	4
Length	1.2 m	2.4 m	4.8 m
Height	0.6 m	1.2 m	2.4 m
Filling Level	60%	60%	60%
Excitation			
α	1	1.961	3.922
A	0.015 m	0.015 m	0.015 m
T_{10}	1.474 sec	2.044	2.890

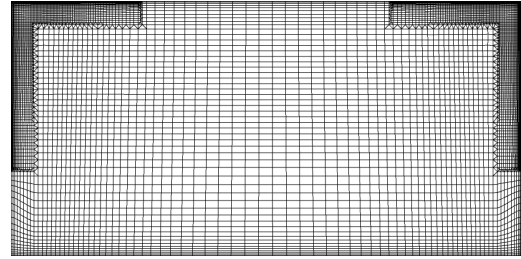case 1. The computational models used in the simulations are given in Table 1.

Figure 6: Typical hybrid grid used in CFD investigations. The grid contains 8652 hexahedral and 708 wedge elements

Figures 7(a) and 7(b) shows the pressure histories at monitor points P4 and P9 respectively for case 3 predicted using grids 1 and 3. At P4, which is dominated by the static pressure component, the pressure histories show reasonable agreement. At P9, the pressure spike captured on grid 3 is not observed using grid 1. Mean fluid speed is less susceptible to grid effects. Figures 7(c) and 7(d) show the mean fluid velocity, which is computed as

$$\text{Mean fluid speed} = \frac{\sum\limits_{mass} m_i\, |v_i|}{\sum\limits_{mass} m_i}. \qquad (7)$$

Figure 7(c) shows acceptable agreement between the mean fluid speed history observed using grids 1 and 3. Finally, mean fluid speed appears to be a quantity well suited for scaling with Equation (5) as shown in Figure 7(d). While the scaled and observed speed histories are out of phase when using grid 1, the predicted magnitudes show good agreement with those observed when scaling from grid 2.

Concluding Remarks

The faithful discretisation of a sloshing problem in CFD depends on the resolution of local flow features. The most severe pressures were confined to small regions in the problem and occurred as a result of an impact jet and consequent air bubble entrapment. While the air bubble size was estimated accurately using a coarse grid, the grid independence of pressure requires a considerably finer grid. Thus, grid guidelines explicitly specifying grid spacing (e.g. Ref [26]) may not be adequate for sufficiently accurate computations. A better approach is to use a coarse

Pressure history at P4

7(a): Pressure at P4

Pressure history at P9

7(b): Pressure at P9

Fluid speed for Case 3
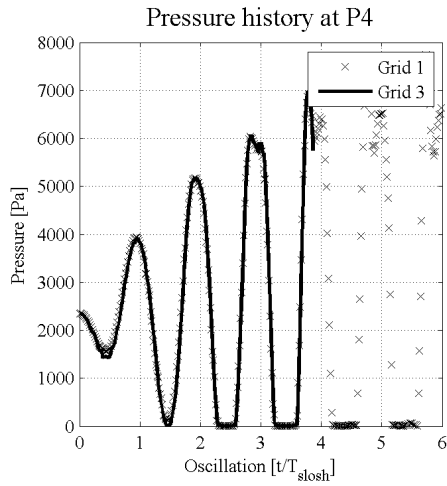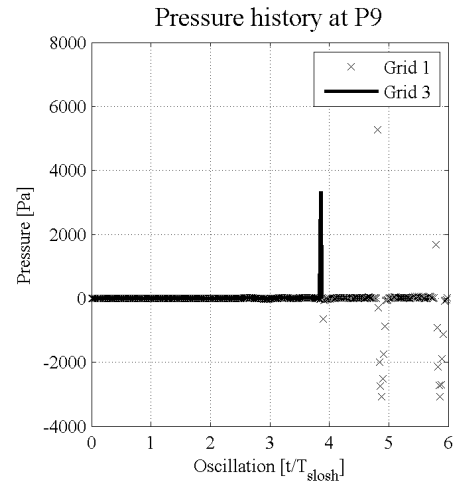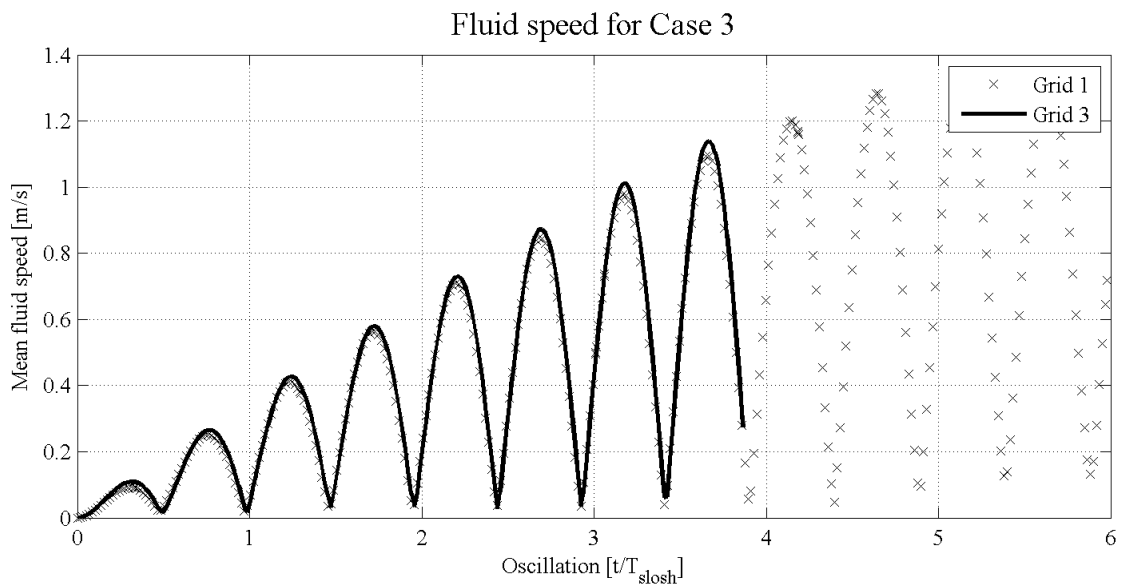
7(c): Grid dependence of fluid momentum

Scaled and observed fluid speed for Case 3
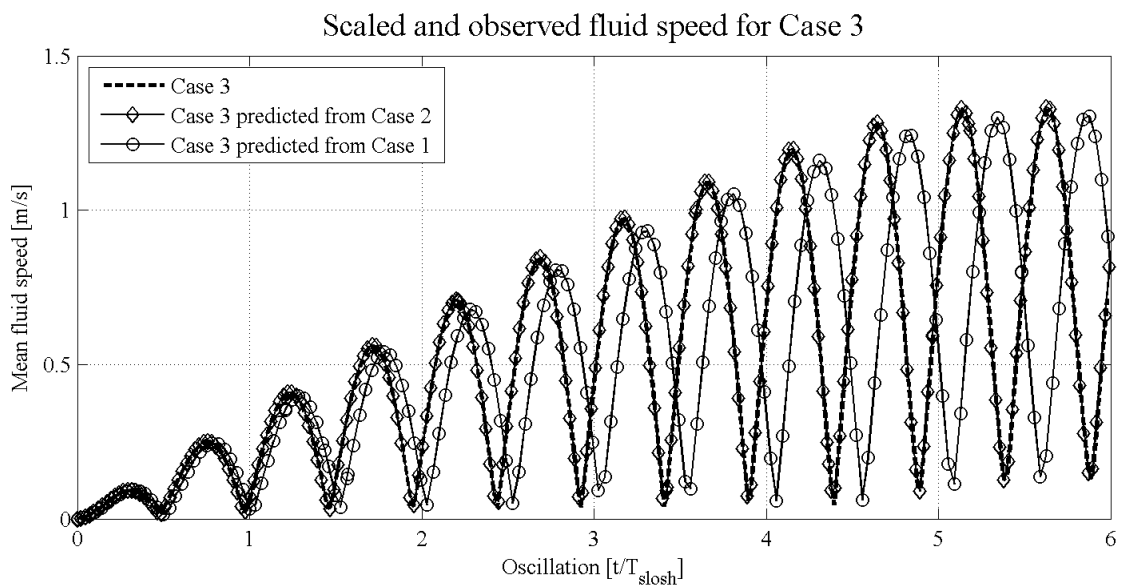
7(d): Predicted and observed fluid momentum

Figure 7: Grid influence on and scaling of fluid momentum

grid to observe critical flow features and repeat the simulation on a grid that adequately resolves local flow features by including information from e.g. Ref [27].

When increasing the tank size, local impact pressures are not captured unless the grid is refined according to the flow field. Moreover, the scaling of sloshing pressures remains a task of some difficulty. The mean fluid velocity defined in Equation (7) appears to be a quantity better suited to scaling. The magnitude of the mean fluid velocity of case 3 is estimated with good accuracy based on grids 1 or 2. However, a lag develops between the solution estimated from grid 1 and the mean fluid momentum obtained from grid 3.

The scaling of mean fluid velocity requires further study for additional validation. The simulations for the systematic variations of tank size should be extended to at least 10 oscillations. A further tank size of 9.6 m by 4.8 m should be included to confirm the scaling properties of mean fluid momentum. Ultimately, the mean fluid velocity may provide an alternative design criterion more suitable for scaling when assessing the safety of LNG tanks.

References

[1] Harald Olsen. What is sloshing? In *Seminar on Liquid Sloshing*. Det Norske Veritas, 1976.

[2] E Rizzuto and R Tedeschi. Surveys of actual sloshing loads onboard of ships at sea. In *NAV 97: International Conference on Ship and Marine Research*, 1997.

[3] Robert L Bass, E B Bowles, and P A Cox. Liquid dynamic loads in LNG cargo tanks. *SNAME Transactions*, 88:103–126, 1980.

[4] T Knaggs. New strides in ship size and technology. *Gas Ships: Trends and Technology.*, 2:1–4, 2006.

[5] Sungkon Han, Joo-Ho Heo, and Sung-Geun Lee. Critical design issues of new type and large LNG carriers. In *Proceedings of the 15th International Offshore and Polar Engineering Conference*, 2005.

[6] James Card and Hoseong Lee. Leading technology for next generation of LNG carriers. In *Proceedings of the 15th International Offshore and Polar Engineering Conference*, 2005.

[7] H Norman Abramson. The dynamic behavior of liquids in moving containers, with applications to space vehicle technology. Technical Report SP-106, National Aeronautics and Space Administration, 1966.

[8] Raouf A Ibrahim. *Liquid Sloshing Dynamics*. Cambridge University Press, 2005.

[9] I Hadzic, Frank Mallon, and M Peric. Numerical simulation of sloshing. Technical report, Technische Universität Hamburg-Harburg, 2002.

[10] Shahrouz Aliabadi, Andrew Johnson, and Jalal Abedi. Comparison of finite element and pendulum models for simulation of sloshing. *Computers and Fluids*, 32:535–545, 2003.

[11] R G Standing, S Amaratunga, F Lopez-Calleja, S Orme, and R Eichaker. Marine hydrodynamics modelling using CFD. In *CFD 2003: Computational Fluid Dynamics Technology in Ship Hydrodynamics*, 2003.

[12] Yonghwan Kim, Jungmoo Lee, Young-Bum Lee, and Yong-Soo Kim. Sensitivity study on computational parameters for the prediction of slosh-induced impact pressures. In *Proceedings of the 15th International Offshore and Polar Engineering Conference*, 2005.

[13] Shin Hyung Rhee. Unstructured grid based Reynolds-Averaged Navier-Stokes method for liquid tank sloshing. *Transactions of the American Society of Mechanical Engineers*, 127:572–582, 2005.

[14] Ould El Moctar. Assessment for tankers. *Shipping World and Shipbuilder*, 204:28–31, 2006.

[15] Mateusz Graczyk, Torgeir Moan, and Olav Rognebakke. Probabilistic analysis of characteristic pressure for LNG tanks. *Journal of Offshore Mechanics and Arctic Engineering*, 128:133–144, 2006.

[16] Munehiko Hinatsu. Experiments of two-phase flows for the joint research. In *Proceedings of SRI-TUHH mini-Workshop on Numerical Simulation of Two-Phase Flows*. National Maritime Research Institute & Technische Universität Hamburg-Harburg, NMRI, 2001.

[17] Bernhard Godderidge, Mingyi Tan, and Stephen Turnock. A verification and validation study of the application of computational fluid dynamics to the modelling of lateral sloshing. Ship Science Report 140, University of Southampton, 2006.

[18] Bernhard Godderidge, Mingyi Tan, Stephen Turnock, and Chris Earl. Multiphase CFD modelling of a lateral sloshing tank. In *Numerical Towing Tank Symposium*, 2006.

[19] C W Hirt and B D Nichols. Volume of fluid (VOF) method for the dynamics of free boundaries. *Journal of Computational Physics*, 39:201–225, 1981.

[20] M Ishii and T Hibiki. *Thermo-Fluid Dynamics of Two-Phase Flow*. Springer Verlag, 2006.

[21] Ansys Inc. *CFX-10 User's Guide*, 2005.

[22] B Godderidge, S Turnock, M Tan, and C Earl. An investigation of multiphase CFD modelling of a lateral sloshing tank. *Computers and Fluids (submitted)*.

[23] C E Brennen. *Fundamentals of Multiphase Flow*. Cambridge University Press, New York, 2005.

[24] Wu-Ting Tsai and Dick K. P Yue. Computation of nonlinear free surface flows. *Annual Review of Fluid Mechanics*, 28:249–278, 1996.

[25] B Godderidge, M Tan, C Earl, and S Turnock. Boundary layer resolution for modeling of a sloshing liquid. In *International Society of Offshore and Polar Engineers*, 2007.

[26] American Bureau of Shipping. Guidance notes on strength assessment of membrane-type LNG containment systems under sloshing loads. Technical report, American Bureau of Shipping, 2006.

[27] Joe F Thompson, Bharat K Soni, and Nigel P Weatherill, editors. *Handbook of Grid Generation*. CRC Press, 1999.

Use of Commercial RANSE Code for Open Water Propeller Calculations

Enrique Haimov (haimov@cehipar.es), Miriam Terceño
Canal de Experiencias Hidrodinámicas de El Pardo (CEHIPAR), Madrid, Spain
Ignacio Trejo (itrejo@seaplace.es) Seaplace, S.L.

INTRODUCTION

Commercial viscous CFD codes enter steadily into the naval engineering practice. Concerning the propeller open water performance prediction, some references can be cited among many others [4–10]. Various publications describe the use of viscous codes for the estimation of the scale-effect on propellers in uniform flow – for instance Ref. [7,8]. The present work reflects the first steps in the use of the code ANSYS CFX [1] in CEHIPAR for propeller predictions. Previously, the use of CFX in propeller applications has been reported by various authors [6,9,10]. We started with the simplest steady case - propeller in open water flow, the main objective being to fix the values of the free parameters, especially the mesh. Two model propellers of very different geometry, used in previous comparative exercises of the ITTC [2,3], were calculated. For sake of evaluation, lifting-surface calculations have been performed using the code MPUF-3A [11,12]. Finally, by computing the same propellers scaled to a typical full size, the scale effect on the forces is shown and discussed.

THE 3-D RANSE SOLVER

The RANSE Solver is the commercial program ANSYS CFX 11.0 with its pre-and post-processors used together with ICEM grid generator (Ref. 1). Its theoretical background is described in various publications and manuals and the program has been validated for various applications. The calculations were carried out in a rotating coordinate system fixed to the blades. The turbulence model chosen is the recommended $k - \omega$ Shear Stress Transportation Model (SST).

DOMAIN DEFINITION AND BOUNDARY CONDITIONS

The CFX-Pre-processor permits various definitions of the flow domain. It consists of two cylinders of different reference frames. The outer one represents the steady undisturbed flow of the entrance and the outlet, while the inner one, containing the propeller, rotates with its rate of rotation. The boundary condition on this fluid-fluid interface is the quasi-steady "Frozen Rotor" as it is known to require least amount of computational effort, being sufficiently precise when the   circumferential velocity is dominant. The wall and no slip conditions are imposed on the blades and the hub. We used two definitions, one shown in the figure below taking advantage of the circumferential symmetry of the flow and the geometry, and the other one is a full cylindrical domain.
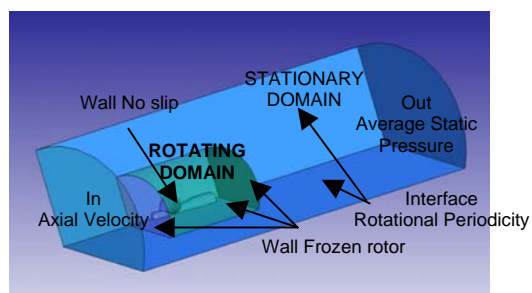
PROPELLER GEOMETRIES AND MESH GENERATION

The propellers calculated are the famous simple-geometry three-bladed P4119 and the more complex geometry five-bladed P4842, both David Taylor Model Basin's model propellers, used in the comparative exercises of the ITTC. A CAD view of the propellers can be seen in Figures 17 and 18. The geometrical characteristics and test results can be found in references [2] and [3].
The full geometry of the propellers blades has been generated by *PropGeo* program (Ref. 12) in ASCII format that was introduced to the commercial CAD program *Rhinoceros* to generate NURBS surfaces. This same code was used to generate the hub surfaces. Finally, ICEM grid generation program has been used for meshing the domain with unstructured grid, as can be seen in Figures 1 - 3.

    As it is well known, the grid generation is the most laborious and tricky work of RANSE applications, so different meshing strategies around the propeller blades have been used, three of them summarized in the following Table 1:

Table 1

| Mesh	Geometry definition	Type of Element
A	Back and face blade surfaces	Tetrahedral
C	Back, face and nose blade surfaces	Tetrahedral
D	Back, face and nose blade surfaces	Tetrahedral and Prism

Here we denoted as a nose, a surface formed by the geometry of the blade around the leading edge, thus separating the high curvature area of the blade from the rest of back and face surfaces. The positive effect of this on the resolution of the geometry can be seen comparing meshes A with C (Figures 1,2). The same resolution, defined for the total blade surfaces (back and face), would increase excessively the number of elements in the whole domain and also the computer time. The influence of the mesh type on the results for the pressure distribution is significant and will be shown later.

GRID SENSITIVITY AND CHOICE

Open water computations have been performed for different mesh density in order to reveal the convergence of the results for the forces. The following figure shows this for the basic regime (J=0.833) of the propeller DTMB P4119:
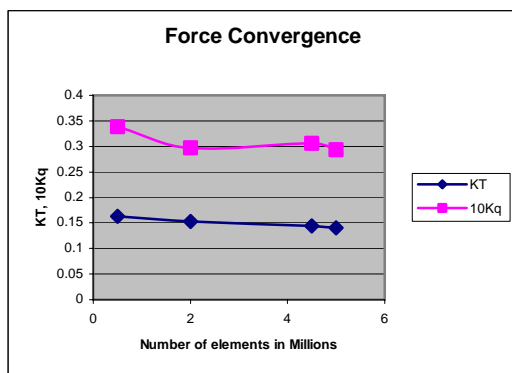
From this study we assumed that more than 3.0 millions of volume elements assure convergence for the forces. For the present calculations, depending on the type of mesh, the number of elements varied between 4.5 and 5.0 millions. The computer time on a work station of 64 bits OPTERON 2.4 GHz processor and 16Gb memory was around 36 hours.

COMPARISONS OF FORCES

DTMB P4119

Table 2 below shows the comparison of the viscous (CFX) and the lifting surface (MPUF-3A) calculations for the hydrodynamic forces on one blade, non-dimensional by $\rho n^2 D^4$, and for the moments (Table 3), non-dimensional by $\rho n^2 D^5$. The regime calculated is for advance coefficient 0.833.

Table 2

	Viscous Code	MPUF-3A
Axial	0.0536	0.0524
Horizontal	0.0307	0.0323
Vertical	0.0075	0.0011

Table 3

	Viscous Code	MPUF-3A
Axial	0.0097	0.0104
Horizontal	0.0175	0.0162
Vertical	0.0014	0.0011

DTMB P4842

Tables 4 and 5 below show the non-dimensional hydrodynamic forces and moments on one blade for advance coefficient J=0.905.

Table 4

	Viscous Code	MPUF-3A
Axial	0.0669	0.0659
Horizontal	0.0392	0.0385
Vertical	0.0026	0.0121

Table 5

	Viscous Code	MPUF-3A
Axial	0.0143	0.0144
Horizontal	0.0222	0.0218
Vertical	0.0016	0.0005

Generally, a very good agreement is observed. The discrepancy found for the vertical forces and moments is probably due to their small values.
Figures 4 and 5 show the open water curves of both model propellers, the lines being the experimental values [2,3]. Both, the RANSE and lifting surface codes reproduce the open water curves quite well.

COMPARISON OF STATIC PRESSURES AND FIELD POINT VELOCITY WITH EXPERIMENT

Post-processing the numerical results of CFX for the P4119 permitted to compare the non-dimensional pressure (C_p) distribution with model experimental data of Ref. 3. Figures 6 & 7 show C_p at relative radius 0.7, corresponding to the meshes A & D, being C quite close to D. The clear advantage of meshes D and C at the leading edges is observed and used for two more radial sections presented in Figures 8 & 9. The big circles and triangles correspond to the experimental data for the back and face, respectively, while the small ones are for the predictions. The next two figures (10 & 11) show C_p at 0.7 radius for two more advances (0.5 and 1.1). The radial distribution of the circumferentially averaged non-dimensional velocity components upstream (x/R=-0.3) and downstream (x/R=0.3281) of this propeller have been calculated and compared in Figures 12 – 16.

SCALE EFFECT ON THRUST AND TORQUE

A suitable application of the viscous code is the estimation of the scale effect. The exercise

consisted in applying a scale factor of 16 to both propeller models used before and running the viscous code for the full scale case too. The feature of ICEM to scale the mesh was used, thus conserving the same grid characteristics for both scales. The impact of the scale on the main forces (thrust and torque) is reflected in Tables 6 and 7 below. For comparison, the full scale prediction was obtained also by correcting the model thrust and torque following the ITTC'78 method.

Table 6 : Propeller DTMB P4119. Scale = 16.
$Rn_m = 8.7 \times 10^5$; $Rn_{fs} = 5.6 \times 10^7$
J = 0.833 ; K_{Tm} exp = 0.146 ; $10K_{Qm}$ exp = 0.280.

	Model scale	Full Scale Viscous Code	Full Scale ITTC'78
KT	0.148	0.158	0.151
10KQ	0.315	0.295	0.296

Table 7 : Propeller DTMB P4842. Scale = 16.
$Rn_m = 1.2 \times 10^6$; $Rn_{fs} = 7.6 \times 10^7$
J = 0.905 ; K_{Tm} exp = 0.310. $10K_{Qm}$ exp = 0.720,

	Model scale	Full Scale Viscous Code	Full Scale ITTC'78
KT	0.318	0.327	0.323
10KQ	0.731	0.718	0.704

where *Rn* is the Kempf's blade section Reynolds number. The viscous code assumes developed turbulent flow in both scales, and in this exercise, the full scale blade roughness is taken unrealistically small. The result is higher scale effect for the thrust than the ITTC'78 formulae.
As expected, the analysis of the force components revealed that almost the total contribution to the scale effect on the blades is due to the tangential forces and moments. For the hub, the normal forces have an important contribution to the scale effect.

CONCLUSIONS

- A suitable mesh generation process has been introduced for the use of a commercial RANSE flow solver for propeller applications.
- The open water predictions of the RANSE code are in good agreement with the model test results, although at this stage of our work, the viscous code did not provide clear advantages of precision compared to the inviscid codes. More cases, and focusing to the details of the flow, will undoubtedly show its usefulness.
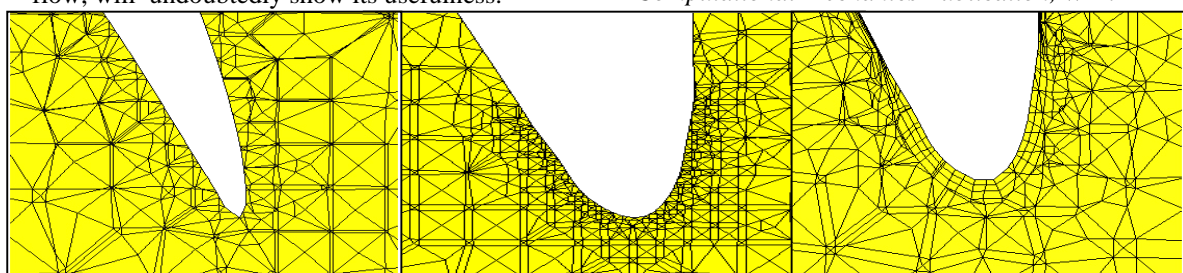
- As expected, the viscous code is sensitive to the scale, but more research, including meshing and benchmark data are needed to evaluate it.

REFERENCES

[1] ANSYS CFX code. *www.ansys.com*
[2] Koyama, K., (1993) *"Comparative Calculations of Propellers by Surface Panel Method", Workshop of the 20th ITTC Propulsor Committee (PC).*
[3] Jessup, Stuart, (1998) *" Experimental Data for RANS Calculations and Comparisons (DTMB P4119)", Workshop of the 22th ITTC PC.*
[4] Pylkkänen, J.V., A.Sánchez-Caja, T.Sundell, (1997) *"Applications of FINFLO RANS solver to naval hydrodynamics", Proceedings of Int. CFD Conference, Ulsteinvik. Norway.*
[5] Kim, H.T., J.Kim, F.Stern, (1998) *"Numerical Simulation of Turbulent Flow around a Marine Propeller", Proceedings of OC'98. Osaka, Japan*
[6] Abdel-Maksoud,M., F.Menter, H.Wuttke, (1998) *"Viscous Flow Simulations for Conventional and High Skew Marine Propellers", Ship Technology Research, vol.45, No.2.*
[7] Michael Stanier, (1998) *"The Application of RANS Code to Investigate Propeller Scale Effects", 22nd ONR Symposium on Naval Hydrodynamics.*
[8] Isao Funeno, (2002) *" On Viscous Flow around Marine Propellers – Hub Vortex and Scale effect" J.Kansai Soc. N.A. , No. 238.*
[9] Pittaluga, C., Cresta G.,(2005) *"RANSE Calculations for the Hydrodynamic Analysis of a Marine Propeller." 8th NuTTS, Varna, Bulgaria.*
[10] Mueller, S. et al. (2006) *" Comparing a Propeller Model with a Rotating Propeller in a CFD-Simulation of the Viscous Flow around a Ship",Proceedings of 9thNuTTS, Le Croisic, France*
[11] Kinnas, S., P.Griffin, A.Mueller, (1997) *"Computational Tools for the Analysis and Design of High-Speed Propulsors", CFD Conf., Ulsteinvik.*
[12] Baquero, A., A.Haimov, (1999) *"Marine Propeller Performance: Computational Prediction and Experimental Validation", CMEM, Sorrento, Computational Mechanics Publication, WIT.*

Figure 1: Mesh type A   Figure 2 :   Mesh type C   Figure 3:   Mesh type D
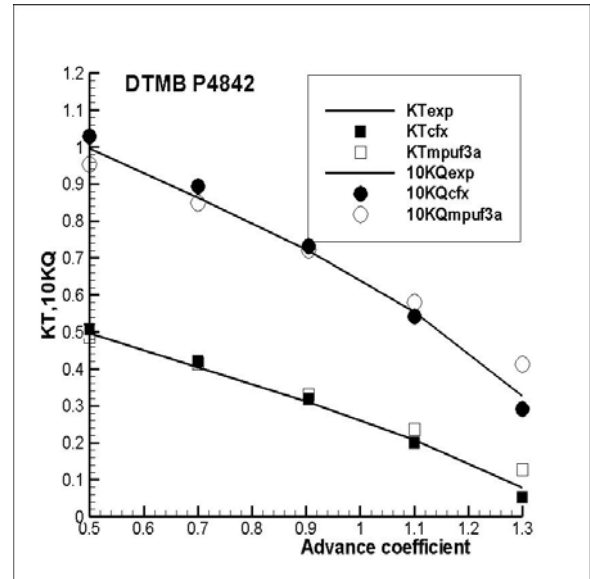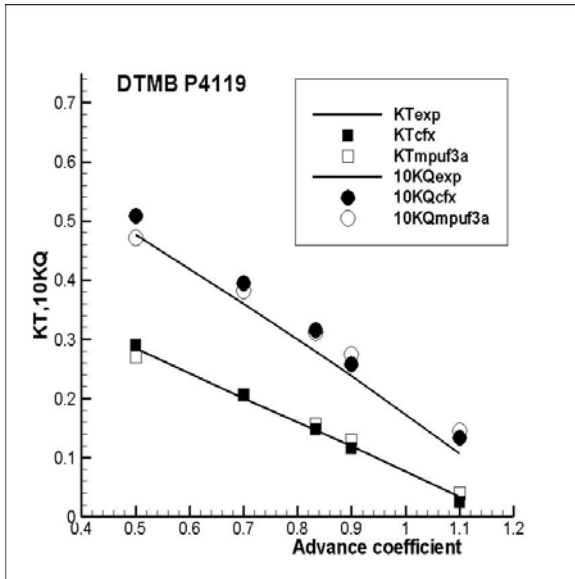
Figures 4 and 5 : Open water curves.
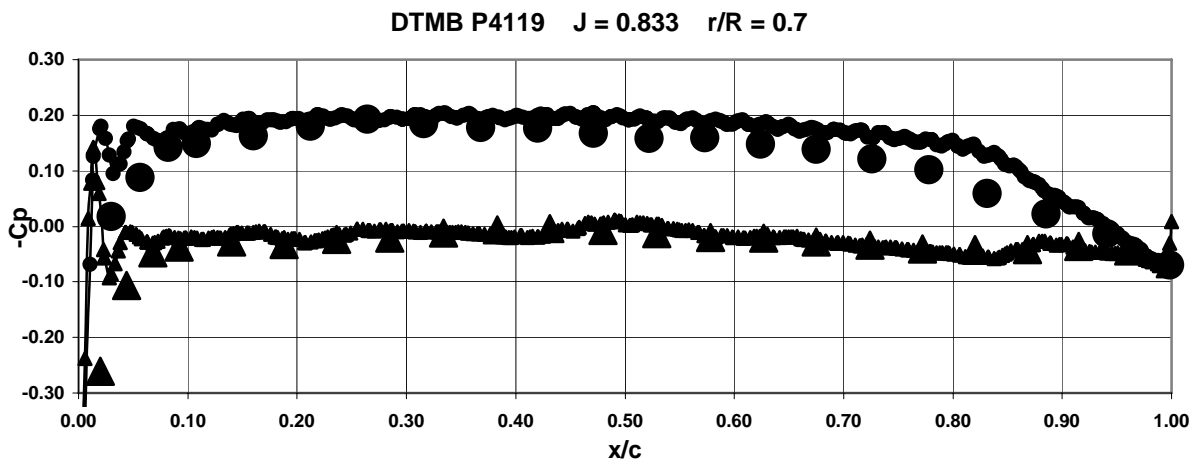
Figure 6:   Chordwise Pressure Distribution at r/R=0.7 for Mesh type A
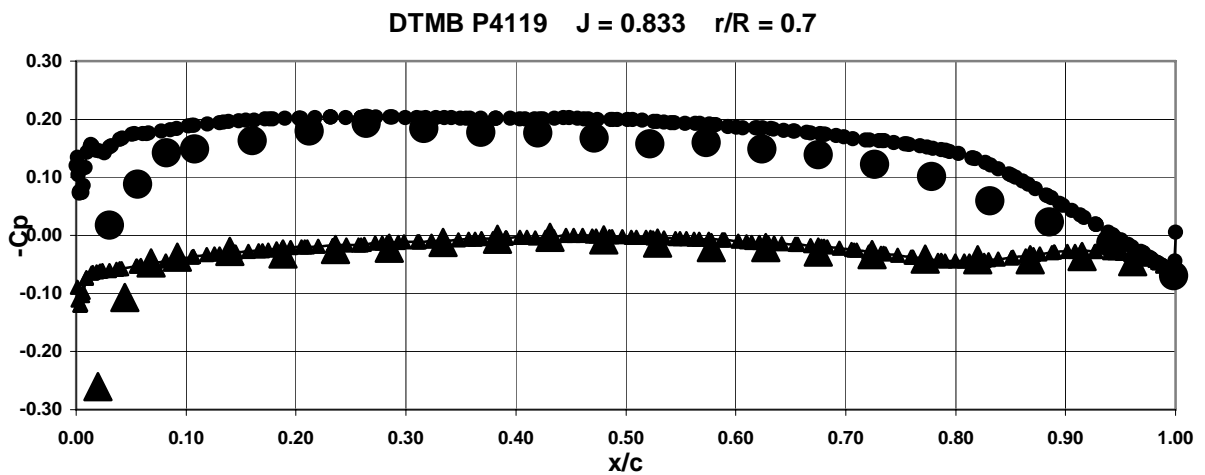
Figure 7:   Chordwise Pressure Distribution at r/R=0.7 for Mesh type D

DTMB P4119   J = 0.833   r/R = 0.3
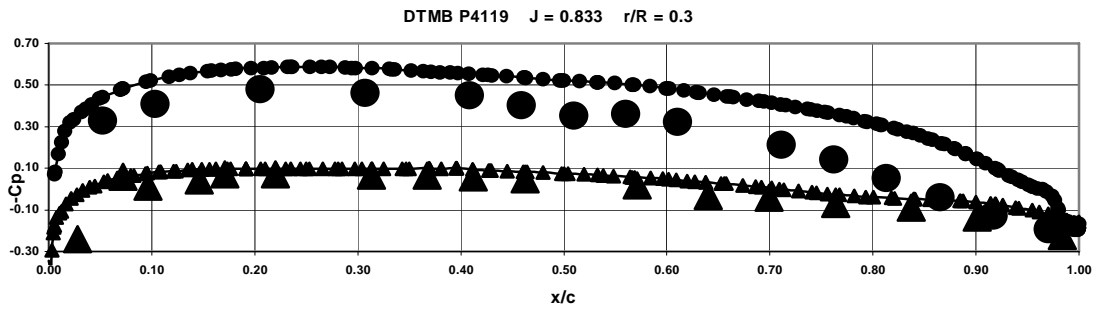
Figure 8:   Chordwise Pressure Distribution at r/R=0.3 for Mesh type D

DTMB P4119   J = 0.833   r/R = 0.9
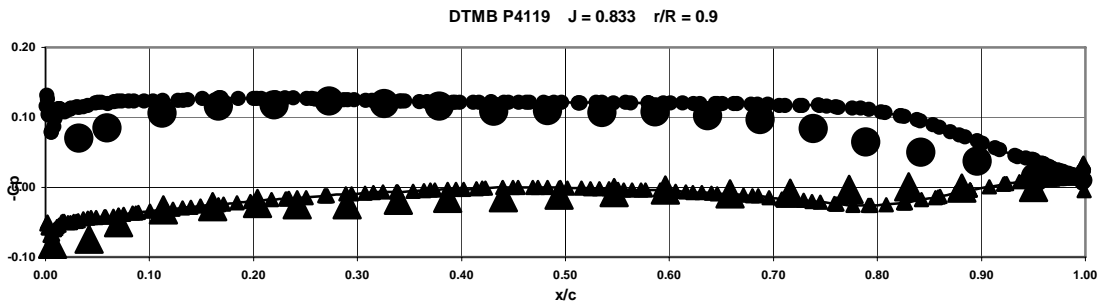
Figure 9:   Chordwise Pressure Distribution at r/R=0.9 for Mesh type D

DTMB P4119   J = 0.5   r/R = 0.7
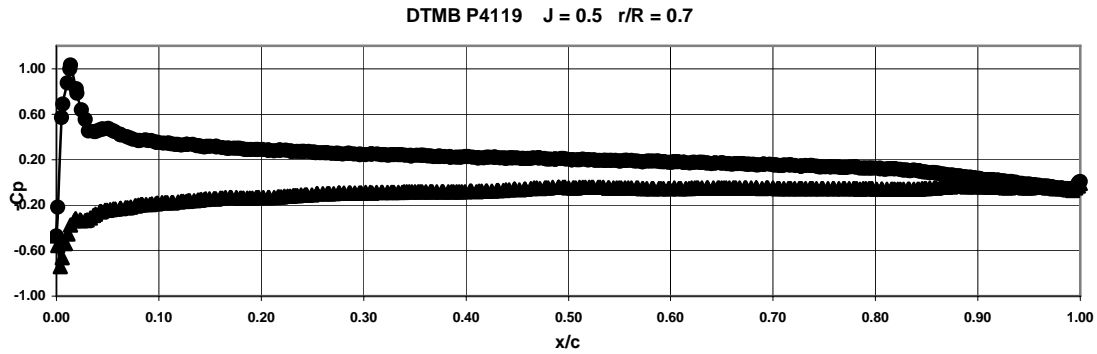
Figure 10:   Chordwise Pressure Distribution at r/R=0.7 for J=0.5

DTMB P4119   J = 1.1   r/R = 0.7
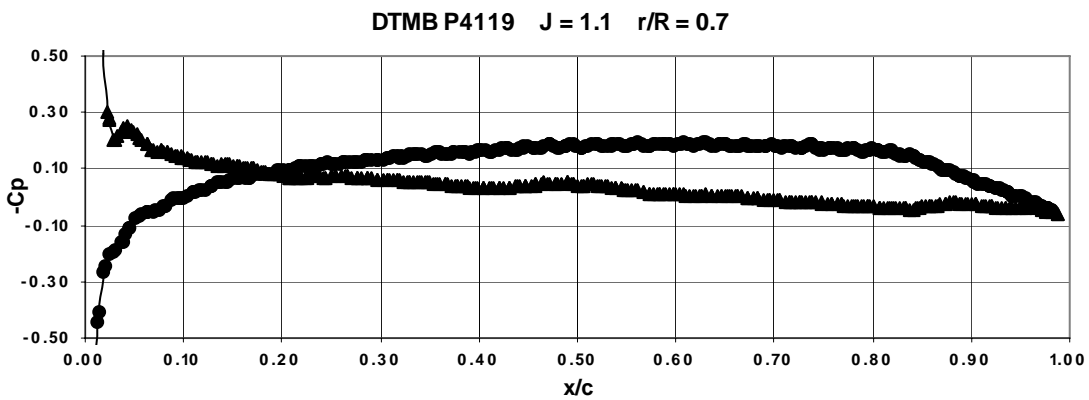
Figure 11:Chordwise Pressure Distribution at r/R=0.7 for J=1.1
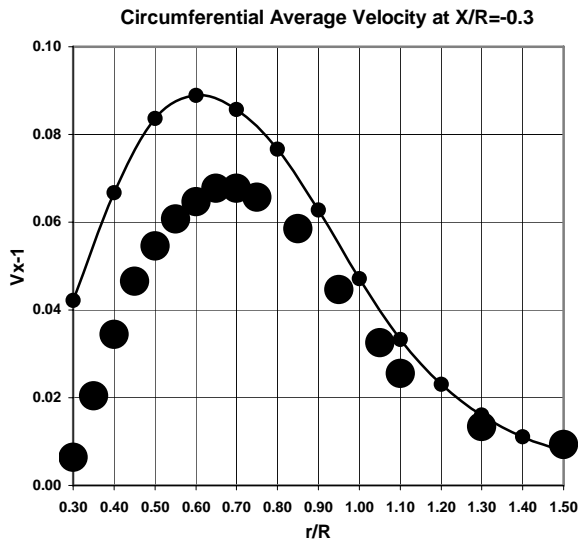
Figure 12: Axial average velocity upstream
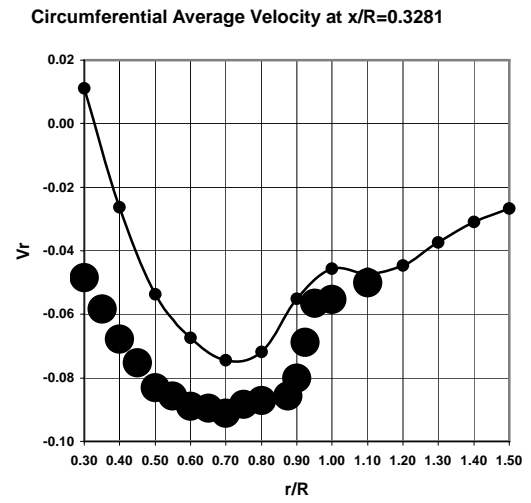
Figure 15: Radial average velocity downstream
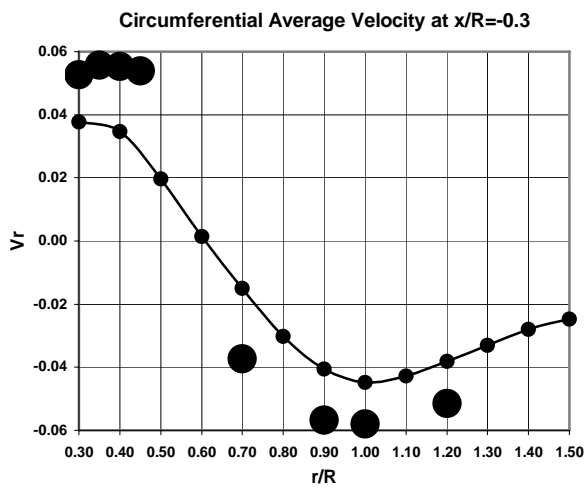
Figure 13: Radial average velocity upstream
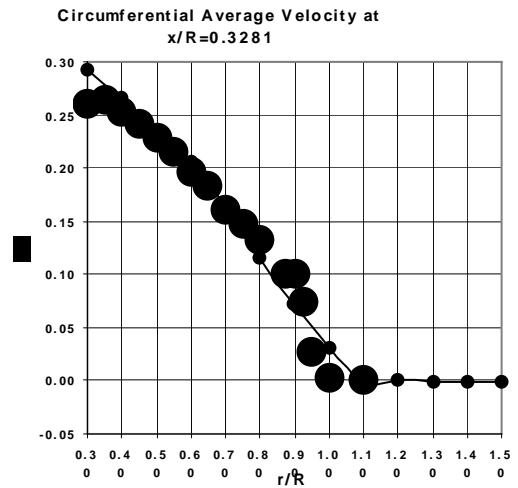
Figure 16: Tangential average velocity downstream
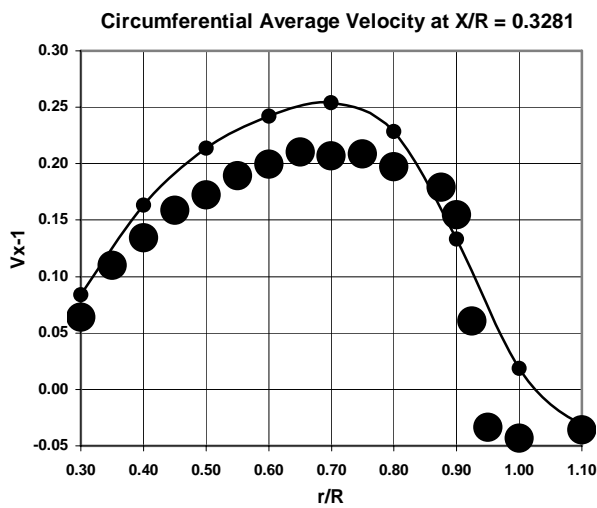
Figure 17: DTMB 4119

Figure 14: Axial average velocity downstream
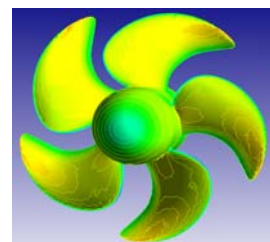
Figure 18: DTMB 4842

A RANS study on the Interaction between a Propeller and a Rudder

in Open Water

K-J Han[1], L. Larsson[2], B. Regnström[3]

[1]Chalmers University of Technology, kaijia.han@chalmers.se

[2]Chalmers University of Technology, lars.larsson@chalmers.se

[3]Flowtech International AB, Sweden, regnstrom@flowtech.se

Introduction

When designing a ship, it is important to estimate accurately the effects of propeller-rudder interaction, as the rudder behind a propeller and a ship has a great effect both on the propulsive and maneuvering performance. In order to both understand the physical phenomenon and validate the RANS solver SHIPFLOW, the interaction between a propeller and a rudder in open water is qualitatively and quantitatively predicted and validated against experimental data. Furthermore, the propeller slipstream deformation is illustrated and the regain of rotational losses by the rudder is estimated.

Open water propeller characteristics

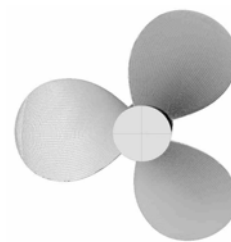In the present work the CFD software SHIPFLOW V3.4 was used. SHIPFLOW is a system for predicting the flow around ship hulls and corresponding forces. SHIPFLOW includes two RANS codes, and the one used in the present work is CHAPMAN [1]. It is linked to a propeller analysis code, which is a lifting line model based on Goldstein's κ theory.

The interactive coupling between CHAPMAN and the lifting line model via body forces is done with the following procedure at regular intervals, normally every 10 iterations in the RANS solver: (i) Interpolate the current approximation of the velocity field from the box grid to an embedded cylindrical grid; see Figure 2. (ii) Obtain the effective wake on the blade of the propeller. (iii) Run propeller model in the effective wake and calculate the blade circulation, force and torque (iv) Distribute the computed force over the volume cells in the cylindrical grid. (v) Interpolate the forces on the cylindrical grid to the box grid and introduce them on the right-hand side of the N-S equations. The fluid that passes through the cells is thus affected by a body force and is accelerated so that the time-averaged action of the propeller is simulated. The sum of the forces will give the fluid passing through the propeller disc a longitudinal and angular momentum consistent with the thrust and torque on the propeller. At convergence the two models are matched in the sense that the absolute wake computed by the RANS method at points sampled in a circular disc in the middle of the cylindrical grid will be equal to the total wake computed by the propeller model at the same points.

P/D=0.6   P/D=1.0

Fig1 Comparisons of open water characteristics between computation and measurement

The performance of the coupled model is validated first by a series of Wageningen B4-70 propellers by comparing the open water characteristics with the experimental 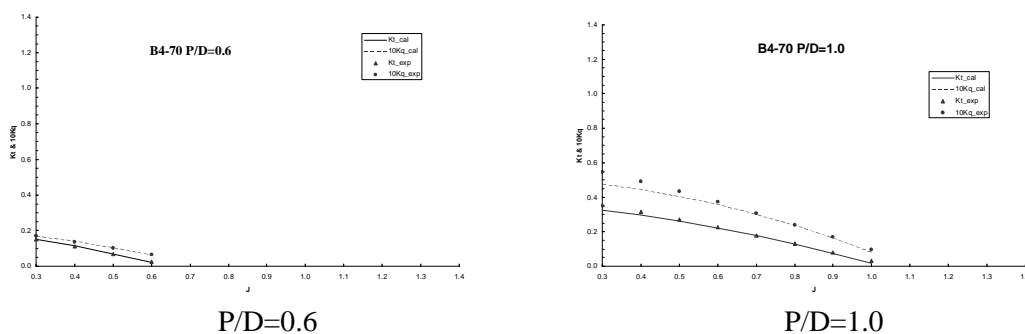data (see Stierman [2]). Fig 1 shows the open water characteristics of the propellers, comparing the calculated and the measured data. It is observed from Fig. 1 that for the propeller with P/D=0.6, the calculated results agree well with those from measurements. For the propeller with P/D=1.0, thrust values are well predicted for all J values but torques are only accurately predicted while J over 0.6. Such under-predictions might be resulted from ignoring the hub effects and the slipstream contraction and from the empirical formulation for viscous drag of the blades. Especially when J is low, the loading on the propeller blade is much higher than at normal condition. The influence of the tip vortex and leading edge separations become more extreme in such conditions and can not be ignored.

Interaction between a propeller and a rudder in open water

To understand and numerically simulate the interaction between a propeller and a rudder in uniform inflow, Stierman's experimental cases are run and compared both quantitatively and qualitatively as followed. In this part, we first compare the absolute values of thrust, torque and rudder forces with the rudder behind to the measured data. Second, the increments of thrust and torque with rudder behind are also compared to the experimental results. Third, the flow field and slipstream deformation are presented and discussed. Fourth, we investigate the influence of different parameters, such as the distance between the rudder and the propeller and the thickness of the rudder on the increments. Finally, regain of rotational losses by the rudder is studied.

In Stierman's experiments [2], a series of open water tests are carried out with the same Wageningen B4-70 propellers calculated earlier in the paper and two rudders located in three longitudinal positions. The rudders used are rectangular (without taper) with a chord length c=0.192m and a span s=0.26m. The rudder profiles are of NACA0012 and NAVA0018 wing sections respectively. The distance between the propeller and the rudder, measured from the aft end of the propeller blade to the leading edge of the rudder, is d/D=0.1, 0.3 and 0.5, respectively. All measurements are carried out at the same rate or revolution 1000rpm. The whole range of advance ratios is covered by varying the speed of advance. The measured data include the speed of advance, the revolution speed, the propeller thrust, the propeller torque and the rudder force. The rudder force is defined as positive (thrust) in the opposite direction of the inflow. The propeller thrust and torque are transformed into non-dimensional coefficients as normal and the rudder thrust coefficient is defined as $K_R = \dfrac{F}{\rho n^2 D^4}$.
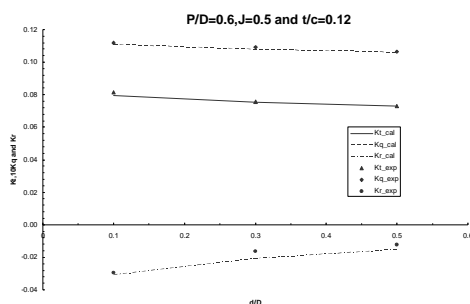

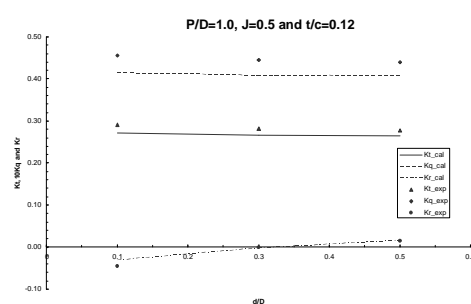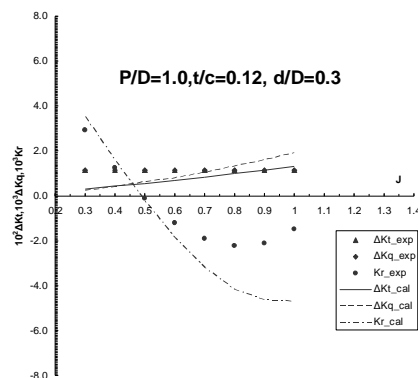Fig 2 Comparison between calculation and experiment at three locations for P/D=0.6

Fig 3 Comparison between calculation and experiment at three locations for P/D=1.0

It is illustrated in Fig 2 that the calculated results for P/D=0.6 agree well with measured data for thrust and torque. The drag on the rudder is higher than from the experiment. It is observed in Fig 3 that for the

propeller with P/D=1.0, the calculated thrust and torque are lower than those measured. Such an under-prediction has similarly appeared in open water propeller prediction, shown in Fig 1. At this specific J value, the force on the rudder varies from drag to thrust with the rudder further away from the propeller. The correlation between the calculated and the measured K_r is generally good.

The increment of the thrust and the torque coefficients, ΔK_T and ΔK_Q, are defined same as those in Stierman, i.e. the difference of K_T and K_Q respectively between the cases with and without rudder behind the propeller. Because of unavailability of the absolute experimental data, the regression formulas of ΔK_T, ΔK_Q and K_R based on the experimental data and derived by Stierman are compared with those from calculations. According to the formulas provided by Stierman, ΔK_T and ΔK_Q are independent on the

advance ratios.

Fig 4 Comparison of ΔKt, ΔKq and Kr between calculation and experiment

It is observed from Fig 4 that at lower advance ratios, the calculated K_R is rather close to the measured data. However, the calculated ΔK_T and ΔK_Q are underestimated. At higher advance ratios, the calculated drags on the rudder are overestimated compared with the experimental data, although ΔK_T and ΔK_Q are close to the measured. It is noted that the calculated ΔK_T and ΔK_Q are linearly increased with increase of J instead of a constant indicated by Stierman's regression formulas.

Deformation of propeller slipstream

The presence of the rudder behind the propeller deforms the slipstream considerably. In order to illustrate and study the influence of the propeller on the flow around the rudder, the axial velocity contours are plotted at four positions along the rudder; at the leading edge, in the middle of the rudder, at the trailing edge and one just behind the trailing edge of the rudder.

Fig 5 shows the flow seen in the upstream direction. As regards the axial velocity component, it is seen that the effect of the propeller influences the rudder flow all along the rudder. At the leading edge of the rudder, the flow behind the propeller is separated because of the thickness of the rudder and not axi-symmetric any longer. There is a region with higher axial velocity hitting on a position close to the root of the rudder on the starboard side and also a position close to the tip of the rudder on the port side. At the station further down the rudder, a tip vortex has started to develop because the pressure difference between the pressure on starboard and port side of the rudder. Such a tip vortex becomes stronger along the rudder and can be observed at the station on the trailing edge and in the wake after. The pressure difference and rotation of the propeller leads the flow on starboard side downwards and flow on the portside upwards. The

same tendency can be also observed along the rudder and in the wake behind the rudder. A vortex close to the hub of the propeller is also observed along the rudder. The position of such a vortex seems higher on the starboard side and lower on port side of the rudder. The last figure shows clearly the slipstream deformation with rudder behind a propeller.

At leading edge

In the middle of the rudder

At the trailing edge

Wake after the trailing edge

Deformation of the slipstream
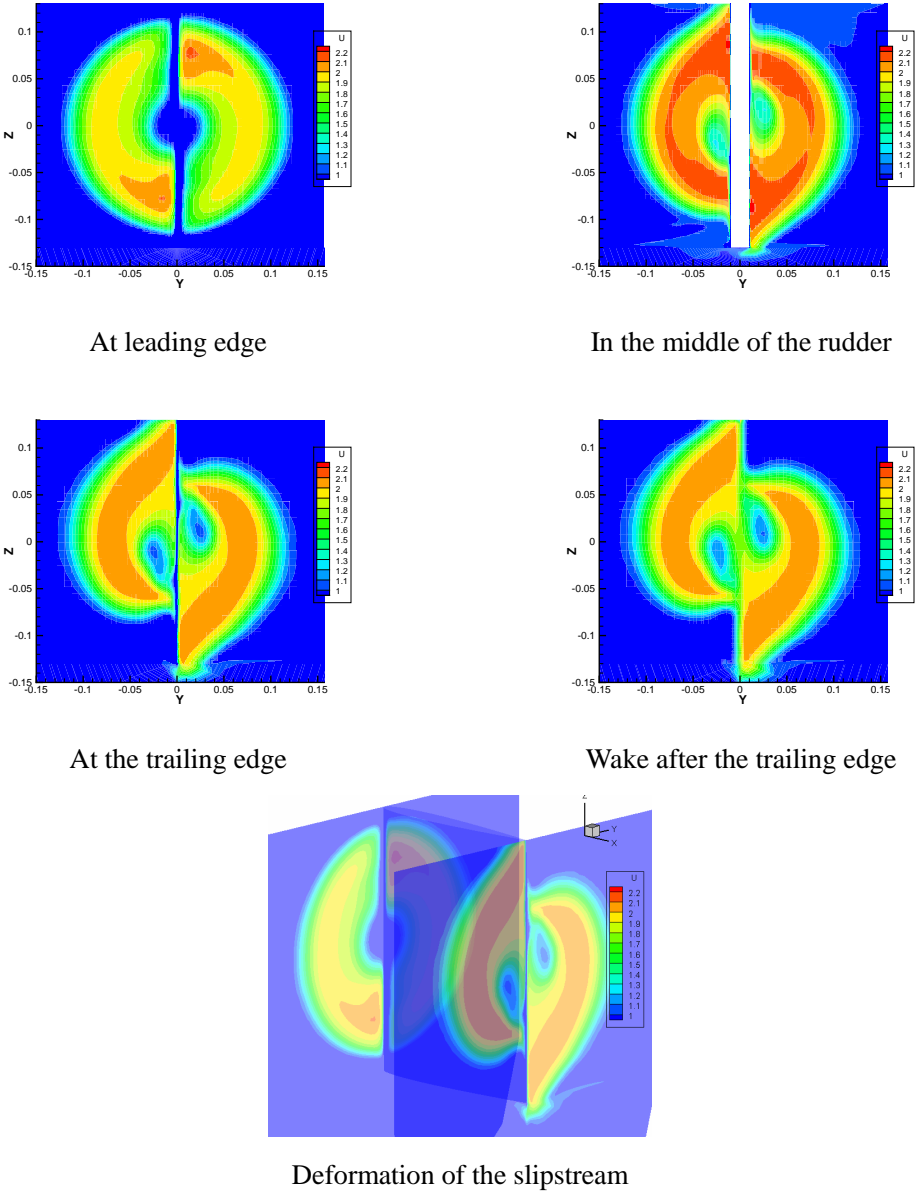
Fig 5 Axial velocity contours along the rudder and slipstream deformation

Influence of parameter distance d/D and rudder's thickness t/c

ΔK_T, ΔK_Q and K_R versus J at different distances d/D are illustrated in Fig 6. It can be seen that the rudder experiences a thrust force at low advance ratios and a drag at higher advance ratios. The closer the rudder is to the propeller, the higher the drag or lower the thrust on the rudder becomes because more pressure drag is induced although the friction drag on the rudder is almost same. With the rudder further away from the propeller, the blocking effect of the rudder is reduced so that the thrust and torque on the

propeller are less influenced by the rudder.

The thrust and torque increments ΔK_T, ΔK_Q and K_R versus J for rudders with different thickness at a distance d/D=0.3 are illustrated in Fig 7. It is observed that with the increase of the thickness of the rudder, the drag on the rudder increases. The blocking effect of a thicker rudder results in a decrease of the total axial velocity, which increases the thrust and torque on the propeller.
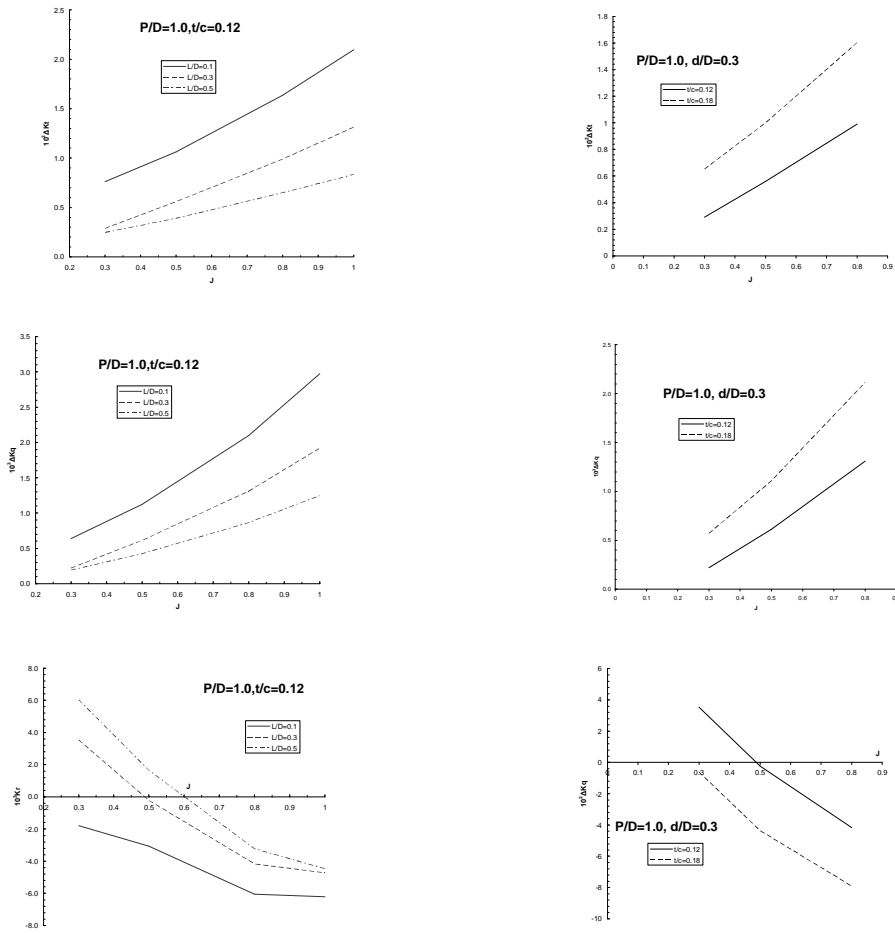
Fig 6 ΔKt, ΔKq and $Kr \sim$ d/D   Fig 7 ΔKt, ΔKq and $Kr \sim$ t/c

Regain of rotational losses by the rudder

According to Chang [3], the open water propeller efficiency can be divided into three parts: axial, rotational and viscous losses, i.e. $\eta_0 = \eta_{AX}\,\eta_{ROT}\,\eta_{VIS}$ where η_{AX} is the axial efficiency which accounts for the momentum losses in longitudinal direction. The rotational efficiency η_{ROT} is the efficiency accounting for the rotational momentum losses. The viscous efficiency η_{VIS} is the efficiency accounting for the viscous losses on the propeller blades. These equations can only be used with a propeller alone.

When a rudder is behind a propeller, the same equation can be applied for η_{AX} but with thrust

loading coefficient defined as $C_T = \dfrac{8(K_T + K_R)}{\pi J^2}$. The equation for the rotational efficiency η_{ROT} can not be used because the assumption for the derivation of this equation is not valid for the cases with a rudder behind. However, as recommended by [3], we can assume that the viscous loss of the propeller is the same with and without rudder. Then the rotational efficiency η_{ROT} can be defined instead as

$$\eta_{ROT} = \frac{\eta_{0_{PR}}}{\eta_{AX_{PR}}\eta_{VIS}}$$ where $\eta_{0_{PR}}$ and $\eta_{AX_{PR}}$ are the open water efficiency and rotational efficiency with

rudder behind the propeller, respectively. Take a case we have investigated earlier, i.e., the propeller with P/D=1.0 and the distance between propeller and rudder at d/D=0.3. The profile of the rudder is NACA0012 and the advance ratio is 0.5. We listed the relative values for such a case without and with rudder behind the propeller in Tab 1.

	Calculation		Experiment	
	Without rudder	With rudder	Without rudder	With rudder
η_0	0.5151	0.5157	0.4966	0.5038
K_T	0.2609	0.2665	0.2710	0.2823
K_Q	0.0403	0.0409	0.0434	0.0456
K_R	0	-0.0002286	0	-0.0001285
C_T	2.657	2.712	2.76	2.873
$\eta_{AX=}$	0.687	0.683	0.680	0.674
η_{VIS}	0.819	0.819	0.800	0.800
η_{ROT}	0.916	0.925	0.912	0.934
Rotational losses	8.4%	7.5%	8.8%	6.6%

Tab 1 Regain of rotational losses

The calculated rotational loss of the open water propeller without rudder behind is rather close to the measured one. However, with a rudder behind, the calculated loss is 7.5% but 6.6% for the experiment mainly because of the over-estimated drag on the rudder. About 11 percent rotational loss is regained by the rudder in the calculation.

Conclusions

A RANS solver, coupled with a lifting line method for propeller performance analysis, is both quantitatively and qualitatively validated with a series of Wageningen B4-70 propellers in uniform inflow and a study on the interaction between a propeller and a rudder in open water. Increments of forces on the propeller are generally well predicted but the drag of the rudder is overestimated. The influence of distance between the propeller and rudder and the thickness of the rudder on the performance of the propeller and force on the rudder show the same tendency as experiments. The propeller slipstream is considerably deformed because of the rudder behind. A tip vortex is observed and developed along the rudder. The regain of rotational losses by rudder is studied and about 11% rotational losses are recovered by the rudder.

To further validate the solver, an interaction study between hull/propeller/rudder will follow.

References

1. XCHAP Theoretical Manual, FLOWTECH International AB, Sweden

2. Stierman, E.J, *The Influence of the rudder on the propulsive performance of ships Part I & II*, International Shipbuilding Progress, 36, No. 407, pp. 303-334, 1989

3. Chang Pin Yu, Noonan, Edward F., Scherer J.Otto, Seibold Frederick and Wechsler Laskar, *Limitations on the maximum power of single-screw ships*, SNAME Transactions, Vol, 87, pp. 121-153,1979

ON THE IMPLEMENTATION OF AN INTERFACE CAPTURING METHOD

Satu Hänninen and Tommi Mikkola
Ship Laboratory, Helsinki University of Technology[1]

1 INTRODUCTION

This abstract describes the implementation of an interface capturing method to the 2D unstructured flow-solver that has earlier been developed at the Ship Laboratory of Helsinki University of Technology, *Mikkola (2006)*. The flow solver already includes an interface tracking method for the simulations of free-surface flows. The reason for the implementation of the interface capturing method is the interest to study phenomena with strongly non-linear behaviour of free-surface. Interface tracking methods cannot handle for instance wave breaking.

Before the actual implementation of the interface capturing method, it was essential to do some modifications to the existing basic flow solver, Section 2. The implemented interface capturing approach and routine are summarised in Section 3. The structure of the coupled flow-solver and the interface routine is given in Section 4. Section 5 represents early results of a dam breaking problem.

2 MODIFIED NUMERICAL METHOD FOR BULK FLOW

Mikkola (2006) has given a detail description of the numerical method that has been used as the basis of this work. In brief, the flow solver uses a 2D unstructured Finite Volume Method and a collocated SIMPLE-type pressure correction scheme. The simulation of time-dependent flows is based on a three level fully implicit scheme. That method is implemented using a dual time stepping, i.e. both a physical and a pseudo time step are used. The momentum equations are solved with the conjugate gradient square stabilised method (CGSTAB) and the pressure correction equation with the conjugate gradient method (CG). In both cases, incomplete Cholesky preconditioning is used.

The flow solver described in *Mikkola (2006)* has previously been tested only with triangular computational volumes. As the easiest way to test the functioning of an interface capturing method is to use square or rectangular computational volumes, the code was slightly modified, so that it can tolerate other cell forms than triangles as well.

In the case of interface tracking, the computational domain is deformed according to the movements of the free-surface level so that the domain contains only water. In the case of interface capturing, the computational domain is extended also to the air domain, in which the water is supposed to flow during the solution. Therefore, the properties of the fluid change dramatically, when an interface-capturing method is used. Practically, this means that the flow solver must tolerate the discontinuation of the density and the pressure gradient over the free-surface level.

As fluid parameters are assumed to be constant inside each computational volume, the possible discontinuation occurs on the faces of computational volumes. This is to say that the interpolation of pressures and densities to the cell faces need a special treatment. A simple distance weighted average for the face values of pressure and density results in significant unphysical velocities on both sides of the discontinuation face.

For simplicity, the calculation of the fluid density on cell faces is eliminated by dividing the momentum equations by density ρ:

$$\int_\Omega \frac{\partial v_i}{\partial t} dV + \int_{\partial\Omega} v_i \vec{v}\vec{n} dS = -\frac{1}{\rho}\int_{\partial\Omega} p n_i dS + \nu \int_{\partial\Omega} \sum_i n_i \frac{\partial v_i}{\partial x_i} dS + \int_\Omega g_i dV, \tag{1}$$

---

[1]Ship Laboratory, Helsinki University of Technology, Tietotie 1, FIN-02015 Espoo, Finland. E-mail: Satu.Hanninen@hut.fi

where $\vec{v}$ is velocity, $\vec{n}$ unit normal vector, Ω computational domain and $\partial\Omega$ its boundary, p pressure, ν kinematic viscosity and g acceleration due to gravity.

The interpolation of pressure to cell faces is done according to *Queutey and Visonneau (2007)*:

$$p_f = \frac{h_r \rho_r p_l + h_l \rho_l p_r}{h_r \rho_r + h_l \rho_l} + U1, \tag{2}$$

where h is the distance between the cell centres on both sides of the face and h_r and h_l the distances from the cell face to the cell centre on the right and left hand side respectively. $U1$ is the contribution from the possible grid unorthogonality. ρ and p denote density and pressure respectively. The indices r and l indicate the values in the cells on the left and right sides of the face.

The pressure gradient divided by density is needed within the pressure correction stage and it is calculated with (*Queutey and Visonneau (2007)*)

$$\left(\frac{\vec{\nabla} p \cdot \vec{n}}{\rho}\right)_f = \frac{1}{\hat{\rho}} \frac{p_r - p_l}{h} + U2, \tag{3}$$

where

$$\hat{\rho} = \frac{h_l \rho_l + h_r \rho_r}{h} \tag{4}$$

and $U2$ is the contribution from grid unorthogonality.

An additional thing to consider with interface capturing is the treatment of the hydrostatic pressure. When free-surface flow simulations have been done previously with the present flow solver, piezometric pressure has been used and the influence of hydrostatic pressure has been introduced through the implementation of the free-surface boundary condition. With interface capturing, it is necessary to include the effect of hydrostatic pressure through the source term. Having the effect of hydrostatic pressure in the source term practically means in most cases that it is the largest term of the source term. If the flow solver is compiled using single precision, unphysical pressure gradients appear. The reason is that the influence of the rounding errors starts to be considerable in the evaluation of pressure differences due to the large absolute value of pressure.

3 INTERFACE CAPTURING

The so-called volume fraction method is used (see, for instance, *Hirt and Nichols (1981)*). The volume fraction α is defined for each control volume as

$$\alpha = \frac{\text{volume of fluid 1}}{\text{total volume}}. \tag{5}$$

The convection of the volume fraction is solved from

$$\frac{\partial \alpha}{\partial t} + \nabla \cdot \alpha \vec{v} = 0. \tag{6}$$

To solve Eq. (6), the volume fraction values need to be interpolated to cell faces. Several papers have been published on different interpolation methods that can be used for accurate capturing of sharp interfaces (see, for instance, *Queutey and Visonneau (2007)*, *Ubbink (1997)*, *Jasak (1995)*). The Inter-Gamma Differencing Scheme (IGDS) presented by *Jasak (1995)* is implemented into the present code. He has introduced the scheme by using the normalised variables $\tilde{\alpha}$:

$$\tilde{\alpha} = \frac{\alpha - \alpha_U}{\alpha_D - \alpha_U}. \tag{7}$$

The lower indices are given in Fig. 1.

IGDS, as *Jasak (1995)* has presented it, is given in the first two columns on Table 1. The implementation of IGDS requires the calculation of the actual volume fractions α_f on the cell faces. This has not been presented in *Jasak (1995)*. The present implementation of α_f is given in the third column of Table 1. Regarding the implemented blending option, it is different from the one given in *Queutey and Visonneau (2007))*.

The three-time level method is used for the time discretisation and CGSTAB is used to solve Eq. (6).
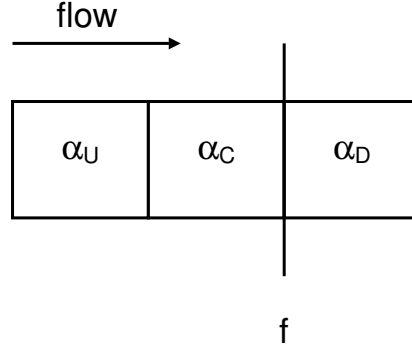
Figure 1: Cell notations in the IGDS description.

Table 1: IGDS

$\tilde{\alpha}_C$	$\tilde{\alpha}_f$	α_f	
$]-\infty, 0$	$\tilde{\alpha}_C$	α_C	UDS
$], \frac{1}{2}[$	$-2\tilde{\alpha}_C^2 + 3\tilde{\alpha}_C$	$4\tilde{\alpha}_f(1-f_x)(\alpha_D - \alpha_C) + \alpha_C$	Blending
$[\frac{1}{2}, 1[$	1	α_D	DDS
$[1, +\infty$	$\tilde{\alpha}_C$	α_C	UDS

4 COUPLED FLOW-SOLVER

The solution process of the coupled bulk flow and interface capturing solver is the following

1. Initialise flow variables.

2. Set time to $t = t + dt$.

3. Iterate the solution of velocity and pressure fields from momentum and pressure equations.

4. Iterate the solution of volume fraction values from Eq. (6).

5. If necessary, return to step 3 to obtain an accurate solution for the present time step.

6. Return to step 2 to proceed to the next time step.

To ensure a bounded solution of volume fraction values, a modified convection velocity field is used within the interface capturing routine, step 4. It is necessary especially, if the bulk flow solution is not computed accurately in step 3 before proceeding to step 4. The velocities on cell faces that are used to calculate the error in mass balance for pressure correction are used. Before the interface capturing routine, those velocities are corrected with the solution of the pressure correction. This ensures that the velocities that are used in the interface capturing routine satisfy the continuity condition in each computational volume.

5 TEST CASE: COLLAPSE OF WATER COLUMN

The collapse of water column is a typical validation case of interface capturing methods, for example *Ubbink (1997)* and *Kim and Lee (2003)*.

This study includes the simulation of the collapse of a water column with the height and width $h = w = 0.025875m$. The computational domain is $6h \times 4h$ large and it consists of uniform 30×20 grid. The slip boundary condition is used on all the boundaries. The water density is set to $1000 kg/m^3$ and the air density to $1 kg/m^3$. The gravity constant $9.81 m/s^2$ was used. The physical time step was set to 0.001s and the courant number for the pseudo time step to 1.
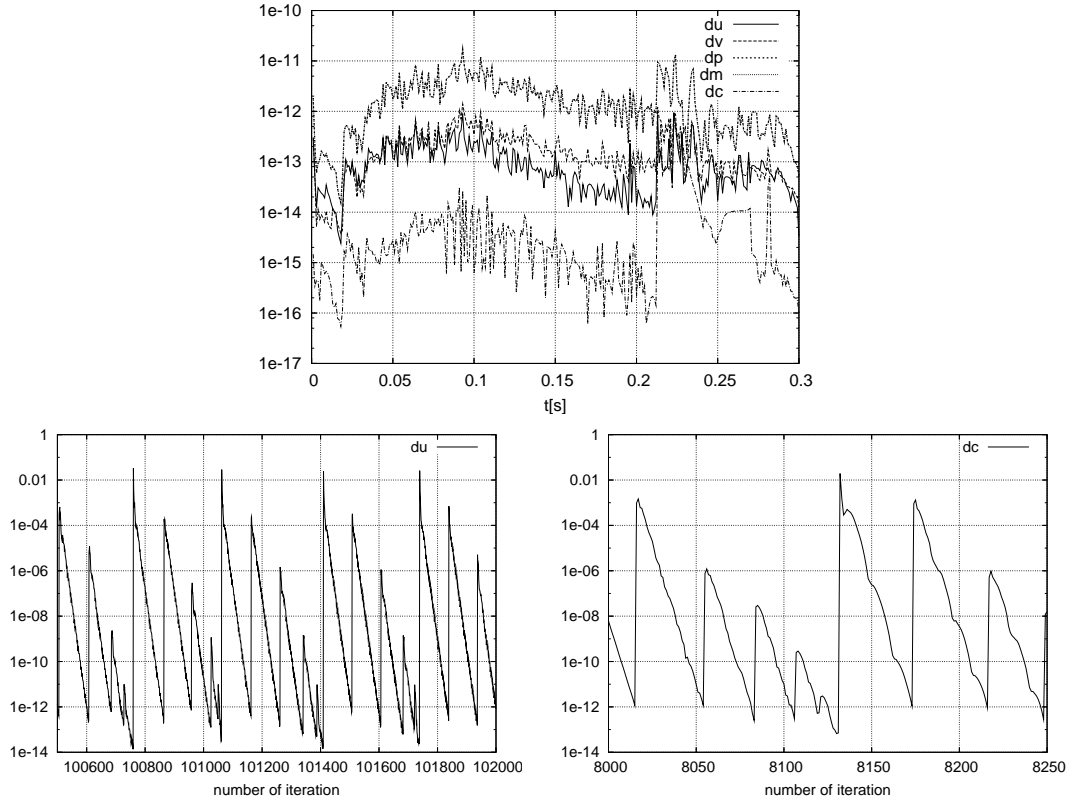
Figure 2: Above: The final velocity residuals du and dv, pressure correction residual dp, mass balance residual dm and volume fraction residual dc as function of time. Below left: velocity residual as function of iteration number. Below right: volume fraction residual as function of iteration number. L-infinity norms.

The results are given in Figs. 2-5. On the top of Fig. 2, the final values of the L-infinity norms at the end of each time step are given. On the bottom of that figure, short pieces of the u-velocity and volume fraction residuals are shown as a function of iteration number. The residuals that are plotted against iteration number shows that the steps 3 and 4 (Section 4) need to be repeated 5 times within one time step to obtain a converged solution. In the convergence history of final residuals, the values suddenly get increased at $t = 0.22s$. At this time, the wave front hit the wall at the other end of the numerical basin. Especially the volume fraction residual rises over three decades. Regarding the accuracy of the solution this is not, however, important as all the residuals are still almost below 1^{-11}.

In Fig. 3, the error in fluids' mass in the computational domain is plotted. The amount of the total mass decreases at the same as the convergence deteriorates slightly.

Fig. 4 shows the deformation of the free surface at four different times. The water wave front and the height of the residual water column are compared to the model-test data published in *Martin and Moyce (1952)* as function of time in Fig. 5. The height of the residual water column is in good agreement with the model test results. The water wave front is not as well predicted, but the results are encouraging in the view of the fact that the grid is very coarse. In Fig. 5, the results are non-dimensional: $t^* = \sqrt{g/h}$, $x^* = x/h$, $h^* = y/h$.

6 ACKNOWLEDGEMENTS
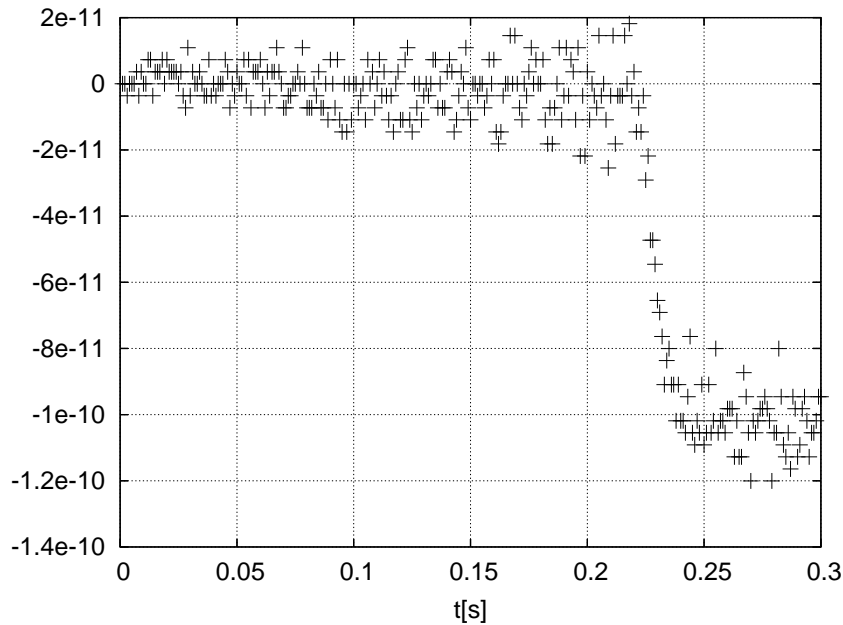
Figure 3: The error in the mass of air and water in the computational domain.

7 REFERENCES

Jasak H, Weller HG. Interface tracking capabilities of the Inter-Gamma differencing scheme. Internal report, Mechanical Engineering department, Imperial College of Science, London, 1995.

Kim MS, Lee WI. A new VOF-based numerical scheme for the simulation of fluid flow with free surface. Part 1: New free surface-tracking algoritm and its verification. Int. J. Numer. Meth. Fluids 2003; 42:765-790.

Martin JC, Moyce WJ. An experimental study of the collapse of liquid columns on a rigid horizontal plane. Philosophical Transactions of the Royal Society of London, Series A. Mathematical, Physical and Engineering Sciences 1952; 224:312-423.

Mikkola T. Time accurate simulation of a plunger type wave maker using unstructured finite volume solver with surface tracking. 26th Symposium on Naval Hydrodynamics, Rome, Italy, September 17-22 2006. p. 259-277.

Queutey P, Visonneau M. An interface capturing method for free-surface hydrodynamic flows. To be published in Comput Fluids 2007.

Ubbink O. Numerical prediction of two fluid systems with sharp interfaces. Ph.D. thesis, Imperial College of Science, Technology & Medicine. University of London. 1997.
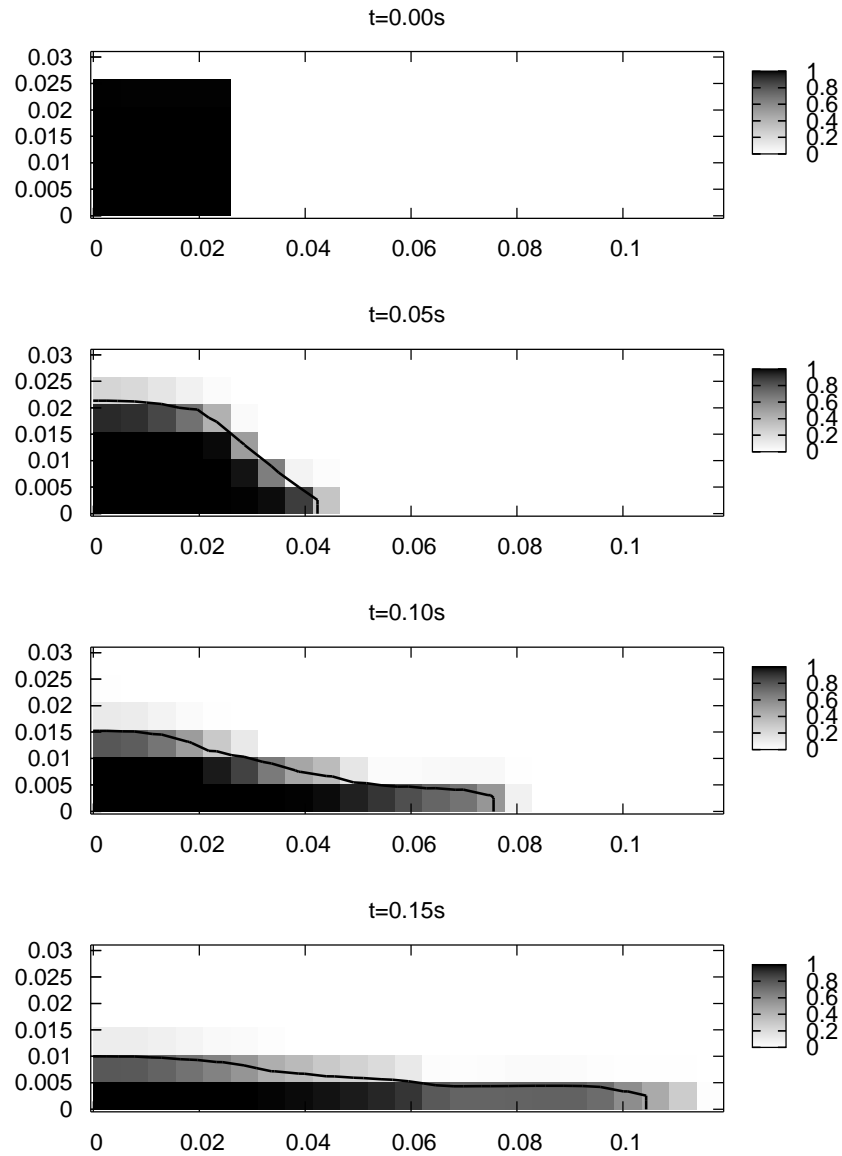
Figure 4: Volume fractions in cell centres and contour line 0.5 of volume fraction.
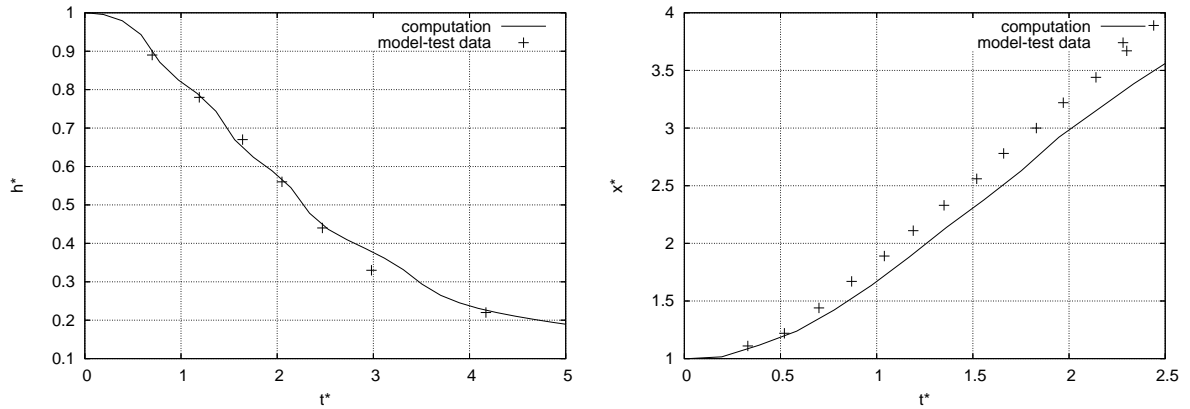
Figure 5: Left: Height of the residual water column. Right: Distance of the wave front from x=0. Model test data from *Martin and Moyce (1952)*

Marine CFD Research at SRI/NMRI
— Review and Prospects —

Takanori HINO
Center for CFD Research
National Maritime Research Institute, JAPAN

1.   Introduction

Computational Fluid Dynamics (CFD) in marine engineering emerged in mid 80s. CFD Research in SRI (Ship Research Institute) started nearly at the same time. Since then, in step with the advancement of computer hardware, marine CFD technology evolved continuously. SRI, now called NMRI(National Maritime Research Institute) has been one of the leading research organizations in numerical ship hydrodynamics. In this paper, a review is given for past research efforts at SRI/NMRI and also state-of-the-art of NMRI CFD technology is presented.

2.   Beginning — 1980s —

CFD research at SRI started in mid 80s. The first paper in CFD appeared in 1985[1], in which Kodama solved a flow around a 2-D circular cylinder. Solution algorithm used is artificial compressibility method with Implicit Approximate Factorization (IAF) scheme. Fig.1 shows the velocity vectors around a cylinder. At the same time, development of a grid generation method based on a geometrical method also started. After applying the methods to 2-D wing section and back-step flow, the first application to a 3-D ship flow was carried out in 1985 [2]. Double model flows around a Wigley hull were computed with the Baldwin-Lomax turbulence model[3]. Fig.2 shows the grid and the pressure distribution of Series 60, which were carried out shortly after.

Free surface flows are particularly important in ship hydrodynamics. A code for free surface flows with viscous effects[4] was developed by Hino based on the Marker-And-Cell algorithm. Fig.3 is the computed wave contours around Wigley hull. The method is later modified to solve the Euler equations and applied to flows around a high speed craft[5]. Fig.4 shows the computed wave field around a high speed boat.

In 1989 5th Conference on Numerical Hydrodynamics was held in Hiroshima, Japan. At the Conference, the papers from SRI were for grid generation and viscous flow simulation around a ship[6] and for free surface viscous flow simulation around a ship[7].

Fig. 1 Velocity vectors around a 2-D circular cylinder

Fig. 2 Computational grid and pressure distribution of Series 60 (Cb=0.6)

Fig. 3 Wave contour around Wigley hull

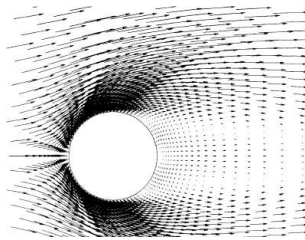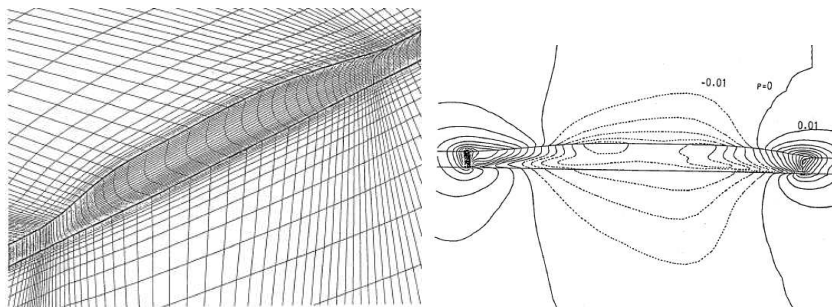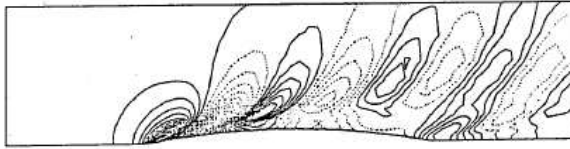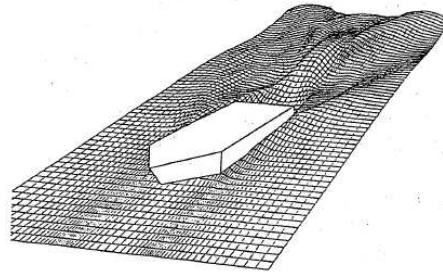Fig. 4 Wave field around a high seed
boat

3. Development — 1990s —

NICE code which had been a main Navier-Stokes solver at SRI/NMRI for many years established its base in 1992[8]. A finite volume method is adopted for spatial discretization in place of a finite difference method of previous codes which gives global conservation property. Accurate resistance predictions were reported.

The grid generation code *GMESH*[9] was also developed in the same period. These programs, together with a post-processing program also developed at SRI, formed a CFD system for ship flow computations. This system was distributed to many Japanese shipyards and helped the spread of CFD technology.

A flow around a propeller was also studied at this period [10]. Fig. 5 is pressure distribution around a propeller.

Various cooperative research projects among SRI, universities and shipyards in Japan were carried out in 1990s. One of the important outcomes from these projects is the improvement of turbulence models. In the CFD workshop in 1991 held in Gothenburg[11], none of CFD results succeeded the prediction of the so-called 'hook' shape of the wake distribution behind a blunt ship. The following studies revealed that this is due to the deficit of turbulence models. The modification of Baldwin-Lomax (BL) zero-equation model[3] known as MBL (Modified BL) was achieved in one on the cooperative projects[12]. This improvement enabled the reproduction of the 'hook' shape of the wake and applicability of CFD methods were enlarged greatly. Fig.6 is the comparison of measured and computed(with BL and MBL) wake distributions behind VLCC.

Another important development is a self-propulsion simulation technology. Since propeller-hull interaction is essential in the estimation of propulsive performance of ships, the self-propulsion simulation is the key issue in marine CFD. Hinatsu developed the method based on *NICE* which can simulate self-propulsion using a potential-based propeller theory[13]. A propeller effect is expressed as a body force. Fig.7 is a wake distribution behind a ship with a propeller effect.

Free surface flow simulation technology also evolved to a finite-volume-based method with interface fitting, in which a grid is re-generated to fit a deformed free surface[14].

An unstructured grid method has larger flexibility for treating complex geometry. In this period, SRI began the development of unstructured grid methods. Starting from 2-D applications, 3-D ship flows were simulated in 1998[15]. This code is called *SURF*. The method was later extended to cope with free surface flows using single-phase level-set method[16].

The development of CFD technology and the advancement of computer hardware opened a new field of CFD application, that is, a shape optimization using CFD. Usual use of CFD is a flow field analysis of a given shape. The shape optimization is an inverse problem, in which a solution is a shape that has desired flow properties. The optimization requires many CFD runs because of the non-linearity of flow problems. Therefore, fast and efficient algorithms are essential in the success of optimization applications.

To this end, SRI developed a new code called *NEPTUNE*[17]. which adopts implicit time stepping based on the quasi-Newton method and convergence is further accelerated by a multigrid method. Fig.8 compares the convergence of solutions between *NICE* and *NEPTUNE*.

The shape optimization of a VLCC using the SQP (Sequential Quadratic Programming) optimizer and *NEPTUNE* was reported in 1999[18]. Fig. 9 shows the shape optimization result of a VLCC hull with respect to the minimum resistance.

In 1994, SRI organized the CFD Workshop[19]. In this workshop, free surface flow simulation was adopted as a test case for the first time together with conventional double model flow cases.

Fig. 5 Pressure distribution around a propeller
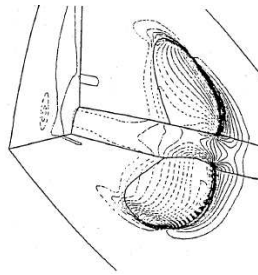
| Measured | Computed (BL) | Computed (MBL) |
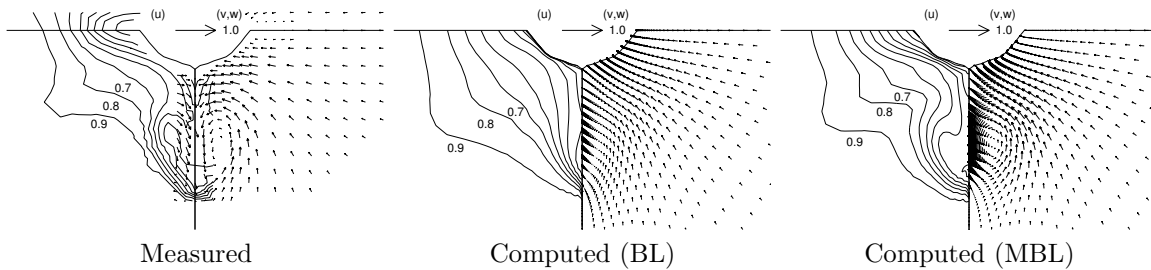
Fig.6 Comparison of measured and computed wake distributions
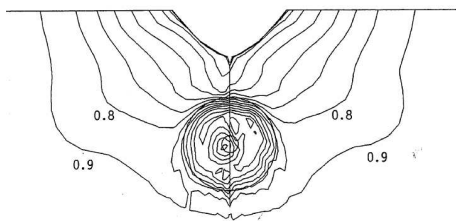
Fig.7 Wake distribution behind a ship with a propeller effect
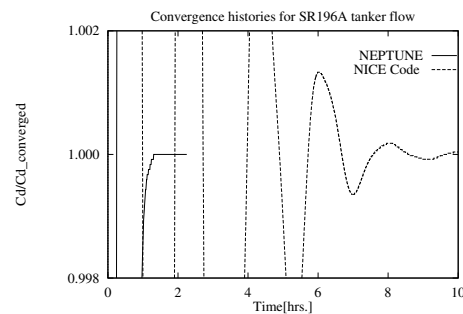
Fig.8 Comparison of convergence between NEPTUNE and NICE
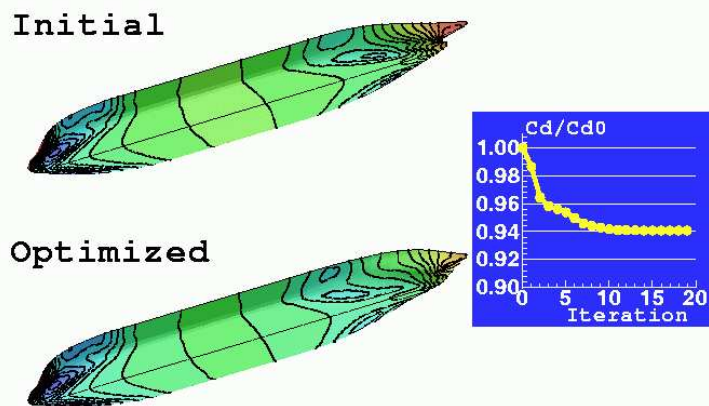
Fig.9 Shape optimization of a VLCC hull for minimum resistance

4. Expansion — 2000s and present—

In the year 2001, Ship Research Institute(SRI) was reformed as National Maritime Research Institute (NMRI) and in the next year Center for CFD Research was established with the mission to spread CFD

technology to shipbuilding industries. Since then, efforts are made toward the enhancement of CFD software toward a practical tool for ship design.

Currently two Navier-Stokes solvers, called *NEPTUNE* and *SURF*, and a grid generation program *HullDes/GMESH* are under development at NMRI.

NEPTUNE[17] is the finite volume code in structured grids and adopts an artificial compressibility approach for velocity-pressure coupling. New turbulence models implemented are the one equation model of Spalart-Allmaras (SA)[20] and its modified version (MSA) [21] for the 'hook'-shaped wake distribution. For free surface treatment, the interface fitting approach is used. Propeller effects are modeled using a body force computed by the simplified propeller theory[22].

The other flow solver under development is the unstructured solver called *SURF*[15] which is also the finite volume code with artificial compressibility. *SURF* employs SA and MSA turbulence models as well. The interface capturing method is used for free surface[16]. Propeller effects are modeled in the same way as in *NEPTUNE*.

Prediction of a velocity field in a propeller plane is particularly important for a propeller design. In Fig.10, the comparison is made between the measured and computed wake fields at the propeller plane of a VLCC hull. The computation is made by *NEPTUNE* with the MSA model[21]. The very good agreement with the wind tunnel measurement can be observed.

Fig.11 shows the result for a ship with shaft-brackets and twin rudders[23]. Unstructured grid capability of *SURF* enables the simulation around the complex geometry as shown in Figures.
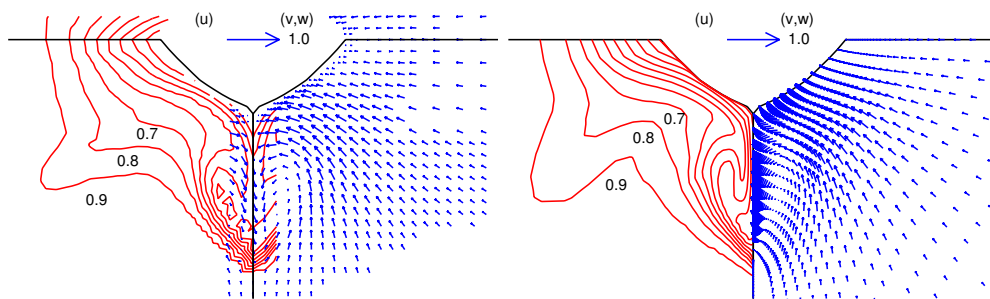
Fig. 10 Comparison of measured (top) and computed (bottom) wake fields at a propeller plane of a VLCC hull.
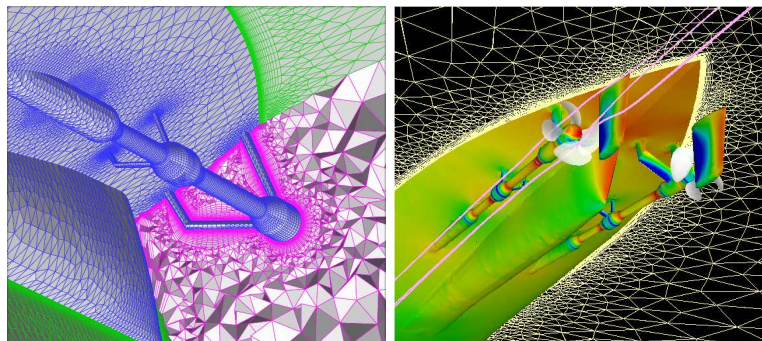
Fig. 11 Unstructured grid and surface pressure around a ship with shaft brackets and twin rudders.

The advantage of interface capturing approaches such as the level-set method is demonstrated by flow simulations of high-speed ships by *SURF*[24] where a free surface deformation is excessive as shown in Fig.12.
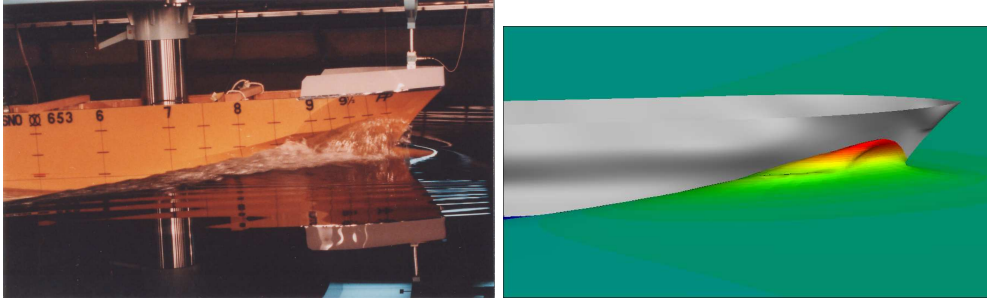
Fig. 12 Bow waves of a high speed ship (left: experiment, right: simulation).

Fig. 13 is the results associated with the simulation of obliquely towed conditions of a VLCC by *NEPTUNE* which is a fundamental case for maneuvering simulations. It depicts surface pressure distribution and streamlines also in the 18 degrees drift case.

Fig.14 shows the result of the fundamental study ([25]) toward seakeeping simulations. A ship with a simple hull form, Wigley, is running in a head sea. Ship motion is computed in a time-dependent manner using transient hydrodynamic forces acting on the ship hull.
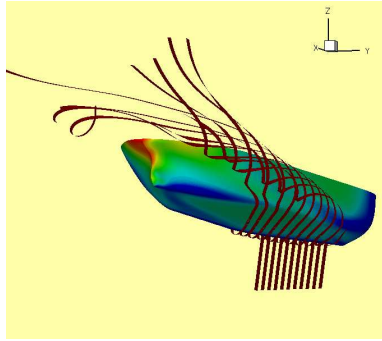
Fig. 13 Surface pressure distribution and streamlines in 18-degree drift case.
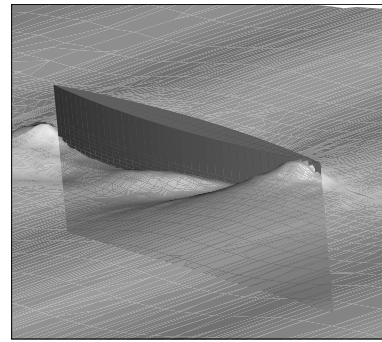
Fig. 14 Wigley hull running in a head sea.

In 2005, NMRI organized CFD Workshop again[26]. Various test cases including maneuvering and seakeeping applications in addition to resistance and propulsion were collected and discussed.

5. Future

CFD is a tool for design and for research. The importance of this tool increases as its area of applications expands. There are many demands for analyzing complex flow physics around complex geometry in practical ship designs. NMRI will keep making efforts in research and development of marine CFD technology.

References

[1] Kodama, Y. (1985a), "Computation of the Two-Dimensional Incompressible Navier-Stokes Equations for Flow Past a Circular Cylinder Using an Implicit Factored Method", *Papers of Ship Research Institute*, 224.

[2] Kodama, Y. (1985b), "Computation of 3-D Incompressible Navier-Stokes Equations for Flows Around a Ship By an Implicit Factored Method", *Proc. Intern. Colloquium on Ship Viscous Flow*.

[3] Baldwin, B.S. and Lomax, H. (1978), "Thin Layer Approximation and Algebraic Model for Separated Turbulent Flows", *AIAA Paper* 78-257.

[4] Hino, T. (1987), "Simulation of Viscous Flow with a Free Surface around a Ship Model", *J. The Society of Naval Architects of Japan*, 161.

[5] Hino, T. et al. (1991), "Calculation of Free-Surface Flows Generated by Planing Crafts", *Proc. FAST '91*.

[6] Kodama, Y. (1989), "Grid Generation and Flow Computation for Practical Ship Hull Forms and Propellers Using Geometrical Method and the IAF Scheme", *Proc. 5th Intern. Conf. Numerical Ship Hydrodynamics*, Hiroshima.

[7] Hino, T. (1989), "Computation of a Free Surface Flow Around an Advancing Ship by the Navier-Stokes Equations", *Proc. 5th Intern. Conf. Numerical Ship Hydrodynamics*, Hiroshima.

[8] Kodama, Y., (1992), "Computation of Ship's Resistance Using an NS Solver with Global Conservation – Flat Plate and Series 60 Hull —", *J. The Society of Naval Architects of Japan*, 172.

[9] Kodama, Y., (1991), "Grid Generation around a Practical Ship Hull Form Using the Implicit Geometrical Method", *J. The Society of Naval Architects of Japan*, 169.

[10] Uto, S. (1993), "Computation of Incompressible Viscous Flow around a Marine Propeller (2nd Report)", *J. The Society of Naval Architects of Japan*, 173.

[11] Larsson L. et al. (Eds.) (1991)*Proc. SSPA-CTH-IIHR Workshop on Viscous Flow*, Gothenburg.

[12] Kodama, Y., (1998) "Scope of CFD for computing ship flows", *Proc. 3rd Osaka Colloquium on Advanced CFD Applications to Ship Flow and Hull Form Design*.

[13] Hinatsu, M., Kodama, Y. et al. (1994), "Numerical Simulation of Flow around a Ship Hull Including a Propeller Effect", *Trans. West-Japan Society of Naval Architects*, 88 (in Japanese).

[14] Hino, T.(1994), "A Study on Grid Dependence in Navier-Stokes Solutions for Free Surface Flows around a Ship Hull", *J. The Society of Naval Architects of Japan*, 176.

[15] Hino, T. (1998)," Navier-Stokes Computations of Ship Flows on Unstructured Grids", *Proc. of 22nd Symposium on Naval Hydrodynamics*, Washington D.C., USA.

[16] Hino, T.(1999)," An Interface Capturing Method for Free Surface Flow Computations on Unstructured Grids", *J. of the Society of the Naval Architects, Japan*, 186.

[17] Hirata, N. and Hino, T.(1999), "An Efficient Algorithm for Simulating Free-Surface Turbulent Flows around an Advancing Ship", *J. the Society of Naval Architects, Japan*, 185.

[18] Hino, T. (1999), "Shape Optimization of Practical Ship Hull Forms Using Navier-Stokes Analysis", *Proc. of 7th International Conference on Numerical Ship Hydrodynamics*, Nantes.

[19] Kodama, Y. (Ed.) (1994), *Proc. CFD Workshop Tokyo 1994*.

[20] Spalart, P.R. and Allmaras, S.R. (1994)), "A One-Equation Turbulence Model for Aerodynamic Flows", *La Recherche Aérospatiale*, 1.

[21] Hirata,N. and Hino,T. (2000), "A Comparative Study of Zero- and One-Equation Turbulence Models for Ship Flows", *J. of Kansai Society of Naval Architects, Japan*, 234.

[22] Ohashi, K., Hirata, N. and Hino, T. (2003), "A Comparative Study of Body Force Models Representing Effects of Contrarotating Propellers", *Trans. West-Japan Society of Naval Architects*, 105.

[23] Hino, T., Ohashi, K. and Ukon, Y., (2003a), "Flow Computations around a Ship with Appendages by an Unstructured Grid Based NS Solver", *Proc. of 8th International Conference on Numerical Ship Hydrodynamics*, Busan.

[24] Sato, Y., Hino, T. and Hinatsu, M. (2004), "Numerical Simulation of Breaking Bow Waves for a Fast Ship", *Proc. of 4th General Meeting of National Maritime Research Institute*.

[25] Hinatsu, M. and Hino, T. (2002) "Numerical Investigation of Influence of Surging Motion on Viscous Flows around a Wigley Hull Running in Incident Waves", *Proc. of ASME Fluids Engineering Division Summer Meeting*, Montreal.

[26] Hino, T. (Ed.) (2005), *Proc. CFD Workshop Tokyo 2005*.

Modelling of the unsteady cavitating flow on a twisted hydrofoil

Tobias Huuva and Göran Bark,
Chalmers University of Technology, Shipping and Marine Technology, 412 96 Gothenburg, Sweden,
tobias.huuva@chalmers.se, bark@chalmers.se

Introduction

Cavitation can occur in a wide range of liquid flows and this complex phenomenon is not yet fully understood. Experimental observations can show many of the phenomena occurring, but together with highly accurate numerical predictions the full picture of cavitation will be much clearer. Predicting the cavity is difficult mainly because the physical properties of the fluid are unknown and these may vary randomly. To be able to overcome these difficulties, a high resolution simulation of a two phase flow can be used in combination with mass transfer models based on different physical properties. Indeed the understanding of this phenomena and the ability to predict cavitation are crucial to prevent or reduce its effects (damages and performance alterations). Consequently numerical prediction of cavitation is of great interest from an engineering point-of-view, especially for the marine and hydraulic industry.

Here Implicit LES (ILES), Grinstein [6], is used to compute flow field, ILES is founded on separation of scales within the flow, accomplished by low-pass filtering of the Navier Stokes Equations (NSE), Sagaut [14]. Large, energy containing, structures that can exist on the computational grid are kept in the LES calculation, whereas the smaller, more isotropic structures are modelled. This gives LES a much higher generality than e.g. Reynolds Averaged Navier Stokes (RANS), Wilcox [19], in which the complete spectrum of turbulent motion is modelled. Furthermore LES gives more physics which also can be useful in cavitation simulation. Earlier Wikström *et al.* [17,18] and Persson *et al.* [13] has presented work on ILES in combination with cavitation modelling and Wosnik *et al.* [20] has presented work with LES and cavitation modelling.

The presented model is tested on a twisted hydrofoil, referred to as Twist11, described by Foeth and Terwisga [2], in which phenomena not present on a 2D foil occurs. Example of such flow phenomena is side jets which cuts the sheet and forms a closure from which a cavity in a hairpin vortex is convected. The side jets forms into a reentrant jet which cuts the cavity at the leading edge. Experimental results from similar hydrofoils are described in Foeth and Terwisga [3,4]. Also computations have been performed on the described geometry, Schnerr [15], using a compressible Euler solver.

Modelling

Cavitation modelling

The governing equations of an incompressible flow consist of the balance equations of mass and momentum for a linear viscous (or Newtonian) fluid, Panton [12]. Resolving all structures in the flow filed, i.e. solving the full NSE, is referred to as Direct Numerical Simulation (DNS). This implies solving for the smallest scales in flow, the Kolmogorov scale, and this gives a computational time which will scale as Reynolds number (Re) cube. This results in too long computational time for present-day computers, even for model scale. DNS may however still be useful for analyzing academic flows to gain detailed insight in the flow physics. The alternatives to DNS all involve some degree of modelling; here Implicit LES is used. In the ILES approach the effects of the subgrid physics on the unresolved scales are incorporated in the functional reconstruction of the fluxes using high-resolution finite-volume methods.

We will here refer to the modelling of the cavity as mass transfer models for cavitating liquids, since the present model works with mass transfer. It is not possible to resolve the mass transfer in a continuum setting and consequently modelling is needed. The cavity in it self is not modelled, since it is present in the simulation, and it would then be confusing to refer to the models as cavitation models. If a true cavitation model should be performed, no cavity should be present in the simulation and the model would account for the influence of the cavity. In the present computations the cavity appears as a part of the basic ILES equations, i.e. as a part of the steady flow field, when the ILES equations are solved together with the mass transfer model, producing vapour inside the liquid when the pressure is below the vapour pressure. Although the production and destruction of vapour, described by the mass transfer model, is a crucial part of the cavitation process, other parts as reentrant jets and shedding being the main subject below, are controlled rather by the ILES equations, we mean here by a cavitation model the entire set of equations solved to describe the flow. This nomenclature is motivated by the fact that changes of the basic flow solver can be of same importance, at least, as changes of the mass transfer model.

Thee free surface is captured using the VOF approach, Hirt [8], where a transport equation for the volume fraction is incorporated into the filtered balance equations of mass and momentum

$$\begin{cases} \nabla \cdot \overline{\mathbf{v}} = 0, \\ \partial_t(\rho\overline{\mathbf{v}}) + \nabla \cdot (\rho\overline{\mathbf{v}} \otimes \overline{\mathbf{v}}) = -\nabla\overline{p} + \nabla \cdot (\overline{\mathbf{S}} - \mathbf{B}), \\ \partial_t\gamma + \overline{\mathbf{v}} \cdot \nabla\gamma = 0. \end{cases} \tag{1}$$

where $\mathbf{B} = (\overline{\mathbf{v} \otimes \mathbf{v}} - \overline{\mathbf{v}} \otimes \overline{\mathbf{v}})$ is the subgrid stress tensor arising from the filtering, see e.g. Fureby et al.[5] for clarification, and the volume fraction, γ, is used to scale the physical properties of vapour and liquid

$$\begin{cases} \rho = \gamma\rho_l + (1-\gamma)\rho_v, \\ \mu = \gamma\mu_l + (1-\gamma)\mu_v, \end{cases} \tag{2}$$

The numerical behaviour of the volume fraction equation can be treated in several different ways, using high and low order, compressive and non-compressive reconstruction schemes for the convection of γ, Ubbink [16].

Kunz mass transfer model for cavitating liquids

Kunz' mass transfer model for cavitating liquids is based on the work by Merkel *et al.* [11], with a modification which corresponds to the behaviour of a fluid near the transition point. The behaviour near a transition point is described by methods within statistical physics and the inventors of the model refer to the Ginzburg-Landau potential [10] and van der Waals equation of state [8], as the basic physics. The mass transfer in this model is based on two different strategies, as compared to most similar models which only rely on one strategy for both creation and destruction of liquid. The destruction of liquid, or creation of vapour $\dot{m}^+$, is modelled to be proportional to the amount by which the pressure is below the vapour pressure and the destruction of vapour $\dot{m}^-$ is based on a third order polynomial function of the volume fraction $\gamma = \dfrac{Volume\ liquid}{Total\ Volume}$

$$\begin{cases} \dot{m}^+ = \left(C_{prod}\rho_v / \rho_l U_\infty^2 t_\infty\right) \cdot \gamma \min\left[0, \overline{p} - p_v\right], \\ \dot{m}^- = \left(C_{dest}\rho_v / t_\infty\right) \cdot \gamma^2(1-\gamma). \end{cases} \tag{3}$$

where $\dot{m} = \dot{m}^+ + \dot{m}^-$ is the specific mass transfer rate, γ is the volume fraction, $\overline{p}$ is the filtered pressure, p_v is the vaporisation pressure, ρ is the density and $C_{dest}, C_{prod}, U_\infty$ and t_∞ is empirical constants based on the mean flow.

The mass transfer terms are incorporated into the flow modelling using source terms in the continuity equation and in the transport equation for the volume fraction,

$$\begin{cases} \nabla \cdot \overline{\mathbf{v}} = S_\rho, \\ \partial_t(\rho\overline{\mathbf{v}}) + \nabla \cdot (\rho\overline{\mathbf{v}} \otimes \overline{\mathbf{v}}) = -\nabla\overline{p} + \nabla \cdot (\overline{\mathbf{S}} - \mathbf{B}), \\ \partial_t\gamma + \overline{\mathbf{v}} \cdot \nabla\gamma = S_\gamma. \end{cases} \tag{4}$$

here S_ρ and S_γ is the source terms. For a volumetric source representation, S_ρ can be expressed as,

$$S_\rho = \dot{m}(\rho_l^{-1} - \rho_v^{-1}), \tag{5}$$

where $(\rho_l^{-1} - \rho_v^{-1})$ handles the bulk volume change when mass is transferred from one phase to the other. The bulk density for liquid and vapour, ρ_l and ρ_v, are kept constant throughout the computation. The source term in the volume fraction transport equation, S_γ, can be estimated from the mass transfer from vapour to liquid at a rate $\dot{m}$. The bulk density change rate can be represented as,

$$D_t(\rho) = -\rho\nabla \cdot \overline{\mathbf{v}} \tag{6}$$

and as

$$D_t(\rho) = (\rho_l - \rho_v)D_t(\gamma).$$

(7)

using equation (2₁). Combining equation (6) and equation (7) and rearranging the terms gives the volume fraction equation as

$$D_t\gamma + \nabla \cdot (\overline{\mathbf{v}}\gamma) = -\frac{\rho_l}{\rho_v - \rho_l}\nabla \cdot \overline{\mathbf{v}}.$$

(8)

Twist11

The 3D hydrofoil used here is referred to as the Twist11 hydrofoil. This hydrofoil is build-up from an NACA0009 profile with an spanwise distribution of the angle of attack. The largest angle of attack is located at the mid section while the lowest angle of attack is located at the walls. The number 11 refers to the difference, in degree, in angle of attack between the centerplane and the outer edges. With this hydrofoil an isolated sheet cavity is created around the centre plane and the hydrofoil is lightly loaded to deny any interaction with the tunnel boundary layer. The three-dimensionality of the cavity, and the hydrofoil, creates a reentrant flow which at some instances is directed sideways at a 90 degree angle with the free flow. This side entrant flow collects fluid towards the centre where the gathered fluid pierces the cavity and leaves a detached cavity which rolls-up into a hairpin. An upstream reentrant jet is now formed, which gathers fluid from the side entrant flow and is directed towards the leading edge of the hydrofoil. The reentrant flow breaks up the sheet around the centerplane on its way towards the leading edge. When the cavity hits the leading edge it is directed towards the outer side of the cavity and a new cavity is started. The cavity which has rolled up into a hairpin vortex is transported towards the trailing edge of the hydrofoil where it finally collapses. After the shedding of the main centre hairpin vortex several smaller vortices is shed from alternating sides of the centerplane until a new cycle is completed.

Cavitation phenomena

In the present numerical simulations of steady inflow cases the cavitation sources are gradually turned on during approximately 1 ms. The first sheet cavity that grows becomes very smooth and symmetric. This development may be influenced by the way in which the cavity sources are turned on as well as the fact that there are no vapour voids downstream, as residues from a cavity of a previous cavitation cycle. When the first cavity, by the reentrant jet, is terminated from the leading edge region and advected downstream, the next sheet starts growing. This second sheet behaves less smooth and symmetric, and its development is supposed to be noticeably controlled by the disturbances of the local flow induced by the residue void from the first sheet. This void is now, simultaneously with the growth of the second sheet, rotating and mowing downstream, and finally it leaves the foil and disappears in the region of higher pressure. Detailed velocity and pressure plots indicate existence of significant disturbances of the flow close to the growing second sheet.

It is noted in passing that Wikström and co-workers [18] record also the first cavity in a transient motion of the foil in the ILES simulations as well as in an experiment. The first growth was described reasonably well but due to the preliminary character of the experiment as well as the simulation, it was not at that time possible to make reliable observations beyond the growth of the first sheet. From an academic point of view an advantage of the first cavitation cycle is that the behaviour of the cavitation model is well defined and relatively easy to evaluate, and as pointed out above, this part can also be important in for example certain propeller cases. The possibly following cavitation cycles become more variable and disturbed by interaction from co-existing shed voids, conditions that are typical for water turbines as well as propellers.

Figure 1a-3a shows the extension of the cavity in an iso-surface of the volume fraction $\gamma = 0.5$ and the direction of the shear stress of the surface of the wing. Figure 1b-3b shows the same iso surface, in combination with the vector field on the centre plane and the vector field in the first cell layer above the surface.
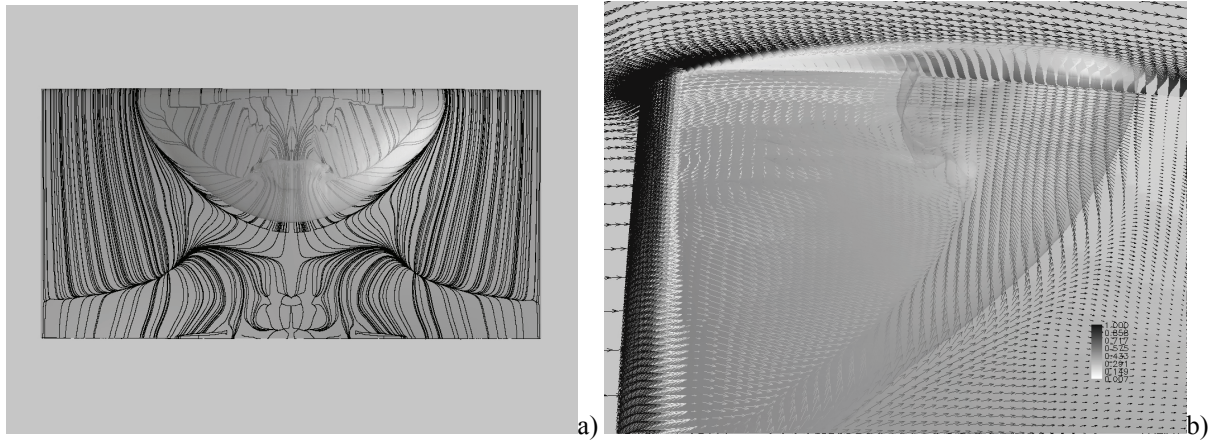
Figure 1. The first cavitation cycle, the cavity has grown to its maximum size and the side jets are fully active to collect fluid towards the closure. a) Computation, top view, b) computation, side view

In figure 1 the first has cavity has grown to its maximum extension regarding cavity length and width. The side entrant jets are clearly visible collecting fluid towards the centre. This fluid gathers to a thicker reentrant jet and forms a closure which snaps of a first cavity in a hairpin vortex. The experiment shows a higher level of bubbles, which the model not is able to predict. But close to the centre plane of the experiments shows similar features as the numerical predictions. From the shear stress restricting lines it is visible that a large recirculation zone has developed close to the trailing edge in the numerical prediction. For the fully wetted only a very small recirculation zone is present close to the centre line.
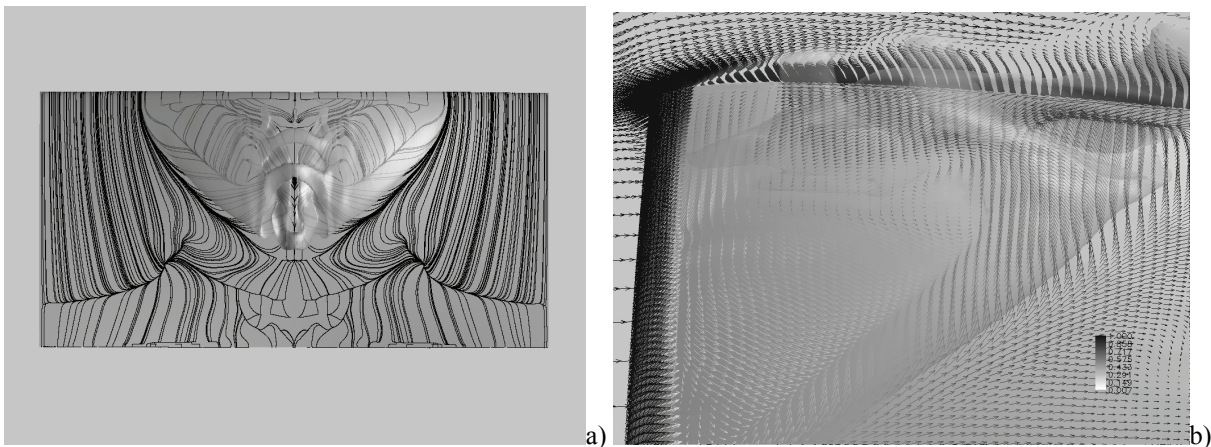
Figure 2. The side jets has formed a reentrant jet which as reached to the leading edge. a) Computation, top view, b) computation, side view

In figure 2 the re-entrant jet has formed at the first closure and it is convected towards the leading edge, in opposite direction to the outer flow. The jet leaves several hairpin vortices in which the cavity grows stronger due to the high vorticity in these regions. The first hairpin vortex is transported towards the trailing edge of the wing and starts to break off from the main cavity. In the experiment the width of the reentrant jet is slightly wider than in the numerical predictions. But the same features are present with the reentrant jet snapping of the centre of the cavity close to leading edge.
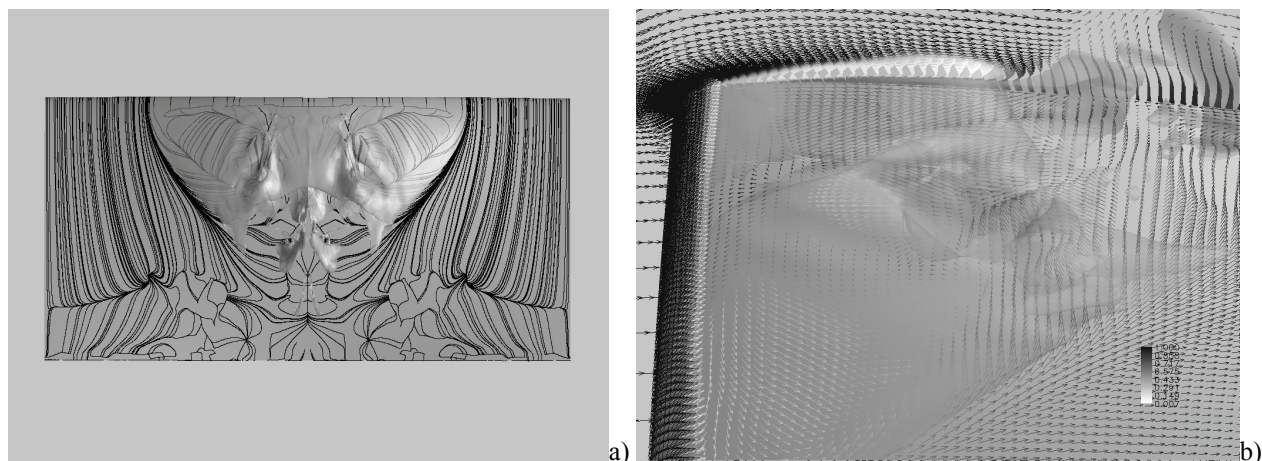
Figure 3. The secondary vortices are being shed and the new sheet is almost fully developed. a) Computation, top view, b) computation, side view

In figure 3 the snapped of part of the cavity is transported into the wake and a new sheet cavity is created close to the leading edge. In the computations this new cavity is clearly affected by the first reentrant jet and it becomes somewhat thinner than the previous sheet and but the gathering off liquid from the side jet, which forms the reentrant jet, is still very distinct. The new sheet is formed on top of a thin layer of liquid and a much thinner reentrant flow is controlling the shedding of this sheet. But still a new hairpin vortex is shed close to the centre plane. As compared with the experiment the computation now becomes more realistic with a less smooth surface of the cavity.

Conclusion

From general experiences regarding experimental observation of cavitation concludes that highly resolved numerical predictions of cavitation is necessary to be able to understand the mechanisms of cavitation behaviour better. Even though it is not possible to numerical predict collapses of cavities, general large scale behaviours can be studied to evaluate the risk of destructive collapses, i.e. erosion, Bark et al. [1]. This kind of early development is what the present cavitation models are able to predicting with relatively high accuracy. To be able to better understand this capability a number of simpler and more advanced validation cases will have to be performed. These validation cases can at a later stage be used to describe the limitation of the numerical simulations and what to expect from computed results regarding grid resolution, turbulence modelling and other numerical parameters.

The test case, the twist11 hydrofoil, is a computationally advanced problem. The cavitating flow over this geometry contains many of the flow characteristics which occur on e.g. marine propellers. This includes features such as periodic shedding of main and secondary cavities in hairpin vortices, side jets and reentrant jets. To be able to predict these phenomena a relatively high resolution of the computational mesh is needed, especially in the spanwise and streamwise directions. The ability to predict this kind of flow structures is very important for predicting the risk of erosion. The experiments performed on the twisted hydrofoil also include controlled shedding frequency using flapped wings in front of the twist11 hydrofoil. This case is more demanding in meshing and setup of the problem, but for solving the problem the natural frequency will be harder to predict then the controlled frequency.

With the present settings the main features of the cavitating flow field is described and the limitations are explained. Further on development towards better flow prediction, i.e. sub-grid modelling and wall handling, as well as more mass transfer models will implemented and tested. We also intend to evaluate these methods on more advanced problems such as propellers and turbines.

Acknowledgement

References

[1] Bark, G., Berchiche, N. and Grekula, M., 2005, "Application of principles for observation and analysis of eroding cavitation - The EROCAV observation handbook", Department of Naval Architecture and Ocean Engineering, Chalmers University of Technology, Gothenburg

[2] Foeth, E.J. and Terwisga, T., 2006, "The structure of unsteady cavitation. PART II: Applying time-resolved PIV to attached cavitation", Cav2006, Wageningen, The Netherlands

[3] Foeth, E.J., van Doorne, C. W. H., van Terwisga, T. and Wieneke, B., 2006, "Time resolved PIV and flow visualization of 3D sheet cavitation", Experiments in Fluids, 40(4),pp. 503-13

[4] Foeth, E.-J. and Terwisga, T., 2006, "The structure of unsteady cavitation. Part I: Observation of an attached cavity on a three-dimensional hydrofoil", CAV2006, Wageningen, The Netherlands

[5] Fureby, C., Bensow, R. E. and Persson, T., 2005, "Scale similarity revisited in LES ", Turbulence and Shear Flow Phenomena, Williamsburg, USA

[6] Grinstein, F.F., Margolin, L. and Rider, W., 2005, Implicit Large Eddy Simulation: Computing Turbulent Fluid Dynamics, Cambridge University Press.

[7] Hill, T. L. (1986). Statistical Thermodynamics, Dover Publications

[8] Hirt, C. and Nicols, B., 1981, Volume of Fluid (VOF) mthod for the Dynamics of Free Boundaries, Journal of Computaional Physics 39(1), pp.210

[9] Hohenberg, P. C. and Halperi,n B. I. (1977). "Theory of dynamic critical phenomena." Reviews of Modern Physics 49(3), pp. 435-79

[10] Kunz, R. Boger, F., Stinebring, D. R., Chyczewski, T. S., Lindau, J. W., Gibeling, H. J., Venkateswaran, S., Govindan, T. R., (2000). "A preconditioned Navier-Stokes method for two-phase flows with application to cavitation prediction." Computers and Fluids 29(8), pp. 849-875.

[11] Merkel, C. L., Feng, J., Buelow, P.E.O. (1998). Computation modelling of the dynamics of sheet cavitaton. 3rd International Symposium on Cavitation. Grenoble, France.

[12] Panton, R. L., 1996, "Incompressible Flow", Wiley-Interscience, New York

[13] Persson, T., Bark, G., Bensow, R. E., Berchiche, N. and Fureby, C., 2006, "Large eddy simulation of the cavitating flow around a wing section", CAV2006, Wageningen, The Netherlands

[14] Sagaut, P., 2001, Large Eddy Simulation for incompressible flows, Berlin Springer Verlag

[15] Schnerr, G. H., 2006, "Shock and wave dynamics of compressible liquid flows with special emphasis on unsteady load on hydrofoils and on cavitation in injection nozzles", CAV2006, Wageningen, The Netherlands

[16] Ubbink, O. (1997). Numerical prediction of two fluid systems with sharp interfaces. Department of Mechanical London, Imperial College of Science, Technology and Medicine. Doctor of Philosophy.

[17] Wikström, N., Bark, G. and Fureby, C., 2003, "Large Eddy Simulation of Cavitating Submerged Objects", The 8th International Conferance on Numerical Ship Hydrodynamics, Busan, Korea

[18] Wikström, N., 2005, "Modeling of Cavitating flow around a Stationary/Moving Wing Profile", 43rd AIAA Aerospace Sciences Meeting, Reno, Nevada

[19] Wilcox, D. C. (1993). Turbulence modelling for CFD, DCW Industries

[20] Wosnik, M., Qiao, Q., Kawakami, D.T. and Arndt, R.E.A., (2005). "Large Eddy Simulation (LES) and time-resolved particle image velocimetry (TR-PIV) in the wake of a cavitating hydrofoil", FEDSM 2005, Houston, Texas, USA

Experimental Investigation and Potential-Flow Computation
of Transom Stern Flows

Ole Hympendahl and Thomas Rung,
Institute for Fluid Dynamics and Ship Theory, TU Hamburg-Harburg
o.hympendahl@tu-harburg.de, thomas.rung@tu-harburg.de

1 Motivation

Potential flow methods are still appropriate in ship design. Many of them are validated against experimental data both for ship's resistance and wave pattern.

Usually the wave pattern is measured in model test by wave probes fixed to the tank.

The ship model passes the probes and the wave elevation is recorded. These wave probes cannot measure the waves before and behind the model.

In a research project together with the Hamburg Ship Model Basin (HSVA) a measuring system for the waves behind the model has been developed. It was applied to four ships each in several conditions. The results are compared to potential flow computations.

2 Experimental Investigation

2.1 Procedure

The measuring system has to travel with the ship model to avoid collision. Probes penetrating the water surface should be avoided, as they would generate waves themselves. Therefore an optical measuring system attached to the carriage was applied.

Photographs of the waves are taken by a digital camera mounted on the carriage at an appropriate side distance from the model (Fig. 1). The transverse position of the wave cut to be photographed is defined by a set of diode lasers projecting a red line onto the water surface.
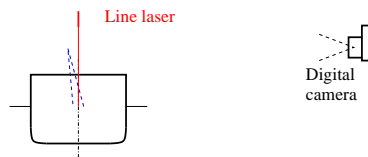
Figure 1: Concept of the measuring system, front view

Because a smooth water surface would hardly reflect any laser light to the camera, the water surface was roughened by spraying a small amount of water onto the water surface (Figure 2).

The images are processed by a simple software which recognizes the red line and converts it to wave elevations. The conversion is based on Tsai's camera calibration algorithm [1]. It uses corrections for translation and rotation of the camera coordinate system against the world coordinate system and corrects distortion of the camera optics.

The whole installation of lasers and water nozzles can be moved sideways for measuring wave cuts at different transverse coordinates.
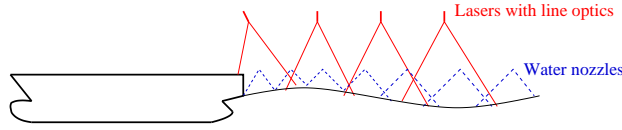
Figure 2: Concept of the measuring system, side view

2.2 Results

Tests have been carried out with four ship models: Two container vessels including 'Hamburg Test Case' [2], a bulker and a twin screw roro vessel.

Each model was investigated in two or more floating conditions, each at five different Froude numbers. All models have been investigated in resistance tests and two of them also in propulsion tests.

Wave cuts have been recorded at four transverse positions behind the model and conventional resistive wave probes have been used to measure the wave elevation at four positions sideways of the model. A fifth laser wave cut was recorded at the position of the innermost wave probe for comparing the two measuring methods. Thus a large number of experimental data are available for the validation of computational approaches.

As indicated by a comparison of the results obtained for the location of the innermost fixed wave gauge (Fig. 3), the agreement between the optical and the conventional measuring system is fair.
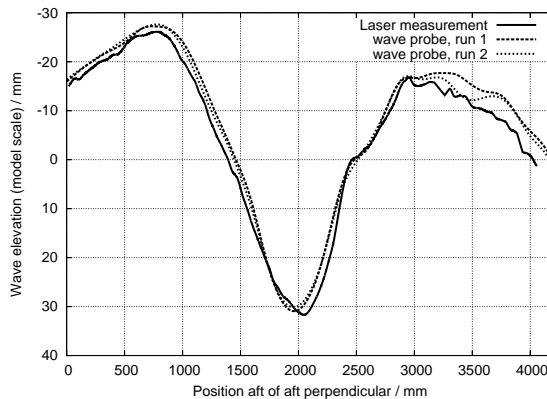
Figure 3: Comparison of laser and wave probe results at the position of innermost fixed wave gauge

3 Potential Flow Computations

Ship waves were computed using a potential flow code being developed at the Institute for Fluid Dynamics and Ship Theory of TUHH.

It uses point sources both inside the hull and above the free surface and evaluates the boundary conditions over hull and free surface patches by integrals over the patch area.

Moreover, the procedure fixes the water surface to a submerged transom edge, thus ensuring a smooth flow from the transom. The radiation condition is satisfied by a downwind shift of the sources above the free surface by one patch length. The nonlinear free-surface and squat conditions are satisfied in an iterative manner.

Fig. 4 reveals that the method shows a reasonably good coincidence with the experimental results sideways of the hull. When attention is drawn to the centerline wake, the predictive performance deteriorates (c.f. Fig. 5)/

The agreement is significantly worse aft of the ship, especially for small transom Froude numbers. The latter is defined as $F_{n,Tr} = U_\infty / \sqrt{g \cdot \eta_{Tr}}$ where η_{Tr} ist the draft of the immersed transom at still
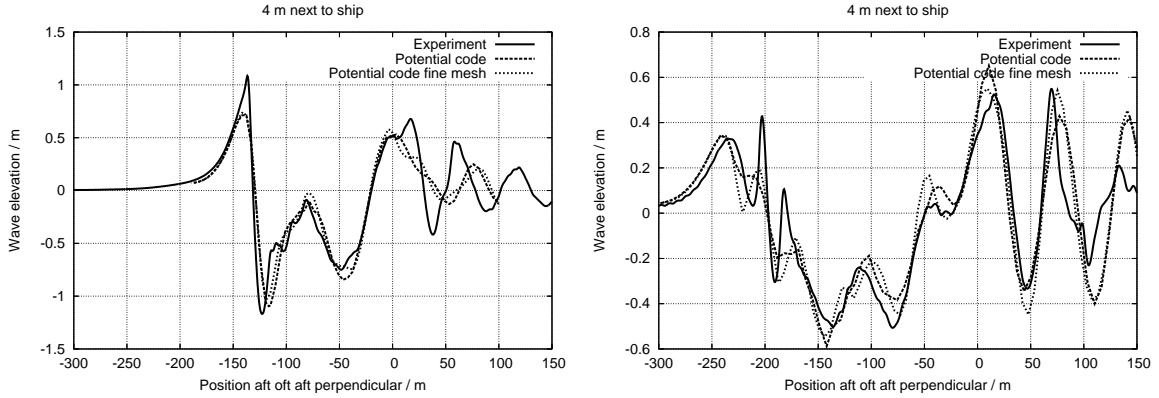
Figure 4: Comparison of experimental and numerical results at position of the innermost wave probe. Left: 'Hamburg Test Case' at speed 19 kts ($F_n = 0.252$) and draft 10.5 m, Transom not immersed at still water level. Right: Container vessel at speed 20 kts ($F_n = 0.209$) and draft 11.3m, $F_{n,Tr} \approx 5.2$.

water.
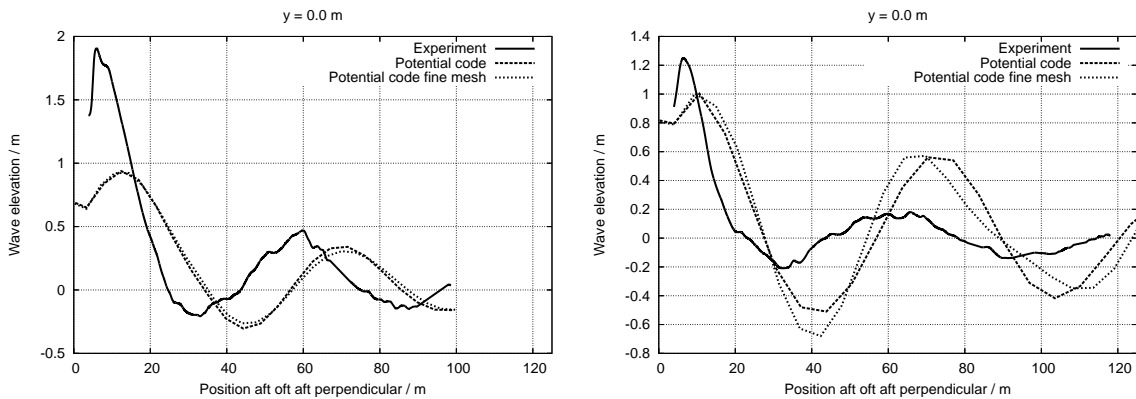
Figure 5: Comparison of experimental and numerical results in the centerplane.Left: 'Hamburg Test Case' at speed 19 kts ($F_n = 0.252$) and draft 10.5 m, Transom not immersed at still water level. Right: Container vessel at speed 20 kts ($F_n = 0.209$) and draft 11.3m, $F_{n,Tr} \approx 5.2$.

Figure 6 shows a comparison of the residual resistance obtained from model tests and from computation. The computed residual resistance containes both the integrated pressure force on the hull and a viscous form factor. The latter takes into account the increased frictional resistance due to over- and under-velocities at the hull surface. Like with the wave cuts the resistance shows a better agreement at higher transom Froude numbers.

The wave patterns can be found in Appendix A. Figs. 7 and 8 show all measured wave cuts of 'Hamburg Test Case' and of the second container vessel together with the corresponding numerical results.

4 Conclusions

The new measurement system has shown its capability to measure the wave field behind a variety of ship models at different speeds. The obtained experimental accuracy is satisfactory. The advantage of the approach is the experimental accessibility of flow regimes crucial to the resistance of a ship, i.e. dead water zones and other areas which are influenced by the viscous wake.
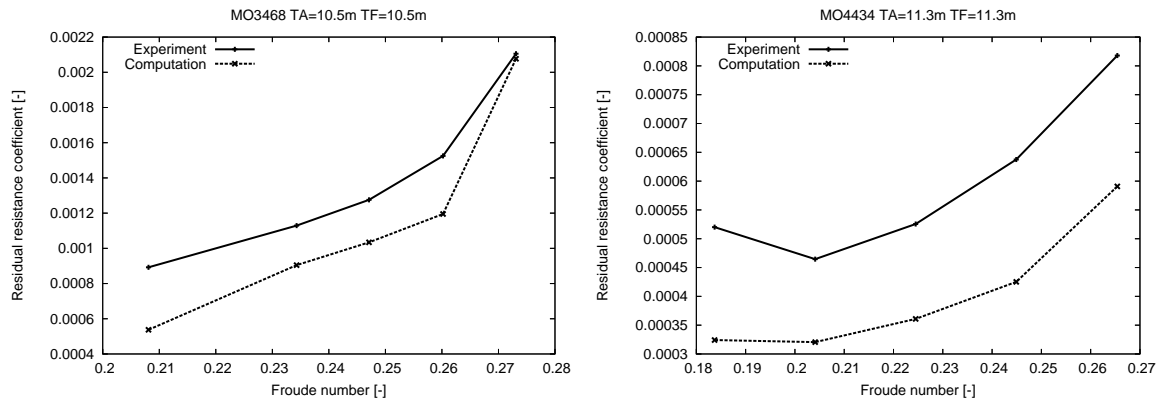
Figure 6: Comparison of experimental and numerical results: Residual resistance coeficient. Left: 'Hamburg Test Case' at draft of 10.5 m, $F_{n,Tr} = \infty$. Right: Container vessel at draft of 11.3m, $F_{n,Tr} \approx 5.2$.

The potential flow method has shown good results at higher transom Froude numbers, where a smooth flow from the transom edge occurs. Results deteriorate significantely at lower transom Froude numbers. This may be explained by viscous effects like a dead water zone behind the transom, which can not easily be modelled by the potential flow methods.

Because viscous methods are still inconvenient for the iterative ship design process, it appears worthwhile to increase the accuracy of potential flow methods by taking into account primary viscous effects of the ship's wake.

5 Acknowledgement

References

[1] Roger Y. Tsai: *An Efficient and Accurate Camera Calibration Technique for 3D Machine Vision*, Proceedings of IEEE Conference on Computer Vision and Pattern Recognition, Miami Beach, 1986

[2] Volker Bertram, Kuo-Yih Chao, Gerd Lammers, Jochen Laudan: *Experimental Validation Data of Free-Surface Flows for Cargo Vessels*, Proceedings of CFD Workshop Tokyo 1994, Vol. 1 pp. 311-320

A Wave Cuts
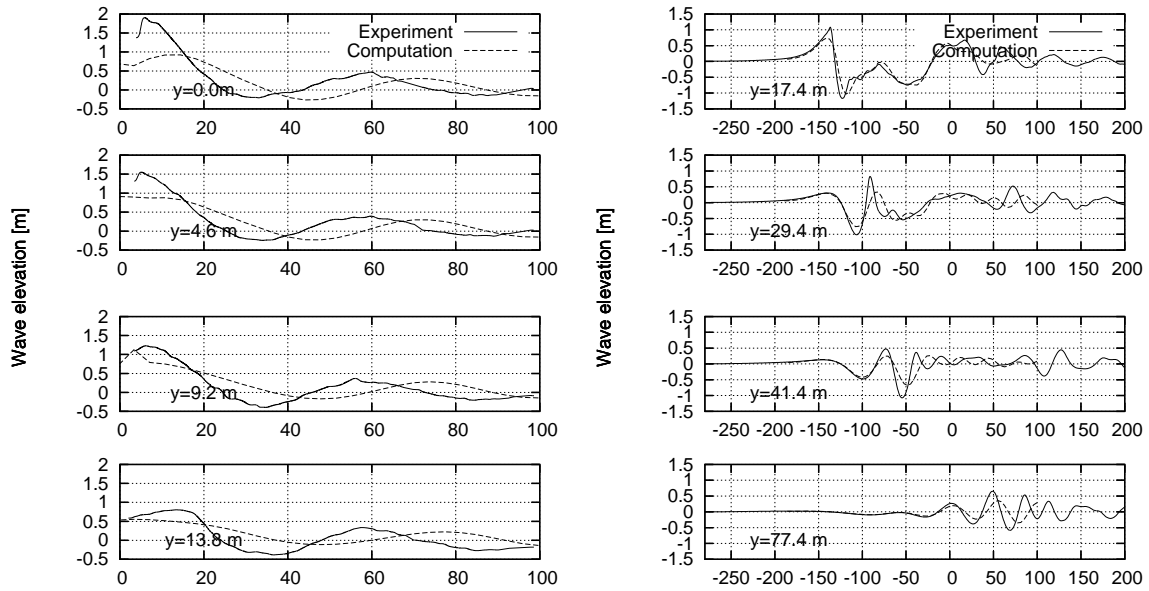
Figure 7: Cuts of wave pattern of 'Hamburg Test Case'. Experimental and numerical results. Draft 10.5 m, velocity 19 kts, Froude number 0.252. Ship's length Lpp 246.4 m, model scale λ 29.1
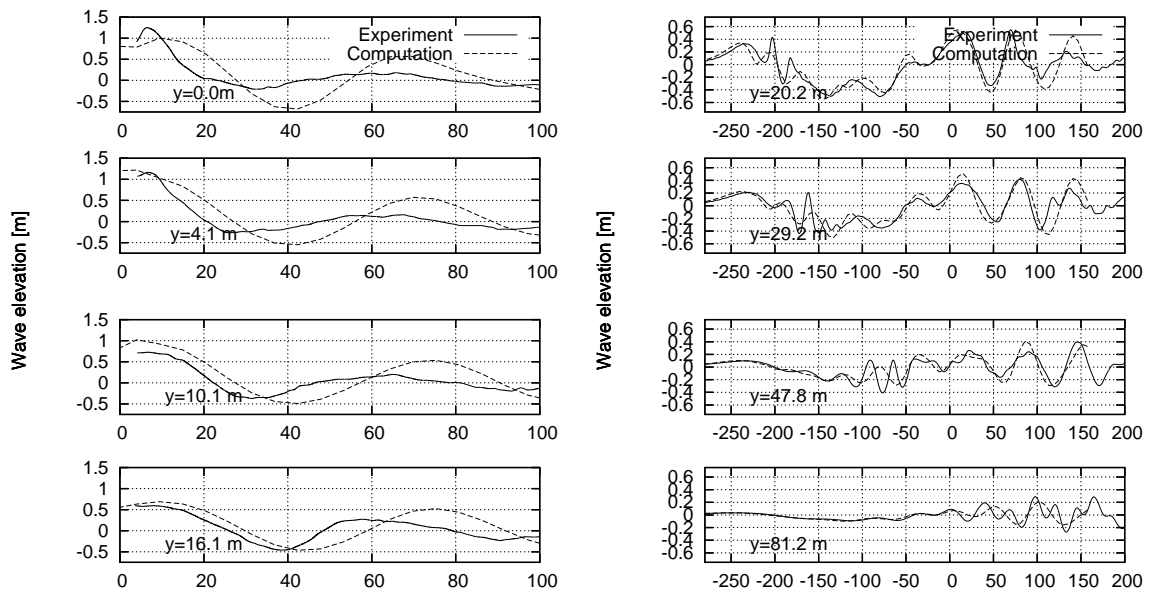
Figure 8: Cuts of wave pattern of container vessel. Experimental and numerical results. Draft 11.3 m, velocity 20 kts, Froude number 0.209. Ship's length Lpp 153.7 m, model scale λ 24.0

High-Speed Planing Catamaran Resistance Simulation, Based on a Three-Dimensional Viscous Free Surface Flow Solver

R. Panahi[1], E. Jahanbakhsh[2], and M.S. Seif[2]

[1] Tarbiat Modares University, Tehran, Iran

[2] Marine Lab., Dept. of Mechanics, Sharif University of Technology, Tehran, Iran

seif@sharif.edu

1- Introduction

CFD modeling based on numerical solution of differential governing equations is a good choice to assess a hydrodynamical design in its early stage. In solving such a problem, one encounters to three subproblems including velocity and pressure distribution, free surface deformation and rigid body motions.

The motion of a floating body is a direct consequence of the flow-induced forces acting on it, while at the same time these forces are functions of the body movement itself. Therefore, the prediction of flow-induced body motions in viscous fluid is a challenging task and requires coupled solution of fluid flow and body motions. In recent two decades, with the changes in computer power, ship motions simulation is the subject of many numerical researches. These studies is started from the restricted motions such as trim or sinkage by Miyata [1], Hochbaum [2] Alessandrini [3] and Kinoshita [4] and continiued to the evaluation of 6-DoF motions by Miyake [5], Azcueta [6], Vogt [7], Xing [8] and Panahi et. al [9].

In this paper, the ability of developed software in simulation of high speed planing craft motions is presented. Comparison of numerical and experimental results in evaluation of a catamaran vessel resistance and trim, shows the performance of the implemented algorithm in such problems.

2- Formulations and Solution Algorithm

Here, a time dependent three-dimensional viscous free surface flow solver is implemented. This solver is based on colocated finite volume discretization on hexahedral cell and VoF free surface simulation approach as proposed by Jahanbakhsh et. al [10]. Besides, a body-attached mesh following the time history of motions is used, to add the ability of 6-DoF motions simulation to developed free surface flow solver [9].

As mentioned earlier, one encounters to three sub-problems in CFD simulation of ship motions. These parts which are marked with dashed lines are solved in a loop as shown in Fig.1.
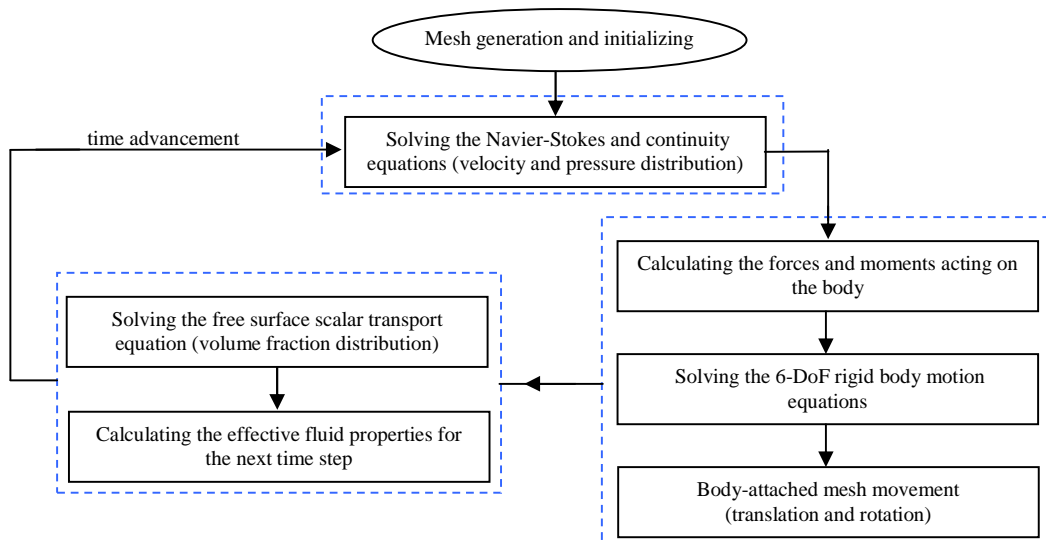
Fig.1: Solution algorithm for numerical modeling

3- Numerical Results

Coupling of rigid body motions with fluid dynamics has been studied by authors in former researches [11, 12, 13, 14 & 15]. Accuracy and precision of the developed software is verified by comparison of numerical and experimental results in such studies.

In this paper, resistance of a high-speed planing catamaran which moves forward in a calm water is evaluated. This includes the changes in craft heave and pitch values based on the hull form produced lift force. Fig. 2 and Table 1 present the geometry and characteristics of the catamaran craft, respectively.
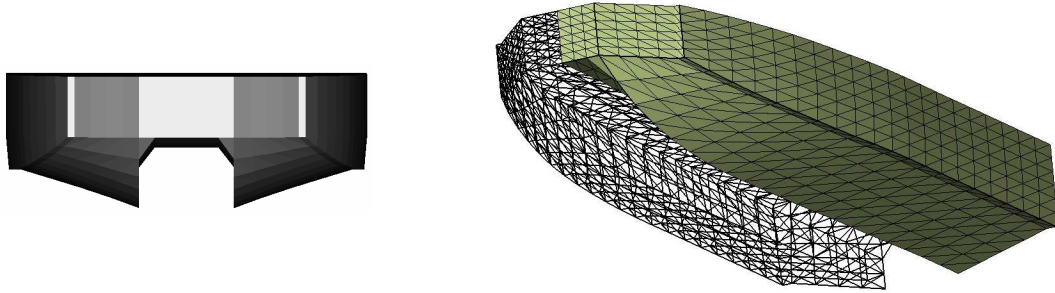
Fig.2: Catamaran geometry

Table 1: Catamaran ship characteristics

Characteristic	Value
Length	12.3 m
Width	4.6 m
Draft	0.45 m
Mass	17850 kg
Vertical mass center position	0.25 m
Longitudinal mass center position	3.81 m
Inertial moment around mass center	$\begin{bmatrix} 53274 & 0 & 0 \\ 0 & 295967 & 0 \\ 0 & 0 & 325563 \end{bmatrix}$

Here a half domain 78000 hexahedral mesh, presented in Fig.3, is used. Catamaran forward motion is modeled by applying thrust force at 0.25 *m* under mass center position, with two approaches. In the first approach, a constant thrust force of 40 *kN* is exerted on craft at initial time and in the second approach, a variable thrust force is used. Steps of the second approach are presented in Table 2. These steps are based on reaching a steady state position after each change in thrust force.
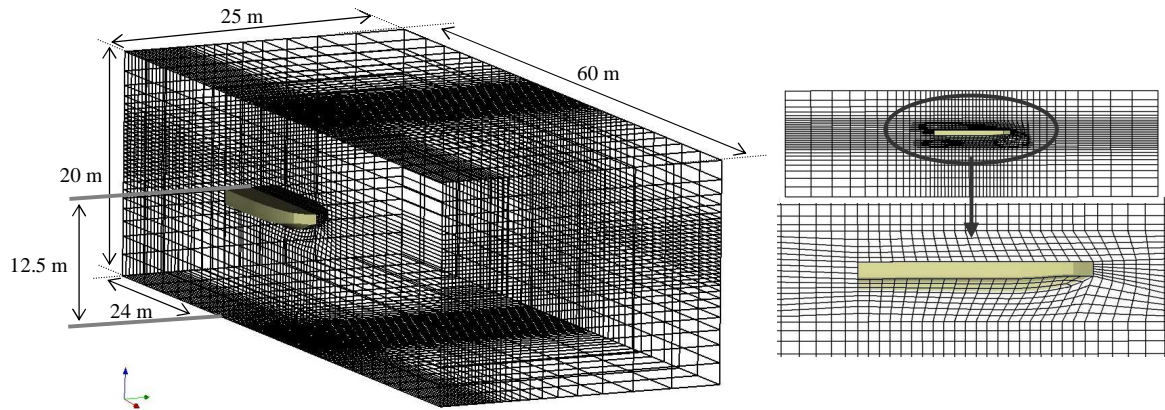
Fig.3: Catamaran forward motion simulation mesh

Table 2: Steps of applying variable thrust force on catamaran

Step	Time Interval (s)	Thrust force (kN)
1	0.0-47.0	15
2	47.0-90.5	25
3	90.5-105.0	30
4	105.0-192.0	40
5	192.0-230.0	45
6	230.0-262.0	50

Time history of results, using second approach, is presented in Figs.4, 5, 6 and 7. As marked on Fig.4, forward motion can be divided into three phases.

In the first phase, which is from t = 0 to t = 100 s, all diagrams behave smoothly. In this phase the craft is lifted about 0.2 m and its trim angle is increased up to 8^0. Velocity is about 10 kn at the end of this phase and experiences small changes except at the initial part of this phase.

The second phase is between t = 100 and t = 250 s. The distinct planing motion is occurred at the beginning of this phase during ten seconds, as it is obvious from the change in heave motion (Fig.5). In this phase, the craft is lifted about 0.55 m. The change in its trim angle is an interesting phenomenon because it is decreased from 8^0 to 4^0 in this phase, after an increase in the previous phase (Fig.6). Besides, velocity is increased abruptly from 10 to 40 kn (Fig. 7).

The third phase of motion is accompanied by huge oscillations in all results. This is because of reaching an unstable dynamical position at the forward speed of 52 kn in this craft. This phenomenon which is accompanied with bow slamming is called propoising, and can be interpreted as a common case for such a hull forms.

Fig.8 shows the plot of mean resistance versus velocity, extracted from Fig.4 and Fig.7. In this plot, the bold lines are curves fitted to result points. The left part of results belongs to 1st motion phase before planing occurrence. At this phase, the resistance experiences a 2nd order increase relative to forward speed. The right part of results belongs to 2nd and 3rd motion phases after planing occurrence. Here a 1st order increase of resistance is obvious. The dashed line which connects these two parts of results is an assumption which can be used as an estimate for the transient region. The gap is because of the fast increase in forward speed at the initial times of 2nd phase. Actually, there is no steady state position and therefore no resistance date in the mentioned interval. However, it is possible to cover this area with additional simulations.
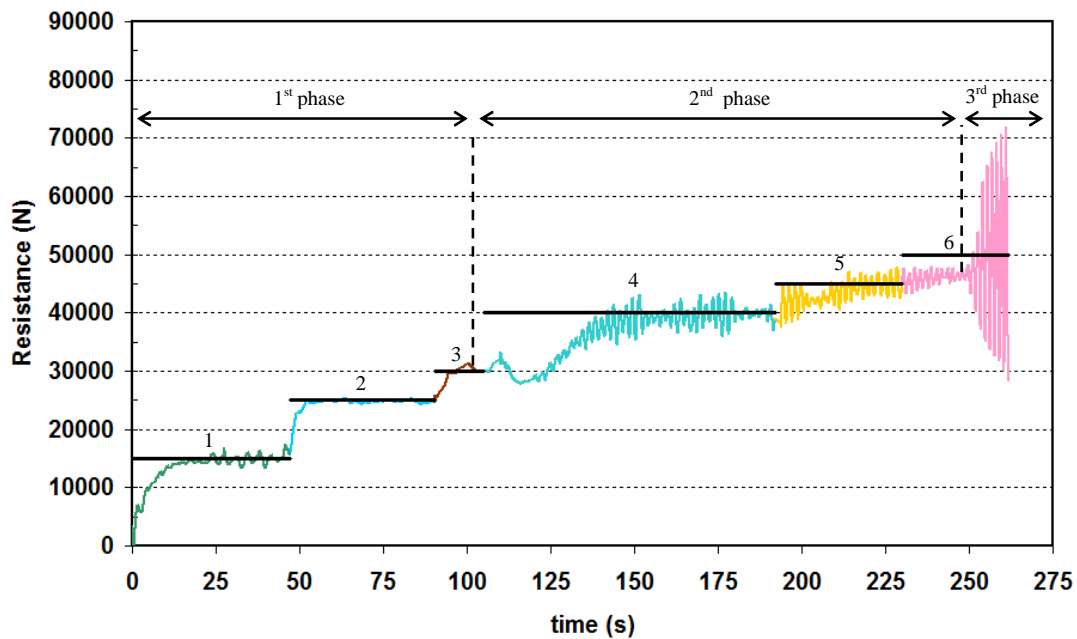
Fig. 4: Resistance time history diagram (Bold lines represent thrust forces)
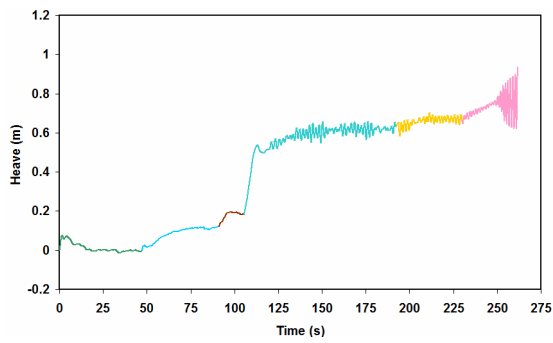
Fig.5 Heave motion time history
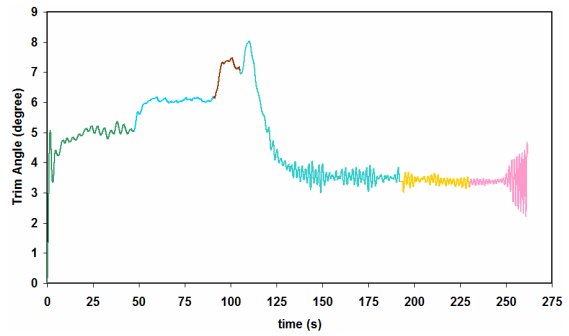
Fig.6 Pitch motion time history
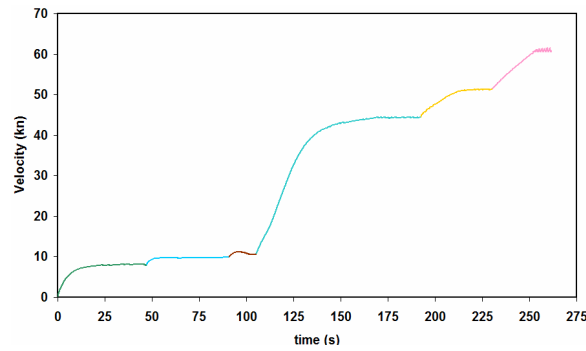
Fig. 7 Velocity time history diagram
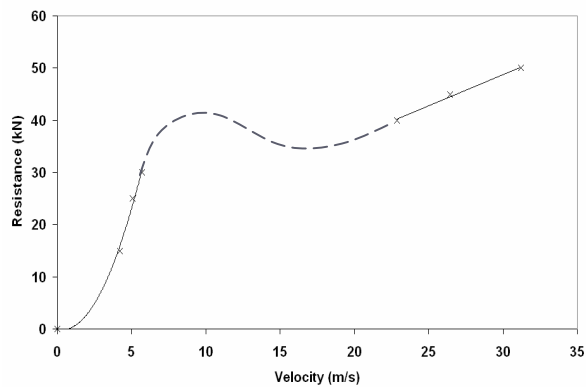
Fig. 8 Resistance versus velocity
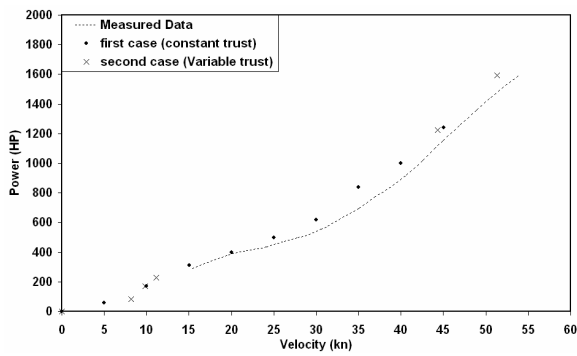
Fig.9: Numerical and experimental power
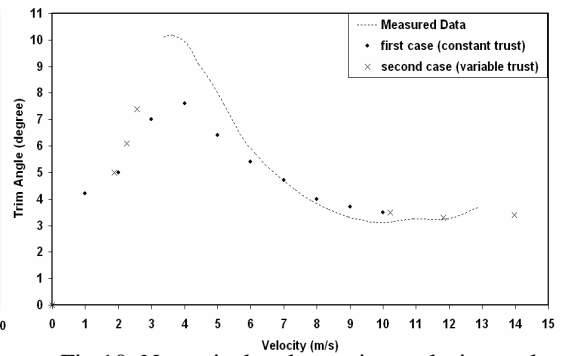
Fig.10: Numerical and experimental trim angle

Figs.9 and 10 show the comparison between numerical and experimental results of power and trim angle versus velocity, respectively. It is Obvious from Fig.9 that, there is a good concordance between numerical and experimental results in the case of catamaran resistance. The first approach (constant thrust) has good performance in prediction of resistance and covers all velocities in contrast with second simulation approach (variable thrust). Besides, the results of the first and the second approach are near to each other. These two properties encourage the use of the first approach which is simpler in practice.

The trim angle of crafts is also plotted in Fig.10. It seems that using the second approach is better than the first approach in the case of trim angle, especially in evaluating its maximum value, although there is no point in that velocity .

Fig.11 shows some snap shots of catamaran in different velocities. The depth of water changes at the stern of craft is reduced as the velocity increased as well as the angle of wave pattern.
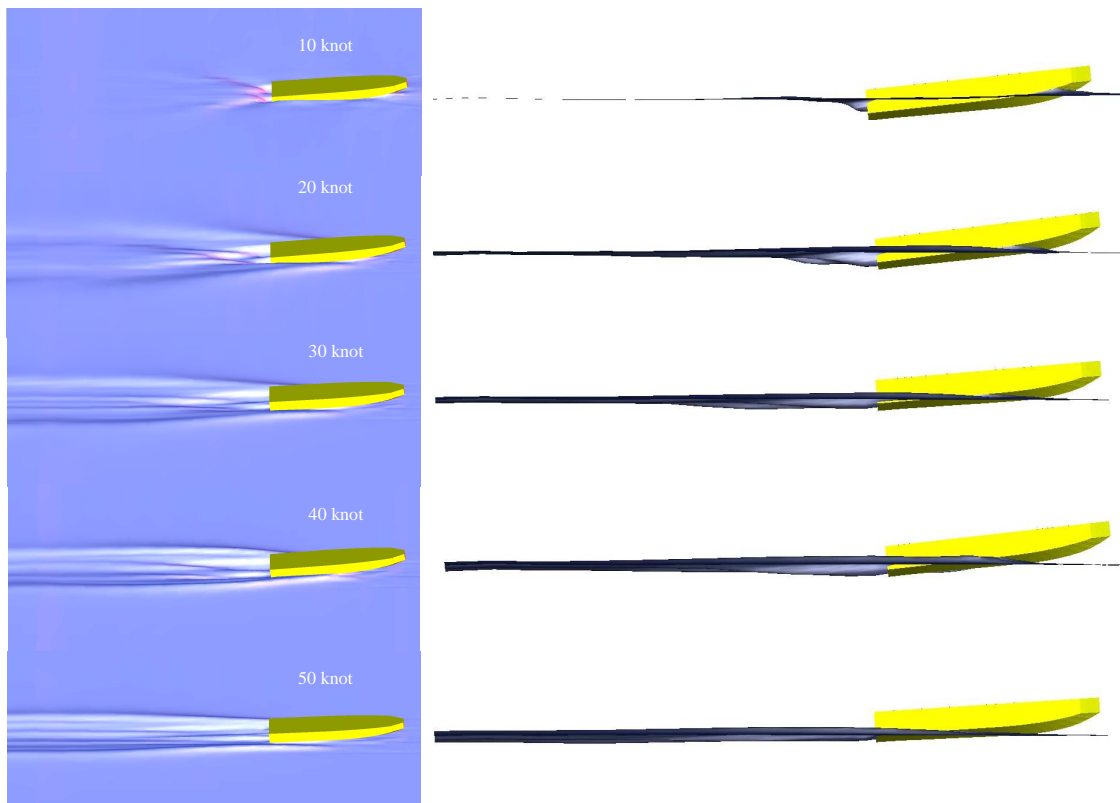
Fig.11 Snapshots and wave patterns of catamaran in different velocities

Wet-deck of the catamaran has different situation relative to water surface in different velocities. In low velocity before planing the wet-deck becomes wet and in higher speeds it rises up from water as clearly represented in Fig.12.

4- Conclusion

The proposed numerical algorithm is capable of simulating complex ship dynamic problems. High speed catamaran investigated in present study was accompanied by some complicated dynamics phenomena like planning and porpoising. However, Numerical results show good agreement with experimental data. As it is described in this and other recent papers by the authors, the developed computer software is used for nonlinear fluid-structure interactions. The method has no geometrical restriction and is applicable for usual ship body forms as well.
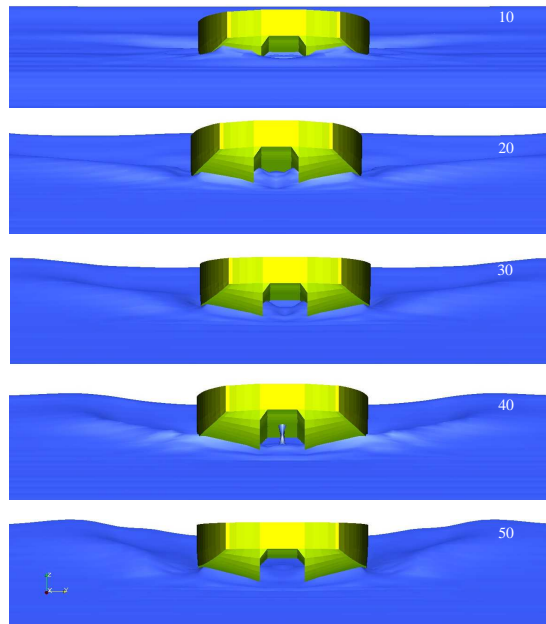
Fig.12 Snapshots and wave patterns of catamaran in different velocities

5- References

1- Miyata, H., Sato, T. and N. Babo, *Difference solution of a viscous flow with free-surface wave about an advancing ship*, J. Comput. Phys., Vol.72, p.393-421, (1987).

2- Hochbaum, C., A finite volume method for turbulent ship flows, Ship Technology Research Schiffstechnik, Hamburg, Germany, (1994).

3- Alessandrini, B. and Delhommeau, G., *Simulation of three-dimensional unsteady viscous free surface flow around a ship model*, Int. J. of Numerical Math. Fluids, Vol.19, p.321-342, (1994).

4- Kinoshita, T., Kagemoto, H. and Fujino, M., *A CFD application to wave-induced floating-body dynamics*, 7th Int. Conference on Numerical Ship Hydrodynamics, Nantes, France, (1999).

5- Miyake, R., Kinoshita, T. and Kagemoto, H., *Ship Motions and loads in large waves*, 23rd ONR Symp. On Naval Hydrodynamics, Val de Reuil, France, (2000).

6- Azcueta, R., *Computation of turbulent free surface flow around ships and floating bodies*, PhD Thesis, Teschnichen Universitat Hamburg-Harburg, (2001).

7- Vogt, M. and Hochbaum, C., *Numerical simulation of ship motions in head waves with a RANSE method*, HSVA Report 1649, Hamburg, Germany, (2002).

8- Xing-Kaeding, Y., *Unified approach to ship seakeeping and maneuvering by a RANSE method*, PhD Thesis, Teschnichen Universitat Hamburg-Harburg, (2004).

9- Panahi, R., Jahanbakhsh, E. and Seif, M.S., *Development of a VoF fractional step solver for floating body motion simulation*, Applied Ocean Research, Vol.28, No.3, p 171-181, (2006).

10- Jahanbakhsh, E., Panahi, R. and Seif, M.S., *Numerical Simulation of Three-Dimensional Interfacial Flows*, International Journal of Numerical Methods for Heat & Fluid Flow, Issue 4, (2007).

11- Jahanbakhsh, E., Panahi, R. and M.S. Seif, *Multi-dimensional free surface flow simulation using two-phase Navier-Stokes solver*, 8th Numerical Towing Tank Symposium (NuTTs), Varna, 2-4 October, (2005).

12- Panahi, R., Jahanbakhsh, E. and Seif, M.S., *Effect of interpolation in interface capturing methods*, 8th Numerical Towing Tank Symposium (NuTTs), Varna, 2-4 October, (2005).

13- Panahi, R., Jahanbakhsh, E. and Seif, M.S., *Development of a numerical hydrodynamic tank for ship motion simulation*, ECCOMAS CFD 2006, Egmond aan Zee, Netherlands, 5-8 Sept. (2006).

14- Panahi, R., Jahanbakhsh, E. and Seif, M.S., *Numerical Investigation on the Effect of Baffle Arrangement in Tanker Sloshing*, 9th Numerical Towing Tank Symposium (NuTTs), Nantes, 1-3 October, (2006).

15- Panahi, R., Jahanbakhsh, E. and Seif, M.S., *Ship Dynamic Simulation, Based on a Three-Dimensional Viscous Free Surface Solver*, 9th Numerical Towing Tank Symposium (NuTTs), Nantes, 1-3 October, (2006).

Mesh Generation Technique for the Analysis of Ducted Propellers Using a Commercial RANSE Solver and its Application to Scale Effect Study

Vladimir I. Krasilnikov[1], Jia Ying Sun[1], Zhirong Zhang[2] and Fangwen Hong[2]

[1]Ship and Ocean Laboratory, MARINTEK, Trondheim, Norway

[2]China Ship Scientific Research Center (CSSRC), Wuxi, Jiangsu, China

Direct correspondence to: E-mail: *Vladimir.Krasilnikov@marintek.sintef.no*; Postal address: P.O.Box 4125 Valentinlyst, NO-7450 Trondheim, Norway

From the point of view of hydrodynamic analysis ducted propeller represents a noticeably more complicated problem compared to open propeller because its performance is defined by the interaction between propeller and duct and, ultimately, by the interaction within the whole system ship hull/propeller/duct. Since such interaction is, to significant extent, viscous in nature, one may expect scale effects on ducted propeller to be more difficult to capture using traditional extrapolation techniques (Stierman 1984), or analysis methods based on potential flow theory (Krasilnikov et al 2005, Krasilnikov et al 2006). Beside overall effect on propeller and duct forces through the changes in lift and drag, the change in Reynolds number is also responsible for the following effects:

1) Change in averaged flow velocity through the duct;
2) Changes in the flow through the gap between propeller blade tip and duct interior surface;
3) Local flow separation on the duct surface, which may develop either on interior or exterior surfaces depending on geometry and loading;
4) Effects at the duct trailing edge and downstream of it where the interaction between the vortex sheets shedding from propeller and duct takes place.

In the present paper the problem of viscous flow analysis around ducted propeller separated from hull is addressed using a RANS equation solution. Modeling of geometry and meshing of computation domain are performed by the pre-processing program, which is built under a joint project by CSSRC and MARINTEK and customized for the analysis of ducted propellers. The solution is performed on a multi-block hybrid mesh in the commercial CFD code FLUENT using a SIMPLE algorithm for velocity/pressure coupling and overall solution procedure. Introducing a Cartesian coordinate system fixed on propeller with the x-axis corresponding to the axis of propeller rotation and directed downstream one can write the incompressible 3D RANS equations in the following normalized form:

$$\frac{\partial u_i}{\partial x_i} = 0 \qquad (1)$$

$$\frac{\partial u_i}{\partial t} + \frac{\partial u_i u_j}{\partial x_j} + a_j \frac{\partial u_i}{\partial x_j} =$$
$$= \frac{\partial p}{\partial x_i} + \frac{1}{Re} \frac{\partial}{\partial x_i} \left(\frac{\partial u_i}{\partial x_j} + \frac{\partial u_j}{\partial x_i} \right) + \frac{\partial}{\partial x_j} \left(- \overline{u_i' u_j'} \right) \qquad (2)$$

where u_i is the *i-th* Cartesian component of the absolute velocity vector, p is the pressure, *Re* is the Reynolds number, and a_j is defined as follows:

$$a_j = \begin{cases} 0 & j = 1 \\ -\Omega z & j = 2 \\ \Omega y & j = 3 \end{cases} \qquad (3)$$

where *Ω* is the rotational speed of propeller.

The SST (shear stress transport) *k-ω* turbulence model (Menter 1994) was applied to calculate Reynolds stresses and, thus, close the system of governing equations. This model has reportedly better computational performance in flows involving separation, which is an important issue in the analysis of ducted propellers, where separation phenomenon may develop on the duct surface as at heavy as at light propeller loading. The SST *k-ω* turbulence model has been recommended for the flow analysis around ducted propellers in (Abdel-Maksoud & Heinke 2002). In combination with standard wall functions and coarse structured meshes, it has also been applied by the authors to the computation of flow around pod propulsors, where the degree of swirl is significant and flow separation occurs on the strut junction and aft end of the gondola (Krasilnikov et al 2007a).

The numerical solution is performed in the commercial CFD code FLUENT using a cell-centered finite-volume method, which allows for the use of computational elements of arbitrary polyhedral shape. Convection terms in the RANS equations are discretized using a second order upwind scheme, while diffusion terms are discretized using a second order central scheme. Overall solution procedure is based on a SIMPLE-type segregated algorithm adapted to unstructured grid. The discretized equations are solved using the Gauss-Seidel iterative procedure, and the algebraic multi-grid method is used to accelerate solution convergence.

The geometry model subject to numerical simulation includes propeller blades, hub and duct. The clearance between propeller blade tip and duct interior surface is

taken into account. The exact geometry of blade/hub fillet is not accounted for, while hub cap geometry can be either inputted by the user, or approximated by elliptic fairing, depending on available information. The computation domain represents a cylinder with its inlet located at four duct lengths upstream of duct leading edge, outlet located at six duct lengths downstream of duct trailing edge, and the radius of cylinder being equal to four duct lengths. The computation domain is divided into 29 blocks (some of which are shown schematically in Figure 1) in order to generate the mesh. The mesh is hybrid combining both the structured and unstructured mesh blocks. Most of blocks outside of the duct feature structured mesh of hexahedral elements. In the domains near the duct leading edge and propeller blades the unstructured meshes of tetrahedral elements are used. The latter domains are characterized by relatively complex geometry, and a high quality mesh requires as little distortion and skewness of the elements as possible.
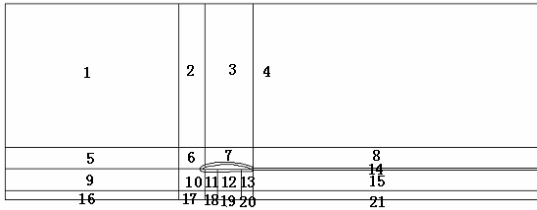
Figure 1. Mesh blocks used in the mesh generation procedure for a ducted propeller.

While it is possible to build a completely structured high quality for the considered problem, it will most likely require customization for each particular geometry. With unstructured meshes employed in some blocks the task of mesh generation can be made, to significant degree, automatic. At the same time, a structured mesh with high orthogonality built in the outer flow domain facilitates stability of numerical procedure and accelerates convergence. In order to simulate the flow in the clearance about ten layers of O-type mesh are laid in the gap between the blade tip and duct interior surface. The O-type mesh in the domain surrounding duct surface is less sensitive to large aspect ratio of cells and it will not affect aspect ratio of cells in the neighbouring blocks. The less total number of elements around the duct surface can be used with O-type mesh employed. The surface meshes on propeller blades and duct are shown in Figure 2. Figure 3 illustrates the interface between unstructured and structured mesh blocks as shown at the vertical section plane passing through the shaft axis.

The developed mesh generation technique supports the cases of isolated duct, open propeller and ducted propeller subject to straight or oblique flow without principal limitations with respect to simulated geometries. While in general case the whole geometry is to be modelled, the steady formulation allows for consideration of only one blade passage as it is shown in Figure 2, the
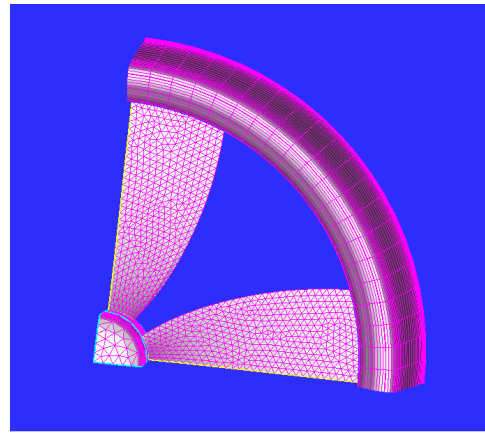
Figure 2. Surface meshes on propeller and duct (one blade passage).
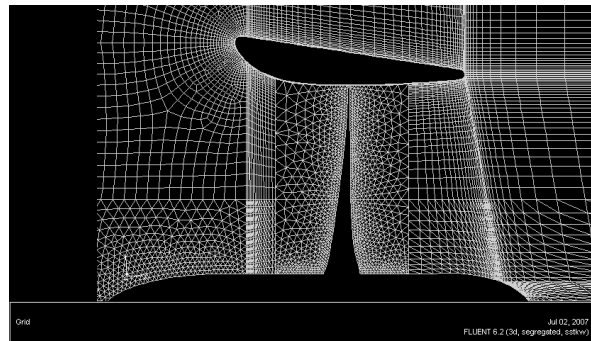
Figure 3. Interface between the structured and unstructured mesh blocks around ducted propeller (longitudinal section).

effect of other blades being accounted for through the periodical conditions set up at the boundaries of the passage sector.

The extensive numerical studies done allowed the authors to elaborate the employed meshing technique, in particular, in such critical domains as tip clearance and duct trailing edge, which have strong influence on performance prediction. It was found, for example, that a higher mesh resolution and orthogonality around duct trailing edge are important for the accurate prediction of propeller characteristics. While duct thrust itself is less dependent on mesh quality around duct trailing edge, propeller thrust and torque are affected to much higher degree. This is due to the mesh effect on flow velocity through the duct. The necessary improvement was achieved by extending the zone of structured mesh inside the duct, upstream of duct trailing edge, as shown in Figure 3. The effect of duct trailing edge shape was also checked. This study resulted in extension of mesh generation pre-processing code to handle automatically the cases of sharp, blunt and round trailing edges, optimizing the mesh each time for inputted geometry. The accurate modeling of tip clearance was also found to be an important factor in the analysis of ducted propellers. This is the place were the interaction between propeller

blade tip and boundary layer on the interior duct surface takes place. Due to the aforementioned interaction the occurrence and behavior of the tip vortex are different from that of open propeller. Propeller torque and duct thrust appear to be the quantities most sensitive to mesh quality in the tip clearance domain. A special study was undertaken to compare the numerical predictions done at different gap sizes with tendencies observed in model tests. Below some comparative results obtained for ducted propellers operating in straight flow are discussed.

The well-known Wageningen series propellers Ka (fixed pitch) and Kcp (controllable pitch) operating in various ducts were simulated and the numerical results were compared with predictions by regression models and experimental charts available from (Kuiper 1992). The examples of such comparisons are presented in Figures 4-6 where relative differences in duct thrust coefficient (KTD), propeller thrust coefficient (KTP) and propeller torque coefficient (KQP) are given for propellers Ka4-55 and Ka4-70 in duct 19A (duct length/diameter ratio L_D/D_D=0.5) and propeller Ka4-70 in duct 24 (duct length/diameter ratio L_D/D_D=1.0). As one can see, the accuracy in prediction of propeller characteristics (KTP and KQP) was very high for all studied advance coefficients.
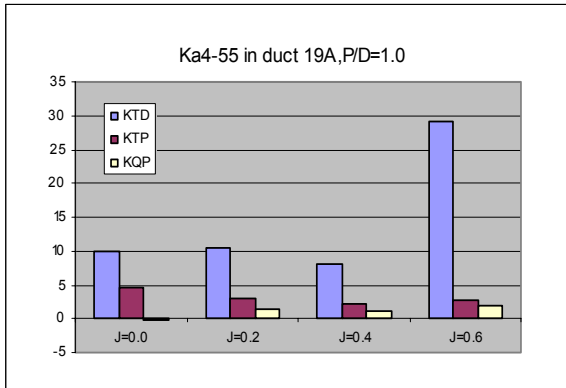
Figure 4. Force coefficients of the series propeller Ka4-55 in duct 19A, P/D=1.0. Relative difference (in %) between the RANS predictions and regression model.
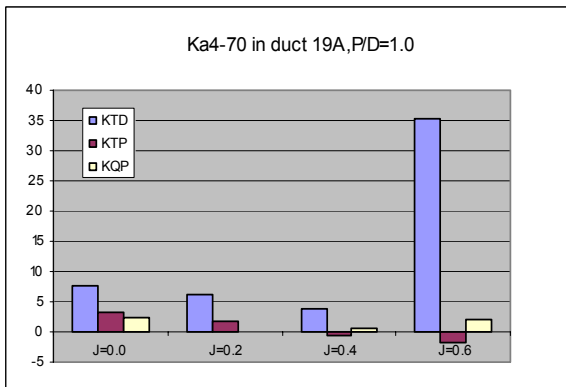
Figure 5. Force coefficients of the series propeller Ka4-70 in duct 19A, P/D=1.0. Relative difference (in %) between the RANS predictions and regression model.
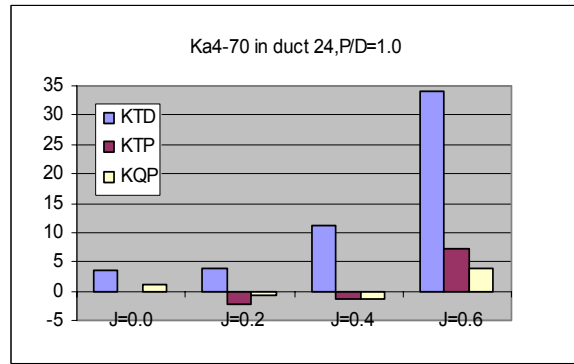
Figure 6. Force coefficients of the series propeller Ka4-70 in duct 24, P/D=1.0. Relative difference (in %) between the RANS predictions and regression model.

The difference from the regression model did not exceed 5%, and in most of the cases it was, actually, smaller. With respect to duct thrust (KTD) this difference lay within 10% except the highest J value of 0.6 where the calculated KTD was significantly overpredicted. The latter result can be explained by several reasons such as small absolute values of KTD, difference in local flow regimes between model tests, where zones of laminar flow may exist, and CFD calculations based on assumption of fully turbulent flow, and, finally, fairing of experimental data in the regression model. It is seen from both numerical analyses and model tests that under such light loading flow separation develops on the exterior duct surface downstream of leading edge.

The computation results obtained with the series controllable pitch propeller Kcp4-55 operating in duct 19A in a range of actual pitch settings can be found in (Krasilnikov et al 2007b). In general, they confirm the tendencies observed with the Ka series. The reasons for a common trend in the aforementioned calculations to overpredict duct thrust were partly revealed in the study with another CP ducted propeller tested at MARINTEK in duct very similar to 19A. In those tests the force measurements have been carried out at different sizes of tip clearance followed by pressure measurements on the duct surface under the same conditions (Zhao 2000). The tip clearance of the initial design amounted 0.5% of propeller diameter, which was D=0.300 m. The different sizes of tip clearance in the following tests were obtained by cutting the tip of the initial blade. Some results of calculation/experiment comparisons for the geometries corresponding to the tip clearances of 0.5% and 1.0% of propeller diameter are summarized in Figure 7 (forces) and Figure 8 (duct surface pressure). At the pitch of 1.30, which is higher than design pitch, both the test results and calculations show the same tendencies in propulsor characteristics. More accurately, with increase of tip clearance the duct thrust and propeller torque slightly decrease, at nearly unchangeable propeller thrust except lowest J-s. This is explained by relatively lower loading
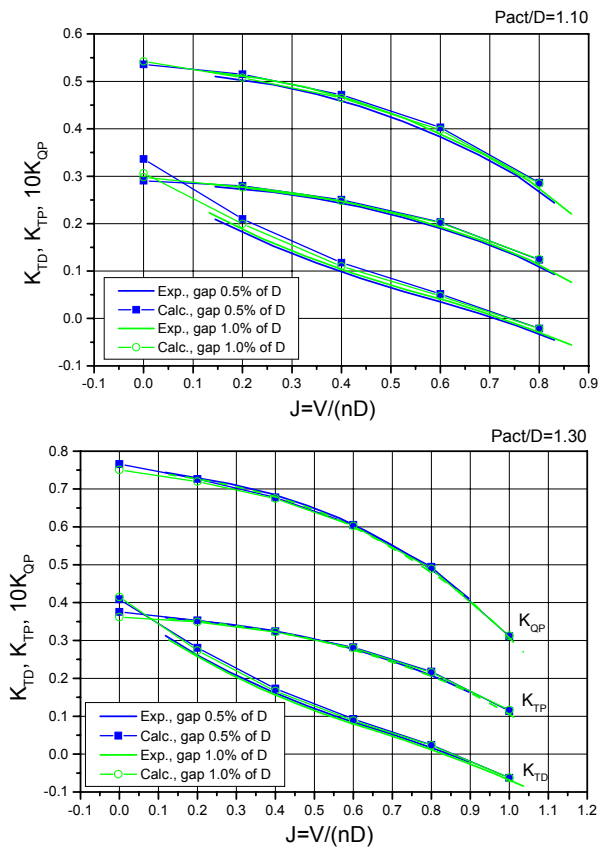
Figure 7. Measured and calculated characteristics of the ducted propeller P1287 at the two different sizes of tip clearance. Actual pitches P(0.7)/D=1.0 and 1.30.

of the blade tip at larger clearance. The decrease in torque is larger at lower J-s (heavier propeller loading) where propeller thrust also decreases slightly. The decrease in duct thrust is larger at moderate propeller loading. At the propeller pitch setting 1.10 (lower than design) the measured duct thrust increases at larger tip clearance, while calculations show the same trend as for the pitch 1.30, i.e. decrease in duct thrust. Experimental values of propeller thrust and torque are higher at larger tip clearance as well. At the same time, the calculated thrust and torque differ very little for the two different clearances, and only at the lowest J-s the numerical analysis shows an increase in propeller forces.

The comparisons between the measured and predicted pressure distributions given in Figure 8 demonstrate that at generally good agreement the calculated pressure values on the interior surface appear to be slightly lower than measured values for the smaller tip clearance of 0.5% of D, while for the larger tip clearance of 1.0% of D they are close. The observed difference becomes more pronounced for the lower pitch setting P(0.7)/D=1.10. This explains why the predicted values of duct thrust are higher than measured. An additional test with the largest tip clearance of 1.5% of D brought the results as agreeable with the experimental data as those at the tip clearance of 1.0% of D. Obviously, at smaller tip
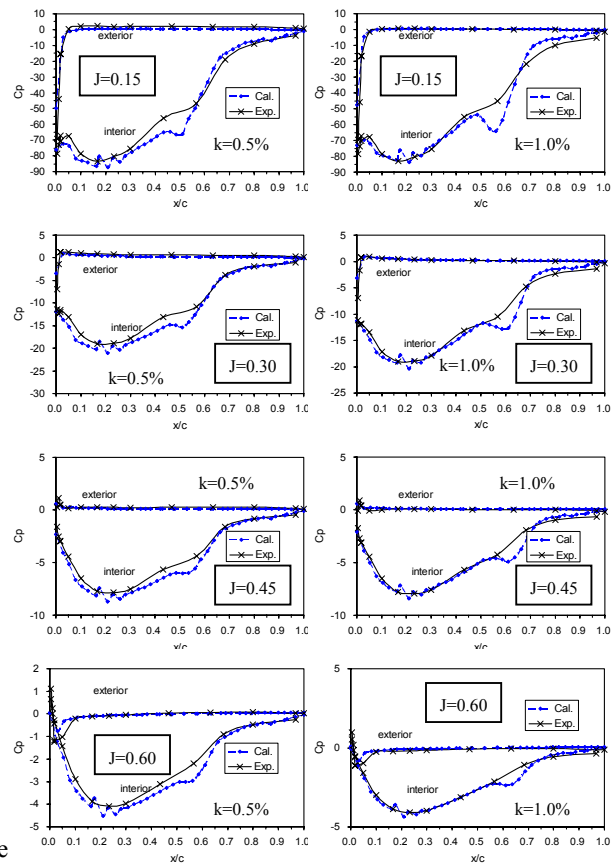
Figure 8. Measured and calculated circumferential averaged pressure distributions on the duct surface at the two different sizes of tip clearance. Actual pitch P(0.7)/D=1.30. Pressure coefficient is based on speed of oncoming flow. J value is based on initial propeller diameter D=0.300 m.

clearances of order of 0.5% of D the numerical model needs more thorough validations to understand the true reasons for aforementioned effects. Similar effects are likely to be the cause of duct thrust overprediction observed earlier on series propellers Ka in duct 19A where tip clearance amounted about 0.4% of D (see Figures 4 and 5).

The developed numerical method was applied to the analysis of some typical ducted propellers under different scale factors (Krasilnikov et al 2007b). At the first stage the focus was made on Kaplan-type series propellers Ka4-55 and Ka4-70 operating in different ducts including duct 19A (L_D/D_D=0.50), duct 24 (same profile as 19A, L_D/D_D=1.0) and a generic duct with lifted TE (so-called "duck-tail" type, L_D/D_D=0.50). The "duck-tail" duct used in this study reproduces (but does not exactly repeat) the main features of duct designs of such type: thicker nose with larger LE radius compared to the duct 19A, lifted TE, also having larger radius and degree of bluntness than those of duct 19A, and noticeably higher diffuser angle aft of propeller plane. These features combined result in a

thicker and more cambered duct profile, almost without cylindrical part around propeller location. The simulated model and full scale conditions are the same for all arrangements and they are summarized in Table 1. The density and viscosity of water in model and full scale calculations were assumed to be the same.

Table 1. Simulated conditions in scale effect study.

	Model	Ship
D, m	0.24	2.4
n, RPM	720	227.2
P/D	1.0	1.0
A_E/A_0	0.55 / 0.70	0.55 / 0.70
Re_P *)	$0.47 \times 10^6 / 0.60 \times 10^6$	$1.50 \times 10^7 / 1.90 \times 10^7$
J	0.0; 0.2; 0.4	

*) $Re_P = 5 \cdot (A_E / A_0) \cdot (1 / Z) \cdot (nD^2 / \nu)$

The summary bar diagrams showing relative difference (in %) between the full and model scale characteristics are presented in Figure 9. Evidently, when changing from model to full scale conditions the duct thrust increases for all studied arrangements at all considered propeller loadings. The scale effect on duct thrust is more pronounced at lighter loadings (higher J-s) where the relative contribution of viscosity is larger. The largest difference between full and model scale values of duct thrust is observed for the long duct 24, while for the ducts 19A and "duck-tail" these differences are comparable. It can also be noticed that blade area ratio of propeller does not seem to have strong influence on increase in full scale duct thrust.

The change in full scale propeller thrust and torque compared to model scale is a complex, combined effect of the following factors: the increase in averaged flow velocity through the duct at higher Reynolds numbers, the decrease in thickness of the boundary layer on the interior duct surface resulting in different local blade loading at the tip (and, ultimately, to different flow picture around the blade tip and its inverse effect on duct characteristics), changes in both lift and drag of blade sections due to increase in Reynolds number. For the considered Ka propellers in the duct 19A the propeller thrust increases on about 0.5-2.0% depending on J values. For the same propellers in the duct of "duck-tail" type this increase amounts already 2.0-4.0%. In both case the larger increase corresponds to lighter propeller loading and this effect is more pronounced for the propeller with larger blade area ratio. The reasons for observed difference between the arrangements featuring duct 19A and duct of "duck-tail" type lie in different influence of Re on velocity distribution inside these two ducts. Under full scale condition inside the "duck-tail" duct the increase in axial flow velocity coming on blade sections r/R<0.95 is slightly smaller than in duct 19A, and, at the same time,
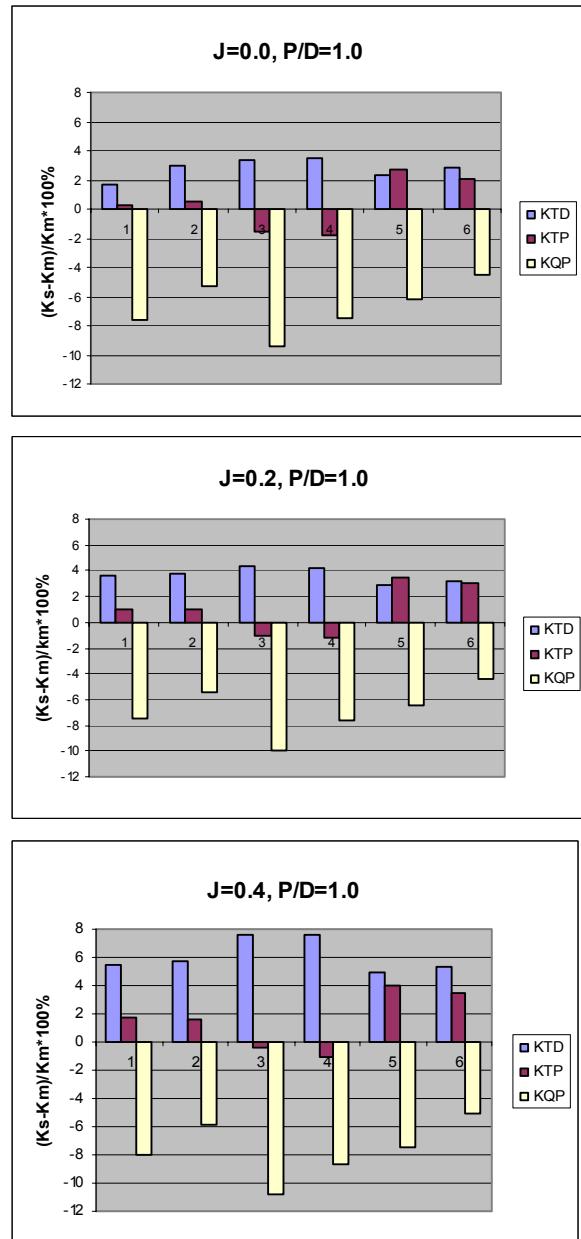
Figure 9. Relative difference between the predicted full and model scale characteristics of different ducted propellers (1 – Ka4-70/D19A, 2 – Ka4-55/D19A, 3 – Ka4-70/D24, 4 – Ka4-55/D24, 5 – Ka4-70/D"duck-tail", 6 – Ka4-55/D"duck-tail").

the axial velocity near the blade tip undergoes a larger change. The latter effect is caused by a relatively stronger decrease in thickness of full-scale boundary layer on the interior surface of the "duck-tail" duct in comparison with duct 19A. Integrating separately the pressure and tangential stress distributions over the blade one can derive that under full scale the two aforementioned effects combined lead to increase of the pressure component of propeller thrust in the "duck-tail" duct,

while in the duct 19A the pressure component decreases. The module of viscous component of propeller thrust decreases for approximately the same magnitude in both ducts. The strongest increase in flow velocity through the duct under full scale conditions is observed on the long duct 24, which results in lower full-scale thrust values compared to model scale.

Regarding scale effect on propeller torque an observation can be made that due to the combined effect of higher flow acceleration and lower blade section drag the propeller torque decreases significantly under full scale. The scale effect on torque of ducted propeller is, therefore, stronger compared to open propeller. This result is in line with conclusions by (Abdel-Maksoud & Heinke 2002). Again, for propeller with wider blades the effect of Reynolds number on torque is more pronounced, and the change in full scale torque is approximately 2% larger than for propeller with smaller blade area ratio. Comparing relative changes in torque for propellers operating in the duct 19A and duct "duck-tail" and having in mind the trends in propeller thrust as discussed above, one can conclude that the same propeller operating in duct of "duck-tail" type will have a better thrust-power ratio under full scale conditions. This is illustrated in Table 2. As one can see, this ratio is 2-3% higher for the propeller operating in the duct of "duck-tail" type, besides, the relative gain in thrust is better at heavier loadings.

Table 2. Thrust-power ratio of ducted propeller Ka4-70, P/D=1.0 operating in duct 19A and duct of "duck-tail" type.

| J | K_{TT}/K_{QP} | |
	Duct 19A	Duct "duck-tail"
0.0	13.43	13.80
0.2	11.01	11.27
0.4	8.96	9.15

While it is convenient to separate propeller and duct to study on scale effects on integral propulsor forces, the interaction between these two components can not be reduced to such simplified model. The interaction is responsible for the effects on the interior surface of the duct and around propeller blade tip. For example, the phenomenon of tip vortex is directly influenced by thickness of boundary layer on the interior duct surface. In its turn, thickness of boundary layer depends on propeller loading and Reynolds number. Figure 10 gives an example of visualization of tip vortex on propeller Ka4-70, P/D=1.0 operating in duct 19A at the two different loadings under model and full scale conditions. At higher full-scale Reynolds numbers the thickness of duct boundary layer decreases, which results in lighter loading of propeller blade tip and, consequently, weaker tip vortex. The presence of blade tip and tip vortex in the duct boundary layer results in high positive pressure

| J=0.4, Model | J=0.4, Ship |
| J=0.0, Model | J=0.0, Ship |
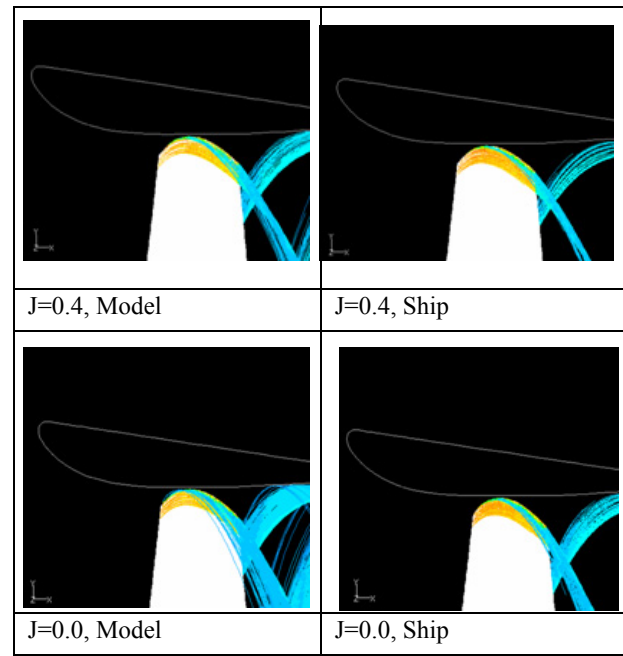
Figure 10. Propeller Ka4-70, P/D=1.0 in duct 19A. Visualization of blade tip vortex (path lines are released from the blade area r/R>0.95).

| J=0.4, Model | J=0.4, Ship |
| J=0.0, Model | J=0.0, Ship |
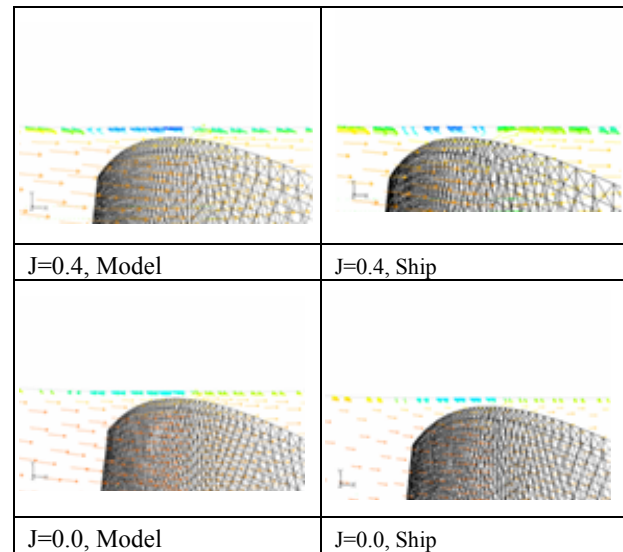
Figure 11. Propeller Ka4-70, P/D=1.0 in duct 19A. Velocity vectors at the longitudinal duct section 0 deg.

gradient and domain of reversed flow above and upstream of the blade tip, which is the cause of local flow separation on the duct interior surface (see Figure 11).

The domain of separation exists in the vicinity of blade tip above propeller blade (duct section 0 deg.) and this is not evident in the location between the blades (duct section 45 deg.). Under model scale conditions the separation zone is larger and it decreases under full scale with decrease of boundary layer thickness and velocity

profiles becoming typical for high-Re flows. At heavier propeller loading the duct boundary layer is thinner due to higher acceleration of flow through the duct. However, the axial extent of separation zone is larger. Comparing the same propeller operating in duct 19A and duct of "duck-tail" type, at the same J value, one can conclude about smaller separation zones occurring on the duct of "duck-tail" type above and upstream of propeller. However, downstream of propeller a higher diffuser angle of "duck-tail" duct creates more favorable conditions for separation to develop as under model as under full scale conditions.

At very light loadings, where duct thrust becomes negative, under model scale ducts 19A and 24 suffer from flow separation on the exterior surface downstream of the leading edge. Due to lighter loading, at the same J value, the separation zone is larger for longer duct 24. However, under full scale exterior side separation is significantly delayed for both ducts. It has to be noted that profiles of the "duck-tail" duct allow for avoiding or delaying separation on the exterior surface compared to duct 19A. For example, in the discussed scale effect study with propellers Ka4-55 and Ka4-70, P/D=1.0 the exterior side separation was not evident on the "duck-tail" duct at J=0.6, while it existed on duct 19A.

Duct 19A

Duct of "duck-tail" type
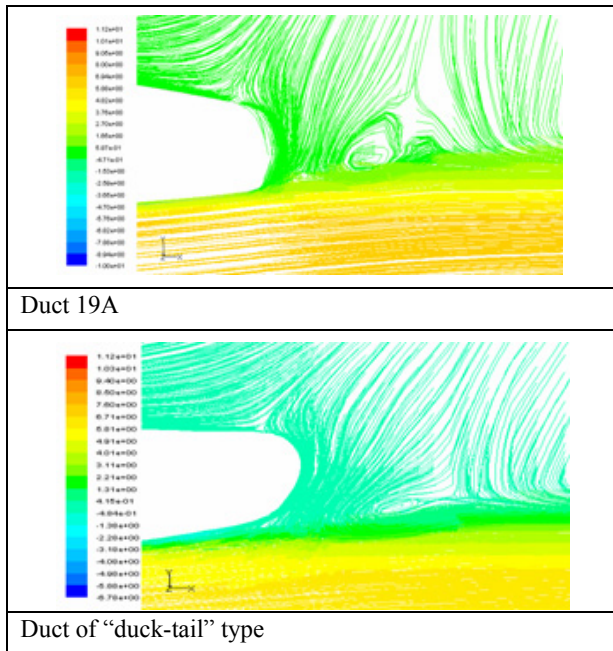
Figure12. Propeller Ka4-70, P/D=1.0 in the two different ducts. J=0.0. Full scale. Visualization of path lines around duct trailing edge.

Different duct designs are expected to produce different flows around duct trailing edge. An example of flow visualization around trailing edges of the two different ducts (19A and "duck-tail") are given in Figure 12 for the J value of 0.0 (bollard pull) where the difference is most pronounced. Instead of three vortices of different sizes existing along the propeller slipstream boundary, downstream of duct 19A, only two are revealed in the analysis of the "duck-tail" duct. Both vortices have comparatively small size and the first one shifts inside the duct.

REFERENCES

Abdel-Maksoud, M. and Heinke, H.J. (2002). Scale Effects on Ducted Propellers. Proceedings of the 24th Symposium on Naval Hydrodynamics, Fukuoka, Japan.

Krasilnikov, V.I., Berg, A., Achkinadze, A.S. and Ponkratov, D.V. (2005). Numerical Study on Interaction Effects in the Pod Propulsive System. Proceedings of the International Workshop on Ship Hydrodynamics IWSH'2005, Shanghai, China, pp 56-67.

Krasilnikov, V.I., Ponkratov, D.V., Achkinadze, A.S., Berg, A. and Sun J. (2006). Possibilities of a Viscous/Potential Coupled Method to Study Scale Effects on Open-Water Characteristics of Podded Propulsors. Proceedings of the Second International Conference on Technological Advances in Podded Propulsion T-POD 2006. L'aber Wrac'h, France (CD-version).

Krasilnikov, V.I., Achkinadze, A.S., Ponkratov, D.V. and Sun, J. (2007a). Prediction of Open Water Characteristics of Podded Propulsors Using a Coupled Viscous/Potential Solver. Proceedings of the 9th International Conference on Fast Sea Transportation, FAST2007, Shanghai, China.

Krasilnikov, V.I., Zhang, Zh., Hong, F., Ponkratov, D.V. and Sun, J. (2007b). Steady Analysis of Viscous Flow around Ducted Propellers: Validation and Study on Scale Effects. Proceedings of the 9th International Conference on Fast Sea Transportation, FAST2007, Shanghai, China.

Kuiper, G. (1992). The Wageningen Propeller Series. MARIN Publication 92-001, May.

Menter, F.R. (1994). Two-equation Eddy-Viscosity Turbulence Models for Engineering Applications, AIAA-Journal, Vol. 32.

Stierman, E.J. (1984). Extrapolation Methods for Ships with Ducted Propeller. International Shipbuilding Progress, Vol.31, No.356.

Zhao, R. (2000). Ducted Propeller Computer Program Development (SKIPRO2001). Verification Tests in Open Water Condition. MARINTEK Report No. 603526.00.01, December, 2000.

Optimization of the Bilge Keel for Short Vessel at Wide Speed Range

Marek Kraskowski

Ship Design and Research Centre S.A., Poland
marek.kraskowski@cto.gda.pl

The paper presents the procedure of the bilge keels design for a 27m research vessel, carried out by means of CFD. The problem was posed as follows:
− The ship operates both at low speed (survey speed) and high speed (transit speed).
− The existing, poorly fitted bilge keels disturb the flow both at low speed, causing the noise interfering with the signal captured by the scientific equipment, and high speed, causing additional resistance and propeller cavitation (due to strong vortex detaching from the end of the keel, interacting with the propeller).
− New bilge keel is to be designed, so as to obtain the best possible compromise, i.e. proper operation in the widest possible speed range.

The following, obvious problems appear in this task:
− The streamlines at survey speed (Froude number ~0.1) and transit speed (Froude number ~0.35) are expected to be significantly different, so the longitudinal range and the run of the bilge keel must be chosen very carefully, in an iterative manner.
− Relatively high Froude number of the vessel at transit speed requires taking into account the dynamic trim and sinkage of the hull, as the changes in trim and draft can significantly influence the streamlines direction in the region of the keels' location.
The method for free hull computations, as well as the approach for the bilge keels design, are described here.

A program allowing for the CFD computations with taking into account the dynamic trim and sinkage (extended user programming for RANSE flow solver COMET) was being developed in CTO in 2004 and 2005, and first results obtained for the test cases were presented in NuTTS'05 in Varna (*Kraskowski, 2005*). Since then, the procedure was somewhat modified, and the program is now used as a standard commercial tool. Major features of it are described below.

Evaluation of the dynamic trim and sinkage of the hull is realized by solving the Newtonian motion equations, using the forces computed by the flow solver. The mesh is rigid, and is moving continuously together with the hull until the equilibrium of forces acting on the hull is obtained.
Because only a steady-state solution is important here, strong damping is applied to the hull motion in order to speed up the convergence. The solution is obtained in three major steps:
− Flow computations for fixed hull, realized until the vertical force and pitching moment acting on the hull become approximately constant.
− Releasing the hull motion in two degrees of freedom (heave, pitch) and further flow computations coupled with evaluation of the dynamic trim and sinkage. This stage is continued until the hull position (draught and trim) converge.
− Fixing the hull again in its dynamic trim and draught and continuation of the computations until final convergence of the forces acting on the hull. This third step is necessary, because the resistance force usually oscillates strongly during the computations for free hull.

Procedure of the computations for free hull (second step) is described in detail, sample solutions are also given.

The motion equations are solved in the coordinate system connected with the hull centre of gravity, advancing together with the hull but not rotating. The numerical method for solving the flow is as follows.

- Compute the linear and angular acceleration in current time step, using the forces computed by the flow solver in the previous time step. For faster convergence, introduce artificial damping, proportional to the velocity:

$$a_t = \frac{F_{t-1}}{m} - \alpha \cdot v_{t-1} \qquad\qquad \varepsilon_t = \frac{M_{t-1}}{I} - \beta \cdot \omega_{t-1}$$

- For stability, average the acceleration values using the values from previous time step (*Azcueta, 2001*):

$$a_t' = 0.5 \cdot (a_t + a_{t-1}) \qquad\qquad \varepsilon_t' = 0.5 \cdot (\varepsilon_t + \varepsilon_{t-1})$$

- Compute the velocity values by adding the velocity increment to the velocity value from previous time step. For faster convergence, the velocity increment is multiplied in each time step by a "delay factor" (*Azcueta, 2001*), lower then 1.

$$v_t = v_{t-1} + DF_v \cdot a_t \cdot \Delta t \qquad\qquad \omega_t = \omega_{t-1} + DF_\omega \cdot \varepsilon_t \cdot \Delta t$$

- Compute the actual position of the hull, by adding the angle and draught increments to the current values:

$$z_t = z_{t-1} + v_t \cdot \Delta t \qquad\qquad \varphi_t = \varphi_{t-1} + \omega_t \cdot \Delta t$$

The sample history of the hull motion during computing its dynamic trim and sinkage (accelerations, velocities, trim and draught changes) is presented in figure 1. First 40 seconds of the simulation were carried out for fixed hull, so the velocity and displacement values are zero. After 40 seconds, the hull was released – the acceleration values quickly decrease, and the velocity increases rapidly at the beginning and then tends slowly to 0. The draught and trim tend to stable oscillation around constant values.
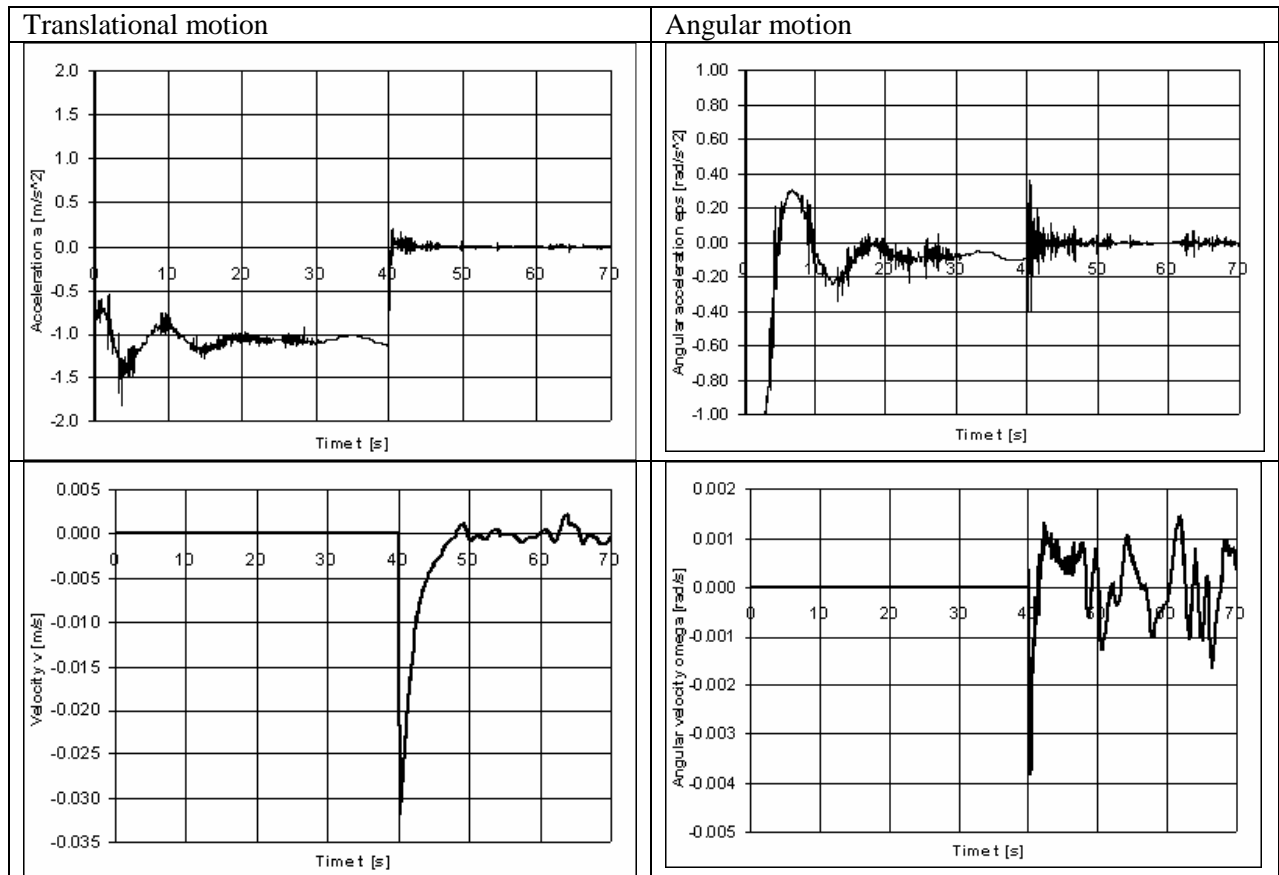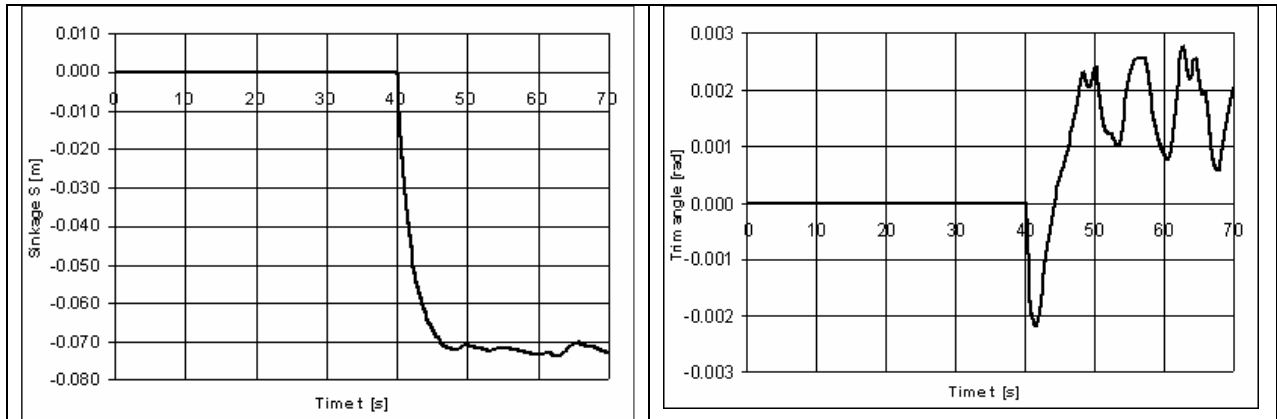
Fig. 1 Sample history of the hull motion.

In this particular case, the tendency to trim is very low, which results in large relative error of the trim angle evaluation (amplitude of the oscillations is comparable with mean value), however, absolute values of the oscillations are small and the accuracy can be considered sufficient for proper prediction of the streamlines direction.

An example of the solution for fixed hull and the solution for the evaluated trim and sinkage is presented in the figure 2 (Olympic canoe was chosen as an example, because the change in wave pattern and hull position is clearly visible here).

Flow for fixed hull	Flow for free hull in equilibrium condition
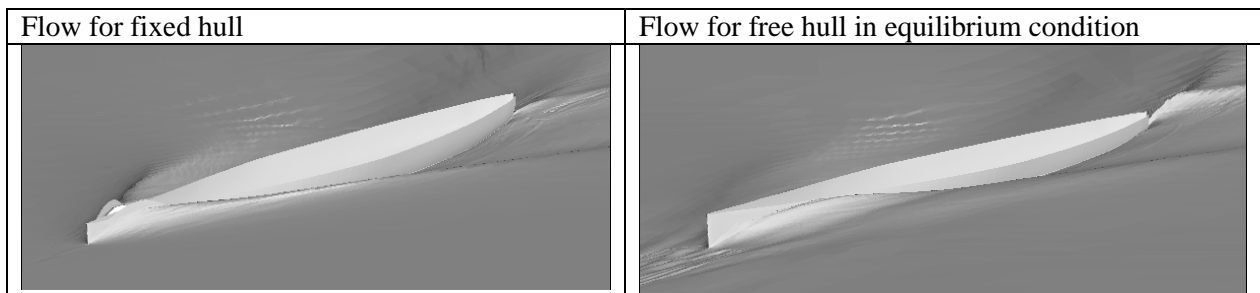
Fig. 2 Solution for fixed hull and for evaluated trim and sinkage

The procedure of bilge keel design started with the flow computations for bare hull at two specified speeds: survey speed (3 knots) and maximum transit speed (11.5 knots). Results of these computations – wave pattern and streamlines – are presented in figure 3 (the dynamic trim of the hull was close to 0, noticeable sinkage can be observed for 11.5 knots).

Results for 3 knots	Results for 11.5 knots
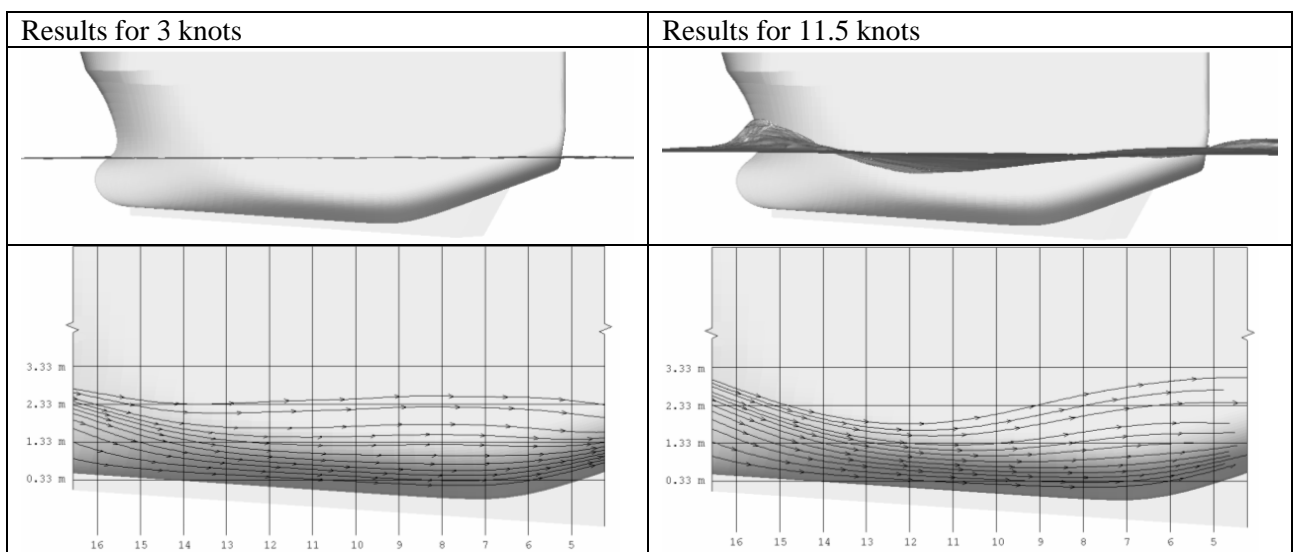
Fig. 3 Results of the computations for 3 knots and 11.5 knots

As it was expected, the difference between streamlines at 3 knots and 11.5 was so large that the reasonable compromise in the bilge keel run was considered not probable. Nevertheless, initial designs for 3 knots and 11.5 knots were done and checked at opposite speeds (design for 3 knots at 11.5 knots and vice versa). Better results were obtained for the keel designed at 3 knots and checked at 11.5 knots – the flow was approximately aligned with the keel in its fore part and detached in the aft part.

An attempt on the "averaged" bilge keel run could result in poor flow in the entire speed range, so it was decided to focus on low speed, hoping that the keel designed for 3 knots will perform correctly in wider speed range that the one designed at 11.5 knots. In order to verify this idea, the streamlines were evaluated at medium speed (8 knots). The streamlines close to free surface at 8 knots are obviously significantly different due to free surface deformation (at 3 knots, it is almost flat), however, close to the required bilge keel location, the streamlines turned out to be almost the same as at 3 knots. Results for 3 and 8 knots are compared in figure 4.
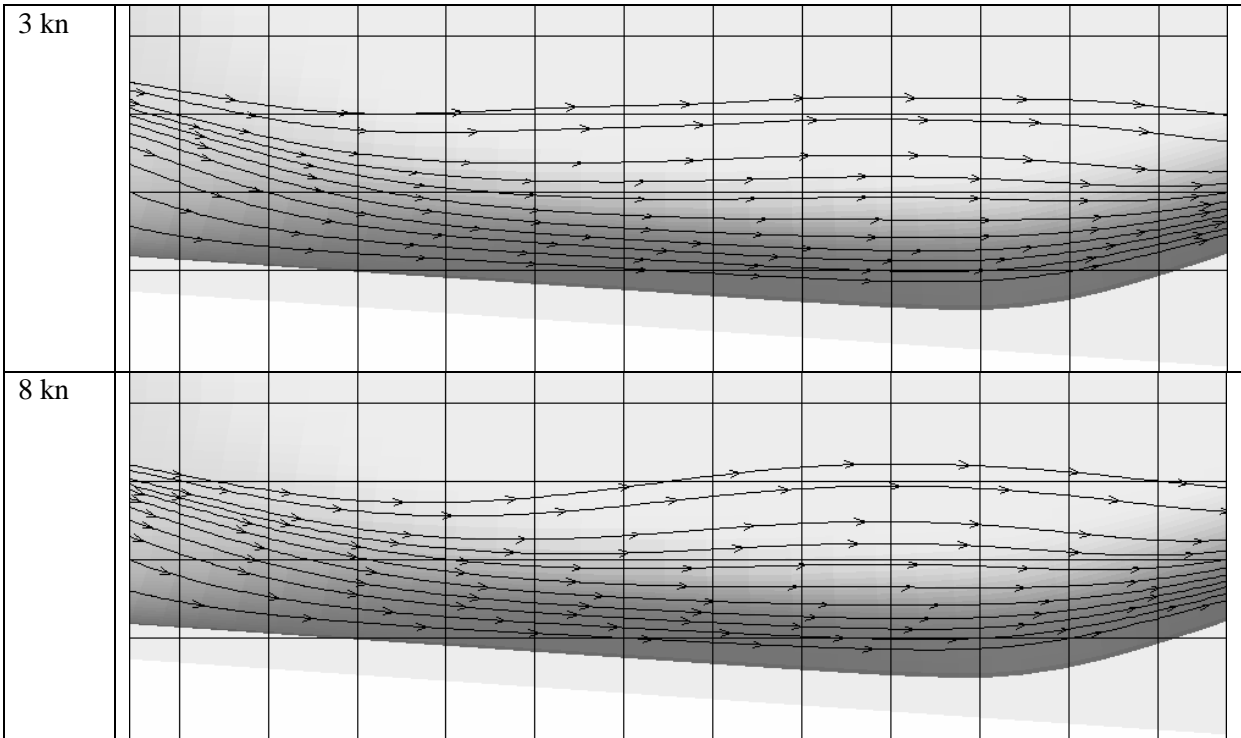
Fig. 4 Streamlines at 3 knots and 8 knots

After evaluation of the flow for 3 speeds, it was suggested to the customer that the bilge keel should be designed for low speed rather than looking for a compromise, because such a keel will perform perfectly at 3 knots and correctly in quite wide range of lower speed values, without a risk of poor performance in the entire speed range. A question then appeared, what would be the exact range of speed, in which the keel performance could be considered acceptable, and it was mentioned that the contract speed of the ship is somewhat lower than the maximum speed mentioned previously and equal to 10.3 knots.

Thus, an attempt was made on a slight compromise, expected not to spoil the flow at 3 knots and to allow for widest possible range of proper operation of bilge keel. Thus, the bilge keel was designed once more, based again on the streamlines at 3 knots but with taking into account the tendencies of the streamlines deformation at increasing speed. Figure 5 shows the streamlines at 3 and 11.5 knots, defined as the distance from the box keel to the bilge keel, measured along the shell plating.

Streamlines at 3 knots	Streamlines at 11.5 knots.
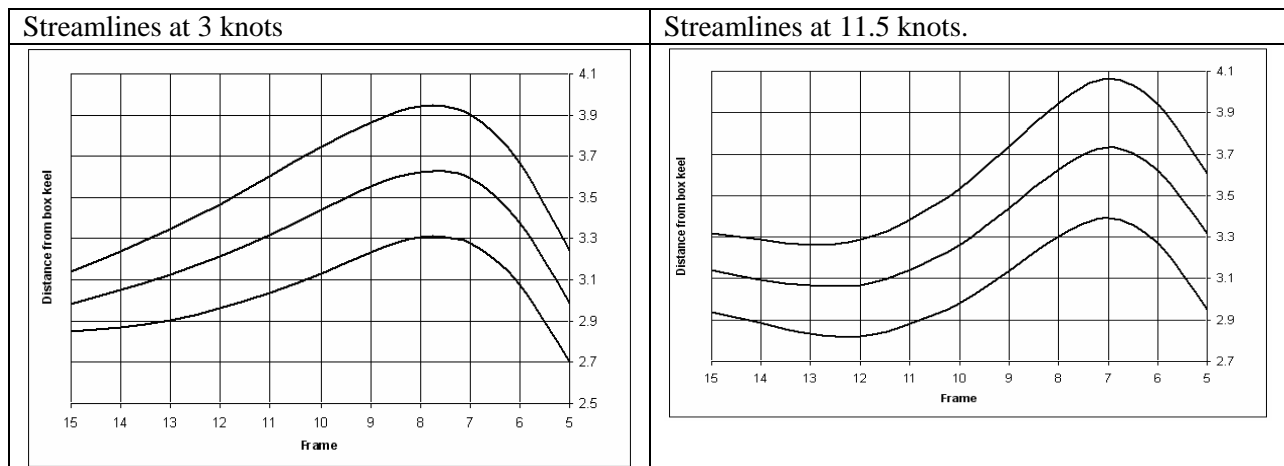
Fig. 5 Streamlines at 3 knots and 11.5 knots.

The following tendency in the streamlines direction can be observed at increasing speed:
- In the fore part, the angle of attack is increasing at higher speed due to increasing bow wave height.
- In the aft part, the streamlines are straightening at higher speeds.

The new designed bilge keel run was aligned with the streamlines at 3 knots on almost entire length of the required bilge keel range, but slightly raised in the fore part and straightened in the aft part. The final shape was obtained in 3 iterations, each shape was tested at 3 knots and at contract speed 10.3 knots. It was assumed that the flow at 11.5 knots will be disturbed anyway, and that the acceptable flow at 10.3 knots would be a satisfactory result. The run of the finally designed bilge keel is presented in figure 6.
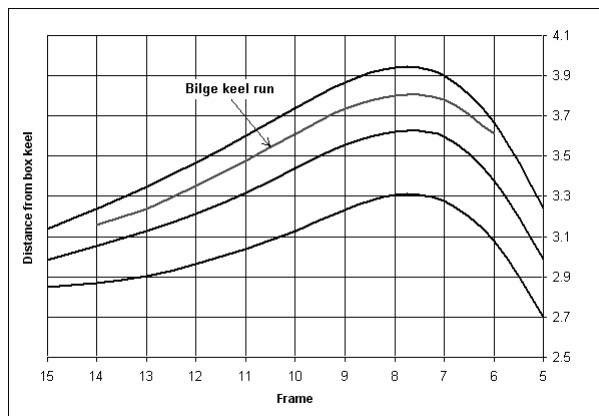
Fig. 6 Bilge keel design

One important thing in the design process was the bilge keel quality criterion. During the process of modifications, the bilge keel quality was evaluated basing on three streamlines, released just behind the leading edge of the keel: one located close to the tip, and two located close to the hull plating, on both sides of the keel.

Final design was checked basing not only on the streamlines, but also on the pressure distribution on the hull surface and velocity field in chosen transversal planes crossing the bilge keel. It was assumed that perfectly designed bilge keel should not generate vortices on the tip or affect the pressure distribution on the hull. The results for 3 knots and 10.3 knots are presented in figure 7. The pressure distribution is not presented, because the details would not be visible in black and white contours.

Results for 3 knots	Results for 10.3 knots
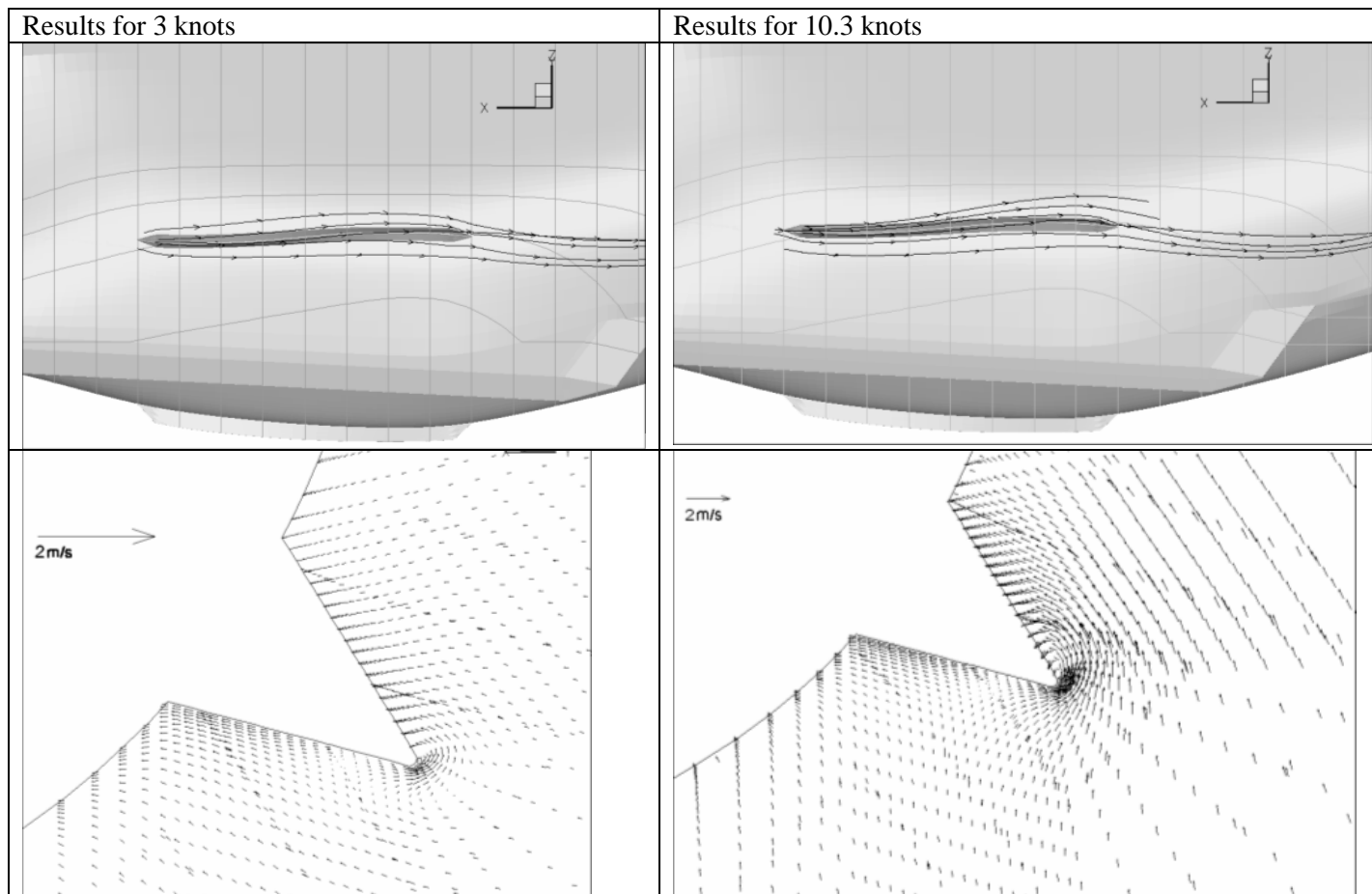
Fig. 7 Results of control computations.

Although the cross-flow at the end of the bilge keel is quite strong, the final bilge keel shape can be considered a reasonable compromise. It was further suggested to the customer to shorten the keel in its aft part by 1 m, as the serious flow disturbance at 10.3 knots appears only at the end of the keel. The customer accepted shortening the bilge keels and the bilge keels are currently under construction, so, hopefully, full-scale verification of the bilge keels performance will be possible soon.

The following conclusions can be done basing on the presented analysis:
 – The elaborated method for solving the free surface flow for the ship hull, free to trim and sink, including strong artificial damping, turns out to be robust and accurate enough for current applications of CFD in CTO, which are comparisons of different hull versions in respect of resistance, and qualitative flow evaluations, e.g. streamlines.
 – In this particular case, the streamlines curvature in the region of required bilge keels location turned out to be approximately constant in wide range of speed, starting from the lowest speed, and change rapidly only at the speed close to maximum. Thus, it was reasonable to focus on lower speeds.
 – Unlike the bilge keels design for one specified speed, which can be easily done during standard model tests at very low cost, the iterative design for wider range of speed should be performed (at least at preliminary stage) with the use of CFD, as it requires many iterations.

References:
[1] Azcueta R., 2001, *"Computation of Turbulent Free-Surface Flows Around Ships and Floating Bodies"*, PhD thesis
[2] Kraskowski M., 2005, *"Computation of theviscous free-surface flow around the ship model free to trim and sink"*, NuTTS'05.

Computation of flows around wetted transom sterns with a potential flow code

Jörn Kröger, Johannes Will, Ole Hympendahl, Thomas Rung

Institute for Fluid Dynamics and Ship Theory (M-8), TU Hamburg-Harburg

joern.kroeger@tu-harburg.de, johannes.will@tu-harburg.de
o.hympendahl@tu-harburg.de, thomas.rung@tu-harburg.de

1 Motivation

The transom stern of a typical merchant ship can be partially submerged in specific loading conditions. At low speed, a dead water may form behind the transom. The dead-water region is associated with viscous pressure losses and significantly influences the wave pattern and the resistance.

Potential codes are sufficient to calculate the wave resistance but cannot predict viscous effects from first principles. Instead they often apply empirical expressions for the viscous resistance. The present work aims to extent an inviscid calculation procedure by an empirical dead-water model.

2 Concept of Dead-Water Models

To address the annotated disadvantage, the dead-water zone can be incorporated into a potential flow procedure using an empirical model. Several similar methodologies have been developed in the automotive industry. The conceptual idea of these approaches is to subdivide the physical domain into three zones [4], i.e. an inviscid exterior flow field, an attached boundary layer and a dead-water zone covering massive tail-flow separation. The inviscid exterior flow field is predicted with potential codes. Boundary-layer effects are usually computed from appropriate boundary-layer methods, but neglected in the context of the present work. The basic principle of all dead-water models is to replace the complex dead-water flow by simple, idealized correlations. In particular, the models do not provide any information about the flow inside the dead water itself, but focus upon the interaction of the inviscid flow with the dead-water zone. The building blocks of the model are the displacement of the invisicd flow by the shape of the dead-water region and the base-pressure acting on the interface between the transom stern and the dead-water zone. Supplementary, the modification of the wave field has to be considered.

The next present section briefly describes the original model and the employed modifications required to perform ship-hydrodynamic investigations. The 4th section outlines the results of the validation for transom stern vessels.

3 Dead-Water Model for Ship Hydrodynamics

The present study refers to a dead-water model originally developed by Kim [3]. The model has initially been developed for immersed blunt 2D-bodies in single-phase flows. In this work, the method has been adapted to flows with a free surface and extended to 3D wake flow geometries.

The coupling procedure between the dead-water module and the baseline algorithm can be summarised as follows:

1.) the dead-water is represented by an additional body attached to the original hull throughout the inviscid calculation. The inviscid exterior flow around the hull and the dead-water zone is updated in each outer iteration.

2.) the shape of the dead-water body is updated in inner iterations. Prior to the the first outer iteration, the dead-water zone is assigned to an initial shape.

3.) the outer iterations are iterated towards a converged inviscid flow field

3.1 2D-Model

The 3D dead-water body is constructed from a 2D-baseline shape in the centerplane at the stern. The employed 2D dead-water model of Kim utilizes a sinusoidal shape function to define the pressure distribution along the boundary between dead water and flow and the initial shape of the dead-water zone in the centerplane.
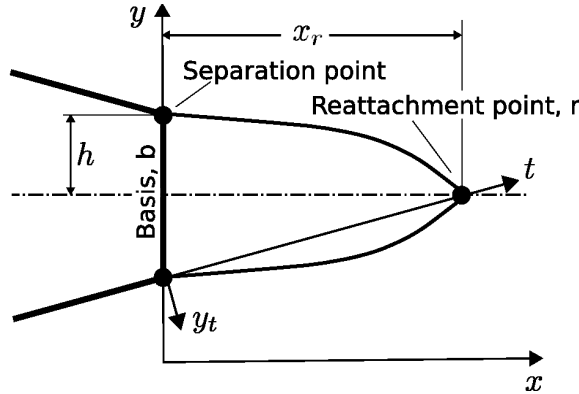
Figure 1: Dead water shape behind a blunt 2D body (side view).

Figure 1 illustrates a side view of the dead-water geometry. The longitudinal position of the reattachement point x_r defines the length of the dead-water zone. The pressure is assumed to vary only in longitudinal direction. The empirical correlation for the pressure distribution (3.1) depends on the pressure coefficient $c_{p,r}$ at the reattachment point r, its longitudinal position x_r and an amplitude factor A_1, viz.

$$c_p(x) = c_{p,r} - A_1\Big(1 - \sin\frac{x}{x_r}\Big). \tag{3.1}$$

The reattachment pressure coefficient follows from an expression (3.2) of Gersten (see Dilgen [1]) which links the pressure coefficient at the reattachment point to the pressure coefficient $c_{p,b}$ at the blunt basis of the body, viz.

$$c_{p,r} = 0.333 + 0.667 \cdot c_{p,b}. \tag{3.2}$$

According to Kim, the pressure at the basis is assumed to be equal to the pressure on the surface of the body immidiately upstream of the basis. The respective 3D approach is based on an average of the wetted part upstream the basis. Moreover, the amplitude factor A_1 can be approximated [1] via

$$A_1 = \frac{1}{2}(c_{p,r} - c_{pmin}) \quad \text{with} \quad c_{pmin} = 1.25(c_{p,b} - 0.2) \ . \tag{3.3}$$

To obtain the initial shape of the dead water, the position of the reattachment point must be specified. In the present proposal, the dead water length x_r simply depends on the height h of the basis multiplied by an empirical constant $\alpha := x_r/h$. The construction of the 2D shape is based on a straight line t between the separation point at the basis and the reattachment point (c.f. Fig.1). Subsequently, the sine-function (3.4) is superimposed which defines the dead water shape according to Kim

$$y_t = A_m \cdot \sin(\pi t^n) \ . \tag{3.4}$$

The constant A_m scales the sine-function. In the present work this factor is assigned to half the height of the basis. According to Kim the exponent n is set to 1.

3.2   3D-model

The 2D-model needs to be modified in order to be applicable at the transom of a vessel. Firstly, the symmetry plane in Figure 1 is assumed to be a fair approximation of the free surface. Secondly, the vertical position of the reattachment point is determined by the dynamic boundary condition at the free surface. In order to make use of the 2D model outlined in section 3.1, the draft along the centerline of the immersed transom replaces the above mentioned height h of the blunt-body basis. Thus, the pressure distribution and the (2D) shape of the dead water along the centerline are known as functions of the pressure and the draft at the stern.

As depicted by Figure 2, the extension of the 2D model to 3D geometries assumes that the shape of dead-water sections, which lie parallel to the transom, is geometrically similar to the shape of the transom itself. The initial shape is manipulated by moving the panels of the dead water body until the pressure distribution at centerline over the length of the body matches the pressure distribution according to Kim (see Fig.3).
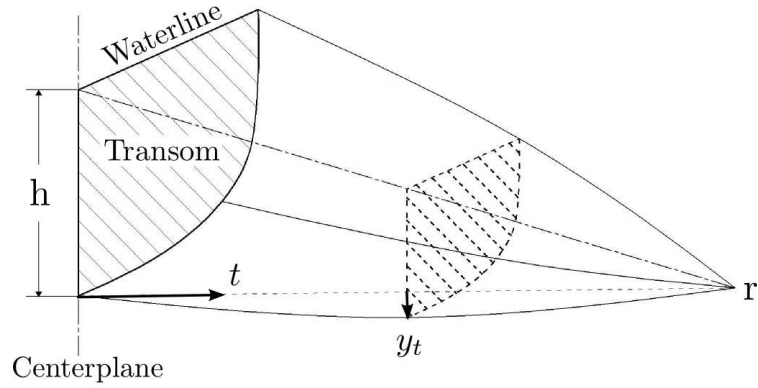
Figure 2: Schematic of the shape of the dead water body in 3D.
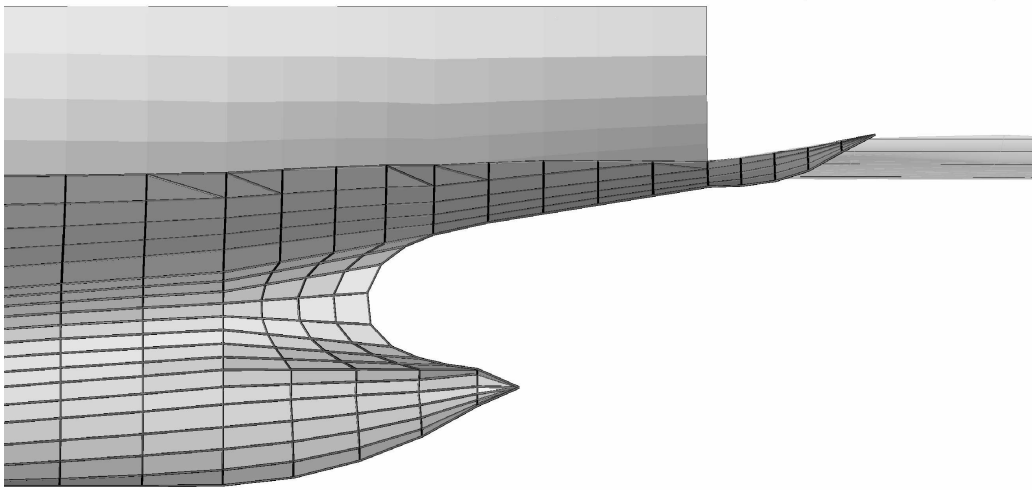
Figure 3: Hull with appended dead-water body at 20 knots ($\alpha = x_r/h = 7$).

4   Results and Validation

The present study supplements a companion experimental study of [2] on the resistance of wetted transom stern flows. The resistance and the wave pattern have been computed for several speeds in line with the experiments. Calculations have been performed with an inhouse stationary potential-flow code using the dead-water model (indicated by DW) and the baseline approach without dead water (indicated by noDW).

Figures 4.a and 4.b display the typical evolution of predicted wave patterns with and without the dead-water model. The predictons show significantly higher waves than the experiments. The computed wave pattern obtained from the dead-water model matches the experimental pattern much better than baseline predictions without dead water.
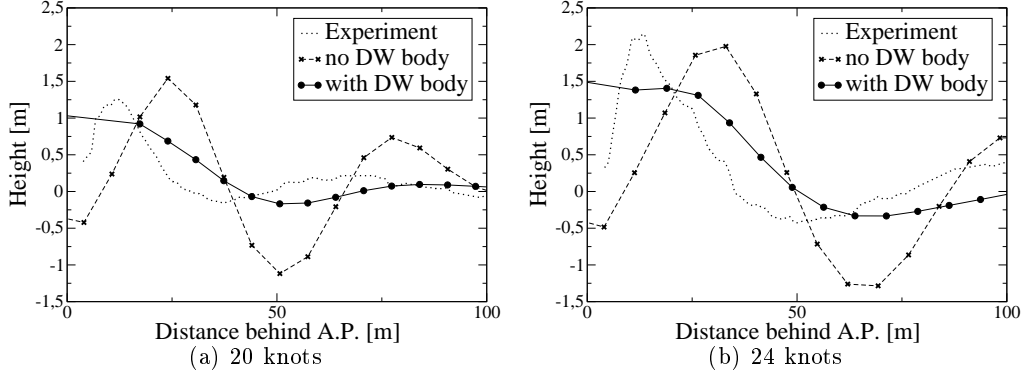
Figure 4: Comparison of predicted and measured wave pattern at the centerplane for 20 and 24 knots ship speed.

Table 1 summarizes the residual resistance coefficient obtained with and without the dead-water model together with the results of the experiment. As expected, results obtained without the dead-water model substantially underpredict the resistance of the hull. When compared to the baseline approach, the dead-water model returns an improved predictive accuracy with respect to the resistance predictions. However, the degree of predictive improvements depends on an appropriate choice of $\alpha = x_r/h \in [1,10]$. The tabulated results are optimal results obtained with different constants α and reveal the potential of the methodology, when used with appropriate parameters.

v [kn]	$c_{r_{noDW}}$	$c_{r_{DW}}$	$c_{r_{ex}}$	$c_{r_{noDW}}/c_{r_{ex}}$	$c_{r_{DW}}/c_{r_{ex}}$
20	0.0003566	0.0004528	0.0004624	0.771	0.979
24	0.0006041	0.0007327	0.0007361	0.821	0.995

Table 1: Comparison of experimentally observed residual resistance coefficients with predicted values obtained with and without dead-water model.

5   Outlook

A procedure to account for dead-water zones behind transom sterns has been implemented into a potential flow code. The appraoch has proven to be robust. Although the model refers to data obtained from 2D experiments without a free surface, it seems to be applicable to free-surface flows.

Results obtained with the present dead-water model are superior to baseline computations with respect to the predicted wave pattern and residual resistance coefficient. The encouraging performance motivates further investigations to optimize the parameterization of the dead-water model for hydrodynamic applications.

References

[1] DILGEN, Peter G.: *Berechnung der abgelösten Strömung um Kraftfahrzeuge: Simulation des Nachlaufes mit einem inversen Panelverfahren*. VDI Verlag, 1994 (Fortschrittsberichte VDI, Strömungsmechanik)

[2] HYMPENDAHL, Ole: *Experimental Investigation and Potential-Flow Coputation of Transom Stern Flows*. NuTTS – 10th Numerical Towing Tank Symposium, Hamburg, 2007

[3] KIM, Moo S.: *Berechnung zweidimensionaler Körperumströmungen mit Totwasser und Relativbewegung gegenüber einer Berandung*. Shaker, Aachen, 1993 (Reihe Maschinenbau)

[4] PAPENFUSS, Heinz-Dieter: *Theoretische Kraftfahrzeug-Aerodynamik - die Struktur des Strömungsfeldes bestimmt das Konzept*. Bd. 99. 1997. – 100 – 107 S.

Simulation of a Free Falling Wedge into Water with Applications in the Prediction of High-Speed Craft Motions

Simon G. Lewis, Dominic A. Hudson, Stephen R. Turnock

Fluid Structure Interactions Research Group, School of Engineering Sciences,

University of Southampton, Southampton, SO17 1BJ, UK, s.r.turnock@soton.ac.uk

1. Introduction

Small boats are often required to operate at as high a speed as possible. The crew experience repeated shocks and vibration, which can lead to a reduction in their physical and mental performance. Accurate prediction of the motions of high speed craft is an essential element in understanding the response of the crew to a particular design configuration. Previous work has been conducted using a non-linear potential flow model.

The problem of predicting planing craft performance and motions is currently solved using one of two principal methods:

- a potential flow solution focusing on predicting wedge impact forces,

- computational fluid dynamics (CFD) solving the full three dimensional (3D) Reynolds averaged Navier Stokes equations (RANSE).

The first numerical method uses a two dimensional (2D) potential flow theory to calculate the forces associated with wedge entry in order to evaluate the added mass and damping terms in the equations of motion.

The second numerical method, using CFD, has been applied to solve the motions of sailing yachts (Azcueta, 2002), planing craft (Azcueta, 2003) and ships in waves (Sato, 1999), with good results. The computational cost of such simulations is significant, despite continual increases in computational power. When predicting the motions of a planing craft in waves, Azcueta (2003) states that a 2s simulation had a processing time of 33 hours on a single processor computer.

Another possible method to predict high speed craft motions is to introduce a hybrid model making use of both a RANSE method and the 2D strip theory discussed by Lewis et al (2006). A simulation that predicts wedge impacts accurately with 2D CFD can be developed and a series of wedges applied to create a 3D hull. Overall craft motions may then be calculated in a similar manner to the 2D potential solver.

A numerical model is used to predict the motions of a planing craft in both regular and irregular waves. The model is based on non-linear strip theory, through calculation of the forces occurring on wedge impact (Zarnick, 1978).

2. CFD Techniques

There are a number of methods that can be applied to simulate a wedge impacting with water. One method incorporates a moving mesh, where the mesh is attached to the surface of a ship and deforms as the ship moves. The grid system is also fixed to the free surface. This approach is adopted by Akimoto (2002) and Ohmori (1998). Sato et al (1999) note that this method cannot cope readily with large amplitude motions. Another method used to predict ship motions using CFD is to use a fixed co-ordinate system introducing the body forces on the ship into the external forces component of the Navier-Stokes equations. This method is adopted by Sato et al (1999).

This investigation uses a commercial RANSE solver (Ansys CFX, 2007) to calculate wedge impacts with water. A body-fixed mesh is used, and the movement of the body is realized by altering the level of the free surface. For the case of a 2D wedge impact, only one degree of freedom is investigated: the vertical motion. The lower boundary of the computational domain is defined as an opening and the water inflow velocity is set as the instantaneous wedge vertical velocity. This method of simulating wedge impact has

the advantage of requiring only one mesh, which can be refined in areas of interest, such as the apex of the wedge and the water jets expected as the water level rises. A high density of mesh cells is required in the vertical direction so that the mean free surface location is well captured. The timestep is chosen ensuring that the maximum Courant number is approximately 1. The Courant number is a non-dimensional variable that is defined as the ratio of the distance the flow moves in each time step to the number of mesh elements that are crossed over this distance. The flow at critical locations, such as the wedge apex, will therefore have a Courant number of much less than 1.

2.1 Turbulence Models

For the required typical small boat slams the flow along the wedge will be viscous. The typical Reynolds number for wedge entry, calculated from data presented by Yettou et al (2006) is $6x10^6$. A suitable turbulence model is required to close the Navier-Stokes equations. Three approaches are investigated to examine the dependence on the method of closure. Initially, the default k-ε turbulence model is used, as it is well known and understood. The two equations governing this turbulence model can be found in Launder and Spalding (1974).

The k-ε model is sensitive to the near-wall grid resolution which is assessed in the dimensionless wall unit y+, which for an unsteady flow is time varying. The near-wall resolution should be such that y+ is always greater than 30 (WS Atkins, 2003). An improvement to the k-ε model is the Renormalization-Group-Based (RNG) k- ε model. This has an additional term that significantly improves the accuracy for rapidly strained flows, making it more accurate for a larger range of flows than the standard k- ε model.

The shear stress transport (SST) k-ω model was developed by Menter (1994). This model provides an enhanced near wall simulation but requires the first mesh cell to have a $y^+ \approx 1$. All the models require the specification of k and either ε or ω on the inlet boundaries, for which the default solver values were used.

2.2 Computational Time

The computational time is dependant on the number of mesh elements, the number of time steps and the desired solution accuracy. The computer used to solve the simulation has a Pentium 4, 3.2 GHz processor, with 2Gb of random access memory. With a coarse grid containing around 9000 elements, to solve a flow in about 500 time steps takes approximately 2.5 hours. For these calculations convergence at each time step was deemed to have occurred when the mass residual for this particular simulation was less than an RMS value of $5x10^{-6}$.

3. Free Falling Wedge Entry

The initial investigation assumed that the impact velocity of the wedge was constant, that is to say, on actual impact the induced force did not reduce the imposed velocity. The simulation was then altered to allow the velocity of the wedge to change during impact. The computational domain is set as a multi-phase problem containing ideal air and water. Ideal air is considered to be a compressible homogeneous fluid by the solver. It has isothermal properties, meaning that the pressure is directly proportional to the density. The amount of each substance in each cell is defined by a volume fraction for that cell. The inflow at the bottom of the computational domain is defined as having a water volume fraction of 1, and an air volume fraction of 0. The RANSE solver locates the level of the free surface by determining the position within a cell that has a volume fraction of 0.5 for each substance.

3.1 Simulation

Initially, a 2D wedge impact is simulated in calm water. The commercial RANSE solver does not support true 2D flow, although a 3D mesh can be constructed that is one cell thick. In effect this is a 2D mesh as there is no flow in the direction of the third dimension. A structured coarse mesh is constructed to enable the overall simulation to be initialised and results obtained relatively quickly. The coarse mesh for a wedge with a deadrise angle of 25° is presented in figure 1.
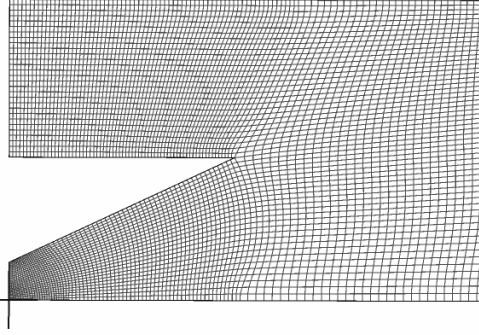
Figure 1: A coarse mesh of a 2D wedge.

The upper boundary is modelled as an opening with an atmospheric pressure condition applied. The boundary on the left side of the domain is a symmetry plane allowing the simulation of half the wedge and therefore reducing the computational time taken to solve the problem. The wedge itself is modeled as a smooth wall, with a no slip condition. The simulation is carried out for varying mesh densities and turbulence models.

The simulation of a free falling wedge requires the inflow velocity to vary according to the vertical force (F) on the wedge. In order to calculate the new velocity (W_{NEW}), the velocity (W_{OLD}) at the previous time step (t) must be known. A FORTRAN program was integrated within the CFD simulation. At each time step the total vertical force acting on the wedge is known and using the wedge mass, a new velocity can be found as:

$$W_{NEW} = W_{OLD} + \left(g - \frac{F}{M} \right) \Delta t \; , \qquad (1)$$

where g is acceleration due to gravity, and M is the mass of the wedge.

As the necessary timestep for the CFD simulation is sufficiently small a simple first order calculation is suitably accurate.

3.2 Experimental Data

In order to analyse the predicted impact it is important to know the pressure distribution along the length of the wedge, as well as time histories of the impact pressures. Yettou et al (2006) conducted experiments on a free falling wedge. Parameters such as the drop height, deadrise angle and wedge mass are varied. Pressure is measured using 12 transducers distributed evenly along the

wedge as illustrated in figure 2. The transducers are numbered from 1 near the wedge apex, to 12 near the edge of the wedge. Wedge position and velocity are also measured.
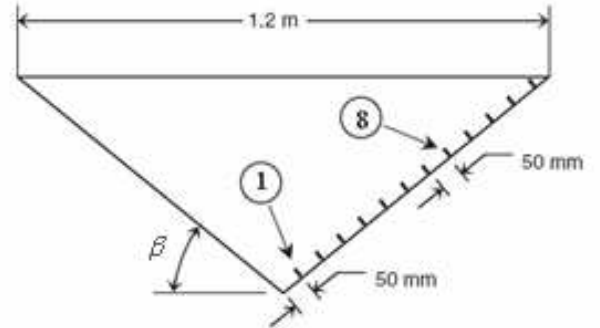
Figure 2: Experimental wedge used in drop tests, showing the pressure transducer positions and numbering system (adapted from Yettou et al, 2006).

These experimental data are used to validate the free falling wedge simulation described in section 4. Although different experiments with a variation in parameters such as drop height and wedge mass were conducted, one case in particular is analysed, as the pressure distribution on the wedge during impact is presented by Yettou et al (2006). A wedge with a mass of 94kg and a deadrise angle of 25° is dropped from a height of 1.3 metres. The impact velocity can be calculated to be 5 m/s.

4. Results

Initial inspection of the results is conducted in a qualitative manner. The free surface is inspected to ensure that a reasonably sharp interface is predicted with a rapid variation of volume fraction across 3 to 5 cells only. Figure 3 illustrates a typical free surface mid way through a simulation for the coarse mesh showing a contour plot of the water volume fraction. This was deemed acceptable with clear identification both of the wedge jet and mean water level.
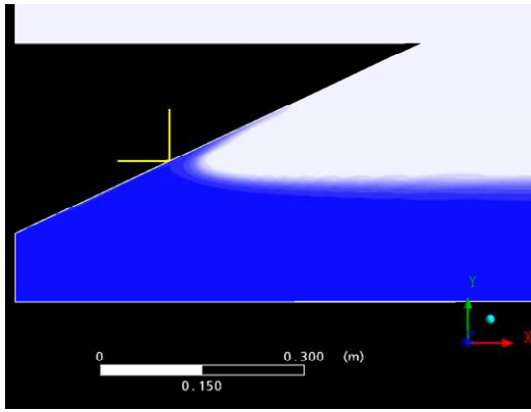
Figure 3: Contour plot of the water volume fraction illustrating the free surface.

The effects of turbulence model and other modelling parameters are investigated using a coarse mesh containing 9000 cells (illustrated in figure 1). There is only a slight difference between the k-ε, k-ε RNG and SST turbulence models. The best results are obtained using the k-ε model with real air and with the solver set to double precision.

The effects of the number of mesh elements on the results are also studied. The experimental pressures measured by Yettou et al (2006) are assumed to be averaged over the diameter of the pressure transducer (19mm). Figure 4 presents a comparison of peak pressures, and averaged pressures at transducer 1. With a fine mesh containing 52000 cells, the averaged pressure gives a more accurate prediction of the experimental value than the peak pressure at the same point.

As the number of cells in the mesh is increased, the accuracy of the prediction of pressure along the wedge increases. It must be noted that this increase in accuracy is accompanied by an increase in computational cost.
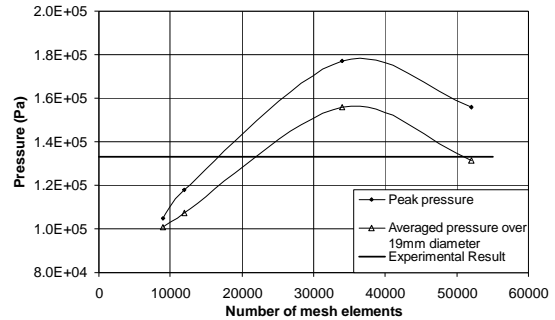
Figure 4: Comparison between peak and averaged pressures for different mesh densities.

Figure 5 presents the computed prediction of the pressure distribution along the wedge at 4 different times. These times correspond to the maximum pressure experienced by transducers 1, 3, 5 and 6. The time is set to zero when the wedge first touches the water. It is noted that each pressure transducer has a diameter of 19mm. Therefore the average maximum pressure over a 19mm section of the wedge must also be considered. The peak pressures are presented in figure 9 as well as the average maximum pressure at the position of each transducer.
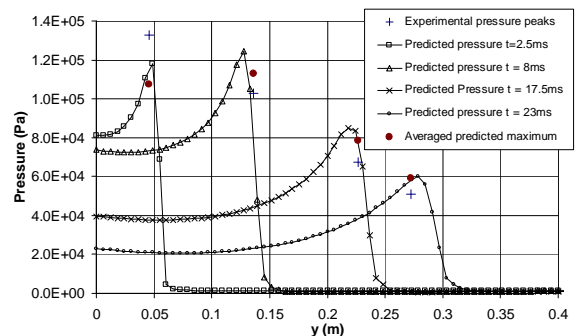
Figure 5: Predicted pressure distribution along the wedge face, with averaged maximum pressure and experimental data.

Peak pressures are under-predicted near the wedge apex, as is the averaged pressure. The pressures are over predicted as the water jet travels up the wedge and the averaged pressure follows the same trend, although with increased accuracy.

Although the pressure time history for each transducer is presented by Yettou et al (2006), the data is only given for the peak pressures. Figure 6 illustrates an adapted graph of the pressure time history presented by Yettou et al (2006). This can be compared with figure 7, the predicted pressure time histories at

transducers 1, 3, 5 and 6. The graphs presented in figure 11 have the same vertical axis scale as those illustrated in figure 10. Over predicted peak values cannot be deduced from figure 7, but are presented in figure 5. The time that each impact occurs is well predicted.
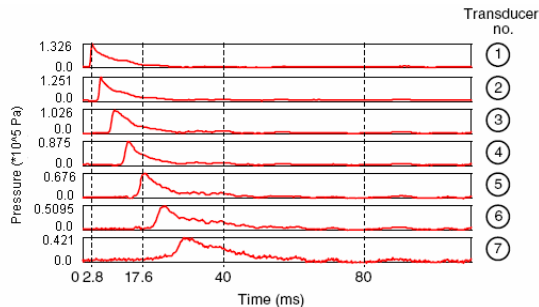
Figure 6: Graph of pressure time histories for transducers 1-7 (adapted from Yettou et al, 2006).
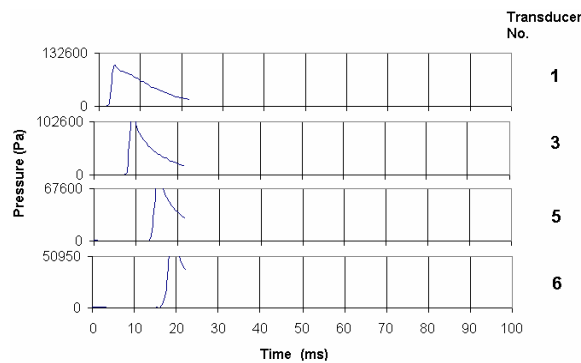
Figure 7: Predicted pressure time histories for transducers 1, 3, 5 and 6.

A possible reason for the inaccuracies near the wedge tip could be due to a large rate of change in the pressure experienced by the wedge. It is possible that modelling water as a compressible fluid could reduce this problem.

While the prediction of pressures acting on the wedge is important, the forces acting on the wedge and its subsequent motions are of primary concern in this study. Figure 8 illustrates the accuracy of various potential flow theories when compared to the experimental results and the current CFD predictions.
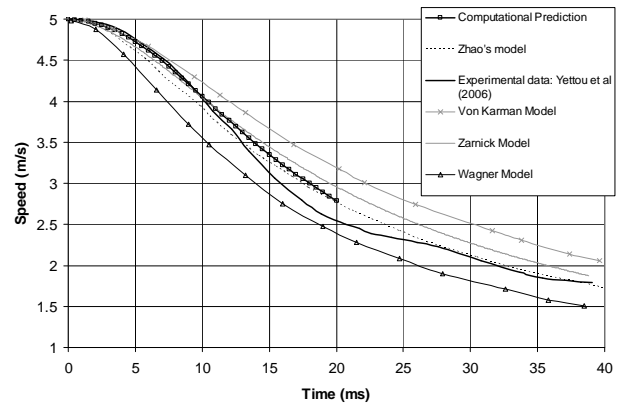
Figure 8: Comparison between computational prediction, experimental data and various potential flow solutions.

Both the experimental data and the CFD predictions differ from the potential theory in a similar manner. Initially, the wedge velocity is well predicted by the von Karman (1929) and Zarnick (1978) models. 25 ms after the impact, Zhao's (1996) model accurately predicts the wedge motion. The CFD predicts the wedge velocity well compared to experimental results from the time of impact until 10ms after impact. After 10ms, the CFD predicts a similar velocity to Zhao's theoretical model.

5.   Conclusions

In this study a hybrid approach is used to improve the accuracy of numerical predictions of planing craft motions. A computational fluid dynamics method using the Reynold's averaged Navier-Stokes equations is applied to solve the problem of a two-dimensional wedge falling into water. The results presented demonstrate that such a CFD approach predicts the magnitude and time history of the pressure distribution accurately as compared to available experimental data. This in turn leads to an accurate prediction of the wedge speed as it enters the water. The latter is especially important when considering the overall motions of the wedge. The forces calculated using this model can then be applied in the equations of motion in the strip theory model as a replacement for those previously calculated using potential flow theories. The results presented illustrate an improvement over potential flow theory predictions.

References

Akimoto, A., Miyata, H., (2002). 'Finite-volume simulation to predict the performance of a sailing boat'. Journal of Marine Science and Technology **7** pp 31-42.

Ansys CFX (2007). CFX version 11. Further information available at http://www.ansys.com/products/cfx.asp.

Azcueta, R. (2002) 'RANSE simulations for sailing yachts including dynamic sinkage & trim and unsteady motions in waves'. High Performance Yacht Design Conference, Auckland.

Azcueta, R. (2003). 'Steady and unsteady RANSE simulations for planing craft' in the 7th Conference on Fast Sea Transportation, FAST'03, Ischia, Italy.

Lewis, S.G., Hudson, D. A., Turnock, S. R., Blake, J. I. R. & Shenoi, R. A. (2006) 'Predicting Motions of High Speed RIBs: A Comparison of Non-linear Strip Theory with Experiments' Proceedings of the 5th International Conference on High Performance Marine Vehicles (HIPER '06) pp 210-224.

Launder, B., Spalding, D. (1974). 'The Numerical Computation of Turbulent Flows'. Computer Methods in Applied Mechanics and Engineering, 3 pp269-289.

Menter, F.R. (1994) 'Two-Equation Eddy-Viscosity Turbulence models for Engineering Applications'. AIAA Journal 32(8) pp 1598-1605, August.

Ohmori, T., (1998). 'Finite-volume simulation of flows about a ship in maneuvering motion' Journal of Marine Science and Technology 3 pp 82-93.

Sato, Y., Miyata, H., & Sato, T. (1999). 'CFD simulation of 3-dimensional motion of a ship in waves: application to an advancing ship in regular waves'. Journal of Marine Science and Technology 4 pp 108-116.

Von Karman, T. (1929): 'The impact of seaplane floats during landing'. Technical Report TN-321. NACA.

Wagner, H. (1932). 'Über Stross-und Gleitvorgänge an der Oberfläche von Flüssigkeiten', ZAMM, **12**, 4, pp. 193–215.

WS Atkins Consultants. (2003). 'MARNET best practice guidelines for marine applications of computational fluid dynamics'. Technical report, MARNET.

Yettou, E-M., Desrochers, A., Champoux, Y. (2006). 'Experimental study on the water impact of a symmetrical wedge'. Fluid Dynamics Research 38 pp47-66.

Zarnick, E.E. (1978). 'A Non-Linear Mathematical Model of Motions of a Planing Boat in Regular waves'. Technical report. DTNSRDC-78/032. David Taylor Naval Ship Research and Development Center.

Zhao, R., Faltinsen, O., & Aarsnes, J., (1996). 'Water entry of arbitrary two-dimensional sections with and without separation'. In Proceedings of 21st Symposium on Naval Hydrodynamics pp 408-423, Washington D.C.

Investigation of a Semi-Balanced Rudder

Lars Ole Lübke (luebke@sva-potsdam.de)

Potsdam Model Basin

Introduction

To transport the increasing volume of world trade, the shipping industry meets the demands by developing larger and faster container vessels. Although there is a tendency to decrease the ship speed for reasons of high fuel prizes, the propeller loadings remain high and have reached a level which was a few years ago considered to be unrealistic. The higher propeller loadings lead to a rise in rotational velocities in the propeller slipstream. The part of the rudder which is inside the propeller slip stream is thus exposed to higher inclination angles.

The size of the rudder increases with the growth in ship size accordingly. Most vessels are configured as single screw vessels with the rudder being located in the propeller slip stream, which requires least investment and is therefore most economical (e.g. compared to twin screw vessels).

The rudder as steering device is essential for the ships safety and manoeuvring capabilities. The classification societies developed rules for the appropriate dimensioning of the rudder system, which have to account for the different propeller loadings. The structure of rudder and hull have to be designed to meet these loads, which is more easily accomplished with semi-balanced rudders compared to full spade rudders, due to the additional bearing/pintle at the end of the rudder horn. For this reason the majority of the very large container ships (VLCS) are equipped with semi balanced rudders.

In consequence of this development new questions arise concerning the appropriate dimensioning of the whole rudder configuration for fast and large container vessels. In co-operation with the German Lloyd (GL) the Potsdam Ship Model Basin (SVA) investigates the loads and shaft moments on semi-balanced rudders for a VLCS.

The flow around the rudder system is a complex unsteady 3-dimensional flow, dominated by the slip stream of the propeller and influenced by the propeller inflow (wake field). The rudder is exposed to an accelerated axial flow with rotational velocity components, which culminate at the rotation axis in the hub vortex.

In consequence the inclination angle of the rudder changes over its height. This implies that there is a pressure and suction side of the rudder blade, even when the rudder is at rest. Pressure equalisation takes place through the gaps of the rudder especially at the rudder horn/pintle area. These regions are especially endangered for the occurrence of cavitation.

In the present study a very large container vessel is investigated by means of experimental and numerical methods. The focus of the work was laid upon the calculation of the rudder forces and moments. The commercial viscous flow solver ANSYS-CFX was employed to solve the time averaged conservation equations for mass and momentum. The experiments were conducted at the towing tank and cavitation tunnel of the SVA. In the course of the investigation different set-ups were considered. The rudder was not only investigated behind the ship with propeller but also with propeller and without ship, as well as free running.

Description of design

The geometry of a very large container vessel (VLCS) was chosen. The ship is designed to transport approximately 8.500 TEU at a ship speed of V_S=25kts. As propulsion system a six bladed fixed pitch propeller is employed, with the direction of rotation being right-handed. The scale ratio was chosen to be $\lambda \approx 40$, giving a ship model length of $L_{PP} \approx 7.5$m and a propeller diameter of $D_P \approx 0.2$. The hub cap is diverging.

The ship is equipped with a semi-balanced rudder, located $0.78 D_P$ behind the propeller plane. In the table below the main particulars of ship, propeller and rudder are given. The rudder profile is of NACA-00 series type, with a rudder height of h≈12m and a maximum and minimum chord length of c≈9m and c≈7m respectively (including rudder horn). At the rudder some cavitation supression devices are present (guide plates, spoiler), which were not considered in model scale. It is assumed that this simplification has no effect on the integral rudder values, such as side force and shaft moment.

Ship			
Length perpendiculars	L_{PP}	[m]	≈ 300.0
Breadth	B	[m]	≈ 40.0
Propeller			
Propeller diameter	D_P	[m]	≈ 8.0
Number of blades	z	[-]	6
Rudder			
Rudder area	A_R	[m^2]	≈ 75
Area, horn	A_{RH}	[m^2]	≈ 20

In Fig. 1 the geometry is shown. The given dimensions are not exact values, but ought to give an impression of the sizes.

Calculation setup and numerical mesh

To calculate the viscous flow around ship, propeller and rudder the RANS equations were solved numerically using the commercial software package ANSYS-CFX. For details on the numerical method see [1]. The k-ω SST model of Menter [2] was employed to model turbulence.

Hybrid grids, consisting out of an unstructured numerical mesh, based on tetrahedral and prismatic elements, around the rudder and a blockstructured numerical mesh around the ship, propeller and in the outer solution domain were generated with the commercial software package ANSYS ICEM-CFD.

As topology of the numerical mesh a multi-domain approach was chosen, with a rudder, a propeller and an outer solution domain. In case the ship was considered the extent of the outer solution domain covers approximately $6 \times L_{PP}$ in longitudinal direction, while without ship the longitudinal extent was chosen to be about $20 \times D_P$. The rudder domain is connected via general grid interfaces to the other domains, while for the propeller sliding interfaces were employed. The ship was investigated at even keel condition, thus the dynamic sinkage and trim were neglected. To catch the influence of wave elevation on the propeller inflow, the wave field was calculated with the panel code KELVIN prior to the RANSE calculations, in order to use the wave elevation to prescribe the upper boundary of the solution domain.

Special attention was laid upon obtaining values for the dimensionless wall distance $y^+ = u_\tau y / \nu$ (with ν being the kinematic viscosity, $u_\tau = \sqrt{\tau_w / \rho}$ the shear velocity and τ_w the shear stress at the wall) below 1 at the ship in model scale, since it is considered to improve the accuracy of the wake field calculation.

In the table below the number of nodes for the different mesh parts are given. For the calculation of ship, propeller and rudder, with an inclination angle of $\delta = 20°$, approximately 6.4 Million grid nodes were employed. The corresponding mesh is shown in Fig. 2.

Part	Type	Nodes [$\times 10^6$]
rudder (0°-35°)	Tetra/prism	1.80-2.30
propeller	Hex	1.52
ship (Bb. only)	Hex	1.38
without ship	Hex	0.82

For the calculations of the flow around the ship with rotating propeller and rudder an unsteady approach was chosen. The ship flow is calculated in a stationary, the propeller in a rotating frame of reference. During the simulation the propeller was rotated by 3° in every time step, employing 5-7 inner iterations. The calculations were continued until periodicity in time is reached, for which at least 4 propeller revolutions were required.

Results

The rudder was investigated for different configurations:

- rudder alone, with hub

- rudder behind the propeller

- rudder behind the ship with propeller

The purpose of the investigations was to obtain the forces and moments on rudder and ship for different rudder angles. The presented numerical results are confined to the calculations in model scale, for which the validation with experimental results is possible. The calculations involving the propeller were carried out, considering the propeller in full detail, with a rotating propeller.

In order to make the comparison between numerical and experimental results easier, the experiments were conducted at a constant rate of revolution (varying torque). In case of large rudder angles the required torque rises to maintain the rate of revolution, which the engine may not be able to deliver. The rate of revolution was chosen according to the following operation point (rudder angle $\delta = 0°$).

Froude number	F_N	[-]	0.232
Reynolds number	R_N	[-]	$1.366 \cdot 10^7$

Prior to the calculation of ship with rotating propeller, the propeller open water curves and the wake field of the ship were calculated and compared to the corresponding measurements.

In Fig. 3 the results of the open water tests are shown for advance coefficients ranging from $0.2 \leq J \leq 1.0$. The thrust coefficient is predicted slightly to low, while the torque coefficient is predicted a little bit to high. The overall agreement of the open water curves is considered to be good.

In Fig. 4 the calculated wake field in the propeller plane is shown, dominated by the wake peak of the

ship. The comparison of the calculated axial velocity component with the corresponding measured values, is given in Fig. 5. The overall agreement of the computed with the measured wake field is considered to be satisfactory, with the largest discrepancies being encountered for the lower propeller radii.

The drag and lift coefficients for the rudder in homogeneous inflow (without propeller and ship) are given in Fig. 6, for rudder inclination angles of up to $\delta=35°$. In the CFD calculations separation occurs for a rudder inclination of $\delta=10°$ in the upper half of the rudder already. In this region an inverse pressure gradient causes the flow to separate. Near the pintle the flow around the rudder is also affected by secondary fluid flow through the gaps between rudder and rudder horn, for reasons of pressure equalisation effects between the pressure and suction side of the rudder. In Fig. 7 the velocity vectors are given in a horizontal plane intersecting the rudder pintle and showing the secondary flow through the gap for a rudder angle of $\delta=20°$. This secondary flow also aids the flow separation, since it is directed opposite to the rudder inflow velocity. Smaller inclination angles than $\delta=10°$ were not investigated, hence no statement can be made regarding the separation inception. Due to the occurrence of separation for relatively small inclination angles the slope of the lift curve is steadily decreasing with higher inclination angles. For a rudder inclination angle of $\delta=30°$ the stall angle is reached for the upper part of the rudder, while for $\delta=35°$ the flow separates also at most of the lower part.

For a rudder inclination $\delta=10°$ no steady solution could be obtained, therefore transient calculations were conducted. The calculations for rudder angles of $\delta=30°$ and $\delta=35°$ were done in both a steady and an unsteady way. No major differences in the integral results could be found between these two approaches.

In Fig.8 the drag and lift coefficients of the rudder behind the propelled ship are shown, for both the computed and measured values. The unsteady calculations were conducted with rotating propeller. The integral values were averaged over one propeller revolution at least. In the table below some integral values for a rudder inclination of $\delta=20°$ are shown and given as ratios between the computed and the experimental values. The deviation between calculations and measurements is about 10% for the rudder. For this rudder angle the separation is confined to the pintle area and a bit above. Differences between measurements and calculations with respect to the gap size are discussed below. In the employed coordinate system the x-direction is pointing along the ship centre line, the y-direction sidewards and the z-direction in direction of the rudder shaft.

CFD/EFD, $\delta=20°$			
Thrust coeff.	K_T	[-]	1.02
Torque coeff.	$10K_\mathrm{Q}$	[-]	1.07
Long. force	$F_{\mathrm{X_{rudder}}}$	[-]	0.91
Side force	$F_{\mathrm{Y_{rudder}}}$	[-]	0.89
Shaft moment	$M_{\mathrm{Z_{rudder}}}$	[-]	0.89

In Fig. 9 to 14 the velocity field $0.65D_P$ behind the aft perpendicular, shortly after the trailing edge of the rudder, is shown for the three configurations. On the left hand side of the page the velocity fields for a rudder angle of $\delta=0°$ and on the right hand side for $\delta=20°$ are shown. On the top of the page the velocity fields are calculated in an undisturbed flow field (rudder alone with hub), in the middle the rudder operates in the propeller flow and on the bottom the rudder operates in the propeller flow behind the ship. The contour plot in each figure shows the axial velocity, while the transverse velocity components are represented by the vector field. All figures are generated with the same number of contour levels. The black regions in the contour plot on the right hand side of the page show the reversed flow of the separation zones. The regions with accelerated flow are of a dark grey and can be found as circular regions behind the propeller. For the rudder angle of $\delta=20°$ the end vortices of the rudder can be clearly identified, as well as the separation zone. For the rudder behind the propelled ship (Fig. 14) the separation zone is clearly smaller compared to the calculations without ship (Fig. 13), which is due to the smaller inverse pressure gradients in the decelerated flow in the wake of the ship outside the propeller slip stream. For this reason the rudder in the behind ship condition has not reached stall with a rudder angle of $\delta=35°$, since the separation zone remains confined to the pintle area and a bit above, compare Fig. 6 with Fig. 8. Comparisons are made, although the thrust loadings of the propeller for the different configurations and rudder angles differ slightly. For further validation PIV measurements of the flow field are planned.

In the context of separation and of course cavitation the gap distance between rudder horn and rudder is of importance. The CFD calculations were carried out on basis of geometric similarity. In the model rudder however, the gap distances at the pintle between rudder and rudder horn are not of geometric similarity. The reason is, that to measure the forces and moments on the rudder, there has to be some clearance between rudder and rudder horn, since the shaft has to have a finite stiffness. This leads to larger gap distances than according to the geometric similarity law. It is also believed that larger gap distances are required in order to have a better agreement with the fluid flow through the gaps in full-scale, since the boundary layer in full-scale is relatively thinner. Particularly for the investiga-

tion of the cavitation pattern in model scale great care has to be laid upon the gap distance. No comment can be made regarding the influence of the gap size on the integral values.

The presented computations and measurements were conducted in model scale, with the pressure being above the vapour pressure. Therefor cavitation is not present nor taken into account during the computations.

Concluding remark

Calculations of a semi-balanced rudder were presented. The numerical results were extensively validated with experimental data. The agreement between measurements and calculations is satisfactory with the largest discrepancies being approximately 10%, for the calculation of the propelled ship with a rudder angle of $\delta=20°$.

In the CFD calculations the separation zones of the rudder are influenced by the gap between rudder horn and rudder, particularly in the pintle area. For the model rudder however, the gap sizes around the pintle area are not manufactured according to the geometric similarity law. To what extent the integral values of the rudder are influenced by the gap size is not yet fully understood.

Numerical methods have the advantage that also the forces of the rudder horn can be retrieved, which was not the case for the presented measurements. Also full-scale calculations can be carried out. According to [5] the drag and lift coefficients have a strong dependency on the Reynolds number, with increasing Reynolds-number C_D decreases, while C_L is rising. The knowledge of scale effects is extreamly important for the extrapolation of model scale results to full-scale.

The author would further express his gratitude towards the "Bundesministerium für Bildung und Forschung" for funding this project.

References

[1] ANSYS-CFX Manual Version 11, April 2007

[2] MENTER, F.
Two-equation eddy-viscosity turbulence models for engineering applications,
AIAA-Journal, 32(8), 1994

[3] L. LÜBKE, K. MACH
LDA Measurements in the Wake of the Propelled KCS Model and its use to Validate CFD Calculations
25th Symposium on Naval Hydrodynamics, 8-13 August 2004, St. Johns, Canada

[4] L. LÜBKE, K. MACH
Validation of CFD Results Behind the Working Propeller of a Ship Model
7th Numerical Towing Tank Symposium, 3-5 October 2004, Hamburg, Germany

[5] H. HEINKE, K. RIECK, M. LAMPRECHT, D. JAKSIC
Kavitationsarme Profile für Hochleistungsruder
SVA-Bericht Nr. 3046, Dezember 2004
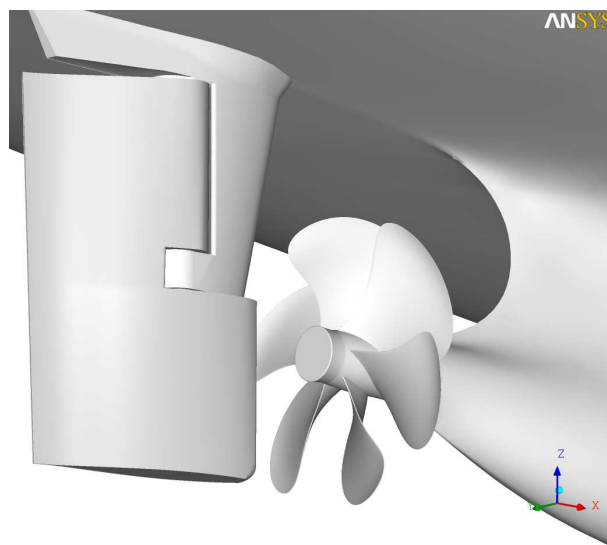
Figure 1: Geometry for numerical calculations
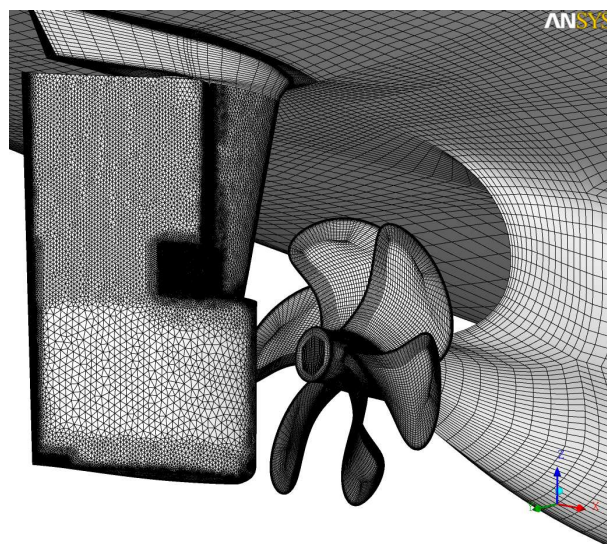
Figure 2: Numerical mesh of aft ship with rudder and propeller
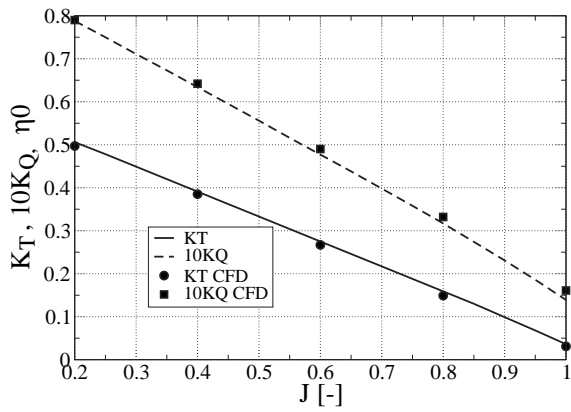
Figure 3: Measured and computed propeller open water test
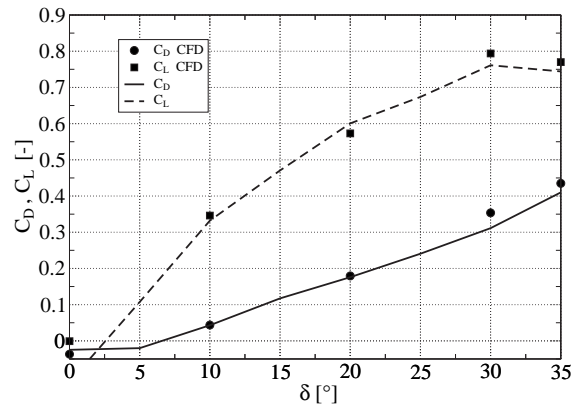
Figure 6: Drag and lift coefficient of rudder
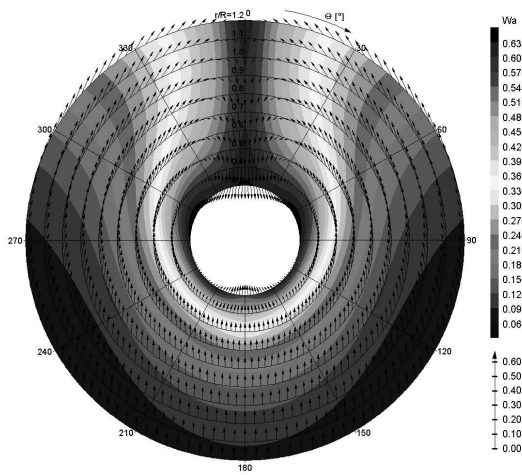
Figure 4: Computed velocity components in propeller plane
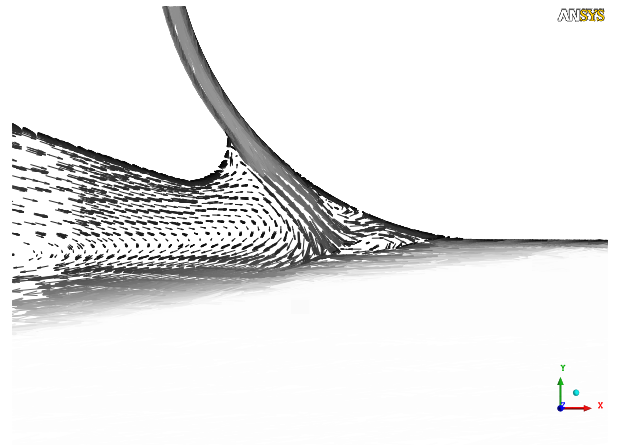
Figure 7: Velocity vector in a horizontal plane intersecting the pintle of the rudder
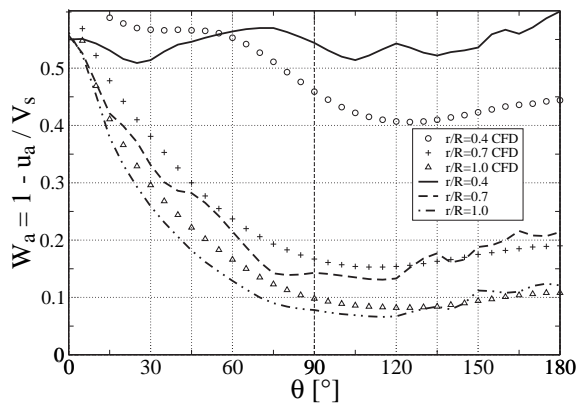
Figure 5: Measured and computed axial velocity component in propeller plane for different radii
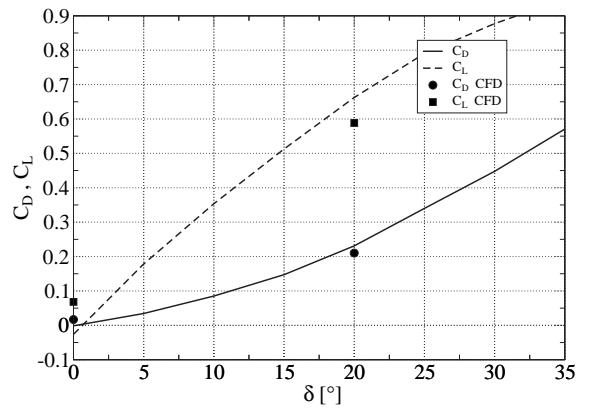
Figure 8: Drag and lift coefficient of rudder behind ship with propeller
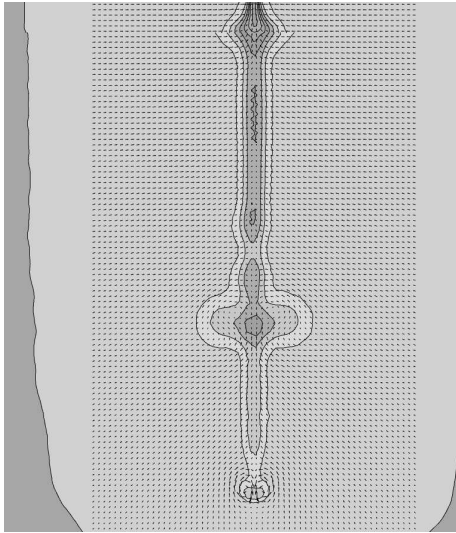
Figure 9: Velocity field $0.65D_P$ behind AP, rudder angle $\delta = 0°$
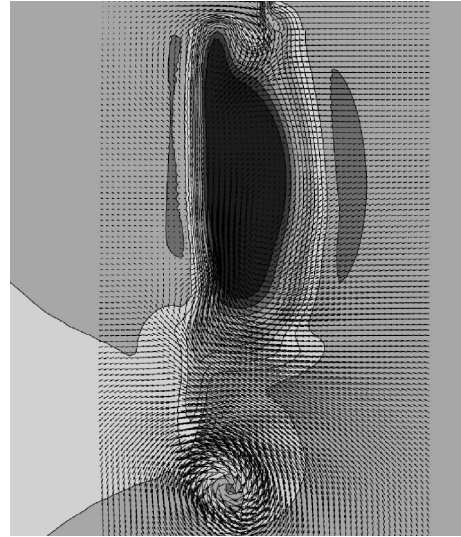
Figure 12: Velocity field $0.65D_P$ behind AP, rudder angle $\delta = 20°$
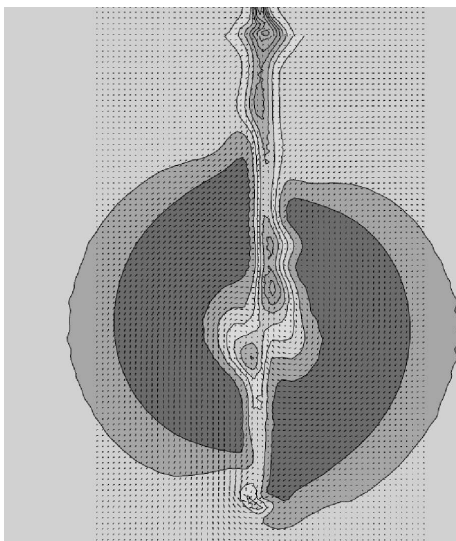
Figure 10: Velocity field $0.65D_P$ behind AP, rudder angle $\delta = 0°$, with propeller $\theta = 0°$
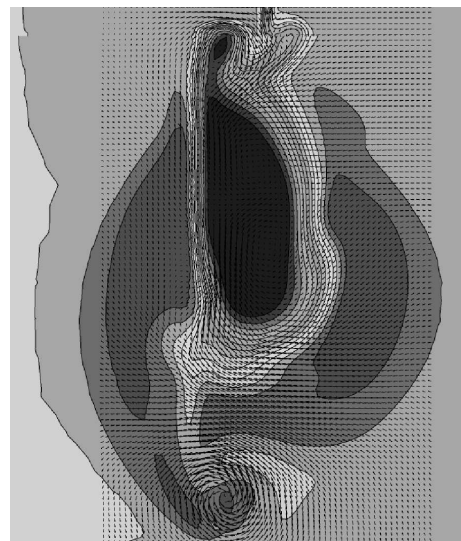
Figure 13: Velocity field $0.65D_P$ behind AP, rudder angle $\delta = 20°$, with propeller $\theta = 0°$
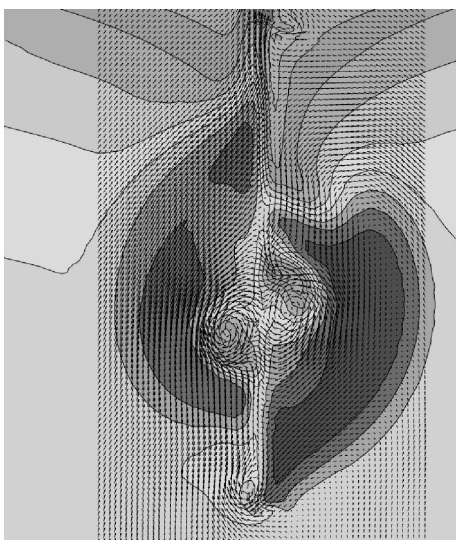
Figure 11: Velocity field $0.65D_P$ behind AP, rudder angle $\delta = 0°$, with propeller $\theta = 0°$ and ship
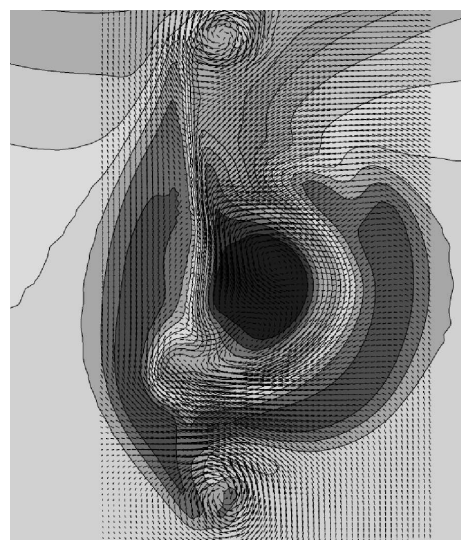
Figure 14: Velocity field $0.65D_P$ behind AP, rudder angle $\delta = 20°$, with propeller $\theta = 0°$ and ship

Modeling of behind condition wake flow in RANS computation on a conventional and high skew propeller

Robert Mikkelsen[1], Poul Andersen, Jens Nørkær Sørensen

INTRODUCTION

RANS modeling of ship propellers in behind condition demands fully unsteady computations to be carried out, although quasi-steady approaches are pursued in order to reduce computing cost. Quasi-steady and unsteady Navier-Stokes computations on ship propellers using CFD tools have been carried out by Li[1] at inclined conditions. Recently, Mikkelsen[2] et al. introduced a method using momentum sources to generate an arbitrary wake in combination with RANS computations of the actual propeller blade geometry. The method was presented and applied to an artificially generated wake, which in the following is developed further to consider actual measured wakes. Typical computations on propellers tend to use large calculation domains in order to reduce un-physical influence from numerical boundaries. As a consequence the increasing grid size of computational cells towards the inflow boundary reduces the numerical ability to convect a flow field with gradients. This implies that a non-homogeneous wake field applied at an inflow boundary is not preserved until impact with the propeller blades. The paper by Mikkelsen et al. presented the technique showing how a 3D non-homogeneous loaded actuator disc represented by concentrated body forces slightly upstream of the propeller plane, generates a corresponding non-homogeneous wake that interacts with the individual propeller blades. Actuator discs are generally applied for computation of the flow field around ship hulls, in order to get the effect of the accelerated propeller wake. However, a reversed approach is pursued in the following where the effect of the ship hull on the propeller is modeled with an actuator disc. The equivalent forces needed to generate a desired wake field are found from a separate numerical computation with an actuator disc only. The present work was carried out within the EU funded research project "Leading Edge" in which state-of-the-art CFD codes were applied to predict the performance of ship propellers and details of the leading-edge tip vortex. The aim of the present investigation is to present a method for including the wake from a ship hull in a fully unsteady RANS computation on a highly skewed and a conventional propeller. Results are shown of the unsteady developing wake and blade loadings.

TECHNIQUE

The actuator disc concept combined with numerical solution of the full Navier-Stokes or RANS equations, has proven to be a convenient way to model the flow field through rotors (see Mikkelsen[3], Madsen[4]) for many engineering purposes. The actuator disc, represented by body forces, is usually considered to have a uniform loading in the azimuth direction. The present investigation suggests to have an actuator disc with non-uniform load distribution located upstream of the actual propeller. The loading applied to the actuator disc should result in a wake field in the propeller plane, which as closely as possible resembles measured wake velocities. One-dimensional axial momentum theory considers the uniformly loaded Rankine-Froude actuator disc. Choosing the z-coordinate as axial direction, the analysis predicts that the non-dimensional axial interference factor $a=1-V_{z1}/V_o$ to the thrust coefficient is $C_T=4a(1-a)$, (see Glauert[5]) for a rotor (a is positive for a turbine rotor) and $C_T=T/(\frac{1}{2}\rho V_o^2\pi R^2)$. Furthermore, the axial velocity in the actuator disc equals $V_{z1}=V_o(1-a)$ and far downstream to the actuator disc $V_{z2}=V_o(1-2a)$. Assuming $w(r,\theta)\approx V_{z2}$ represents a desired axial wake field from the hull, measured some distance downstream of the location of the applied loading, a first estimate of the local loading and power needed to create the desired wake field is

$$\Delta T = \Delta \dot{m}(V - w), \qquad \Delta P = \tfrac{1}{2}\Delta\dot{m}\left(V_o^2 - w^2\right) = \tfrac{1}{2}\Delta\dot{m}(V_o - w)(V_o + w) \tag{1}$$

where $\Delta T(r,\theta)$ [N] and $\Delta P(r,\theta)$ [W] are the local thrust and power, respectively, and ΔA a local surface area element. The mass flow is given by $\rho u\Delta A=\rho w\Delta A_1$ at the disc and far wake position. Using the work done by the force and combining the above equations leads to

$$\Delta P = u\Delta T = \tfrac{1}{2}(V + w)\Delta T \quad\Rightarrow\quad \Delta\dot{m} = \tfrac{1}{2}\rho(V + w)\Delta A \quad\Rightarrow\quad \Delta T = \tfrac{1}{2}\rho\left(V_o^2 - w^2\right)\Delta A \tag{2}$$

which assumes that the expansion not is too severe, i.e. that ΔA and ΔA_1 do not differ too much. Thus, it is assumed that each small stream tube with area element ΔA is preserved downstream, where the resulting far-wake velocity V_{z2}, corresponds to the applied loading ΔT within the same stream tube. Letting $\mathbf{f}=(f_r, f_\theta, f_z)$ denote applied body forces, the loading in the axial direction are given by $f_z=\Delta T/\Delta V$. Numerically, the loading is applied as concentrated momentum sources around the actuator disc using a convolution with a Gaussian smearing function, whereby the loading is applied to all cells. The above method is combined with the EllipSys3D general purpose flow solver, which is developed in cooperation between Department of Mechanical Engineering[6,7] at the Technical University of Denmark, DTU and the Department of Wind Energy[8] at Risø National Laboratory. The EllipSys3D code is a multi-block finite-volume discretization of the incompressible RANS equations in general curvilinear coordinates. The turbulence in the boundary layer is modeled by the k-ω SST model of Menter[9]. Further technical details about EllipSys3D may be found in Sørensen et al. The computations are carried out in a rotating frame of reference where

---

[1]Correspondence to: R. Mikkelsen, rm@mek.dtu.dk, Phone: (+45) 4525 4320, Fax: (+45) 4593 0663, Dept. of Mech. Eng., Technical University of Denmark, Building 403, Nils Koppels Alle, DK-2800 Lyngby, Denmark

the flow field rotates relative to the computational domain which is fixed. Consequently, the body forces generating the wake form the ship hull, rotate relative to the computational mesh. Further, the applied rotating body forces govern how large time steps are applicable. Thus, the time step multiplied by the rotational angular velocity should be smaller than the average angular width of the computational cells.

ACTUATOR DISC COMPUTATIONS ON WAKES

Separate computations are carried out using a 3D actuator disc in order to evaluate the generated wake that later will be applied to the actual propeller computation. The simulations are carried out on a simple Cartesian structured grid with 8 blocks and 32^3 cells in each block. The total domain extends 5 diameters in all directions from the centre and the rotor actuator disc is represented by 24 cells across the diameter. The advantage of using an actuator disc compared to full simulations is the huge reduction in computational cost. Furthermore, good results may be obtained by only solving the laminar Navier-Stokes equation (see Mikkelsen) when comparing with one-dimensional inviscid axial momentum theory. Madsen extended the usual axi-symmetric actuator disc with a 3D actuator disc solving the RANS with turbulence models. Two different wakes are considered: a symmetric single wake which is
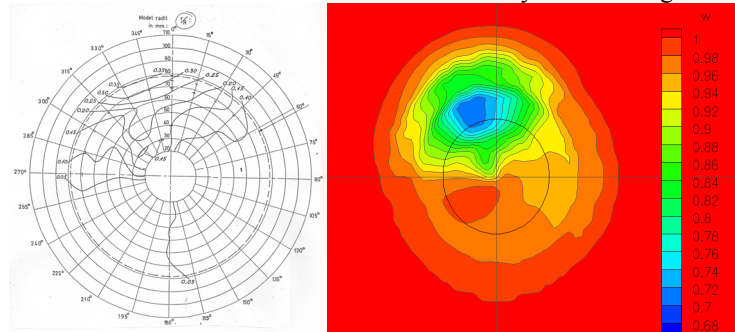
Figure 1 Measured (right) and computed wake by actuator disc computations (left), axial velocity. The circle indicates the diameter of the propeller. Twin screw wake for high skew propeller.

applied to the conventional propeller and a non-symmetrically wake for the high skew propeller which is considered mounted on a twin screw ship. The wake fields are typical, but they are not the wake fields of the ships for which the propellers were actually designed, tested or operated. Figure 1 depicts the measured wake for the high skew propeller. For the symmetric single screw wake all three velocity components are available and could be included in
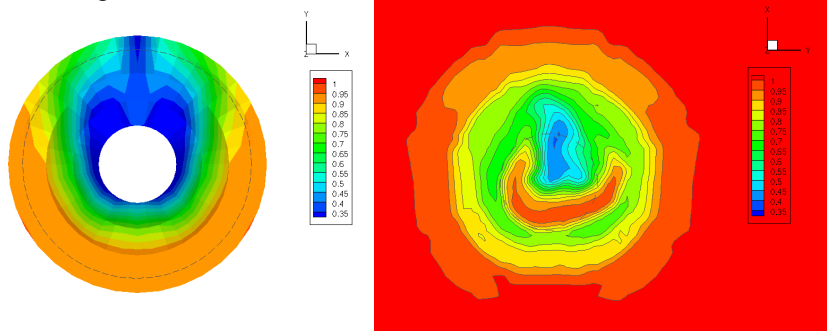
Figure 2 Measured (right) and computed wake by actuator disc computations (left), axial velocity. The circle indicates the diameter of the propeller. Single screw wake for conventional propeller.

the loading of actuator disc, however, the present analysis is restricted to the axial velocity component. Figure 2 displays contour plots of the measured and computed single wake. The load level for this wake is rather high with an average value w_a=0.363 based on the affected rotor area. The average reduction factor for the twin screw wake is w_a=0.10. It should be noted that the actuator disc generating the wake is located about 1.0 diameter upstream to the propeller plane for the high skew propeller and due to the higher loading, about 1.5 diameters for the conventional propeller.

HIGH SKEW AND CONVENTIONAL PROPELLER MESH

The investigation concerns a highly skewed and a conventional, 4 bladed right turning full scale propeller with a diameter of 5.2m and 6.6m, respectively. Good block-structured mesh generation of a highly skewed propeller is complicated by the high solidity of the ship propeller blades, since the cyclic boundaries will tend to skew the cells away from the blades. Presently, the EllipSys3D code only supports cyclic boundaries with point to point match, which forces grid lines to skew in some areas. An O-O topology was found feasible as near domain structure and an H-topology away from the near domain to the far field boundaries was applied. Thus, the computational domain is divided in two with an inner O-O topology and an outer H-topology. The main idea of the new layout is to twist the blocks in the span-wise direction on the surface of the propeller, in order to meet the cyclic boundaries better. It should be noted that, the surface mesh was first generated together with the near-domain boundaries. Volume meshing was carried out using an in-house hyperbolic mesh generator which operates purely hyperbolically near the propeller surface and shifts to transfinite interpolation towards the near-domain boundaries.
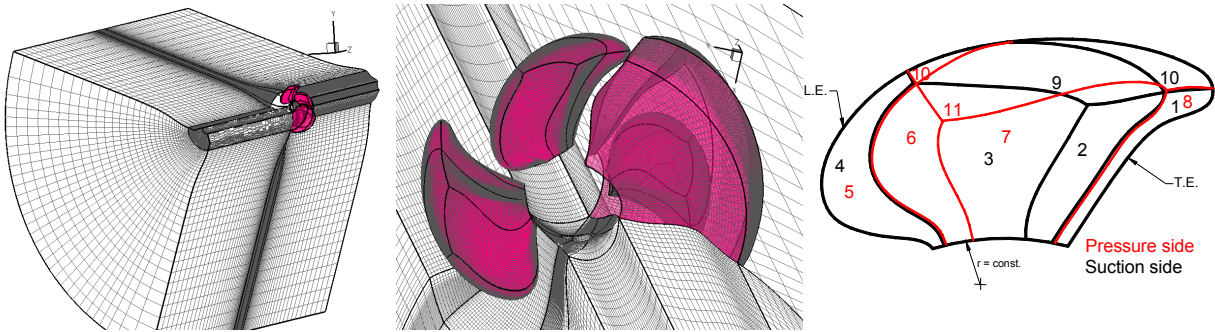
Figure 3 Part of computational mesh (left), near domain mesh, (centre) and blade surface topology (right).

Figure 3 shows the final mesh for one blade. The mesh consists of 11 blocks in the near domain and 7 blocks in the outer domain in total, 18 per blade and 72 blocks for a 4 bladed propeller. Each block consists of 64^3 cells in total, in all 18M cells. Finally, the full domain extends about 5 diameters in all directions away from the propeller. The computational mesh for the conventional propeller is generated in a corresponding manner to the highly skewed with 8 surface blocks, 12 blocks per blade and 48 blocks in total, in all 12M cells. Figure 4 displays the outline of the surface mesh and the topology of the near block domain and spherical far domain boundaries.
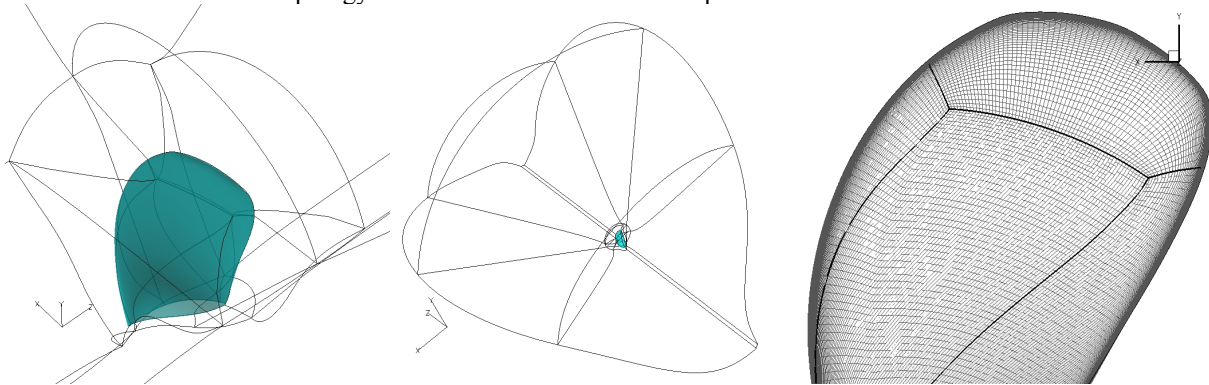
Figure 4 Block structure for conventional propeller: near domain (left), far domain (centre) and surface mesh (right).

For the simulation, the propeller is considered to operate in an infinite flow field, hence, free stream conditions are applied at the inflow boundary and a zero axial gradient is enforced at the outlet. Since the actual propeller hub is not resolved but replaced with a cylinder extending through the entire domain, a slip or Euler condition is applied there, while the propeller blades have no-slip.

BOUNDARY-ELEMENT COMPUTATIONS

The boundary-element method (BEM) is considered the standard tool for calculation of pressure distributions on propellers, both in the case of uniform inflow and for the propeller operating behind the ship. It is therefore of interest to compare results of RANS calculations with those of the boundary-element method. A number of such comparisons have been published in the literature, for instance the ITTC[10] workshop, and recently Becchi & Pittaluga[11]. The boundary-element method used here is a simple method with constant source and dipole strengths over each element that moreover is planar. It has a non-linear Kutta condition by means of which the pressure difference at suction and pressure sides of the midpoints of the elements close to trailing edge is zero. A simple procedure is used to calculate the geometry of the blade wake, based on the lifting-line method, Lerbs[12]. The results
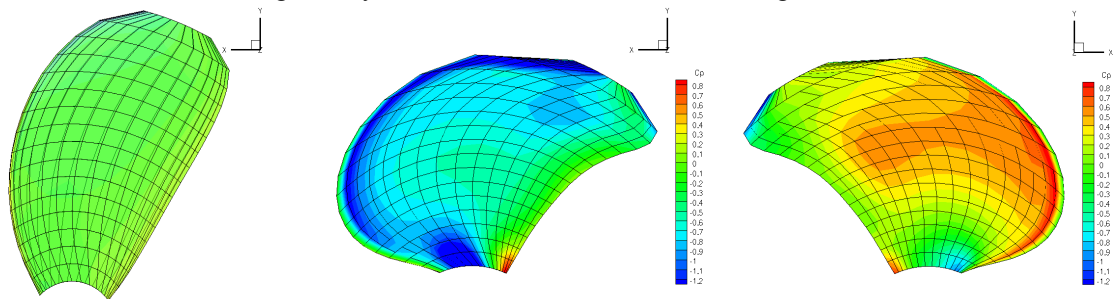
Figure 5 Propeller grid for potential boundary element computations. Conventional propeller (left), high skew suction side (centre) and pressure side (left).

shown here do not include effects of viscosity although this can be taken into account by boundary-layer calculations. Calculations were carried out using the calculation meshes shown in figure 5. This mesh is basically the same as the one used for the RANS propeller. The mesh has 2048 elements for each blade, 32 elements over the chord and 16 span-wise, and 2176 nodal points. It has a refined distribution towards leading and trailing edges, but it has no hub and the blades are open at the root and the tip.

STEADY COMPUTATIONS

In order to reduce simulation time, steady computations without the wake-generating actuator disc was first carried out for the full scale propellers at a J-value of V/nD=0.736 and J=0.4 for the high skew and conventional propeller, respectively. The steady state convergence history is displayed in Figure 6 for the flow variables and integral quantities K_T and $10K_Q$. The jumps in residuals are the result of a three level multi-grid solution procedure. At the coarse levels the convergence is excellent whereas at the finest level, the solution is slightly unsteady. Table 1 summarizes the findings for the main propeller characteristics, showing a reasonable agreement between model
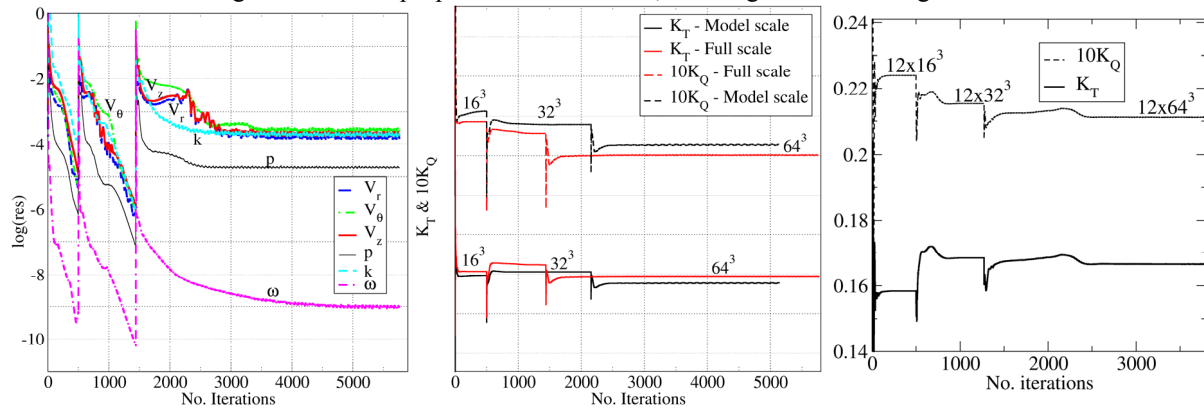
Figure 6 Convergence for steady state computations. Flowvariables (left), K_T & $10K_Q$ for the high skew propeller (centre) at model and ful scale and model scale conventional propeller (right).

scale experiments and corresponding scale computations. It is believed that better predictions demand accurate modeling of the boundary layer transition process. However, this task is very complicated and with the present state

Table 1 Computed and measured coefficients, K_T and $10K_Q$ for the conventional and high skew propeller.

	J	K_T	$10K_Q$	Exp.K_T	Exp.$10K_Q$	K_T err.	K_Q err	Scale.
Conventional, Model	0.40	0.1664	0.2104	0.164	0.194	1.4	8.4	0.281m
Conventional, Full	0.40	0.1705	0.1937	-	-	-	-	6.60m
Conventional, Potential	0.40	0.164	0.206	-	-	-	-	6.60m
High skew, Model	0.736	-	-	-	-	6.5	7.2	0.233m

of the EllipSys3D code, it remains to be carried out in full in 3D. No further details about the steady computation will be presented as the focus of the paper is on the unsteady.

UNSTEADY COMPUTATIONS – HIGH SKEW PROPELLER

The unsteady simulation is restarted based on the steady solution. At this point the wake-generating body forces are applied. The body forces are non-uniform across the disc, but do not vary in time. Figure 7 (left) depicts part of the flow solution. Contours are shown of the axial velocity for the accelerated propeller wake and the decelerated ship
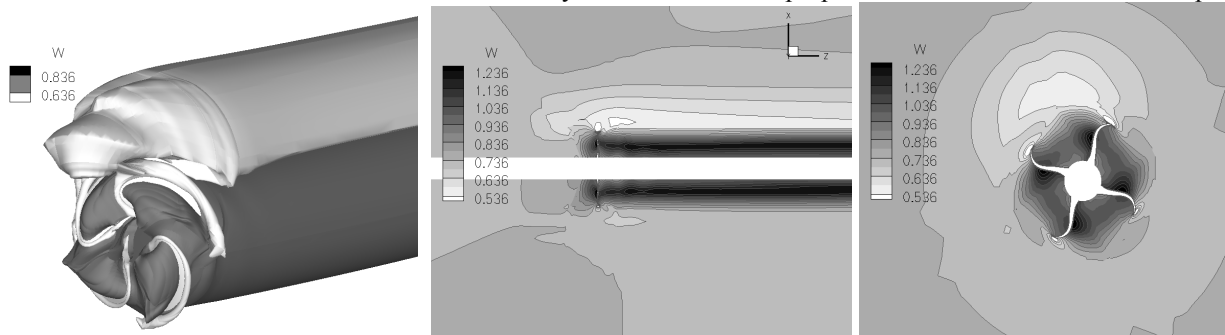
Figure 7 Axial velocity field, decelerated wake from ship hull and accelerated wake behind propeller, 3D (left), vertical cross section (centre) and through propeller plane.

hull wake generated by the body forces. The fully developed periodic solution reveals that the affected part of the propeller is quite narrow compared to the full circle and a first hand visual evaluation suggests that the impact seems reasonable. Figure 7 (right) shows a planar cut of the axial velocity distribution, which also is clearly non-symmetrical. Although the impact of the hull wake in the upper region is significant, the accelerated propeller wake appears not to be highly influenced; however, as will be seen from the blade loadings, the blades are substantially affected by the applied body forces. Contours of the surface pressures coefficient $C_p=(p-p_o)/(^1/_2\rho n^2 D^2)$ are displayed in figure 8. The contours appear to be smooth and without major kinks indicating a well resolved solution. The pressure coefficient reveals that the most affected blades at the current time step is the blade at the bottom. Surface skinfriction lines are presented in figure 8 (right), revealing the origin and separation of the leading-edge tip vortex. For the given J-value the skinfriction lines only vary slightly during on revolution but at higher loadings the pattern may shift dramatically to include standing vortex structures and separation patterns. A more detailed picture of the instantaneous pressure variation is given in figure 9 which depicts sectional C_p curves at radii r/R=0.7, 0.8 and 0.9
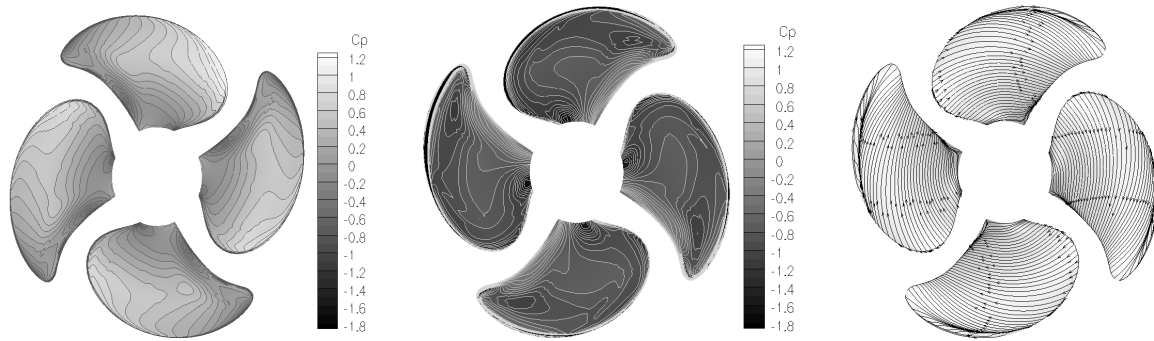
Figure 8 Cp contours for pressure (left) and suction side (centre), skinfriction lines (right).

on the 4 blades. The angles indicate the blade azimuth angle where the most affected blade at 270° is at the bottom. At r/R=0.7 and 0.8 the differences in Cp are minor between the blades, whereas at r/R=0.9 significant differences are seen on the suction side. At 270° a low pressure region formed at the leading edge extends downstream with a
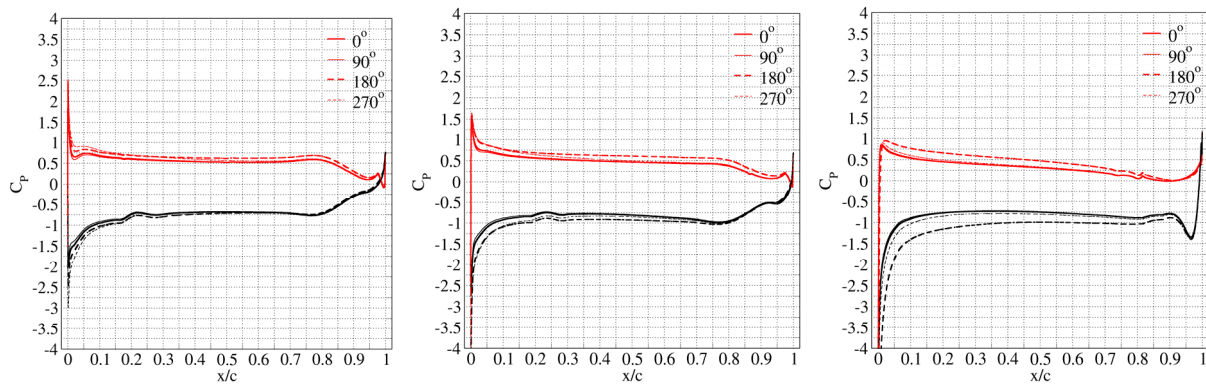
Figure 9 Sectional Cp(x/C) for r/R = 0.7 (left), r/R = 0.8 (centre) and r/R =0.9 (right).

low point at x/C=0.12 of Cp=-3.8. At the leading edge Cp_{min} values of -5.1 are found due to the high curvature changes in this region. The pressure side at r/R=0.9 reveals only minor differences over the whole chord length. The integrated blade K_T and $10K_Q$ is shown in figure 10 (left) during the transient development. About 6-10 revolutions are needed to establish a converged periodic solution as shown in figure 10 (centre) for one revolution for one blade.
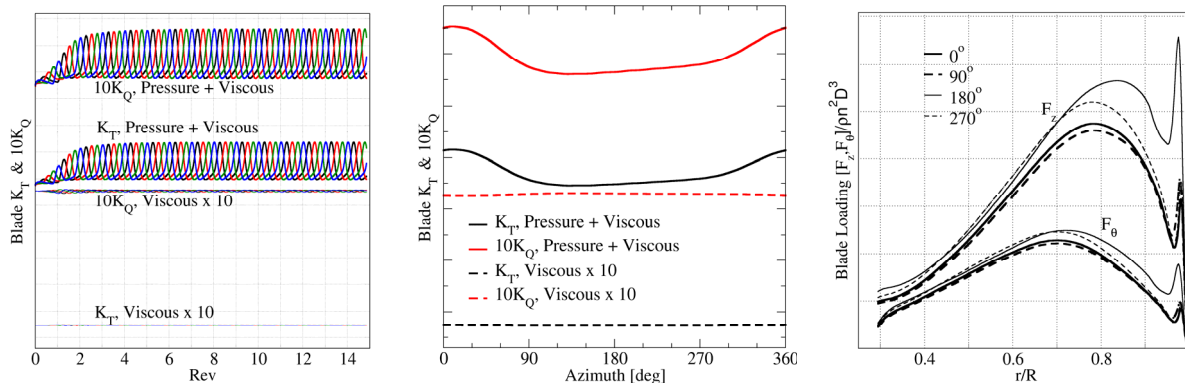
Figure 10 Transient developments of K_T and $10K_Q$ (left) and during one revolution (centre), blade loading (right).

The highest blade loading is located around 20° azimuth and compared to the unaffected region from about 90° to 270°, the level in this region is about 20-30% lower than the max value. The viscous contributions are included separately multiplied by a factor of 10 and it is seen that for K_Q the viscous part should be added whereas for K_T it is subtracted the part from pressure. Looking at the spanwise blade loading in figure 10 (right), the axial and tangential loadings are seen to vary considerably, with the blade at 0° having the highest loading. The blade at 270° is about to leave the affected region in order to level off at the level blade 90° and 180° experiences. Towards the tip of the blade, a peak in the loading is observed which is explained by the position of the leading edge vortex, which boosts the suction pressure over a large part of the chord in this region. The maximum axial loading is around r/R=0.8, but the tangential loading attains its maximum value near r/R=0.72.

CONVENTIONAL PROPELLER

Computations were carried out for the conventional propeller affected by the single wake shown in figure 2. The load case is, as mentioned, rather high. Simulations are carried out at J=0.4, however, the effective behind condition advance number is reduced to $J_A=(1-w_A)J=0.254$. Figure 11 shows the computed pressure distribution and y^+ showing that the resolution is within recommendations using the *k-ω SST* turbulence model. The solution appears

smooth with high peaks at the leading edge. It is difficult to give detailed interpretation of the individual blade load situation based on pure visual view of the solution for the present case. Extraction of individual sectional distributions presented in figure 12 reveal a limited variation of Cp at r/R=0.7 and 0.80. At r/R=0.90 there are larger
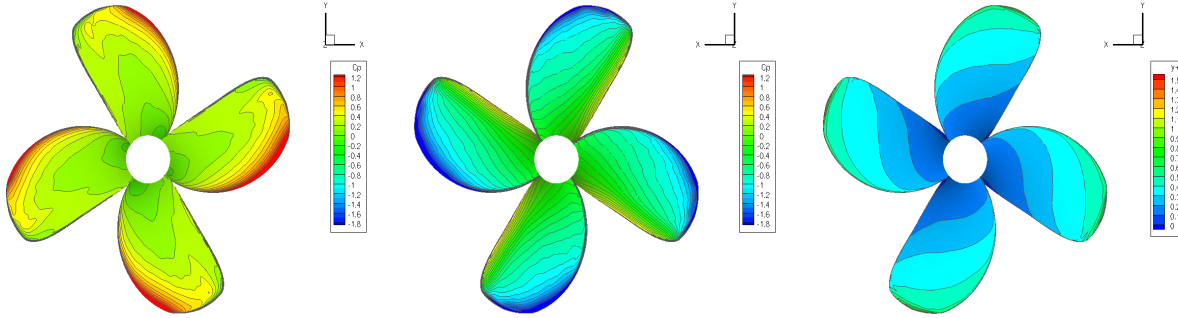
Figure 11 Cp contours for pressure (left) and suction side (centre), y^+ suction side (right).

differences towards the leading edge, seen as generally higher loading in the region 180-270 deg at the current time step. Extreme leading edge Cp-values, are computed using both RANS and the boundary element method with values above 20, sure to onset cavitation, which with the present state of modeling remains to be included. The load distribution for each individual blade is given in figure 13. The start up transient is somewhat longer for the conventional due to the location of the wake generating actuator disc. About 10-12 revolutions are needed to achieve
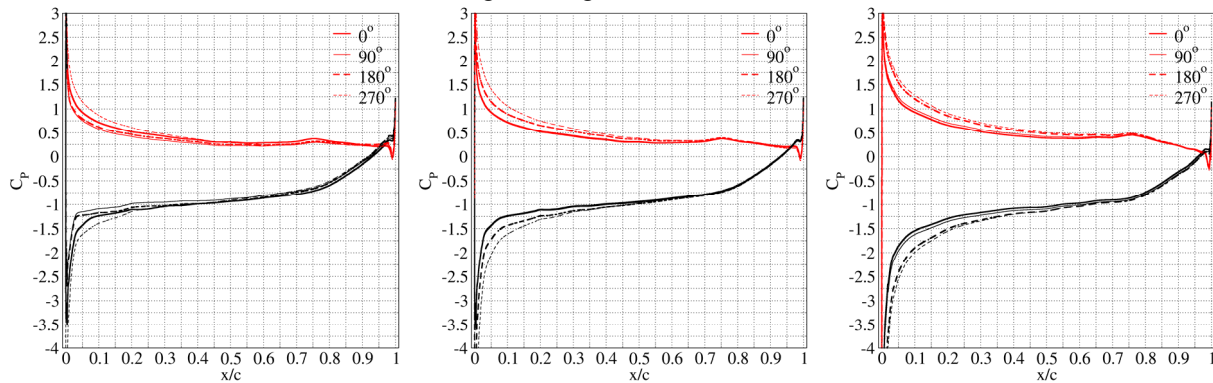
Figure 12 Sectional Cp(x/C) for r/R = 0.7 (left), r/R = 0.8 (centre) and r/R =0.9 (right).

converged periodic solutions. Depicted in figure 13 (centre) are the variations during one revolution together with comparable boundary element computations. The agreement on general trends are reasonable, however, the level is clearly higher using the boundary element method. It is difficult to comment on which prediction best resembles actual condition since measurements for the given cases are unavailable. Spanwise normalized load distributions are
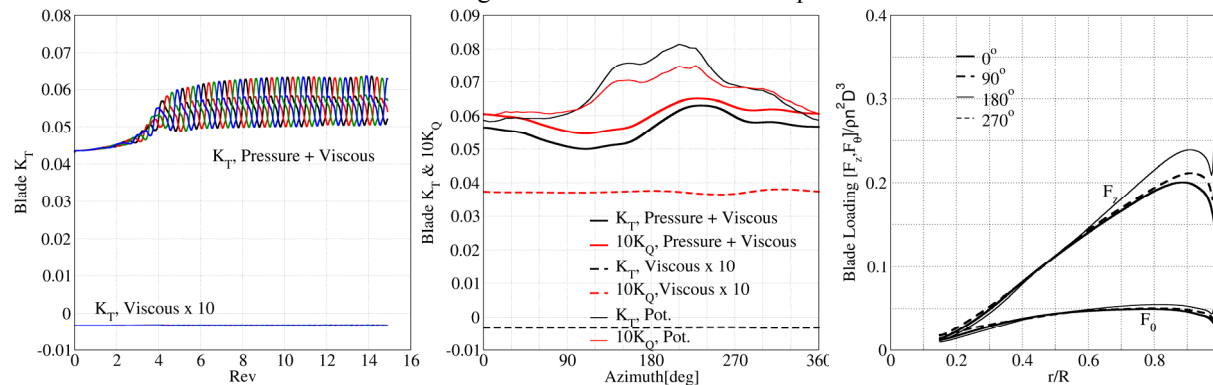
**Figure 13 Conventional propeller: Transient developments of K_T and $10K_Q$ (left) and during one revolution (centre), blade loading (right).**

shown in the last figure for the 4 blades at the given time step. At the present step the blade at 180° appears to have the highest loading. Finally, the computed characteristics are displayed in figure 14 compared with model experiments for both propellers. The open-water computations generally compare well, using both RANS and BEM, with measurements although there are deviations between predictions. The azimuth averaged values for the unsteady computations are also plotted using the effective behind condition advance number, which is reduced to $J_A=0.662$ and $J_A=0.254$ for the high skew and conventional propeller, respectively. It should be noted that for the conventional propeller the velocity variation over the wake field is rather pronounced.
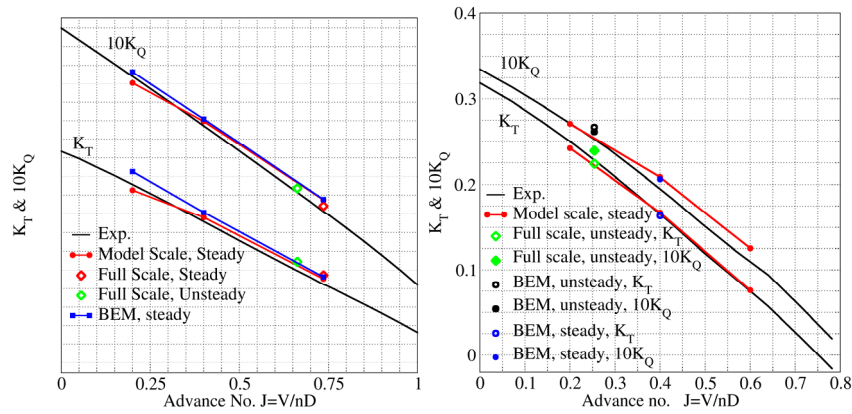
Figure 14 K_T and $10K_Q$ characteristics for the high skew (left) and conventional propeller (right).

CONCLUSIONS

Unsteady RANS computations have been carried out on a high skew and a conventional propeller in a simulated behind condition. The wakes from the ship hull was generated using body forces, inserted into the RANS mesh. The technique appears to be feasible for investigating flows about propellers in behind conditions. The presented result predicts considerable variations in blade loadings as the individual blades pass through the wake generated by body forces. Separate actuator-disc computations are a feasible tool for tuning the needed actuator-disc loading in order to obtain a desired ship hull wake. The main characteristics computed at steady-state model-scale conditions, compare well with corresponding experiments. The unsteady simulations at full scale conditions reveal that the method is feasible of capturing expected blade-load variations which in future computations should be compared in more detail with experiments. Comparing results between RANS and conventional boundary-element method, both methods capture the main expected behavior for the considered cases; however, there are considerable deviations in magnitude in the region of the most affected blade position.

ACKNOWLEDGEMENT

[1]Li DQ, Leer-Andersen M. Quasi-steady and unsteady RANS calculation of a highly skewed propeller in an inclined flow, Proc. *IWSH 2005*, Shanghai, China.

[2]Mikkelsen R, Andersen P, Michelsen JA, Sørensen JN. Unsteady RANS computation on a high skew propeller in behind condition. *IMaREST, WMTC conf.,* 2006 London, UK.

[3]Mikkelsen R. Actuator disc methods applied to wind turbines, *Ph.D. dissertation*, MEK-PHD-FM-2003-02, Fluid Mechanics, MEK, Technical University of Denmark, DTU. Web: www.fm.mek.dtu.dk/Publications/ phd.html

[4]Madsen HA. Yaw simulation using a 3D actuator disc model coupled to the aeroelastic code HawC. Proc. 13th IEA Symp. on the *Aerodynamics of Wind Turbines*, Stockholm, 1999; 133-145.

[5]Glauert H. Airplane propellers. In Durand WF(ed). *Aerodynamic Theory*. Dover, New York, 1963; **4**(Division L): 169-269

[6]Michelsen JA. Basis3D - a platform for development of multiblock PDE solvers. *Report AFM 92-05*, Dept. of Fluid Mechanics, Technical University of Denmark, DTU, 1992

[7]Michelsen JA. Block structured multigrid solution of 2D and 3D elliptic PDE's. *Report AFM 94-06*, Dept. of Fluid Mechanics, Technical University of Denmark, DTU, 1994.

[8]Sørensen NN. General purpose flow solver applied to flow over hills. *PhD Dissertation, Risø-R-827(EN)*, Risø National Laboratory, Roskilde, Denmark, 1995.

[9]Menter FR. Zonal two equation k-ω turbulence models for aerodynamic flows. *AIAA Paper 93-2906*, 1993.

[10]ITTC: 22nd ITTC Propulsion Committee Propeller RANS/Panel Method Workshop. Eds. B. Gindroz, T. Hoshino, J. Pylkkänen. 1998.

[11]Becchi, P. Pittaluga, C.: Comparison between RANSE calculations and panel method results for the hydrodynamic analysis of marine propellers. In *Proc. MARINE CFD 2005: 4th International Conference on Marine Hydrodynamics*. RINA, London, 2005.

[12]Lerbs, H.: Moderately loaded propellers with a finite number of blades and an arbitrary distribution of circulation. *Trans. SNAME*, vol. 60, pp. 73-123. SNAME, New York, N.Y. 1952.

VERIFICATION OF A FREE SURFACE CODE WITH METHOD OF MANUFACTURED SOLUTIONS

Tommi Mikkola[1]
Ship Laboratory, Helsinki University of Technology

1 INTRODUCTION

In this paper the definition for Verification and Validation advocated by e.g. Roache (2002) and Salari and Knupp (2000) is adopted. Here Verification is concerned with solving the equations right and Validation with solving the right equations. With this definition Verification is purely a mathematical exercise and does not deal with the correctness of the equations in terms of physical laws. The latter is dealt with by Validation.

Verification is further divided into two parts: Verification of Codes and Verification of Calculations. The former deals with error *evaluation* using a known solution, whereas the latter deals with *estimation* of the error of a numerical solution. To avoid confusion Salari and Knupp (2000) recommend that the term Solution Accuracy Assessment (SAA) is used for the latter. Verification of Code should always precede Verification of Calculations (or SAA), which should precede Validation (Roache 2002). However, for a code it is sufficient to perform Verification of Code just once, but after modifications the verification has to be repeated (Salari & Knupp 2000). On the other hand, as the name suggests, Verification of Calculations has to be performed for each individual simulation case. In this work the focus is on Verification of Codes. Roache (1998) states that verification is about solving the given partial differential equations with given boundary conditions *consistently*, i.e. as a measure related to the discretisation, such as the cell size or time step, approaches zero the numerical solution approaches the corresponding continuum solution. Furthermore, based on the discretisation used one usually knows the order at which the error should approach zero.

This process obviously requires the knowledge of the continuum solution. The best solution for comparison is an exact analytical solution for a problem. However, analytical solutions for the Euler or the Navier-Stokes equations exist only for very simplified problems. With free surface included additional complication is introduced by the non-linearity of the free surface boundary condition. This problem of lack of analytical solutions can be circumvented by using the Method of Manufactured Solutions (MMS) first presented by Steinberg and Roache (1985). Here the governing equations are modified with source terms such that a known, exact, analytical solution exists for the modified equations. In the presented work MMS has been applied for the study of the behaviour of the numerical error of a time accurate, surface tracking free surface solver on unstructured grids.

2 METHOD OF MANUFACTURED SOLUTION

The basic idea behind MMS is to start off with the solution rather than with the equations to be solved. That is, a solution is first manufactured and the equations are then modified by adding source terms to provide the given solution. This apparently complex procedure is in fact straightforward and simple to perform, wherein lies the elegance of the method.

Roache (2002) and Salari and Knupp (2000) have presented some remarks on the choice of the manufactured solution. Firstly, the solution should not be trivial. On the other hand, the solution does not have to be physical either. In fact, some physical solutions, such as those for the Poiseuille or Couette flows, are undesirable as they do not activate the advection terms in the equations. Namely, one requirement for the solution is that it exercises all terms being tested in the equations. Roache (2002) further adds that one wants a solution, which exercises also all ordered derivatives in the error expansion.

The necessary steps in MMS are briefly described in the following. For a more thorough explanation with some examples the reader is referred to e.g. (Roache 2002). In MMS one starts by taking a suitable analytical solution, i.e. the manufactured solution, and substitutes it into the original governing continuum equations. If the solution does not satisfy the equations a residual is left over from the substitution. The modified equations are produced by substituting a source term equal to this residual into the original equations with the manufactured solution now satisfying these modified equations. The boundary conditions are provided by the manufactured solution or the applied boundary conditions should be combatible with the manufactured solution.

---

[1] Ship Laboratory, Helsinki University of Technology, Tietotie 1, FIN-02015 Espoo, Finland – E-Mail: Tommi.Mikkola@tkk.fi

The modifications in the equations, i.e. in practise just the source terms, are then implemented into the solver in question. Solution of the modified equations with the solver gives a numerical approximation of the manufactured solution. The accuracy of the approximation depends on the discretisations of the equations and the corresponding discretisation parameters, such as cell size. Code verification can now be based on the comparison of the numerical solution and the known analytical solution. As the discretisation parameters are reduced the numerical solution should approach the analytical continuum solution. The coupling of manufactured solutions with mesh refinements for the estimation of the order of accuracy and, thus for more thorough code verification, was first presented by Steinberg and Roache (1985).

3 THE FLOW SOLVER AND GRID GENERATION

The flow solver YAFFA (Yet Another Fine Flow Analyser) has been used in this work. A detailed description of the method can be found in (Mikkola 2006), and therefore only some of the main features are briefly discussed here.

The numerical method is based on 2D unstructured finite volume method. A collocated SIMPLE-type pressure correction scheme is used for the solution of the bulk flow, with velocities and pressures stored at the cell centres. Free surface flows are simulated using a surface tracking approach, in which free surface deformation is solved from the kinematic boundary condition and dynamic boundary condition is coupled to the pressure correction equation. Grid updating is performed with a linear/torsional spring analogy (Batina 1991), (Farhat et al. 1998), with a Laplacian smoothing or with a combination of these two. Solution of time accurate flows is based on a dual time step approach, in which pseudo time derivatives are added into the unsteady flow equations and solution is iterated in pseudo time for each physical time step until these additional terms vanish.

All of the results presented in the following have been simulated with double precision (64-bit). Each time step has been iterated in pseudo-time until the L_{inf}-norm of the change of the flow variables between iterations has reduced to machine zero. This removes the influence of the iteration error due to incomplete convergence (see e.g. Eça and Hoekstra, 2006). Thus, the numerical error consists only of the discretisation and round-off errors. With double precision the latter is negligible in comparison.

Two approaches have been used for the generation of the grids for the refinement studies. In the first option each grid has been generated separately with Delaundo grid generator (Müller 1996) based on the frontal Delaunay method. Delaundo takes as input the point distribution on the boundaries and some parameters controlling the grid generation procedure. The refinement has been applied for the boundary point distributions, and the same control parameters have been used for each grid to maximise geometrical similarity of the grids. In the second approach a base grid has first been generated with Delaundo. The refined grids have been generated from this grid sequentially by bisecting each edge of the grid and dividing each triangle into four triangles with the same shape.

4 VERIFICATION OF THE SPATIAL DISCRETISATION

Before studying the behaviour of the numerical error in the case of time accurate free surface flow solution the spatial discretisation of the bulk flow equations has been verified. For the verification the manufactured solution presented by Salari and Knupp (2000) has been used. Here the velocities and pressure are given by

$$u(x,y) = u_0 \left[\sin(x^2 + y^2) + \varepsilon \right] \tag{1}$$

$$v(x,y) = v_0 \left[\cos(x^2 + y^2) + \varepsilon \right] \tag{2}$$

$$p(x,y) = p_0 \left[\sin(x^2 + y^2) + 2 \right] \tag{3}$$

The resulting source terms are presented in (Salari & Knupp 2000) and have been left out for brevity. The rectangular solution domain is the same as the one used by Salari and Knupp, i.e. x is between -0.1 and 0.7 and y is between 0.2 and 0.8. Similarly, the same number of points on the boundaries has been used. However, the corresponding numbers of elements are considerably higher than in their case as in this work triangles have been used. Two different sets of grids have been used. In Set A each grid has been generated separately with Delaundo. In Set B the coarsest grid from Set A has been used as the base grid for the refinement approach.

As Euler equations have been considered in the verification of the time accurate method, the viscosity has been left out also in this case. Furthermore, ε has been set to zero. For the numerical solution fixed velocity and extrapolated pressure has been used on the left hand and bottom boundaries, whereas fixed pressure and extrapolated velocity has been applied on the right hand and top boundaries.

Two approaches have been tested for the approximation of the pressure term in the momentum equations. In the

first approach the term is evaluated using Gauss theorem and skewness corrected averaging for the pressure on the face (Mikkola 2006). In the second approach the term is evaluated directly as the volume integral of the pressure gradient. In both approaches the gradient – in the former approach used for the skewness correction – is evaluated using the least-squares approach (Demirdžić & Muzaferija 1995).
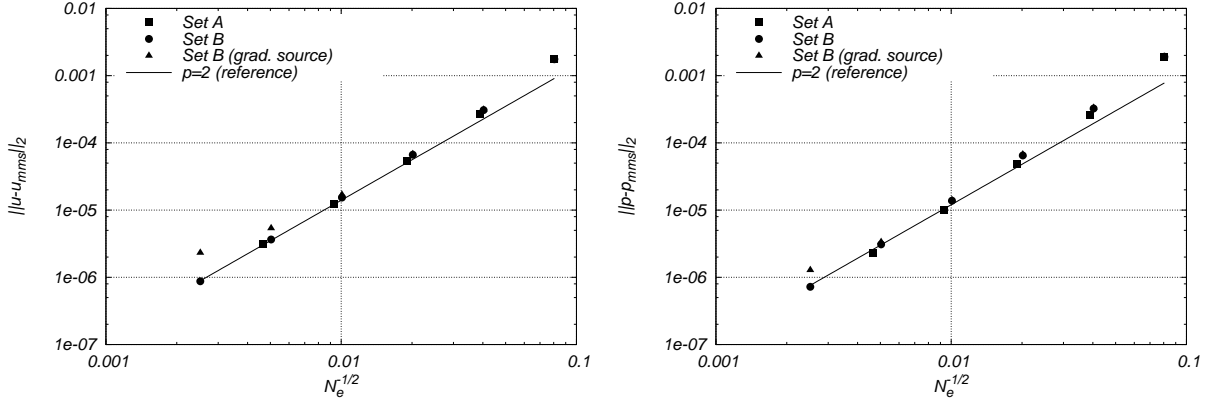
Figure 1: Verification of the spatial discretisation of the bulk flow equations using the test case by Salari and Knupp (2000). The L2-norms of the error in numerical solution as functions of generalised cell size.

Fig. 1 shows, how the numerical error – i.e. the difference between the numerical and manufactured solution – behaves as a function of a generalised measure of the cell size. Here the measure is taken as the inverse of the square root of the number of elements. The results show second-order accuracy for both the velocity and pressure with the Gauss based pressure term as the asymptotic range is approached. This is expected as the implementation is believed to be second order accurate and thus the method is verified in this respect. It can also be seen that both approaches for grid refinement give similar results.

However, the approximation of the pressure term directly with the evaluated pressure gradient shows reducing order of accuracy as the cell size gets smaller. At the time of writing the reason for this is unclear. Nevertheless, a preliminary study of the results indicate that this may be caused by the behaviour of the numerical error close to the corners of the domain. Differences are considerable especially close to those corners, at which a variable is extrapolated on both boundaries.

5 VERIFICATION OF THE TIME ACCURATE FREE SURFACE SOLUTION

5.1 The simulation case and the manufactured solution

The manufactured solution used in this study is the linearised potential flow solution for a standing wave in a rectangular container. The flow field (u, v, p) and the free surface shape ζ are given by (Paterson 1983)

$$u(x,y,t) \quad = \quad \frac{\zeta_0 \omega}{\sinh(kh)} \cosh[k(y+h)] \sin(kx) \sin(\omega t) \tag{4}$$

$$v(x,y,t) \quad = \quad -\frac{\zeta_0 \omega}{\sinh(kh)} \sinh[k(y+h)] \cos(kx) \sin(\omega t) \tag{5}$$

$$p(x,y,t) \quad = \quad \frac{\rho g \zeta_0}{\cosh(kh)} \cosh[k(y+h)] \cos(kx) \cos(\omega t) \tag{6}$$

$$\zeta(x,t) \quad = \quad \zeta_0 \cos(kx) \cos(\omega t) \tag{7}$$

Here $k = m\pi/L$, $\omega^2 = gk\tanh(kh)$, h is the depth of the container, L is the length of the container and m is an integer constant. In this work $h = 1.6$, $L = 40$, $\zeta_0 = 0.2$ and $m = 4$ giving two waves over the length of the tank. Based on the manufactured solution mirror boundary condition has been applied on the vertical sides of the container and slip boundary condition is used for the bottom.

5.2 The source terms

The source terms are produced simply by substituting the manufactured solution given by Eqs. (4)-(7) into the governing equations. In this case the equations are the Euler equations, the continuity condition as well as the

kinematic and dynamic boundary conditions

$$\frac{\partial u}{\partial t} + u\frac{\partial u}{\partial x} + v\frac{\partial u}{\partial y} + u\frac{\partial u}{\partial x} + u\frac{\partial v}{\partial y} = -\frac{1}{\rho}\frac{\partial p}{\partial x} \tag{8}$$

$$\frac{\partial v}{\partial t} + u\frac{\partial v}{\partial x} + v\frac{\partial v}{\partial y} + v\frac{\partial u}{\partial x} + v\frac{\partial v}{\partial y} = -\frac{1}{\rho}\frac{\partial p}{\partial y} \tag{9}$$

$$\frac{\partial u}{\partial x} + \frac{\partial v}{\partial y} = 0 \tag{10}$$

$$\left[1 + \left(\frac{\partial \zeta}{\partial x}\right)^2\right]^{-1/2}\left(\frac{\partial \zeta}{\partial t} + u\frac{\partial \zeta}{\partial x} - v\right) = 0 \tag{11}$$

$$p|_{fs} - \rho g\zeta = 0 \tag{12}$$

The substitution gives the following source terms for the above equations.

$$Q_u = \frac{\zeta_0^2 g k^2}{\sinh(2kh)}\sin^2(\omega t)\sin(2kx) \tag{13}$$

$$Q_v = \frac{\zeta_0^2 g k^2}{\sinh(2kh)}\sin^2(\omega t)\sinh[2k(y+h)] \tag{14}$$

$$Q_m = 0 \tag{15}$$

$$Q_{kin} = -\frac{\zeta_0\omega\sin(\omega t)}{\sinh(kh)\sqrt{1+[\zeta_0 k\sin(kx)\cos(\omega t)]^2}}\left(\cos(kx)\left\{\sinh(kh) - \sinh\left[k(h+\zeta_{ms})\right]\right\}\right. \tag{16}$$

$$\left. + \zeta_0 k\sin^2(kx)\cos(\omega t)\cosh\left[k(h+\zeta_{ms})\right]\right) \tag{17}$$

$$Q_{dyn} = \rho g\zeta_{ms}\left[\cosh(k\zeta_{ms}) + \sinh(k\zeta_{ms})\tanh(kh) - 1\right] \tag{18}$$

Here ζ_{ms} is the wave height (7) from the manufactured solution. The source term for the continuity condition vanishes as the potential flow solution itself is based on the satisfaction of the continuity condition. The source terms for the momentum equations are produced purely by the advection terms as the manufactured pressure is such that the pressure gradient cancels the inertia terms. The finite volume integrals of these source terms are approximated in the solver using the value of the source term at the geometric centre of each finite volume.

5.3 Discretisation parameters

The case has been simulated with six grids and six time steps for one oscillation period. The left half of the coarsest grid with maximum free surface deformation is shown in Fig. 2. For the boundary nodes a refinement
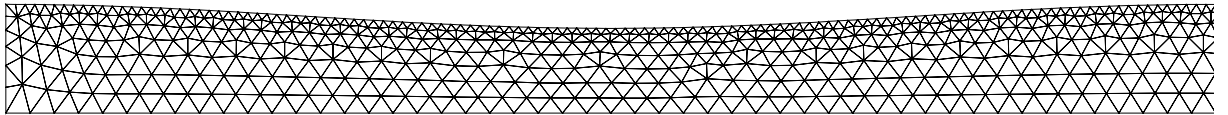
Figure 2: The left half of the coarsest grid at $T = 0$.

factor $r = \sqrt{2}$ has been used. The number of faces on the free surface N_{fs} and the total number of elements N_e for the different grids are given in Tab. 1. The number of time steps per one period N_T is given in the same table.

Table 1: The number of free surface faces and the total number of elements as well as the number of time steps per one oscillation period for different cell size and time step refinement levels.

Level	0	1	2	3	4	5
N_{fs}	1413	1000	706	500	353	250
N_e	67845	33630	17040	8320	4243	1980
N_T	284	200	142	100	71	50

6 ANALYSIS OF THE RESULTS

For the analysis the spatial wave for each time step has been Fourier analysed. The first harmonic frequency used corresponds to the length of the manufactured wave. The analysis presented here is based on the study of the time

evolution of this first harmonic component of the wave, i.e.

$$\zeta(x,t) = \zeta^1(t)\cos(kx) \qquad (19)$$

Fig. 3 compares the time evolution of $\zeta^1(t)$ for different cell and time step sizes with the other parameter kept fixed at the finest value. The refinement studies show monotonic convergence towards a solution with numerical error originating only from the parameter kept fixed.
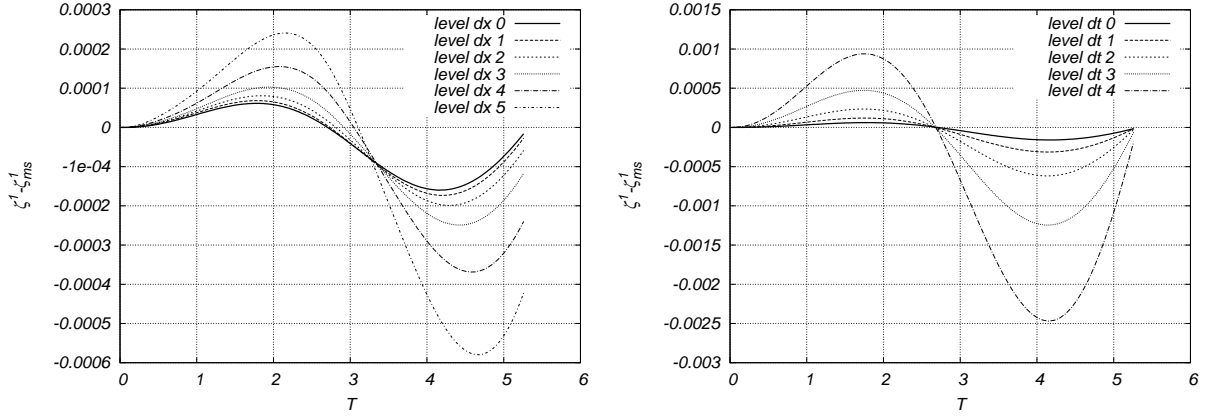
Figure 3: The difference between the numerical and manufactured first harmonic component of the spatial wave. On left: results with different grids using the finest time step, on right: results with different time steps using the finest grid. Results with direct approximation of the pressure gradient.

For the study of the numerical damping and phase error the time variation of the first harmonic component is represented as an exponentially decaying harmonic funtion

$$\zeta^1(t) = \zeta_0 e^{-\alpha t}\cos(\omega t) \qquad (20)$$

The damping factor α and the frequency ω are solved by nonlinear fit of the function to the numerical solutions. The results of the fit are shown for different levels of grid refinement and time step in Fig. 4. A significant difference
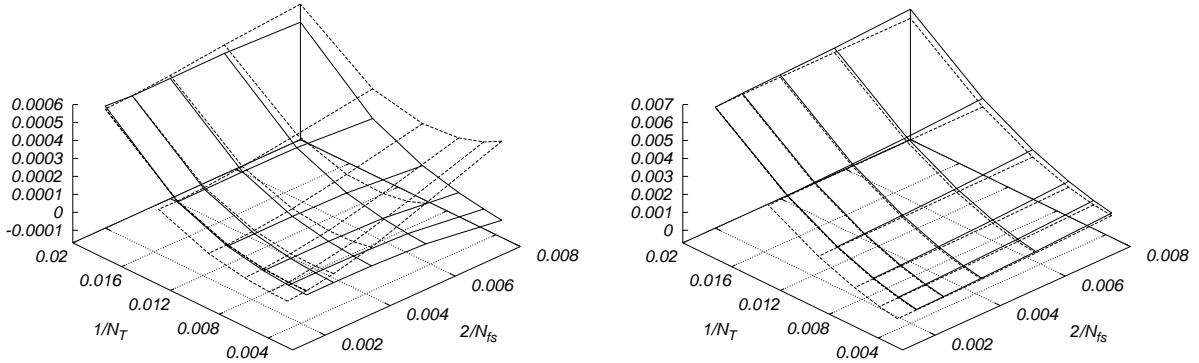
Figure 4: Discretisation error as a function of discretisation parameters. Pressure term with Gauss integral (solid) and direct gradient approximation (dashed). On left: damping factor α, on right: frequency ω.

in the behaviour of the damping factor is observed between the two pressure term approximations – especially for small time steps and large cell sizes. If the pressure term is approximated directly with the pressure gradient the damping factor starts to increase with smaller time steps. For the phase errors the differences between the pressure discretisations are small. For both approaches the phase error is nearly independent of the cell size within the tested range.

With unsteady cases the manufactured solution can only be reached if both the cell size and the time step approach zero at the same time. Fig. 5 shows the numerical error for the damping factor and the frequency as the grid and time step are refined with the same ratio. Again, the results with the Gauss based approximation of the pressure term show the expected order of accuracy for both the damping and the phase error. On the other hand, increasing deviation from the expected order for the damping is observed in the case of gradient based approximation.
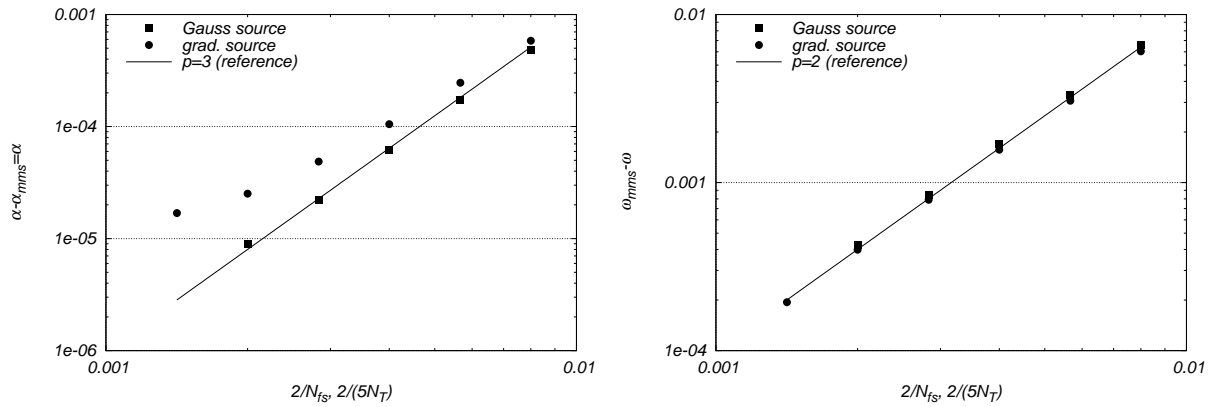
Figure 5: Numerical error with the grid and time step refined at the same time. On left: damping factor α, on right: frequency ω.

7 CONCLUSIONS

The method of manufactured solutions has been used for the verification of a time accurate, surface tracking, free surface flow solver. The bulk flow and time accurate free surface discretisations have been verified separately using two different manufactured solutions. The study has shown that the method of manufactured solutions can be used easily and effectively also for the verification of surface tracking free surface discretisations, i.e. with a highly nonlinear boundary condition.

The results show that the spatial discretisations of the bulk flow for both the velocities and pressure are second order accurate, which is the expected order. Similarly, the free surface discretisation shows expected order of accuracy and the method is thus verified for the options used in the study. However, some deviation from the expected order of accuracy has been observed if the pressure term in the momentum equations is evaluated directly using the approximated pressure gradient. The reason for this should be studied further.

REFERENCES

Batina, J. T. (1991), 'Unsteady euler algorithm with unstructured dynamic mesh for complex-aircraft aerodynamic analysis', *AIAA Journal* **29**(3), 327–333.

Demirdžić, I. & Muzaferija, S. (1995), 'Numerical method for coupled fluid flow, heat transfer and stress analysis using unstructured moving meshes with cells of arbitrary topology', *Computer methods in applied mechanics and engineering* **125**, 235–255.

Eça, L. & Hoekstra, M. (2006), On the influence of the iterative error in the numerical uncertainty of ship viscous flow calculations, *in* '26th Symposium on Naval Hydrodynamics', Rome, Italy.

Farhat, C., Degand, C., Koobus, B. & Lesoinne, M. (1998), 'Torsional springs for two-dimensional dynamic unstructured fluid meshes', *Computer methods in applied mechanics and engineering* **163**, 231–245.

Mikkola, T. (2006), Time accurate simulation of a plunger type wave maker using unstructured finite volume solver with surface tracking, *in* '26th Symposium on Naval Hydrodynamics', Rome, Italy.

Müller, J.-D. (1996), On triangles and flow, PhD thesis, University of Michigan.

Paterson, A. (1983), *A First Course in Fluid Dynamics*, Cambridge University Press.

Roache, P. (1998), *Verification and Validation in Computational Science and Engineering*, Hermosa Publishers, Albuquerque NM.

Roache, P. (2002), 'Code verification by the method of manufactured solutions', *Journal of Fluids Engineering* **124**.

Salari, K. & Knupp, P. (2000), Code verification by the method of manufactured solutions, Technical Report SAND2000-1444, Sandia National Laboratories.

Steinberg, S. & Roache, P. (1985), 'Symbolic manipulation and computational fluid dynamics', *Journal of Computational Physics* **57**(2).

How to Avoid or Minimize of Rudder Cavitation

Ould el Moctar, ould.el-moctar@gl.group.com
Germanischer Lloyd, Advanced Engineering & Strategic Research, Hamburg, Germany

Intoduction

Cavitation occurrence on ship appendages is the source of undesirable effects such as erosion, structural vibration and loss of efficiency. The ensuing loss of performance and the necessary repairs can noticeably reduce the profitability of ship operation. Also for safety reasons it is necessary to avoid extensive rudder erosion. Germanischer Lloyd has developed recommendations for the prevention of erosive rudder cavitation [1].

Erosion caused by cavitation occurs particularly at ship speeds exceeding 22 knots and high propeller loading (P/(0.25D²π)>700 kw/m², P denotes power at propeller and D the propeller diameter). Cavitation erosion is of interest only if it occurs within the range of rudder angles ±4 used for course keeping. For large rudder angles (>15°) cavitation is unavoidable. In order to minimize or avoid rudder cavitation, the effort is put into the prediction of cavitation danger, especially in the design stage.

High flow velocities result in low pressures. If the pressure drops below the vapour pressure of the water, cavities form and fill up with vapour. The cavities disappear again when the pressure increases. They grow and collapse rapidly. Cavitation involves highly complex physical processes with strongly nonlinear multi-phase flows. Cavitation erosion occurs when small bubbles filled with vapour collapse on or near to the surface of the rudder. It causes small cracks and erosion, which in sea water may be magnified by corrosion (galvanic loss of material). To estimate the likelihood of cavitation in a flow the non-dimensional cavitation number σ is used:

$$\sigma = \frac{p - p_v}{0.5 \cdot \rho \cdot v^2}$$

p is the pressure including atmospheric pressure and hydrostatic pressure, p_v is vaporization pressure (Water at 15 °C, p_v = 1 700 Pa). In water with sufficient impurities, cavitation will occur when the local pressure drops below the vapour pressure. In reality, cavitation occurs earlier.

There are different types of rudder cavitation:

– Cavitation on the rudder side plating, see Fig.1

– Rudder sole cavitation, see 2

 Due to the pressure difference between both sides of the rudder, a flow component around the rudder sole from the pressure to the suction side occurs. It causes a rudder tip vortex which may cause damage if it attaches to the side of the rudder

– Propeller tip vortex cavitation

 Propellers cause tip vortices. These are regions of low pressure, often filled with cavitation tubes. Behind the propeller they form spirals which are intersected by the rudder, see Fig.3

– Propeller hub cavitation

 Behind the propeller hub a vortex is formed which is often filled by cavitation tubes, see Fig.4

– Cavitation at surface irregularities

 Surface irregularities disturb the smooth flow velocities over convex surfaces and edges, leading to low pressures and frequently cavitation erosion, see Fig.5

– Gap cavitation

 Gap cavitation may lead to erosion of structurally important parts of the rudder, see 6.

Prediction Methods for Rudder Cavitation

Numerical methods
Methods based on computational fluid dynamics (CFD) can be used to estimate the extent of cavitation. However, they cannot predict the occurrence of erosion. If CFD methods are used to avoid cavitation, the problem of erosion is essentially solved. The advantage of using CFD methods is that a design can be optimized and that repair measures can be worked out (e.g., effect of installing guiding plates).

Model tests
Model tests can be used to estimate cavitation on full scale rudders. For prediction of erosion extensive experience of personnel is essential. However, model tests are costly and, thus, inappropriate for optimizing a design.

Full-scale measurements
Full-scale measurements are reliable, but expensive. They are well suited to detect the occurrence of erosion although, from a design standpoint, it generally is too late.

Applied Numerical Methods

The Reynolds-averaged Navier-Stokes (RANS) solvers which implement interface-capturing techniques of the volume-of-fluid (VoF) type are today the obvious choice for computing the cavitating flow around the rudder operating in the propeller slip stream. The conservation equations for mass and momentum serve as starting point. The solution domain is subdivided into a finite number of control volumes that may be of arbitrary shape. The integrals are numerically approximated using the midpoint rule. The mass flux through the cell face is taken from the previous iteration. The unknown variables at the centre of the cell faces are determined by interpolation from the cell centres. The spatial distribution of each of the two phases is obtained by solving an additional transport equation for the volume fraction of one of the fluids. The modelling of cavitation consists on seed distribution, convection of vapour bubbles and description of bubble growths and collapse. Cavitation is modelled as two phase flow, containing the phase of water and vapour. The transport equation of the concentration (standard-VoF) is extended by a source term for producing and deleting the vapour volume. Growth and collapse of vapour bubbles are described by the Rayleigh-Plesset-equation. Two-equation-turbulence models are typically used, [2], [4].

Computational Procedure

Because pressure is proportional to the flow speed squared at the rudder, an accurate determination of the propeller slipstream is required to correctly predict the pressure distribution of the rudder because the velocity field in the propeller slip stream influences the pressure field considerably. Therefore, the following procedure should be applied. The procedure comprises the following steps:

– Computations at full-scale Reynolds number

– Geometric modelling of the rudder including all details such as gaps and shaft

– Geometric modelling of the rotating propeller

– Ideally, geometric modelling of the hull. This modelling requires high computational and modelling effort. Alternatively, the influence of the hull can be imposed on the estimated nominal full-scale wake at the inlet boundary of the computational domain.

– The numerical grid should fit to the physical demands of the respective flow problem and more grid points should be concentrated in regions where variable gradients are high und where cavitation is expected to occur. Typical grid size is two and half million cells, see Fig.7.

Flow computation without cavitation model

The cavitation danger can then be estimated using the total pressure value p:

$$p = p_{dyn} + p_{stat} + p_{atm}$$

pdyn = dynamic pressure (negative), which is determined using CFD methods, see Fig.8.

pstat = static pressure

= $\rho \cdot g \cdot h$

h = distance between the respective point on the rudder and the water surface

ρ = mass density of water

patm = atmospheric pressure

= 103 kPa

If the total pressure p drops below the vapour pressure of water, cavitation may occur, see 8.

Computation of the cavitating flow

The concentration of vapour is computed. For visualization of the cavitation iso-surfaces of the

vapour concentration can be plotted. The comparison of observed cavitation in experiments and an iso-surface for the computed cavitation volume is difficult for different reasons. The observer in experiments interprets subjectively which region he associates with cavitation and which cavitation form he associates with which regions. The cavitation impression depends on the visualization. On the other hand, the extent of the computed cavitation depends on the selected vapour concentration. Comparison of CFD computed and measured cavitation is discussed in [2].

A comparison between observed and CFD computed cavitation volume on a hydrofoil is shown in Fig.9. Fig.10 shows results of computed rudder cavitation.

Preventive Measures [1]

Profile selection

Use the appropriate profile shape and thickness, see below. Computational Fluid Dynamic (CFD) analysis for rudder considering the propeller and ship wake can be used. The computational procedure is described above.

Use profiles with a sufficiently small absolute value of pressure coefficient for moderate angles of attack (below 5°). The pressure distribution around the pro-file should be possibly smooth, see Fig.11. The maximum thickness of such profiles is usually located at more than 35 % behind the leading edge [3], [4].

Use a large profile nose radius for rudders operating in propeller slipstream [4].

Use profiles with an inclined (relative to the mean rud-der plane) or curved mean line to decrease the angle of attack. For a right-turning propeller, the rudder nose should be on port side above the propeller axis and on starboard side below the propeller axis, see Fig.13, [3], [5].

Rudder sole cavitation

Round (two-dimensional) out the leading edge curve at rudder sole, see Fig.14, [6].

Propeller hub cavitation

Fit a nacelle (body of revolution) to the rudder. This nacelle functions as an extension of the propeller hub [7].

Cavitation at surface irregularities

Grind and polish all welds.

Avoid changes of profile shape. Often rudders are built with local thickenings (bubbles) and dents to ease fitting of the rudder shaft. Maximum changes in profile, shape should be kept to less than two percent of profile thickness see Fig.5.

Gap cavitation

Round out all edges of the part around the gap.

Gap size should be as small as possible.

Use guiding plates (see. Fig. 15) to reduce the gap size between rudder blade and rudder horn. To avoid flow separations, guiding plates should be in align-ment with rudder profile. The guiding plates are to be welded to the rudder and the weld has to end before the curvature, [8]

Place gaps outside of the propeller slipstream.

General measures [1]

Propeller loading

For ship speeds exceeding 22 knots the propeller loading coefficient (Cth) should sufficiently small, for example smaller than 1.0.

$$C_{th} = \frac{30.2 \cdot T}{\rho \cdot \pi \cdot D^2 \cdot (1-w)^2 \cdot v^2}$$

T is the propeller thrust in [kN], D is the propeller diameter in [m], w ist the nominal wake number and v ist the ship speed in [kn].

Cladding

Strips (200mmx7mm) of stainless steel are to be welded on the cavitation endangered area (see. Fig. 16), [9] .Special attention is to be paid towards the welding procedure.

Explosive cladded plates can also be used for cladding. These need not to be strips, but can also be plates covering a larger area of the cavitation endangered area, [9]

Coating

Apply a special soft surface coating, see Fig.17.

Apply a high abrasion-resistant surface coating (for example special surface coating used for icebreakers)

References

[1]   el Moctar, O. " Recommandations for preventive measures to avoid or minimize rudder cavitation" Germanischer Lloyd 2004, TPI-1-1

[2]   Lindenau, O. Bertram, V. "RANSE Simulation of Cavitating Flow at Foil", Ship Technology Research, Vol. 50/2, 2003

[3]   Söding, H. (Ed. Brix, J.E.): Manoeuvring Technical Manual. Seehafen-Verlag, Hamburg, 1993

[4]   el Moctar, O.: Abschätzung und Berechnung der Kavitationsgefahr bei Hydroprofilen mit Feldmethoden. Germanischer Lloyd report No. ESH.2002.161

[5]   Brix, J.E., Baumgarten, B.: Entwicklung eines kavitations- und vibrationsarmen Ruders mit geringem Widerstand und quasisymmetrischem Drehmoment". FDS-Bericht 152/1984, 1984

[6]   Brix, J. E., Nolte, A., Heinzel, S.: Konstruktive Maßnahmen zur Verhinderung der Kavitation an der Rudersohle HANSA 16/1971

[7]   Nishiyama, S.: Experiment on Rudder Cavitation and its Preventive Measure. Proceedings 14th ITTC, Ottawa 1975

[8]   Brehm, Andreas, el Moctar, O. " Prediction of ruudder cavitation using CFD", Germanischer Lloyd report, 2005

[9]   Kray, N., Eickelpoth, M., de Bruyne-Ludwig, T. Germanischer Lloyd, Demage and Repair, Hamburg, 2005

Figures

Fig.1: Bubble cavitation, from [3]

Fig.2: Rudder sole cavitation, GL photo
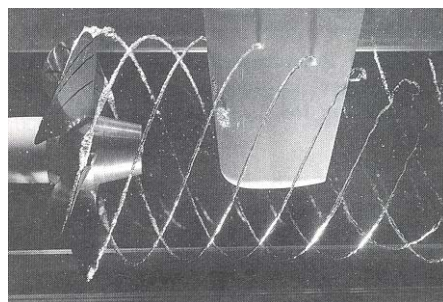
Fig.3: Tip vortex cavitation, from [3]
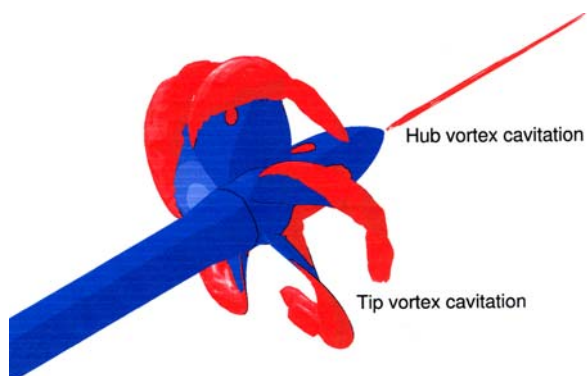
Fig.4: Hub cavitation, GL computation

Fig.5: Example of surface irregularities, GL-CAD mode

Fig.6: Gap cavitation, GL photo
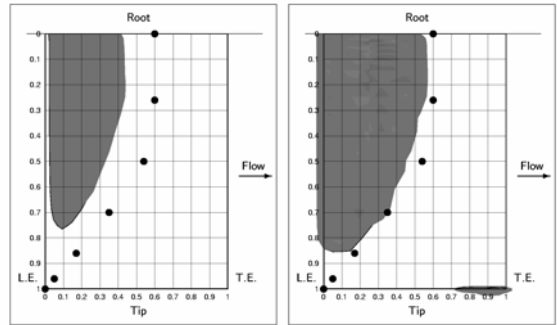
Fig.9: minimum and maximum computed cavitation (grey) compared to average cavitation in experiment, from [2]
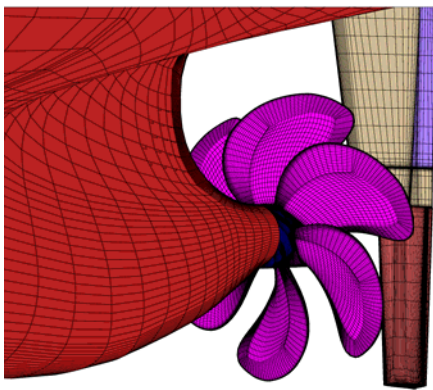
Fig:7: Numerical grid, GL computations
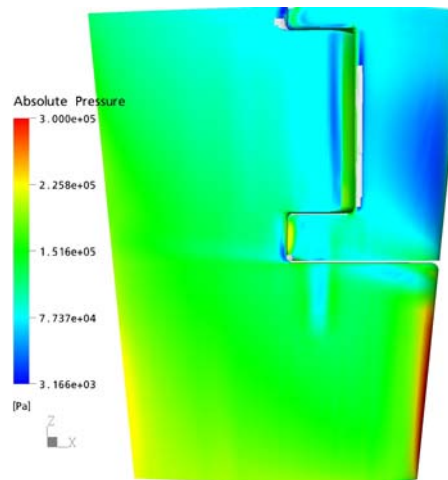
Fig.10: Computed rudder cavitation, GL computation
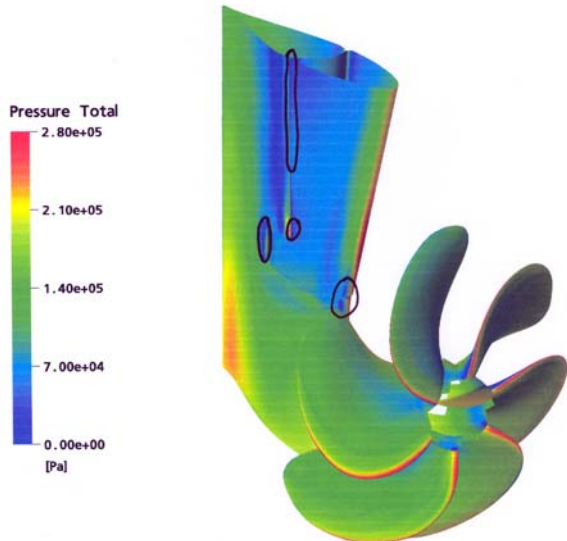
Fig.8: Total pressure distribution on rudder, computed cavitation danger, GL computation
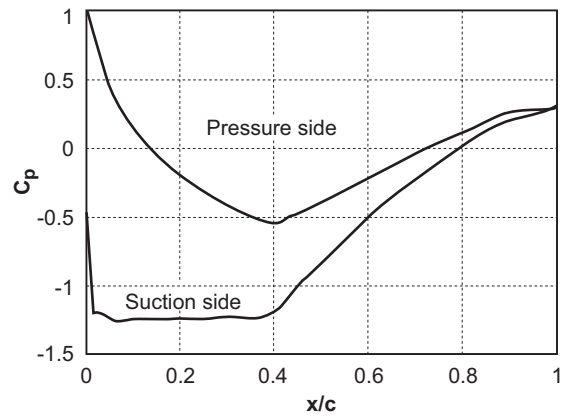
Fig.11: Good example of pressure distribution. Pressure coefficient Cp as function of
x = location along profile length,
c = profile length,
x/c=0=leading edge,
angle of attack=5°, GL computation from [4]
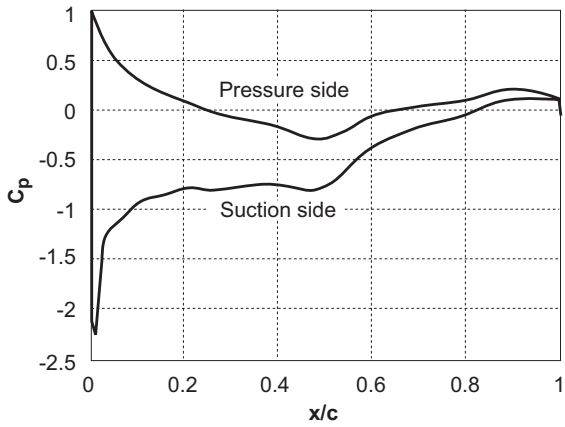
Fig.12: Bad example of pressure distribution, angle of attack=5°, GL computation from [4]
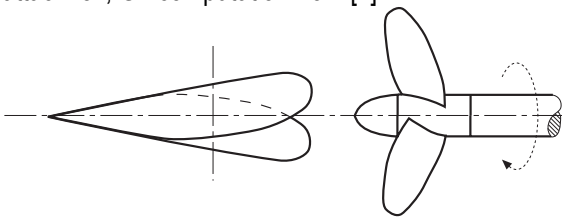
Fig.13: Starcontra rudder
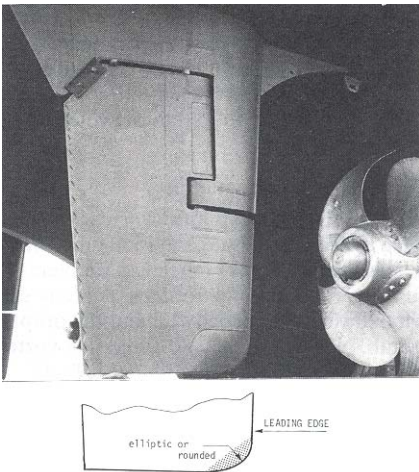
Fig.14: Rounded leading edge, from [3]
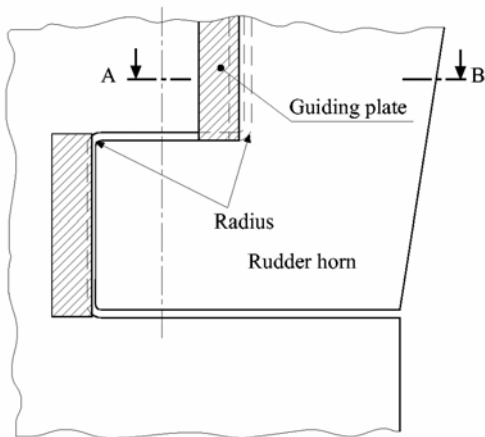
Fig.15: Arrangement of guiding plates, from [1]
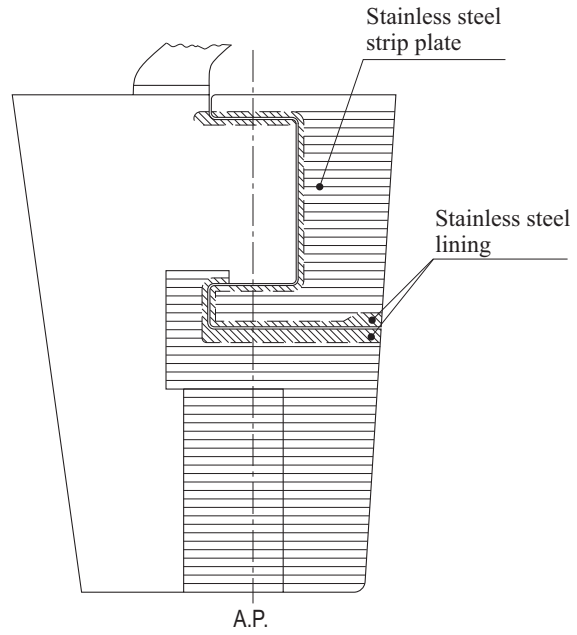
Fig.16: stainless steel strips, GL figure from [1]

Fig.17: Special soft surface coating, GL photo

The Use of Computational Fluid Dynamics in the Optimisation of Marine Current Turbines

R. F. Nicholls-Lee, S. R. Turnock

Abstract—**The use of Computational Fluid Dynamics (CFD) in research and development in industry has become much more commonplace. Technological advances have improved the accuracy of codes although this is at the expense of computational power. CFD is a powerful tool if implemented correctly, and in order to do this it is important to understand when to use the different levels of code. This paper illustrates the relative merits of codes ranging from simple three dimensional panel codes to Reynolds Averaged Navier stokes equations with regards to the optimisation of marine current turbines. It goes on to discuss turbulence models, fluid structure interactions and ultimately design, search and optimisation.**

Index Terms—**Computational Fluid Dynamics, renewable energy, marine current turbine.**

NOTATION

σ	Cavitation number
P_O	Reference static pressure (N/m^2)
P_V	Vapor pressure (N/m^2)
ρ	Water density (kg/m^3)
V	Free stream velocity (m/s)
P_{AT}	Atmospheric pressure (N/m^2)
g	Acceleration due to gravity (m/s^2)
h	Head of water (m)
C_P	Pressure coefficient

I. INTRODUCTION

THE oceans are an untapped resource, capable of making a major contribution to our future energy needs. In the search for a non polluting renewable energy source, there is a push to find an economical way to harness energy from the ocean. There are several different forms of ocean energy that are being investigated as potential sources for power generation. These include thermal energy, wave energy, offshore wind energy, tidal energy and ocean current energy [1], but these can only be applied if the technology can be successfully developed to exploit such resources reliably and cost effectively.

Tidal energy has the advantage of invulnerability to climate

R. F. Nicholls-Lee is with the University of Southampton, Southampton, SO17 1BJ, UK (phone: +44 (23) 8059 6626; fax: +44 (23) 8059 3299; e-mail: rnl@soton.ac.uk).

S. R. Turnock is also with the University of Southampton (e-mail: srt@soton.ac.uk).

change; whereas wind, wave, and hydro are all susceptible to the unpredictable changes in renewable fluxes brought about by shifts of climate regimes. An advantage of the tidal current resource is that, being gravitation bound, it is predictable and quantifiable both spatially and temporally. Devices designed for tidal energy extraction come in a plethora of shapes, sizes and forms although, principally, they are all harnessing either potential energy or kinetic energy from the tide, and converting it into electricity. It is the second group that renewed interest has been focused in the past few years, and it is expected to be this category that a breakthrough is made. Figure 1 illustrates a typical horizontal axis free stream marine current turbine.

Fig. 1. A typical horizontal axis free stream marine current turbine.

Horizontal Axis Tidal Turbine (HATT) design has to confront problems that do not occur when operating such a system in air, and as a result the blade topography will differ from those used on a Horizontal Axis Wind Turbine (HAWT). Due to differences in fluid density, for instance, the thrust on a HATT is typically three times greater than that experienced by a HAWT of a given rated power, despite the tidal device having a significantly smaller swept area. Other forces present on a HATT include increased cyclic loads, cavitation, boundary layer interference and wave loading. The variation in static pressure and velocity across the vertical water column also impose interesting dynamic effects on the rotor blades [2].

Many tidal sites are relatively bi-directional, however, some sites can have flow reversal of 20° or more away from 180° such as the flow around islands [3] and headlands [4] e.g.: Portland Bill, UK, where a swing upon flow reversal of around 35° from rectilinearity is apparent. It has been shown

by experimentation and calculation that an increase in turbine yaw angle causes a consistent power decrease and thus a fully rectilinear flow is more desirable [5].

Computational fluid dynamics (CFD) is one of the branches of fluid mechanics that uses numerical methods and algorithms to solve and analyze problems that involve fluid flows. CFD is a powerful tool which, when used either singly or in conjunction with other tools, can provide vital information as to the performance of a marine current turbine in varying flow conditions. As well as obtaining the turbine performance data, lift and drag that can be converted into thrust, torque and power estimates, and also pressure distribution on the device enabling computation of likely cavitation, CFD can give a detailed picture of the flow around the turbine enabling a more advanced outlook on possible environmental problems such as scour, erosion and the change in tidal magnitude to be understood and also provides vital data regarding the positioning of tidal device arrays.

This paper aims to discuss the benefits and disadvantages of the more common CFD techniques and turbulence models. It will then proceed to consider the further uses of CFD in conjunction with other analysis techniques such as fluid structure interactions. Ultimately a discussion into the relevancy of design, search and optimisation with respect to complex fluid modelling is undertaken.

II. PANEL METHODS

The fundamental basis of any CFD problem are the Navier-Stokes equations, which define any single-phase fluid flow. These equations can be simplified by removing terms describing viscosity to yield the Euler equations. Further simplification, by removing terms describing vorticity yields the full potential equations. Finally, these equations can be linearised to yield the linearised potential equations.

A. Two Dimensional Analysis

Historically, methods were first developed to solve the Linearised Potential equations. Two-dimensional methods, using conformal transformations of the flow about a cylinder to the flow about an airfoil were developed in the 1930s; the computer power available paced development of three-dimensional methods.

In the two-dimensional realm, quite a number of Panel Codes have been developed for airfoil analysis and design. These codes typically have a boundary layer analysis included, so that viscous effects can be modelled. Some incorporate coupled boundary layer codes for airfoil analysis work. Codes such as XFOIL use a conformal transformation and an inverse panel method for airfoil design. XFOIL is a linear vorticity stream function panel method with a viscous boundary layer and wake model and has been found to be suitable for producing section performance data and cavitation criteria for a marine current turbine at the preliminary design stage [6], although care should be taken to recall the apparent underestimation of drag and the overestimation of leading edge pressure coefficient [7].

Two dimensional analyses can be achieved using most CFD programs, although some are more suited to the technique. Section performance data at this stage includes the lift and drag coefficients of differing sections from which estimates of the power, thrust and torque on the turbine rotor and structure can be attained.

Evaluation of ventilation and cavitation of marine current turbine blades are required in the design process. Cavitation inception is assumed to occur when the local pressure on the section falls to, or below, that of the vapour pressure of the fluid. Cavitation tends to occur towards the ends of the blades on the face and near the tip reducing the efficiency of the blades and thus the turbine as a whole, as well as possible erosion of the blade material. Experimental evidence suggests that tidal turbines may experience strong and unstable sheet and cloud cavitation, and tip vortices at a shallow depth of shaft submergence [8]. Figure 2 illustrates a model turbine in a cavitation tunnel exhibiting both sheet and cloud cavitation, and tip vortices.
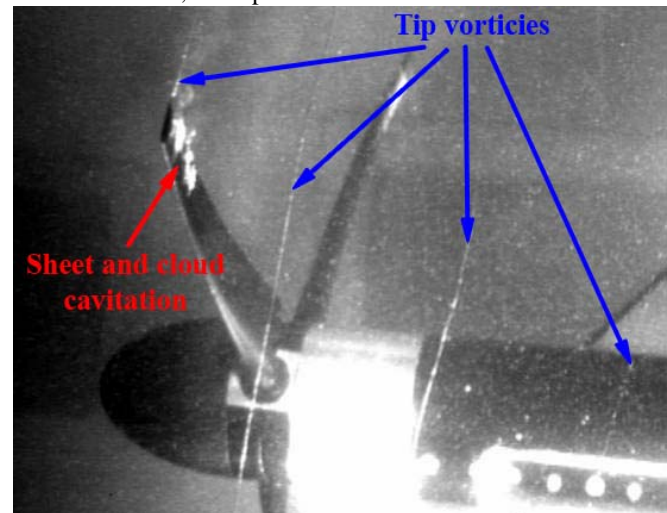
Fig. 2. Cavitation on a model turbine on test in a cavitation tunnel [9]

Cavitation number is defined as:

$$\sigma = \frac{P_O - P_V}{0.5\rho V^2} = \frac{P_{AT} + \rho gh - P_V}{0.5\rho V^2} = -C_P . \qquad (1)$$

Cavitation inception can be predicted from the pressure distribution since cavitation will occur when $P_L = P_V$, or the minimum negative pressure coefficient, $-C_P$, is equal to σ. Figure 3 illustrates a typical pressure distribution over a changing foil section as the result of a two dimensional analysis. The greater the pressure peak on the surface of the foil the more likely cavitation is to occur at this point. It can be observed that as the section trailing edge deflection is increased, the pressure peak decreases thus reducing cavitation inception at this angle of attack.

Some two dimensional analysis codes also provide fundamental section structural characteristics such as second moment of area, with minor modifications to the base section made within the program. This data can be used for basic structural analysis of the turbine blade which is important at this stage in the design process. Computational times are very

short – in the order of seconds.
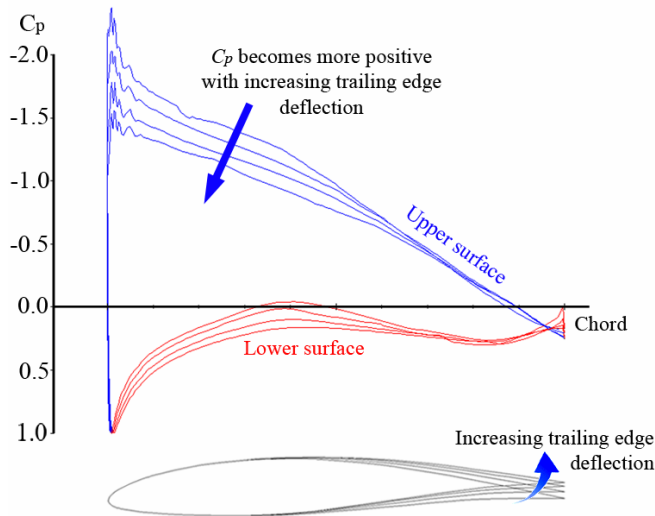
Fig. 3. Pressure distribution over the NACA 63-815 section with a variation in the deflection of the latter part of the foil at an angle of attack of 8°.

The process is very easy to parameterise and optimise due to its simplicity. Two dimensional analyses prove a powerful tool at the preliminary design stage for a tidal turbine and should not be underestimated at the preliminary design stage, however it is apparent that for more integral design information a more complex code able to model more complex situations in three dimensions is required.

B. Three Dimensional Analysis

Surface panel codes allow a more thorough analysis of the performance of the turbine to be attained. Such codes calculate the characteristics of each panel over the surface of the body under analysis to produce a pressure distribution and lift and drag data for the panel, and ultimately the body as a whole. The codes can be used as a more detailed prediction of cavitation inception on the turbine blades and also as a source of detailed blade loading data for further structural calculations. Since the panels are geometric shapes and are flat, an increased panel density will obviously model a three dimensional, complex curved shape such as a marine current turbine more efficiently.

Surface panel codes are more computationally intensive than two dimensional analysis methods. The panel distribution over the turbine model becomes very important with relation to the accuracy of the results and the time taken for each calculation. However, during previous studies it has been found that an optimum panel distribution can be achieved that maintains the accuracy of the result that comes with a finer distribution but reduces the calculation time to around twenty minutes. Paramaterisation and optimisation of surface panel codes is relatively simple, due to the low process times implementing multiple runs – over 30 at a time – is very feasible. Using a frozen wake model it is possible to reproduce the helical wake characteristic of marine current turbines.

These simple three dimensional analysis codes provide a much more detailed picture of the pressure distribution over the turbine blades and body therefore giving a much more comprehensive picture of areas of the blade at which cavitation will occur. Figure 4 illustrates the pressure distribution of a three bladed marine current turbine obtained from a surface panel code. The areas of red illustrate those parts of the blade where low pressure occurs, i.e. where the pressure coefficient is a minimum and cavitation is likely to occur. Those areas of green are those with a more even pressure, and those nearing blue are areas tending towards stagnation.
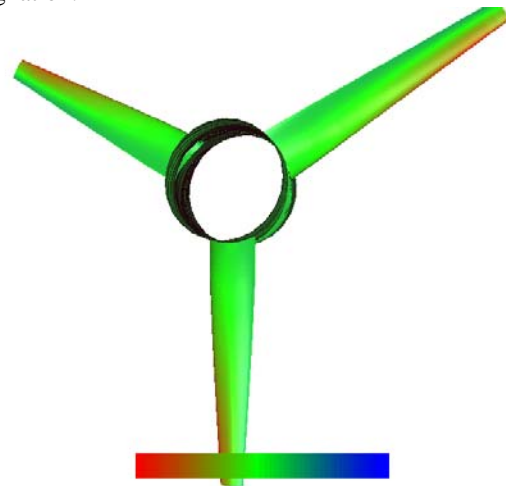
Fig. 4. Pressure distribution over a three bladed turbine obtained using a surface panel code.

Surface panel codes however, struggle to measure severe changes in the flow regime, i.e. stagnation and recirculation. Despite being a powerful tool to predict cavitation inception, once cavitation has occurred the analysis becomes unstable and is unable to complete. It is therefore apparent that more advanced numerical simulation of the area around the turbine is necessary for a full design.

C. Reynolds Averaged Navier Stokes Equations

The Reynolds-averaged Navier-Stokes (RANS) equations are time-averaged equations of motion for fluid flow. They are primarily used while dealing with turbulent flows. These equations can be used with approximations based on knowledge of the properties of flow turbulence to give approximate averaged solutions to the Navier-Stokes equations.

The nature of RANS equations leads to the need for complex domain discretisation schemes as well as complex modelling with large numbers of elements or cells. This often leads to complex mesh structures on which the equations must be solved, and building such meshes is time consuming.

Turbulent flows contain many unsteady eddies covering a range of sizes and time scales. The RANS equations are averaged in such a manner that unsteady structures of small sizes in space and time are eliminated and become expressed by their mean effects on the flow through the Reynolds, or turbulent, stresses. These stresses need to be interpreted in terms of calculated time-averaged variables in order to close the system of equations thereby rendering them solvable. This

requires the construction of a mathematical model known as a turbulence model, involving additional correlations for the unknown quantities [10].

D. Turbulence Models

Most flows of practical engineering interest are turbulent, and the turbulent mixing of the flow then usually dominates the behaviour of the fluid. The turbulent nature of the flow plays a crucial part in the determination of many relevant engineering parameters, such as frictional drag, flow separation, transition from laminar to turbulent flow, thickness of boundary layers, extent of secondary flows, and spreading of jets and wakes.

It is possible to solve the Navier Stokes Equations directly without any turbulence model. This means that the whole range of spatial and temporal scales of the turbulence must be resolved. Direct numerical simulation (DNS) captures all of the relevant scales of turbulent motion, however this approach is extremely computationally expensive for complex problems, hence the need for turbulence models to represent the smallest scales of fluid motion. The choice of which turbulence model to use, however, is a far from trivial matter.

The simplest turbulence modelling approach rests on the concept of a turbulent viscosity. This relates the turbulent stresses in the RANS equations to the gradients of time averaged velocity similarly to the classical interpretation of viscous stresses in laminar flow by means of the fluid viscosity. Such models are widely used for simple shear flows such as attached boundary layers, jets and wakes. For more complex flows where the state of turbulence is not locally determined but related to the upstream history of the flow, a more sophisticated model is required [10].

The one-equation models attempt to improve on the zero-equation models by using an eddy viscosity that no longer depends purely on the local flow conditions but takes into account the flow history.

Two equation turbulence models are one of the most common type of turbulence models. Models like the k-epsilon model [11] and the k-omega model [12] have become industry standard models and are commonly used for most types of engineering problems. By definition, two equation models include two extra transport equations to represent the turbulent properties of the flow. This allows a two equation model to account for history effects like convection and diffusion of turbulent energy. The performance of two-equation turbulence models deteriorates when the turbulence structure is no longer close to local equilibrium. Various attempts have been made to modify two equation turbulence models to account for strong non-equilibrium effects. For example, the SST (shear stress transport) variation [13], leads to marked improvements in performance for non-equilibrium boundary layer regions such as may be found close to separation.

The two-equation turbulence models are reasonably accurate for fairly simple states of strain but are less accurate for modelling complex strain fields arising from the action of swirl, body forces such as buoyancy or extreme geometrical complexity. The Reynolds stress transport models dispense with notion of turbulent viscosity, and determine the turbulent stresses directly by solving a transport equation for each stress component. This form of model can handle complex strain and can withstand non-equilibrium flows. However, it is complex, expensive to compute, can lead to problems of convergence and also requires boundary conditions for each of the new parameters being solved. For these reasons it has not yet been widely adopted as an industrial tool.

Large eddy simulation (LES) is based on an implication of Kolmogorov's theory of self similarity [14] is that the large eddies of the flow are dependant on the geometry while the smaller scales more universal. This feature allows one to explicitly solve for the large eddies in a calculation and implicitly account for the small eddies by using a subgrid-scale model. This method is more computationally expensive than a RANS model but less so than a DNS solution.

The difficulties associated with the use of the standard LES models, particularly in near-wall regions, has lead to the development of hybrid models that attempt to combine the best aspects of RANS and LES methodologies in a single solution strategy. An example of a hybrid technique is the detached-eddy simulation (DES) approach [15]. This model attempts to treat near-wall regions in a RANS-like manner, and treat the rest of the flow in an LES-like manner.

It should be considered that there is no universally valid general model of turbulence that is accurate for all classes of flows. Validation and calibration of the turbulence model is necessary for all applications. In the context of marine current turbines this can be achieved through wind tunnel testing, tank testing and open water tests.

E. Fluid Structure Interactions

Fluid-structure interactions (FSI), that is interactions of some movable or deformable structure with an internal or surrounding fluid flow, are among the most important and, with respect to both modelling and computational issues, the most challenging multi-physics problems.

FSI occurs when a fluid interacts with a solid structure, exerting pressure that may cause deformation in the structure and, thus, alter the flow of the fluid itself. If a problem involving structure flexure, or possibly adaptive materials is to be analysed it is highly beneficial to couple both the fluid dynamics and the structural analysis programs to produce iterative solutions for complex problems.

In the context of a composite adaptive marine current turbine blade [16], FSI is particularly useful to both analyse and visualise how the blade will respond to the complex varying loads imposed upon it both through vertical and horizontal pressure and velocity fluctuations.

FSI coupled problems are, however, very computational expensive to compute. For complex geometries calculations it is not yet feasible to use such a method, however for simpler problems it can be a very powerful tool when combined with wind tunnel and on site model tests.

III. DESIGN SEARCH AND OPTIMISATION

Design search and optimisation is the term used to describe

the use of formal optimisation methods in design [17]. Literally "to optimise" means: find the solution to a problem, which gives the best results with respect to certain decisional criteria, varying a limited number of variables, and respecting certain constraints. Generally, the optimisation process is the search for the absolute maximum (or minimum) of a function, which depends on certain variables, respecting certain constraint equations [18]. Figure 6 illustrates the "classical" optimisation problem, where the global optimum needs differentiating form the local optimum.
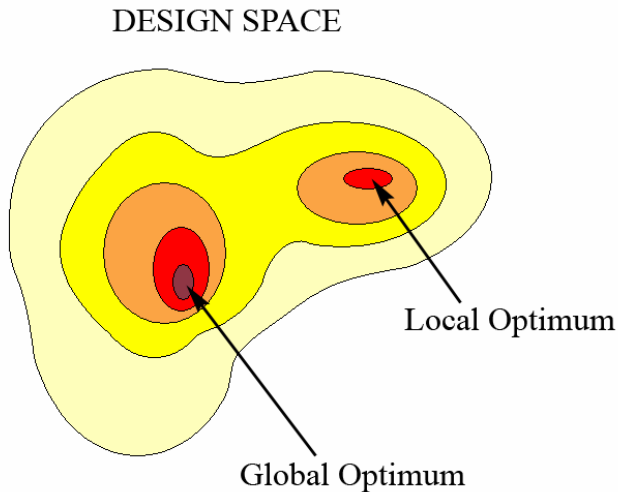

Fig. 6. The "Classical" optimisation problem

Often optimising the design for one variable adversely affects the configuration according to other variables, e.g. minimizing weight and resulting material costs could lower durability. The traditional trial and error approach requires that numerous loops of the design spiral are undertaken which, when using CFD and especially FSI, are both computationally expensive and time consuming. There is therefore an increasing need to use advanced optimisation software to help achieve an optimum design or solution with the minimum effort.

Optimisation algorithms can be classified in different ways. Firstly a distinction can be made between gradient based algorithms and stochastic algorithms, a second between mono-objective algorithms and multi-objective algorithms. Each type of algorithm is applicable to certain design problems, and it is essential to use the correct algorithm for each case in order to determine accurately the global optimum and not any number of local optima that may be present. For example in Figure 6, a gradient approach is as likely to solve to the local optimum as it is to the global optimum, whereas a multi-objective algorithm can differentiate between the two.

The accuracy, robustness and convergence velocity of algorithms are also important. Robustness is the algorithm's capability to find the absolute maximum of the objective function. The accuracy is the algorithm's capability to reach a value as close as possible to the real value of the objective function maximum. The convergence velocity is the number of iterations required to reach the convergence [18].

Other important concepts of the optimisation theory are

Design Of Experiment (DOE), Statistical analysis and Response surfaces. The first two are useful in every optimisation process and particularly if they are used together. Relationships among different variables or among variables and objectives can be selected and the most interesting areas of the objective functions domains may be localised, thus reducing the optimisation calculation time. Response Surfaces are very powerful tools when the calculation time of each single design in an optimisation process is high, a key feature of complex CFD calculations and most FSI coupled problems. A Response Surface approximates the real behaviour of the objective function within its domain and so the total optimisation time drastically decreases.

Most DOE methods seek to efficiently sample the entire design space by building an array of possible designs with relatively even but not constant spacing between the points. In contrast to interpolating data to find results, the data in RSM is regressed to find the global optimum. Traditional methods tend to be less capable of distinguishing between the myriad of local basins and bulges that can occur in more complex engineering problems. A Kriging approach allows the user to control the amount of regression as well as accurately model the user data. It also provides measures of probable errors in the model being built that can be used when assessing where to place any further design points. It also allows for the relative importance of variables to be judged [17].

Figure 7 illustrates a relatively simple composition of trigonometric functions with imbedded polynomial arguments. Under such circumstances, it is essential to use a proper global search strategy. Furthermore, instead of 'exact' solutions, most typically one has to accept diverse numerical approximations to the globally optimal solution (set) and optimum value.
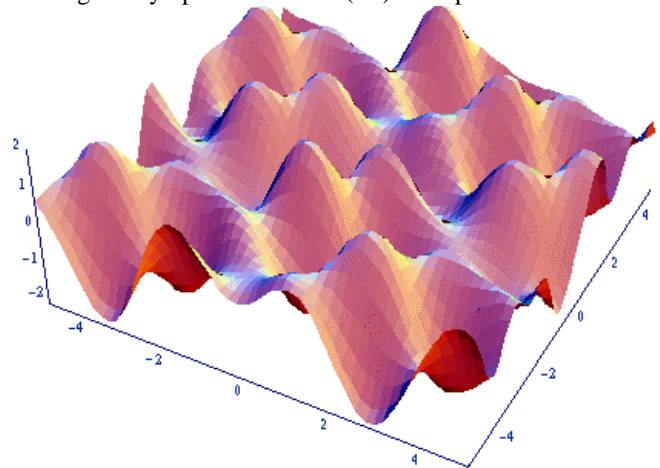
Fig. 7. A more realistic design space for an engineering problem illustrating many local and global maxima and minima.

To carry out high-quality trade-off studies, designers must synthesize and analyze alternative design configurations. To do this cost effectively and quickly requires tools that support automation, evolutions and innovation. Automation stems mainly from the desire to reduce the high costs associated with professional manpower and, at the same time, to reduce

design cycle times. A variety of technologies are coming together in providing a new class of tool that automatically optimizes designs based on multiple variables. Mechanical design synthesis is a next-generation solution combining optimization technologies with CAE simulation methods and parametric CAD into an integrated solution. These types of tools find that optimal part dimensions for resonant frequency is below a certain level, for example, or weight and stress are minimized.

Automated design is now usable (with appropriate care) for relatively straightforward, single discipline problems, however improvements are needed in automatic meshing of complex geometries. CAD geometry parameterization is likely to offer benefits for multidisciplinary optimisation. Engineering judgment in the modelling assumptions, design parameters and design targets is crucial [19].

IV. CONCLUSION

With the need for renewable energy sources becoming ever more important, a focus is being brought to predictable and quantifiable marine sources such as marine currents, or tides. The design and optimisation of tidal energy extraction devices is paramount, as they undergo intense forces in their hostile subsea environment.

CFD is a powerful tool which, when used correctly, can provide valuable data regarding the performance of such devices. It is important not to underestimate the use of simpler CFD techniques, such as panel codes, at the preliminary design stage where an insight into cavitation characteristics and energy extraction can be achieved, justifying the need for further work. At a more advanced design stage RANS solvers are required to model the complex flow situations occurring around the turbines.

Ultimately coupled fluid-structural analysis is required to better understand how the flow affects the structural integrity of both the rotor and supporting structure.

Design, search and optimisation play a key role in the use of computationally expensive processes such as CFD and FEA, and especially FSI. The proper use of optimisation algorithms could significantly reduce the number of design iterations required, producing optimal answers without the expense of huge amounts of both computational and human time.

Whilst all the methods discussed in this paper require validation, be it using wind tunnel tests, towing tank data or open ocean experiments, ultimately the use of CFD, FSI and design, search and optimisation could cut design process times and negate the need for costly testing of model scale devices.

ACKNOWLEDGMENT

REFERENCES

1. VanZwieten, J., Driscoll, F.R., Leonessa, A., and Deane, G., *Design of a Prototype Ocean Current Turbine - Part I: Mathematical Modelling and Dynamics Simulation.* Ocean Engineering, 2006.
2. Fraenkel, P.L., *Power from Marine Currents.* Journal of Power and Energy, 2002. **216**(1): p. 1-14.
3. Myers, L. and Bahaj, A.S., *Simulated Electrical Power Potential Harnessed by Marine Current Turbine Arrays in the Alderney Race.* Journal of Renewable Energy, 2005. **30**: p. 1713-1731.
4. Blunden, L.S. and Bahaj, A.S., *Initial Evaluation of Tidal Stream Energy Resources at Portland Bill, UK.* Journal of Renewable Energy, 2006. **31**: p. 121-132.
5. Batten, W.M.J., Bahaj, A.S., Molland, A.F., and Blunden, L.S., *Yawed Performance of Horizontal Axis Marine Current Turbines*, in *Conference on Renewable Energy in Island Maritime Climate.* 2006: Dublin.
6. Molland, A.F., Bahaj, A.S., Chaplin, J.R., and Batten, W.M.J., *Measurements and Predictions of Forces, Pressures and Cavitation on 2-D Sections Suitable for Marine Current Turbines.* Proceedings of the Institute of Mechanical Engineers, 2004. **218**(M): p. 127-138.
7. Drela, M. and Youngren, H., *XFOIL 6.94 User Guide.* 2001.
8. Wang, D. and Atlar, M., *Experimental Investigation on Cavitation Performance, Noise Characteristics and Slipstream Wash of an Ocean Stream Turbine*, in *World Maritime Technology Conference.* 2006, IMarEST: London.
9. Bahaj, A.S., Molland, A.F., Chaplin, J.R., and Batten, W.M.J., *Power and Thrust Measurements of Marine Current Turbines Under Various Hydrodynamic Flow Conditions in a Cavitation Tunnel and a Towing Tank.* Renewable Energy, 2007. **32**(3): p. 407-426.
10. Atkins, W., *MARNET Best Practice Guidelines for Marine Applications of Computational Fluid Dynamics.* 2003, MARNET.
11. Launder, B. and Spalding, D., *The Numerical Computation of Turbulent Flows.* Computer Methods in Applied Mechanics and Engineering, 1974. **3**: p. 269-289.
12. Wilcox, D., *Turbulence Modelling for CFD.* 2nd ed. ed. 1998: DCW Industries.
13. Menter, F., *Zonal Two Equation k-w Turbulence Models for Aerodynamic Flows.* 1993, AIAA Paper.
14. Kolmogorov, A., *Dissipation of Energy in a Locally Isotropic Turbulence.* Doklady Akad. Nauk SSSR, 1941. **32**.
15. Spalart, P., Jou, W., Strelets, M., and Allmaras, S., *Comments on the Feasibility of LES for Wings, and on a Hybrid RANS/LES Approach*, in *1st AFOSR Int/ Conference on DNS/LES.* 1997, Greyden Press: Rustin, LA.
16. Nicholls-Lee, R. and Turnock, S., *Enhancing Performance of a Horizontal Axis Tidal Turbine using Adaptive Blades*, in *Oceans '07.* 2007, IEEE: Aberdeen, Scotland.
17. Keane, A. and Nair, P., *Computational Approaches for Aerospace Design The Pursuit of Excellence.* 2005, Chichester: John Wiley & Sons, Ltd.
18. Campos, F., Weston, S., and Schumacher, T., *Automatic Optimisation of CFD Engineered Designs*, in *Automated Design & Optimisation Techniques Using CFD.* 2006, IMechE: London, UK.
19. Chew, J., Doherty, J., Gillian, M., and Hills, N., *Practical Applications of Automated Design and Optimisation Techniques using CFD*, in *Automated Design & Optimisation Techniques Using CFD.* 2006, IMechE: London, UK.

Rachel F. Nicholls-Lee was awarded a Master of Engineering with First Class Honours in Ship Science (Yacht and Small Craft) at the University of Southampton, Southampton, United Kingdom in 2004. She worked as a Naval Architect from 2004-2006 and is currently studying towards a PhD researching adaptive materials and their use in free stream tidal turbine blade design at the University of Southampton.

Stephen R. Turnock is a Senior Lecturer in Ship Science in the School of Engineering Sciences. He joined the University of Southampton in 1988 to work on wind turbine section design and completed a PhD in ship rudder-propeller interaction in 1993. His main areas of research lie in the synthesis of computational and experimental fluid dynamics techniques for maritime design. Recent has been in the areas of autonomous underwater vehicles, tidal turbines and in sports engineering.

A Simplified Approach to Investigate Fluid-Structure Coupling Effects on Slamming Loads of Ships

Jan Oberhagemann (Germanischer Lloyd)
jan.oberhagemann@gl-group.com

Ould el Moctar (Germanischer Lloyd)
ould.el-moctar@gl-group.com

ABSTRACT

In this paper we will present an algorithm to consider hydroelastic effects during transient RANS computations of hydrodynamic loads of ships in a seaway. Rigid and elastic motions of the ship are treated seperately by solving different equations of motion. The fluid grid is updated according to the nonlinear rigid body motions and the linear elastic deformations. In order to save computation time, the ship structure will be represented by a finite element beam allowing to compute hull vibrations in the fundamental bending modes. This simple structural model is not only efficient by means of computation time, but also permits to update the fluid grid in a fast and straightforward way.

INTRODUCTION

The scope of this work is to present and implement a computational algorithm that takes into account the large scale effects of elasticity of a body during transient fluiddynamic computations, aiming to assess the impact of whipping on the sectional ship loads during slamming events. The presented method will be able to superimpose rigid body motions with elastic deformations, whereas the former can be of large amplitude and the elastic deformations have to be small compared to the rigid body motion. The slamming impact causes an excitation of vibration of the ship structure in a wide range of frequencies. Assuming that the low bending eigenmodes contribute most to the total vibration energy our aim was to use a structure representation that is capable to display only the fundamental hull girder bending vibrations. This suggests to apply a finite element Timoshenko beam oriented in the longitudinal direction of the ship with bending and shear deformation being taken into account. The structural model will be coupled to the commercial RANS solver COMET [3]. This software solves the Reynolds-averaged Navier-Stokes equations in their integral formulation on a finite number of control volumes constituting the solution domain.

An additional conservation equation is solved for the transport of the two involved fluids water and air. For details on the computation method please refer to [2]. The integrated pressure and friction forces on the hull surface excite the rigid and elastic motions of the ship. In return, these motions influence the surrounding fluids. The fluid grid is transformed according to the translations and rotations of the ship and adapted to the vibration displacements of the hull surface.

MATHEMATICAL MODEL

The use of two different solution domains brings up the need to name these two solutions. We will call the fluid solution $\mathbf{W}$, the structure solution will be denoted by $\mathbf{U}$. This distinction is only done for reasons of clearity, but of cause $\mathbf{W}$ and $\mathbf{U}$ are depending on each other. We will make use of two different coordinate reference frames. The first is a Newtonian coordinate system $\mathbf{O}'(\xi, \eta, \zeta)$ which is moving with the mean ship velocity, the second is a local reference frame $\mathbf{O}(x, y, z)$ moving with the center of gravity of the body. The rotary matrix $\mathbf{S}$ performs the transformation from local to global coordinates as the result of the three consecutive Euler rotations:

$$\mathbf{S}_{(\Psi, \Theta, \Phi)} = \mathbf{S}_\Psi \, \mathbf{S}_\Theta \, \mathbf{S}_\Phi \qquad (1)$$

To obtain the position of any material point of the body, its motion will be split into a translatory and rotatory component deriving from the rigid body motion and a component deriving from the elastic displacement relative to the local coordinate frame, see figure 1. $\vec{r}$ is the position vector of any material point of the undeformed body, expressed in local coordinates. Thus, $\vec{r}$ is time independent. Any displacement at the position of $\vec{r}$ caused by deformations of the body will be called $\vec{u}$. In other words, a distinct relation between the undeformed body and the actual configuration is given by $\vec{u}_{(\vec{r},t)}$. The location of a point $\vec{x}$ is the sum of its location vector $\vec{r}$ in the reference configuration and the actual displacement $\vec{u}$. The relation between $\vec{x}$ and $\vec{\xi}$ is then established by:

$$\begin{aligned} \vec{\xi} &= \vec{\xi}_O + \mathbf{S}\vec{x} & (2) \\ &= \vec{\xi}_O + \mathbf{S}(\vec{r} + \vec{u}) & (3) \end{aligned}$$

The translatory and rotary acceleration $\ddot{\vec{\xi}}_O$ and $\dot{\vec{\omega}}$ of the center of gravity are obtained by solving the following equations of motion:

$$\begin{aligned} \vec{F} &= m\ddot{\vec{\xi}}_O & (4) \\ \vec{M} &= \mathbf{SIS}^T \dot{\vec{\omega}} + \vec{\omega} \times \mathbf{SIS}^T \vec{\omega}, & (5) \end{aligned}$$

where $\vec{F}$ and $\vec{M}$ are the external force and moment about $\mathbf{O}$ acting on the body, m is the ships mass and

I is the mass inertia matrix, expressed in the local coordinate frame. The accelerations are integrated twice with the trapezoidal Euler scheme to obtain the position of the center of gravity. For a more detailed description see [1]. Since the elastic deformations of the body will be computed by means of a finite element beam extending in only one space dimension, in the following the body will be divided lengthwise into cross sections. This does not touch the general validity, but leads to a more purposive formulation. We first consider an equilibrium of external fluid force and translatory acceleration force on a cross section of the body,

$$\vec{f} - \mu \ddot{\vec{\xi}}_g = \vec{0} \qquad (6)$$
$$\vec{m} - \vec{\omega} \times \mathbf{SI}_s\mathbf{S}^T\vec{\omega} - \mathbf{SI}_s\mathbf{S}^T\dot{\vec{\omega}} = \vec{0}. \qquad (7)$$

where $\vec{f} = \frac{d\vec{F}}{dx}$ is the fluid force per length, μ the mass per length, $\vec{\xi}_g$ the center of gravity of the section, $\vec{m}$ the external moment per length acting on the section and I_s is the sections mass inertia per length, expressed in coordinates of the local reference frame and related to $\vec{\xi}_g$. Usually we can not assume the equilibrium of forces according to equations 6 and 7 to be valid and hence a corrective force per length $\vec{f}_c$ is introduced:

$$\vec{f} - \mu \ddot{\vec{\xi}}_g = \vec{f}_c \qquad (8)$$

The same has to be done for the equation of rotational acceleration:

$$\vec{m} - \vec{\omega} \times \mathbf{SI}_s\mathbf{S}^T\vec{\omega} - \mathbf{SI}_s\mathbf{S}^T\dot{\vec{\omega}}. = \vec{m}_c \qquad (9)$$

In case the equations 6 and 7 are valid for every single section, the body will not experience elastic deformations. If the $\vec{f}_c$ or $\vec{m}_c$ are non-zero at any station, they will be used to construct the excitation force vector of the elastic deformations. The ship structure will be modelled by a Timoshenko beam that describes vertical displacements and rotations about the ship's horizontal axis. Shear is accounted for by means of a rotation of the beam cross sections, according to an assumed constant transverse distribution of shear stresses. This assumption is equivalent to a planar rotation of the sections. In the following we will use the local coordinate frame to derive the equations of motion of the finite element formulation. f_c^* and m_c^* are the transverse resp. tangential components of the exciting terms $\vec{f}_c$ and $\vec{m}_c$, transformed to the local coordinate system. Transverse force F_c and bending moment M_c are related to f_c^*, m_c^*, the displacement z and the rotation ψ by:

$$z' - \psi = \frac{F_c}{GA_S} \quad ; \quad \psi' = \frac{M_c}{EI_y} \qquad (10)$$

$$\frac{d\,F_c}{dx} = f_c^* \quad ; \quad \frac{d\,M_c}{dx} = m_c^*. \qquad (11)$$

E denotes the Young´s modulus, G the shear modulus. I_y is the sectional moment of inertia and A_S the effective shear area. $()' = \frac{d()'}{dx}$ denotes the spatial derivative in longitudinal (x-) direction. The equation of force equilibrium and momentum equilibrium at a cross section can be derived, leading to the differential equations for the displacement and the rotation of the beam sections:

$$(GA_S\,(z' - \psi))' - \mu\ddot{z} = 0 \qquad (12)$$
$$(EI_y\psi')' + GA_S\,(z' - \psi) - \bar{\mu}\ddot{\psi} = 0. \qquad (13)$$

$\bar{\mu}$ denotes the mass inertia per length. The finite elements of the beam are assumed to have constant properties E, G, I_y, A_S, μ, $\bar{\mu}$ and a length l_E. Every element has four degrees of freedom, namely the displacement and rotation at both ends of the element. The distribution of displacement and rotation along the element is determined by shape functions of third order. The shape functions are hence applied to compute the elements of the stiffness matrix $\mathbf{M}$ and mass matrix $\mathbf{K}$ as well as the force vector $\hat{\vec{f}}$. The complete derivation can be found in [5]. The result is the system of linear equations

$$\mathbf{M}\,\vec{a} + \mathbf{K}\,\vec{d} = \hat{\vec{f}}, \qquad (14)$$

where $\vec{d}$ is the vector of nodal displacements and rotations, $\vec{a}$ its second time derivative. Equation 14 is solved for $\vec{a}$ and time integration is done with the second order Newmark scheme. The solution procedure is described in [4].

The solutions $\mathbf{U}^n$ and $\mathbf{W}^n$ are solved in every time step. The described method allows for both implicit or explicit coupling. Implicit coupling requires iterative computation of both solutions $\mathbf{U}^n$ and $\mathbf{W}^n$ in each time step since they depend on each other. Hence the grid has to be updated several times. This leads to a significant increase in computation time. Explicit coupling is more favourable with respect to computation time as only one solution couple ($\mathbf{U}^n$,$\mathbf{W}^n$) has to be computed. On the other hand, explicit coupling may lead to unphysical results since $\mathbf{U}^n$ can only depend on solutions $\mathbf{W}^{n-1}$ of previous time steps and vice versa.

GRID DEFORMATION

In the present work only small deformations in the x, z-plane of the beam are considered. This allows to use a very simple grid deformation algorithm without significant loss of mesh quality. The new update $\vec{d}^n$ of the beam nodal displacements z_j and rotations ψ_j is used to obtain the actual deflection line of the

ship body, according to the shape functions. Beyond the edges of the beam a linear shape of the deflection line is assumed. The displacement of the grid node $\vec{x}$ is a superposition of a rotation about $\psi^n_{(\vec{x})}$ and a translation $z^n_{(\vec{x})}$ around the reference point $\vec{x}_{ref}$ on the beam axis. Figure 2 sketches the deformation procedure. The grid deformations result in larger relative displacements between adjacent grid nodes far off the hull surface while the relative displacements are smallest close to the hull. Though the expected body deformations are small, cells at the outer regions of the grid can experience a high degree of deformation or even become degenerated. This can be overcome by multiplication of displacement and rotation with a decay function $e^{\sigma_{(\vec{x})}}$ that minimizes the displacements far off the fluid-structure interface. $\sigma_{(\vec{x})}$ is a reduction factor that is based on $r_{(\vec{x})}$ – the distance between the grid node and the nearest point on the beam axis – and a parameter ϱ that can be adjusted depending on the expected deformations and the grid quality.

$$\sigma_{(\vec{x})} = \left\{ \begin{array}{lll} r_{(\vec{x})} \leq r_S & : & 0 \\ r_{(\vec{x})} > r_S & : & \frac{\varrho}{r_S^2}(r_{(\vec{x})} - r_S)^2 \end{array} \right. \qquad (15)$$

r_S is the greatest distance between a grid node at the fluid-structure interface and the beam axis. Figure 3 illustrate an undeformed and deformed grid obtained with this technique.

NUMERICAL RESULTS

To investigate the abilities of the developed code, a simulation for a vessel of 190m length was performed. An impact load was imposed to the ship by a water bubble plunging on on the bow of the ship, while the ship was sailing at zero speed in calm water. The water impact was intended to excite heave and pitch motions as well as elastic vibrations. Both kinds of motions should dampen with time and tend to zero due to hydrodynamic damping. The lengthwise mass distribution was chosen according to the stillwater floating condition in a way that the resulting transverse forces $\vec{f}_c$ and bending moments $\vec{m}_c$ should vanish. Nevertheless, the discretization by a finite number of mass points introduces a small deviation resulting in a non-zero bending moment, see figure 4. The ship mass was set to $m = 16810\,t$, the mass inertia moment about the y-axis was $\mathbf{I}_{2,2} = 33.44 \cdot 10^6\,tm^2$. For the structural representation the ship was segmented into eight beam elements of identical length, bending stiffness and shear stiffness. The latter were arbitrarily set to $EI_y = 2.06 \cdot 10^{10}\,kNm^2$ and $GA_s = 1.585 \cdot 10^8\,kN$, respectively. The fluid computation grid consisted of 281000 cells. Only the port side was modelled.

A computation was performed using explicit coupling and second order explicit time integration. Another computation without elastic deformations was carried out as a reference. For both computations, the fluid forces were averaged over five timesteps to avoid strong oszillations. The time step size was set to $\Delta t = 0.037355\,s$.

Figure 5 shows the ship $0.75\,s$ before and $1.5\,s$ after the water impact. Although the water front of the bubble was not very distinct due to the coarse grid, the impact caused a steep increase of the accelerations acting on the body. Rigid body motions were excited as well as elastic vibrations. In figures 6 and 7 one can obviously observe that the superposed elastic deformations had very small influence on the accelerations and integrated motions of the ships center of gravity. On the other hand, the vibrations increased the maximum occuring section bending moments and transverse forces, see figure 8 for the longitudinal distribution of the bending moment.

Elastic vibrations were expected to be excited in a wide range of frequencies. Figure 9 shows the accelerations computed for selected element nodes. The excitation decreased with time and tended to zero. The corresponding nodal displacements show a strong domination of the two-node bending mode, and in the time series a vibration corresponding to the eigenfrequency and eigenmode can be found three seconds after the impact. The deformations in the time between the impact and this time instant can not be related to a single eigenfrequency, see figure 10. As can be seen in figure 11, the vibration deformations decayed and were almost zero at the end of the computation.

CONCLUSIONS

The described method seems to produce reasonable results. Although the elastic deformations in the presented simulation were not small, the influence on the numerical stability and convergence behaviour was neglectable. A clear distinction between nonlinear rigid body motions and linear elastic deformations has been established, allowing for a simplified treatment of fluid structure interaction. Further on, the applicablity of an explicit coupling scheme also reduces the computational effort needed to take whipping effects into account. The time spent for solving the timoshenko equations and updating the grid was about 16.5 percent of the overall computation time.

References

[1] BRUNSWIG, J. : *Prediction of Ship Motions in Waves using RANSE*, University of Technology Hamburg-Harburg, Diplomarbeit, 2004

[2] FERZIGER, J. ; PERIĆ, M. : *Computational Methods for Fluid Dynamics*. 3rd. Berlin Heidelberg New York : Springer Verlag, 2002

[3] ICCM: *User Manual COMET*. 2.0. Hamburg : Institute of Computational Continuum Mechanics GmbH, 2000

[4] OBERHAGEMANN, J. : *A Computational Method to Assess Effects of Whipping on Global Loads of Ships*, University of Technology Hamburg-Harburg, Diplomarbeit, 2006

[5] SÖDING, H. : *Schiffsvibrationen*. Vorlesungsmanuskript, Institut für Schiffbau der Universität Hamburg, 1987

[6] SÖDING, H. : *Berechnungen der Schwingungen von Timoshenko-Balken, die gleichzeitig große Starrkörperbewegungen ausführen*. 2006. – theoretical considerations
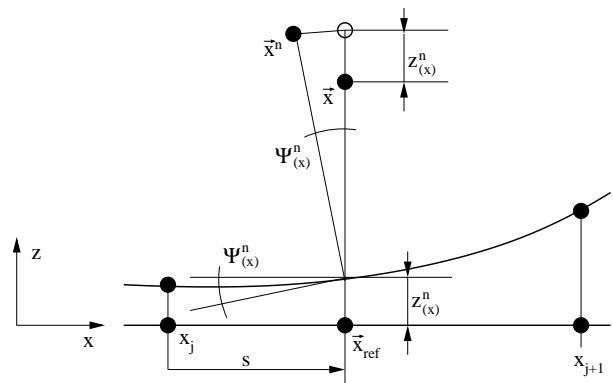
Figure 2: Actual configuration $\vec{x}^n$ of grid node $\vec{x}$ at time instant $t = t_n$
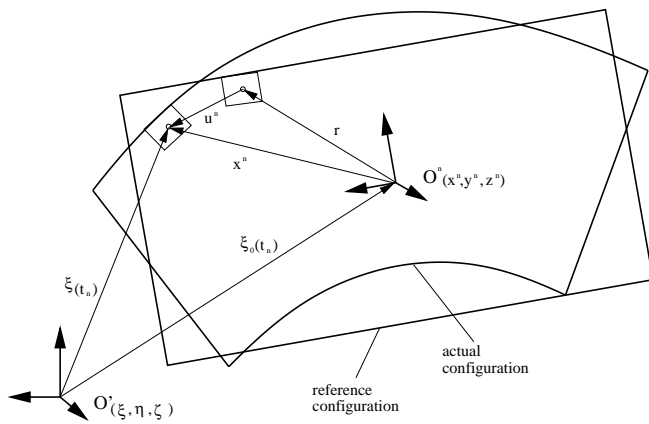

Figure 1: Global and local reference frame, undeformed and actual configuration at time instant $t = t_n$
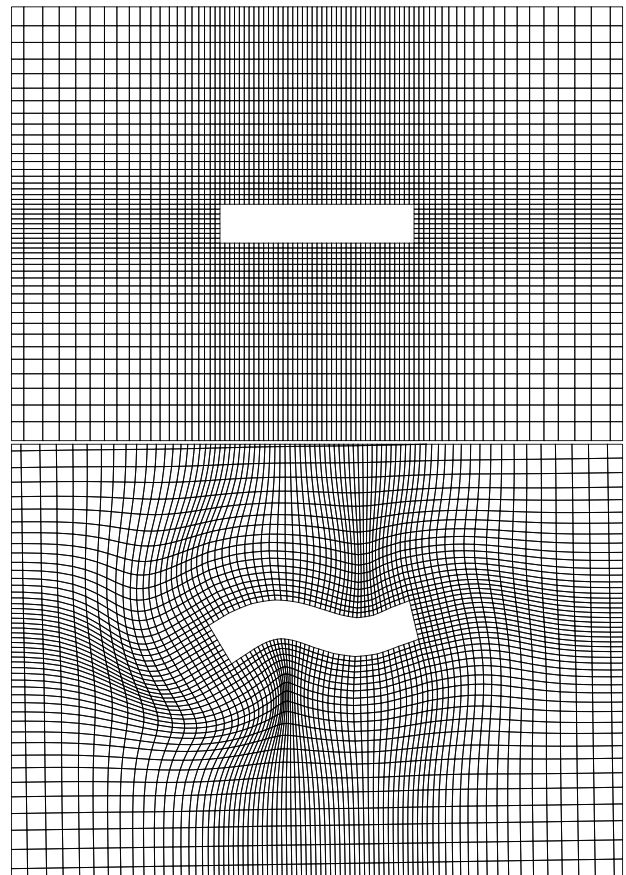

Figure 3: Example of undeformed (top) and deformed grid (bottom)
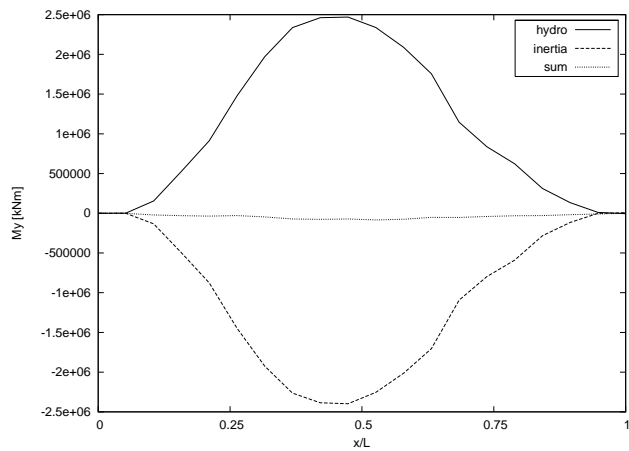
Figure 4: Stillwater bending moment of 190m vessel

Figure 6: Heave and pitch acceleration, Comparison of rigid and elastic ship
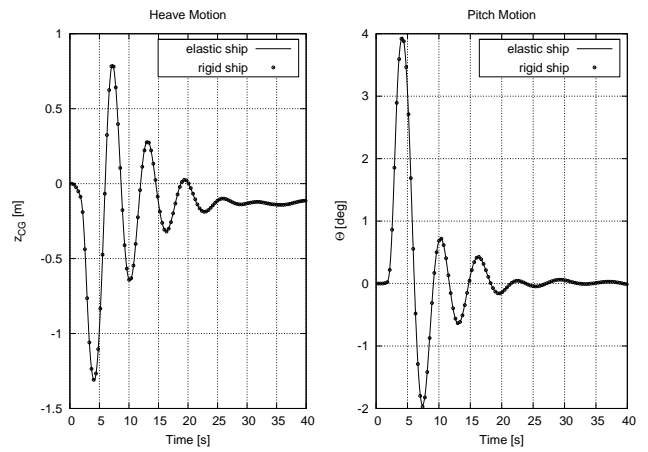
Figure 7: Heave and pitch motion, Comparison of rigid and elastic ship

Figure 5: Ship immediately before and after impact

Figure 8: Distribution of maximum bending moments over ship length

Figure 9: Vertical acceleration of selected element nodes

Figure 10: Vertical displacement of selected element nodes

Figure 11: Time series of vertical displacements at element nodes

Prediction of Transitional Flows Past Hydrofoils

by

V. Papakonstantinou, P. Katsaridis and G. Tzabiras
(vkpapnav@central.ntua.gr, tzab@fluid.mech.ntua.gr)

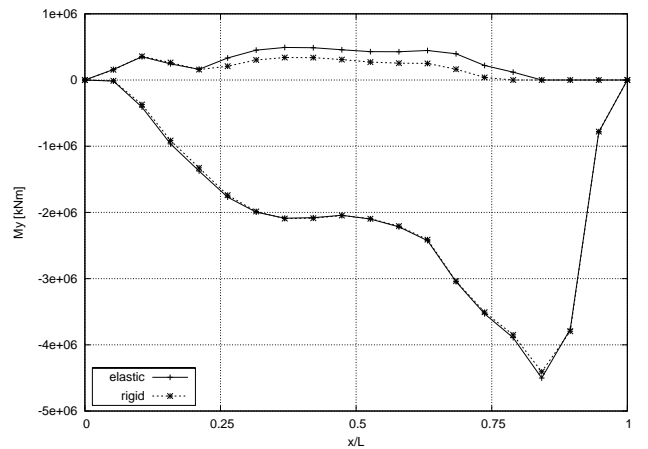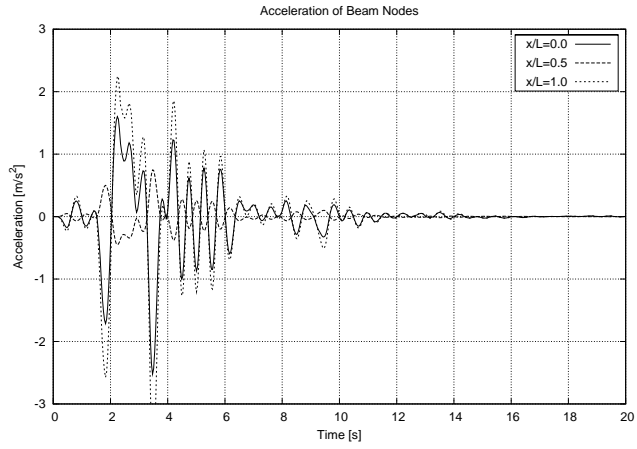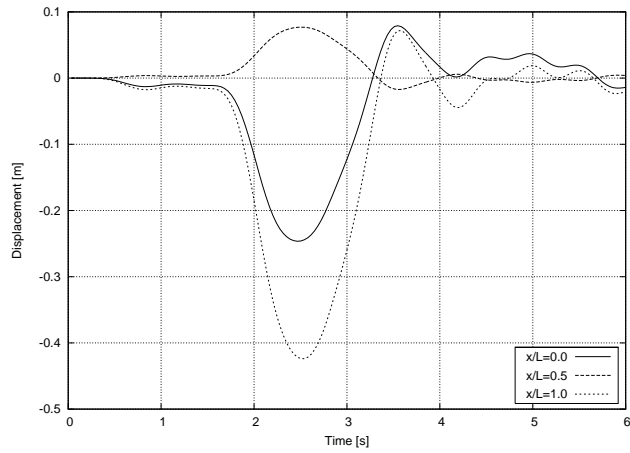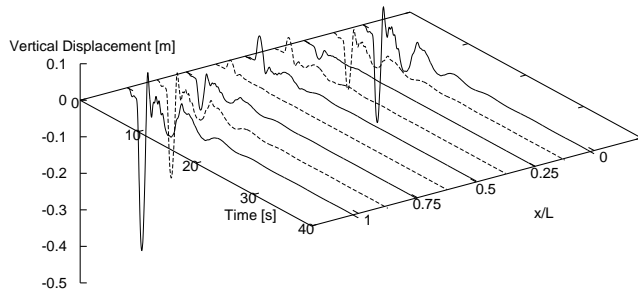School of Naval Architecture and Marine Engineering
National Technical University of Athens

1 Introduction

The calculation of transitional flow past lifting surfaces exhibits special interest in many applications of marine hydrodynamics like, e.g., appendages or yacht keels which may affect considerably the resistance components. Owing to their restricted length (with respect to the body) such appendages subject to extended laminar flow regions. In general, the computation of external transitional flows is a quite complicated task even in 2D problems. Sophisticated approaches have been developed to solve the problem for complex flow situations, e.g. [1]. However, there are cases where simpler tools can be applied to calculate adequately the lift and drag characteristics [2]. The calculation of transitional flows past hydrofoils at angles of incidence below stall is a characteristic example. The scope of this work is to employ simplified and empirical tools that can be easily involved in CFD codes in order to perform free-transition computations and to compare the calculated results with available experimental data.

2 The numerical method

The RANS equations past the hydrofoil are solved numerically in a C-type orthogonal grid generated by the conformal mapping technique [3]. In this system, the velocity components are aligned with the grid lines. The flow is characterized by three zones: laminar, transitional and turbulent. The Reynolds stresses in the transitional and fully turbulent part are calculated through the eddy-viscosity k-ω-*SST* model of Menter [4]. The transport equations are integrated in staggered control volumes and their discretization leads to the standard form of non-linear algebraic equations [5]. Diffusion terms are approximated by the classical second order finite differences being always positive in orthogonal systems. A second order scheme is applied for the convection terms [6]. It is a MUSCL approximation which requires a limiter function in order to obtain bounded solutions. The compressive minmod limiter function is used in the present calculations.

Boundary conditions are applied on all boundaries of the calculation domain. On the external boundary the velocity components are calculated as components of the undisturbed flow at infinite (Dirichlet conditions). On the same boundary k and ω are set equal to proper limiting values which characterize the laminar flow at the outer part. At the exit boundary non-reflecting boundary conditions for the velocity components and the pressure are applied, e.g. [5]. Finally, since all transport equations are solved up to the solid boundary (wall) the velocity components and the turbulent kinetic energy k are set equal to zero on it. To apply this condition, the adjacent to the wall nodes should lie in the laminar sub-layer region. Besides, a Dirichlet boundary condition for ω is imposed on the first node next to the wall so that the eddy viscosity follows the standard zero-equation model.

The developed technique for the determination of the transition area is based on the calculation of the boundary layer parameters in the laminar region around the stagnation point of the hydrofoil, [2]. These parameters are approximated by applying the integral method of Polhausen, [7]. The method requires as input

the velocity distribution at the edge of the boundary layer. This is derived under the Bernoulli equation using the pressure field on the foil contour, which is calculated by the solution of the RANS equations. Then the characteristic boundary layers thicknesses δ, δ_1 and δ_2 are computed. According to [7] the transition zone is defined as the intermittent area between the point of instability *(i)* and the point of transition to turbulence *(tr)*. Instability appears when the Reynolds number based on the displacement thickness exceeds an empirical, critical value Re_{crit}, i.e.

$$Re(\delta_1) = \frac{U(s)\delta_1(s)}{\nu} \geq Re_{crit} \tag{1}$$

In (1), *s* denotes the curvilinear distance from the stagnation point on the leading edge (c_P=1) The location of the transition point is determined when the difference of the δ_2-Reynolds number with respect to the one at the instability point exceeds, again, an empirical, critical value

$$\delta Re(\delta_2)_{crit} = \left(\frac{U\delta_2}{\nu}\right)_{tr} - \left(\frac{U\delta_2}{\nu}\right)_i \tag{2}$$

Evidently, the flow is laminar before the instability point and turbulent after the transition point. A simple interpolation law is assumed to hold in the transitional, intermittent region where the eddy viscosity ν_{ti} is given by:

$$\nu_{ti} = \left(\frac{s - s_i}{s_{tr} - s_i}\right)^2 \nu_{tr} \tag{3}$$

In the same region, the complete *k* equation is solved while, since ν_t is specified by (3), the ω values are explicitly calculated as

$$\omega_i = \frac{k_i}{\nu_{ti}} \tag{4}$$

The steady-state transport equations are solved by the pressure correction method [5] following the steps of the classical SIMPLE algorithm. When the free-transition problem is solved, the procedure includes one more algorithmic step that is, for a specified number of SIMPLE-iterations the transition points are fixed and, then, they are recalculated until the whole procedure converges. Convergence is reached when the non-dimensional sum of the absolute residuals of the discretized momentum and continuity equations becomes lower than a specified value.

3 Test Cases

In order to validate the ability of the adopted method to calculate transitional flows, computations were performed past the NLF(1)-0416 airfoil, for which extended experimental data are available, [8]. Two Reynolds numbers were examined i.e. Re=2x10^6 and Re=4x10^6 and the incidence angles covered the range from 0 to 16 deg. (about stall). The successive grid refinement technique [9] was employed in all applications to accelerate convergence and perform grid dependence studies. Table 1 shows the variation of the position of transition points as well as the lift and drag coefficients at Re=4x10^6 and a=14.23^0. The grid resolution is defined by two numbers, the first denoting points parallel to the foil contour while the second representing points in the normal direction. The external boundaries were placed six chord lengths apart the foil surface and the final non-dimensional y^* values on the adjacent to the wall grid points were below 1 in all cases. Evidently results converge at the finer grids, which is a sequence of the second order scheme that is applied. The finest grid has been used in all applications.

Table 1: Grid dependence tests (Re=4x10^6, α=14.23^o)

Grid	Iterations	x_{tr}/c suction	x_{tr}/c pressure	C_L	C_D
500x75	4056	1.75E-02	6.79E-01	1.89E+00	2.18E-02
1000x150	1956	1.71E-02	6.82E-01	1.89E+00	2.22E-02
2000x300	3480	1.73E-02	6.82E-01	1.88E+00	2.27E-02
4000x600	3900	1.75E-02	6.83E-01	1.88E+00	2.29E-02

`The computed and measured lift (C_L) and drag (C_D) coefficients are plotted in Figs. 1 and 2, corresponding to the two Reynolds numbers. In general, the lift coefficient is in good agreement with the experimental data, except the near-stall region where the turbulence model fails to predict accurately the separation area on suction. The drag coefficient is over-predicted with respect to measurements up to the stall angle, but we should take into account that C_D is much more sensitive in both calculation and experimental procedures. It is also useful to note here, that the calculated pressure field at Re=4x10^6 and a=14.23^0 is in very good agreement with the measured, Fig.3.

Finally, in Figs. 4 and 5 the calculated transition points are plotted vs. the measured, which include also the experimental uncertainty. The location of the transition points depends on both the Reynolds number and the incidence angle. As expected, on the pressure side they move to the trailing edge as the incidence angle becomes higher. Conversely, they move closer to the leading edge when the *Re no* increases, since the flow becomes more turbulent. Opposite trends are observed at the suction side. In any case, calculations show that the adopted empirical method produces satisfactory results at least up to the stall angles.

References

[1] HOLLOWAY, S., WALTERS K. and LEYLEK, J., (2004), *Prediction of unsteady, separated boundary layer over a blunt body for laminar, turbulent and transitional*, International Journal for Numerical Methods in Fluids, 45, pp. 1291-1315

[2] PAPAKONSTATINOU, V., TZABIRAS, G. and VOUTSINAS, S. (2002), The role of transition on the performance characteristics of hydrofoils, 5th NUTT Symposium

[3] TZABIRAS, G., DIMAS, A. and LOUKAKIS, T., (1986), *A numerical method for the calculation of incompressible, steady, separated flows around aerofoils*, Int. J. for Num. Methods in Fluids, 6, pp. 789-809

[4] MENTER, F., (1993), *Zonal two equation turbulence models for aerodynamic flows*, 24th Fluid Dynamics Conference, AIAA, paper no 93-2906, Orlando, Florida

[5] TZABIRAS, G., (1997), *A numerical investigation of 2D, steady free surface flows,* Int. J. for Numerical Methods in Fluids, 25, pp. 567-598.

[6] LIEN F.S., LESCHZINER M.A., (1994), *A general ono-orthogonal collocated finite volume algorithm for turbulent flow at all speeds incorporating second-moment turbulence-transport closure, Part 1: Computational implementation*, Computer methods in applied mechanics and Engineering,114, pp.123-148

[7] SCHLICHTING, H., (1968), *Boundary Layer Theory*, ed. McGraw-Hill.

[8] SOMERS, D. M., (1981), *Design and experimental results for a natural laminar airfoil for general aviation applications*, NASA TP 1861.

[9] TZABIRAS, G., (1992), *A numerical investigation of the Reynolds scale effect on the resistance of bodies of revolution*, Ship Technology Research, 39, pp. 28-44
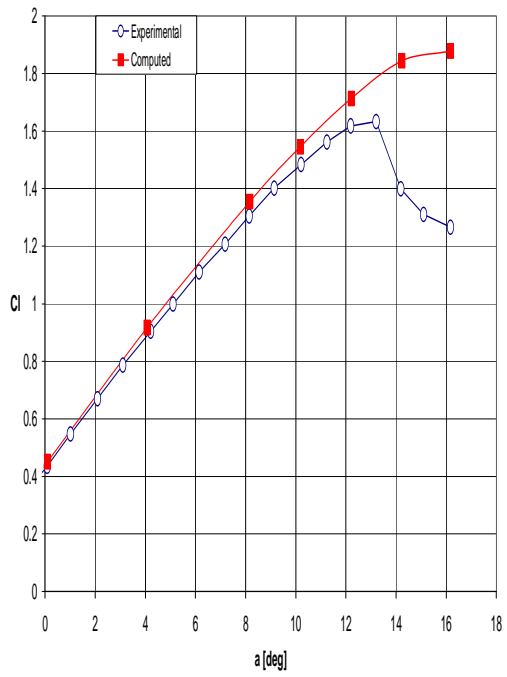
Figure 1a: C_L-a at Re=2x10^6
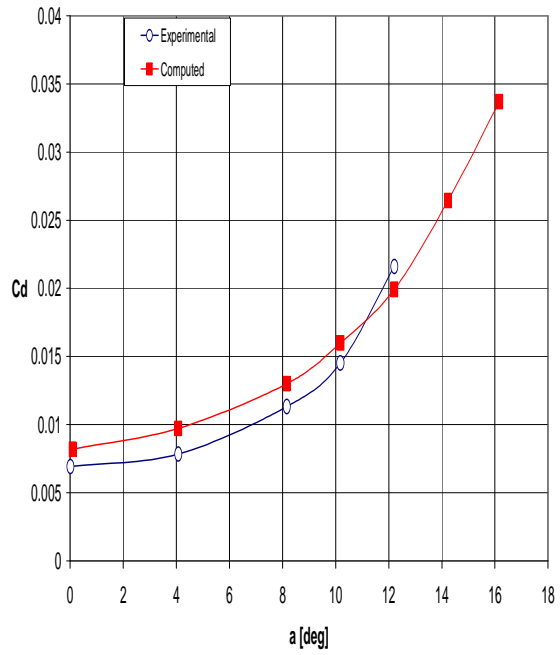
Figure 1b: C_D-a at Re=2x10^6
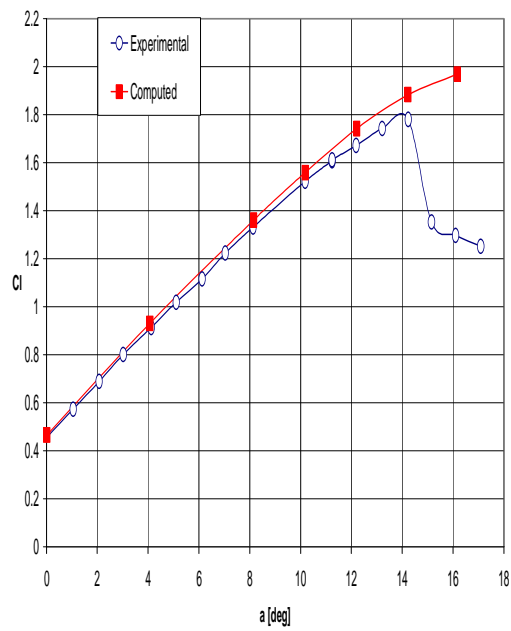
Figure 2a: C_L-a at Re=4x10^6

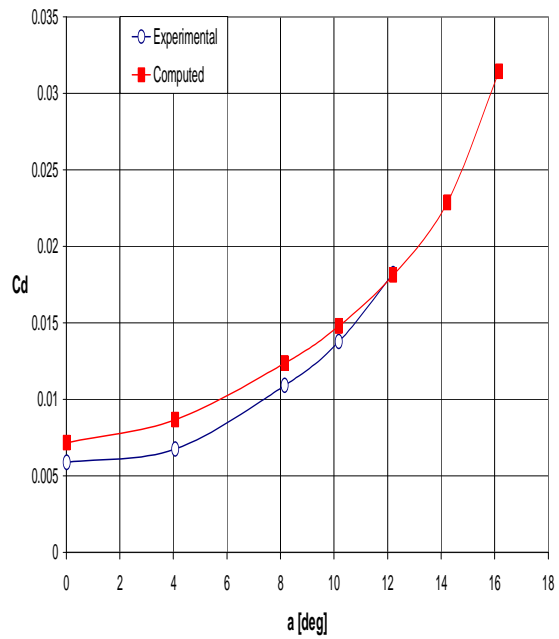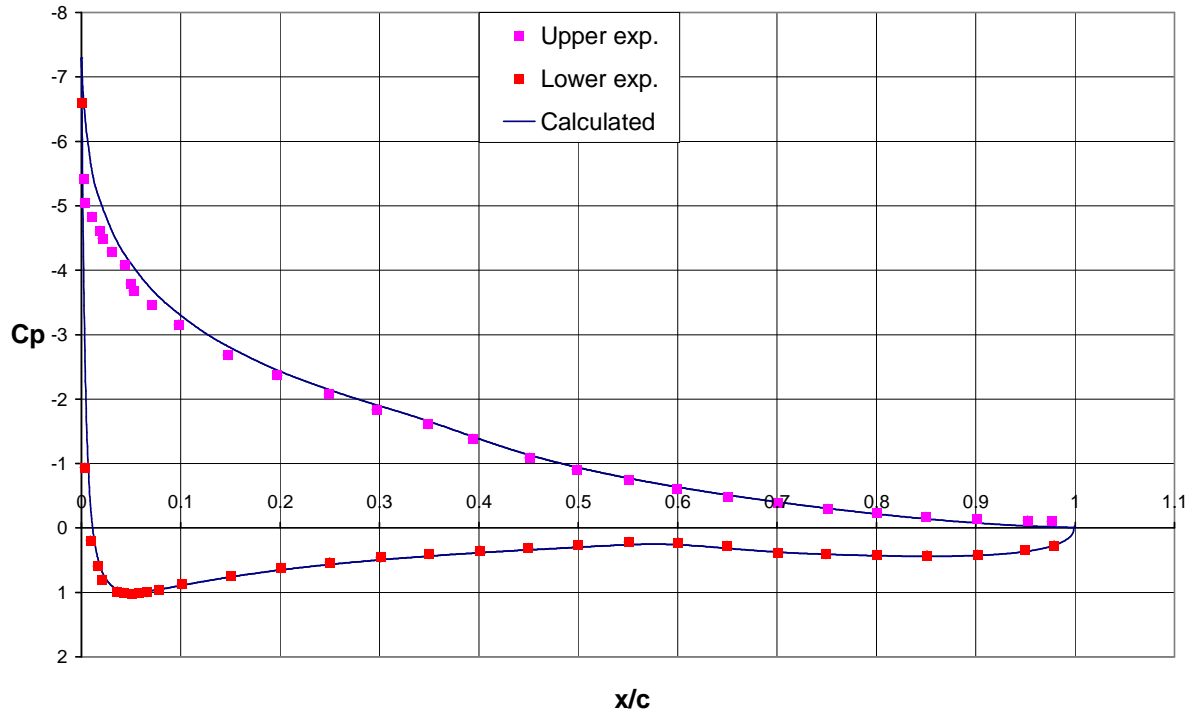Figure 2b: C_D-a at Re=4x10^6

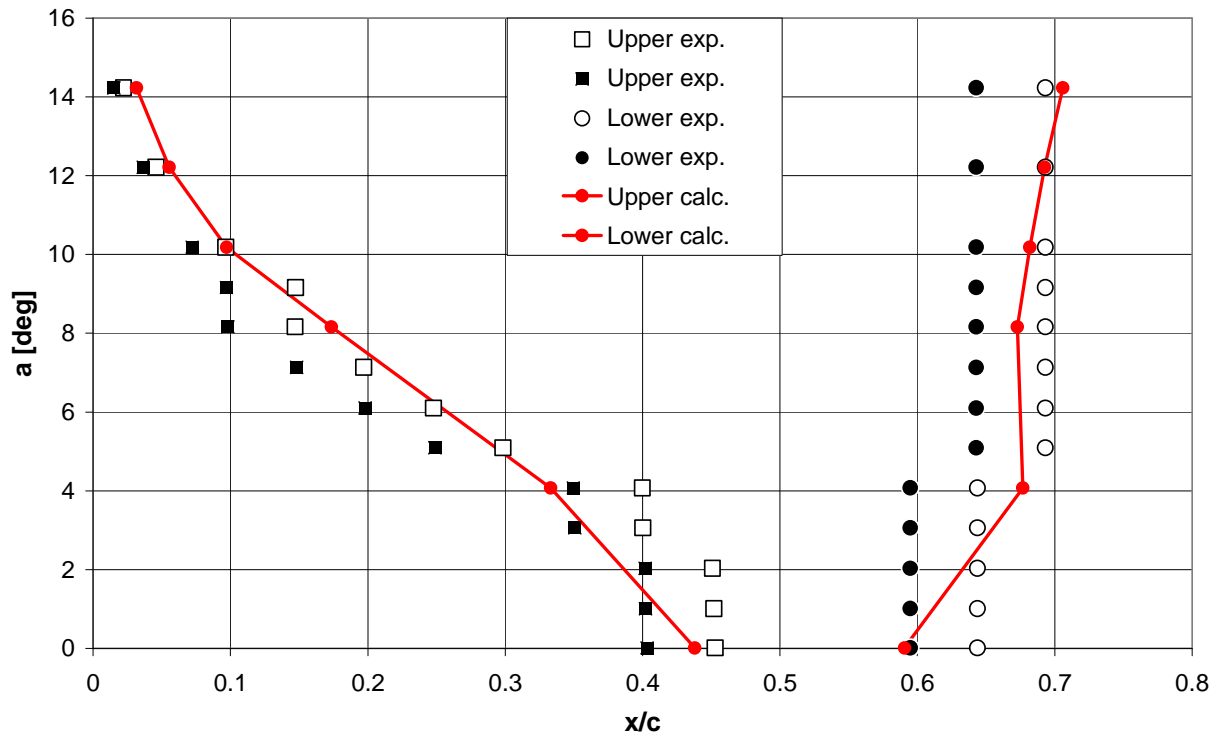Figure 3: c_p-x/c for $Re=4\text{x}10^6$ and $a=14.23^0$

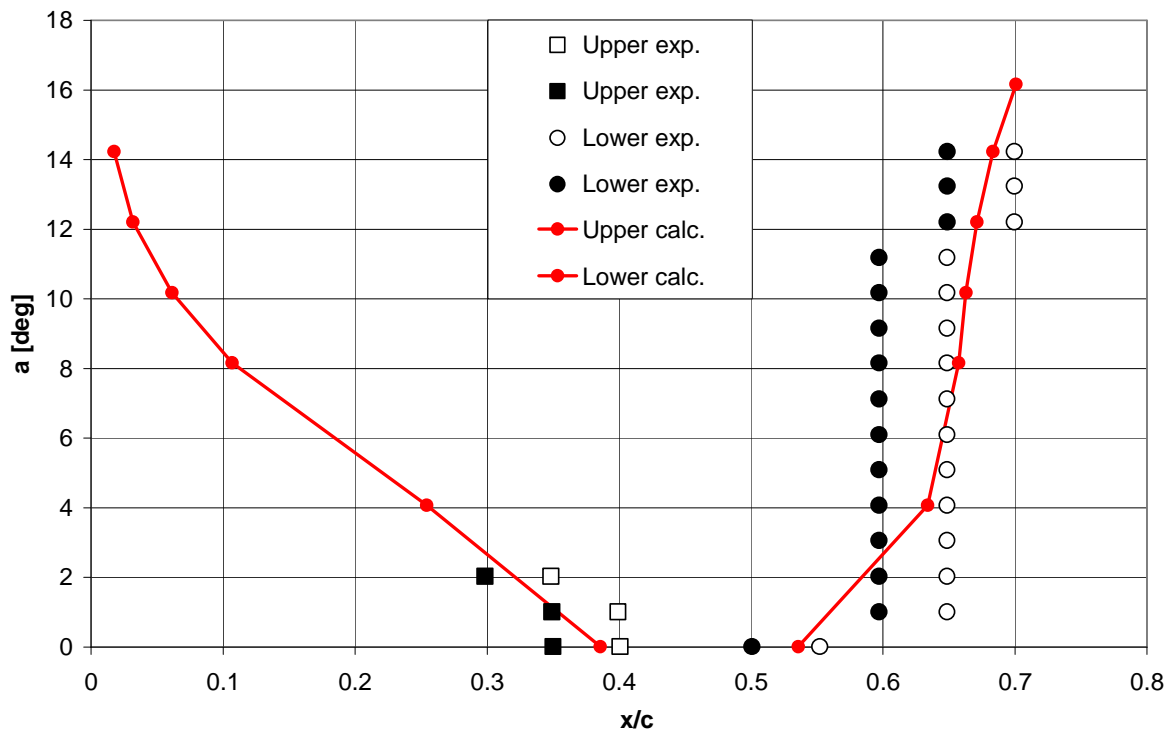Figure 4: Calculated vs. measured transition points, $Re=2\text{x}10^6$

Figure 5: Calculated vs. measured transition points, $Re=4\mathrm{x}10^6$

Marine CFD: Advances of Past Decade and Future Trends

Milovan Perić, CD-adapco, Nürnberg (milovan@de.cd-adapco.com)

This abstract summarizes the author's view of the major advances in CFD for marine applications over the past decade, as well as the expected trends for the future. No equations or graphics are included in the abstract, but animations and pictures will be used in the presentation for illustration purposes.

Although there is a long tradition of using numerical methods for the prediction of flow and body motion in marine research and applications, the past decade has brought an especially large step forward. Several new developments have widened the range of applicability of CFD in marine industry and enabled its routine use, not only in research but also in design and production:

- *Interface-capturing schemes* (VOF, level-set) have been developed, which allow simulation of flows with an arbitrary free-surface deformation, including breaking waves, sloshing and slamming phenomena. The most recent advances in this field enable interface resolution within one control volume and also allow for compressibility effects in both gas and liquid phase to be taken into account. Numerical mixing of the phases has been minimized so that long-term simulations (e.g. sloshing over hundreds of periods of oscillations of tank motion) are now possible. Also, more than two fluids can be involved (e.g. water, oil and air), so that environmental issues related to oil leakage and recovery can be addressed.

- *Automated mesh generation,* starting from a CAD-description of geometry that may include all the details, has become possible, thus reducing the effort to set-up a simulation. Unstructured meshes made of polyhedral control volumes or trimmed Cartesian meshes with local refinement and prism layer along walls to resolve boundary-layer effects are typically used in automatic grid generation tools. The control of mesh quality in important zones (wave resolution at free surface, wake resolution behind appendages, higher resolution around edges and highly curved surfaces etc.) in a user-friendly environment helps to improve the quality of solution and reduces the turn-around time.

- The use of *moving grids* and sliding interfaces has made the simulation of transient effects and hull-propeller-rudder interaction possible (including complex motions like in the case of Voith-Schneider propeller). The optimization of individual components is nowadays being replaced by optimization of the full system, thus accounting for all interaction effects.

- *Turbulence models* have also been improved over the past decade, and their validation in marine applications has resulted in a better understanding of which model works best in which kind of simulation. Especially the Reynolds-stress models (for steady-state results) and large-eddy type simulations of transient phenomena have been found to deliver solutions of acceptable accuracy.

- *Modeling of cavitation* has also been substantially improved, making the prediction of cavitation on propeller and rudder under full-scale and realistic operation conditions (e.g. rotating propeller and moving rudder) with reasonable accuracy

possible.

- *Parallel computing,* accompanied by the availability of relatively cheap but powerful workstation- and PC-clusters has made simulation of complex, transient flow phenomena in marine applications practicable. In addition to domain decomposition in space, methods for a simultaneous computation for several time steps (usually 2 to 5) have been developed, thus reducing simulation times for such applications to acceptable levels, in spite of large number of control volumes and time steps required for accuracy reasons.

- *Coupled simulation of flow and flow-induced motion of floating or flying bodies* has also become a commonplace in recent years. Although still computationally very intensive, such simulations are necessary for the prediction of vessel stability and manoeuvreability under the influence of sea waves. Especially for tanker ships, accounting for the interaction between external sea load on vessel, the internal load due to sloshing in tanks, and vessel motion is important for an accurate prediction of behavior of the whole system. Recently reported simulations of launching of rescue boats – which include the flying phase through the air, water entry, short diving period, and eventually attaining the final floating position – have demonstrated the versatility of modern CFD tools for marine applications.

- *Simulation of fluid-structure interaction* has also been successfully undertaken by several research teams. This involves coupling of CFD-code with usually FE-code that computes structural deformation including flow-induced loads. While in most such simulations an explicit coupling (with data exchange between the two codes once per time step) has been used and structural deformation was not taken into account when computing fluid flow, simulations with a full two-way coupling have also been reported.

The above advances have been documented in many publications and presented at many dedicated conferences and workshops; NuTTS has played an important role in making the marine community aware of the latest developments.

There is no doubt that CFD will in the future be increasingly used in marine industry and all areas related to maritime transportation and environment. It is expected that the following trends, which can be recognized today, will continue in the near future:

- *Wider application of CFD in practice* is anticipated. While it is nowadays routinely used to predict resistance of bare hulls and performance of a propeller in free stream, more and more manufacturers of marine vessels, propulsion devices and other equipment are already adopting CFD as part of their design and optimization process. For example, VOITH as manufacturer of Voith-Schneider propeller (VSP) usually performs simulation of the whole system (hull, VSP, guard plate, other appendages, superstructure), including 6 degrees-of-freedom motion, free surface deformation, wind loads on superstructure etc., for every VSP delivered. In this way it is possible to optimize the performance of VSP for the intended vessel and application conditions, including vessel shape optimization. Such system simulations, requiring close collaboration between manufacturers of each component (hull, propeller, rudder etc.), have to be performed in the early design stage to obtain optimal performance of the final product, rather than optimizing

each component by itself or relying on experience and engineering intuition. It is also expected that in the future more unconventional designs will emerge, to which the experience with more conventional designs cannot be extended.

- CFD will be more and more used as *replacement or complement to experiments*. Especially for new, unconventional designs, CFD will be used for full-scale analysis while experiments will be used for validation of CFD-prediction at model scale when it is deemed necessary. CFD can also be used to determine transfer functions (to extrapolate from model experiments to full scale) or hydrodynamic coefficients (for use in simpler prediction methods). As more and more experience with CFD in practice is gained, it will become obvious where experiments are no longer needed; on the other hand, experiments will in the future become more sophisticated, since their primary role will be to provide various detailed data required for the validation of CFD, rather than just delivering integral quantities like forces or moments.

- *Coupled simulation of flow, motion and deformation* of marine vessels and structures will receive more and more attention in the future. CFD codes are being extended to become applicable to prediction of stresses and deformations in solid structures, but the range of applicability of such monolithic tools will be limited (e.g. to study flow and deformation of propeller blades or rudders). For the vessel or off-shore structures as a whole, coupling of CFD codes and FE-codes for structural analysis is inevitable. The progress in this field is becoming to happen by providing for two-way coupling and iteration between the two codes within one time step. This allows the use of implicit methods with larger time steps and ensures that at the end of each time step, all non-linear effects and coupling of various phenomena is fully taken into account.

- It is expected that within the coming decade CFD will find its way into the *rules of classification societies*. Once the best practices for certain types of simulations are established so that reliable results can be obtained using standard commercial CFD software by a knowledgeable, but non-expert user, classification societies will require that such analysis be performed as part of the design process. Other than increasing performance and fuel economy, safety and environmental issues will become important application areas for CFD in marine industry.

- *Computer performance* will continue increasing and CFD tools will benefit from this development. It is expected that – after the establishment of message-passing interfaces for parallel computing in the past decade – the next generation of parallel computers will require further software adaptation to obtain optimal performance. For example, it is possible that parallelization in time (solving for multiple time steps simultaneously) will be more closely adapted to chip architecture (multiple cores) while parallelization in space (pieces of solution domain assigned to a particular chip) will be performed in a classical way.

Further development of CFD methods in all above-mentioned areas and more know-how from the application of current tools will make CFD an indispensable part of the design and optimization process in marine industry. I am looking forward to the 20th NuTTS in another decade of exciting progress on all fronts!

The use of Computational Fluid Dynamics to Determine the Dynamic Stability of an Autonomous Underwater Vehicle

Alexander Phillips[*], Maaten Furlong[**] & Stephen R Turnock[*]

*Fluid-Structure Interaction Research Group, School of Engineering Sciences, University of Southampton, Highfield, Southampton SO17 1BJ, UK
**National Oceanography Centre, Southampton, European Way, Southampton, SO14 3ZH, UK

Corresponding author's email: abp@soton.ac.uk

Introduction

Various forms of Autonomous Underwater Vehicles (AUVs) have evolved to solve different subsea mission requirements, these can be loosely grouped into two types: torpedo style AUVs and hovering AUVs. Torpedo AUVs were initially developed to be launched from torpedo tubes and consequently resemble torpedoes with a propeller and control surfaces at the rear, these vehicles have poor slow speed maneuverability due to inefficiency of the control surfaces at low speed but have good straight line performance due to their streamlined shape. AUVs of this type are predominantly used for pipeline inspection, environmental monitoring, scientific research and other long range applications.

Hovering AUVs tend to be used for applications where a greater level of slow speed maneuverability is required. These vehicle use a number of thrusters to maintain depth and heading control.

The eventual aim of the program of work under way is to develop specific AUV hull concept design techniques that are robust and reliable. To this end, Computational Fluid Dynamics (CFD) analysis methods are being investigated which combine automated meshing and parametric hull shape definitions to reduce overheads when evaluating the design of a concept AUV hull. Since each AUV application requires varying levels of dynamic stability and maneuverability this work uses steady state CFD analysis to determine numerically the dynamic stability of an AUV. In order to verify the methodology the procedure has been performed for the torpedo style AUV Autosub, (see Fig 1), for which there is suitable experimental data to benchmark the solutions.

Figure 1: Autosub

Autosub is a large AUV developed by a team of engineers and oceanographers at the National Oceanography Centre, Southampton. Autosub's principle dimensions are listed below:

- Length 7 m

- Diameter 0. 9 m

- Speed Range 1.0 - 2 m/s

- Operating Reynolds Number (RN) $5.9 \ 10^6$ - $11.8 \ 10^6$

Autosub is a torpedo shape AUV controlled by four movable control surfaces mounted at the rear of the vessel in a cruciform arrangement. Two vertical rudders control the yaw of the vessel, while two horizontal stern planes adjust the pitch of the vessel. Autosub has been employed in scientific research projects ranging from mapping manganese distributions in a sea loch to ground breaking under ice exploration in the Arctic and Antarctic [9] [10]. Autosub's missions predominantly comprise of long range transit missions where good dynamic stability is an advantage.

The dynamic stability of an AUV in the horizontal determines the vehicles behaviour when disturbed while initially travelling on a straight course with no control plane input.
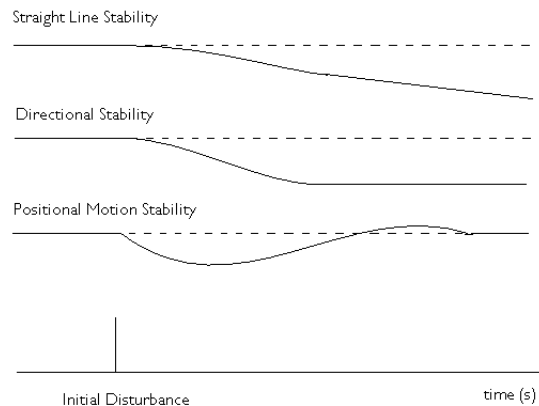

Figure 2: Dynamic Stability

The levels of motion stability are detailed in Figure 2 which illustrates show the response of a vehicle to a disturbance at time zero :-

- Straight line stability - the final course some time after the disturbance is straight but heading is not maintained.

- Directional stability - the final course is straight on the same heading, but with a different position.

- Positional stability - The final path is the same as the initial path.

With zero control input the equations of motion of a submerged vehicle in the horizontal plane reduce to [1]: -

$$(m - Y_{\dot{v}})\dot{v} = Y_v v + (Y_r - mV)r \tag{1}$$

$$(I_{zz} - N_{\dot{r}})\dot{r} = N_v v + Y_r r \tag{2}$$

By applying the Routh stability criteria the determinant of dynamic stability in sway and yaw is:-

$$N_r Y_v - N_v(Y_r - mV) > 0 \tag{3}$$

Dividing through by Y_v and $(Y_r - mV)$ results in

$$\frac{N_r}{(Y_r - mV)} - \frac{N_v}{Y_v} > 0 \tag{4}$$

The first term represents the ratio of the moment caused by yaw rotation divided by the force due to the rotation hence equates to the point of action of the force due to the yaw motion $\bar{x}_r$. Similarly the second term equates to the point of action of the force due to the sway motion $\bar{x}_y$. Hence the criteria for dynamic stability in the horizontal plane is $\bar{x}_r - \bar{x}_y > 0$ For a more detailed discussion see [1].

Rewriting Equation 4 as the horizontal stability margin G_H:-

$$G_H = 1 - \frac{N_v(Y_r - mV)}{N_r Y_v} \tag{5}$$

The calculations are similar in the vertical plane. Since Autosub is axisymetric in the xz and xy planes the stability margin in the vertical plane, G_V, will have the same value as G_H at higher speeds.

Hydrodynamic derivatives N_r, N_v, Y_r and Y_v are traditionally derived from model tests [6] [4] or empirical formulations [7], but have also been derived numerically from invisid flow methods or from observations[5].

Either steady state experiments using a combination of steady state, drift tests and rotating arm experiments or unsteady Planar Motion Mechanism (PMM) tests can be used. For this study the steady state experiments are replicated numerically.

Yawed drift angle tests in a towing tank tests induce a sway velocity (v) component and the corresponding sway force (Y) and yaw moment(N) acting on the model can be deduced and plotted from which Y_v and N_v may be determined from the gradient of the graph.

Rotating arms are used to measure the rotary derivatives of a vessel, by imposing an angular velocity on a vessel by rotating it an at the end of a rotating arm. The vessels centre line is aligned with

the tangent of the circle while the transverse direction is orientated with the arm. By rotating the vessel at a fixed angular velocity (r) a constant surge velocity (u) is imposed u=Rr, where R is the radius of the arm. The transverse velocity v is zero at all times.

The model is rotated at constant linear speed u at various radius R thus varying r while the dynamometer measures the force Y and moment N. These results are plotted and the values Y_r and N_r may be determined from the gradient of the plot.

Experimental rotating arm experiments have several limitations: -

- rotating arm experiments require large specialised and expensive facilities. In order to determine the values of Y_r and N_r at r=0 the radius of the turn R should be large in relation to the vehicle length (L).

- the model must be accelerated and tests performed within a single revolution to ensure the vessel is not disturbed by its own wash, this limits the duration of each run.

By performing virtual tests in a numerical towing tank these limitations can be overcome.

Model scale tests were performed on a 2/3 rd scale model of the Autosub hull form by Kimber et al. [6] at the HASLAR facility (270 m × 12.2 m × 5.5 m deep). Steady state experiments where performed at steady state drift angles of $\pm 0°$, $\pm 2°$, $\pm 4°$, $\pm 6°$, $\pm 8°$ and $\pm 10°$ with a control angle of $0°$. Rotating arm experiments were performed at radius of 13, 17.358 and 26m all at a velocity of 2.69m/s

Method

The fluid flow around Autosub has been modelled using the commercial finite volume code ANSYS CFX 11 (CFX) [3]. For these calculations the fluid's motion is modelled using the incompressible (6), isothermal Reynolds Averaged Navier Stokes (RANS) equations (7) in order to determine the cartesian flow field $(u_i = u, v, w)$ and pressure (p) of the water around an AUV hull:

$$\frac{\partial \overline{U_i}}{\partial x_1} = 0 \tag{6}$$

$$\frac{\partial \overline{U_i}}{\partial t} + \frac{\partial \overline{U_i U_j}}{\partial x_j} = -\frac{1}{\rho}\frac{\partial P}{\partial x_i} + \frac{\partial}{\partial x_j}\left\{\nu\left(\frac{\partial \overline{U_i}}{\partial x_j} + \frac{\partial \overline{U_j}}{\partial x_i}\right)\right\} - \frac{\partial \overline{u_i' u_j'}}{\partial x_j} + f_i \tag{7}$$

By time averaging the Navier Stokes equations to generate the RANS equations, 6 further unknowns have been created, termed the Reynolds stresses: $\frac{\partial \overline{u_i' u_j'}}{\partial x_j}$. Various turbulence models have been proposed to provide solutions to the Reynolds stresses in terms of known quantities to allow closure of the RANS equations [11]. Different turbulence models have been tailored to different types of turbulent flows. The $k - \epsilon$ model is a commonly used turbulence model for engineering simulations due to its robustness and application to a wide range of flows. However it is known to

be poor at locating the onset and extent of separation [2]. An Alternative the Shear Stress Transport (SST) model is better at predicting separation [2] likely to be found at the aft of the AUV.

To determine the relative performance of these two turbulence models both the $k - \epsilon$ and SST model have been used for this study.

The rapid production of high quality grids for a parametric series of AUV orientations is desirable if consistent set of quality meshes are to be produced. For this study, the meshes are produced by careful parameterisation of the AUV hull using Tool Command Language (TCL) script files for driving the meshing package ANSYS ICEM CFD.

Numerical Drift Tests

For the steady state drift tests the scripts produce high quality multi-block structured grids with detailed control over the essential mesh parameters. The fluid domain is defined as a cuboid fixed in space. An inlet boundary condition is positioned 0.5 bodylengths upstream with an inflow velocity of 2.69m/s and a inflow turbulence of 5%. An outlet boundary condition with zero relative pressure is defined 3 body lengths downstream. Free slip wall boundary conditions are applied to the 4 remaining walls which are 3 diameters from the AUV and a no slip boundary condition is applied to the hull, see figure 3
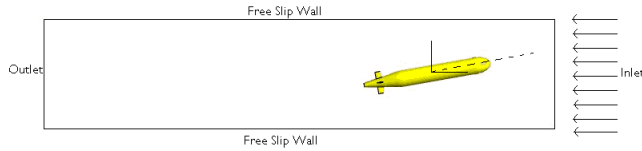

Figure 3: Boundary Conditions for the Numerical Drift Tests

The far field is modelled using a H topology with a O grid topology wrapped around the AUV to give control over the boundary layer parameters. Prior to running simulations the mesh parameters required to adequately model the boundary layer were estimated using the following equations proposed by CFX [3].

The first layer thickness for a desired $y+$ can be estimated from: -

$$\Delta y = L \Delta y^+ \sqrt{80} R_n^{-13/14} \qquad (8)$$

The boundary layer for a blunt body can be estimated using the following equation: -

$$\delta = 0.035 L R_n^{-1/7} \qquad (9)$$

From these equations a first cell thickness of 1mm was selected this results in a $20 \leq \Delta y^+ \leq 200$ with a total of 15 elements within the boundary layer.

Numerical Rotating Arm Experiments

For comparison purposes the rotating arm tests the scripts produce unstructured tetrahedral meshes with inflated prism layers surrounding the AUV.

To replicate the rotary motion the domain is defined as a rotating domain with its origin at the fixed end of the rotating arm. The fluid modelled comprises of a segment of a ring with a rectangular cross section, see figure 4.
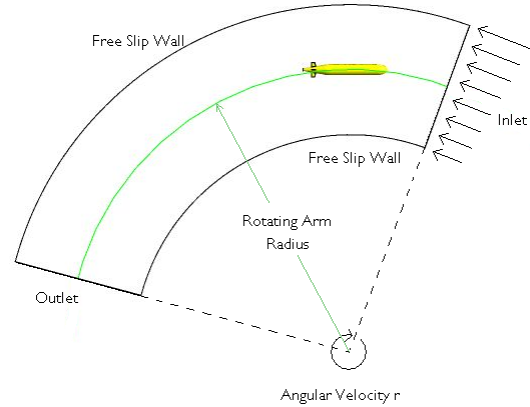

Figure 4: Boundary Conditions for the Numerical Rotating Arm Experiments

For each rotating arm radius the angular velocity is modified to give a velocity of 2.69m/s along the centreline of the AUV.

Computer Simulation

Simulations were run on a high specification desktop pc running 64 bit Windows XP with 4 GB of RAM. Solutions presented have been calculated using the high resolution advection scheme. The residual mass error was reduced by four orders of magnitude and lift and drag forces on the AUV were monitored to ensure convergence. Typical run times were wall clock two hours for completely submerged cases, and twelve hours for simulations including the free surface.

Results

The results are non-dimensionalised by the length of the vehicle (L) the velocity of the vehicle (V) and the density of the fluid (ρ), a prime symbol is used to signify the non dimensional form for example:

$$v' = \frac{v}{V} \qquad (10)$$

$$Y' = \frac{Y}{1/2\rho L^2 V^2} \qquad (11)$$

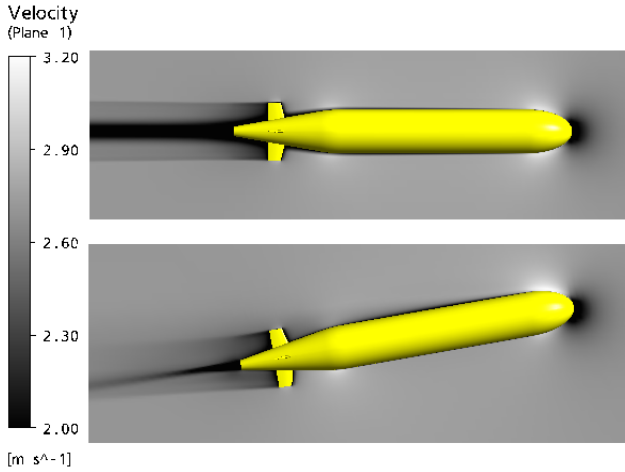$$N' = \frac{N}{1/2\rho L^3 V^2} \qquad (12)$$

Figure 5: Velocity profile about Autosub at 0° *(top)* and 10° *(bottom)* incidence

Drift Tests

Figure 5 compares demonstrates the variation in fluid velocity around the hull at an angle of incidence of 0° and 10°, this equates to a sway velocity of 0m/s and 0.47m/s respectively. Plots of X' versus sway velocity (v'), Y' versus sway velocity (v'), N' versus sway velocity(v') are presented in Figures 6, 7 and 8.
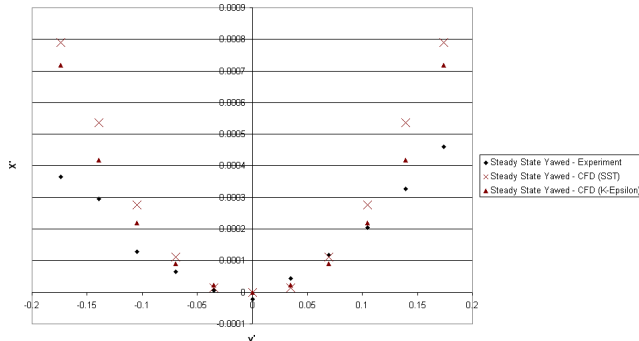

Figure 6: Drift Test - Variation of Surge Force with Sway Velocity

Rotating Arm

Figure 9 illustates the fluid velocity around Autosub in a rotating domain with a radius of 17.328m. Plots of Y' versus yaw velocity (r')and N' versus yaw velocity (r') are presented in Figures 10 and 11.

Dynamic Stability

Table 1compares the numerical and experimental values for the hydrodynamic derivatives derived from gradients of the previous plots.

Entering the results from table 1 into equation 5 gives an experimental stability margin of $G_H = 0.75$
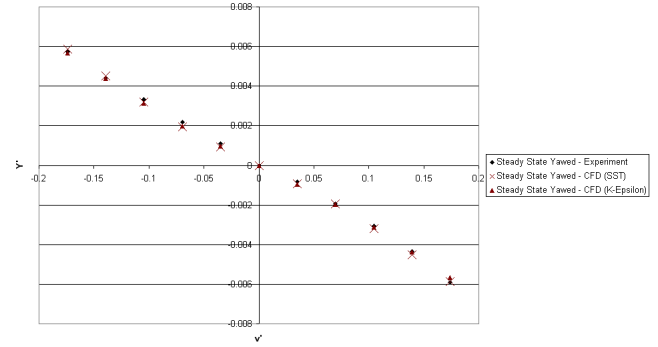

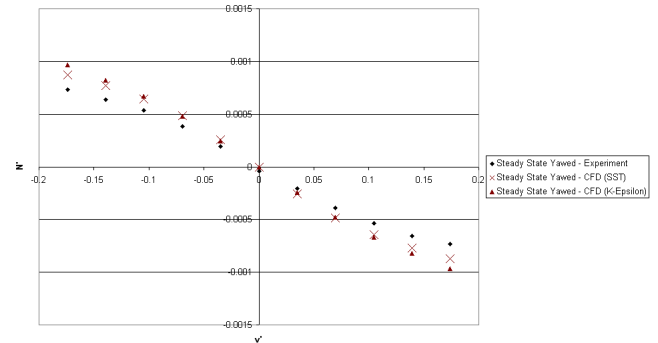Figure 7: Drift Test - Variation of Sway Force with Sway Velocity

Figure 8: Drift Test - Variation of Yaw moment(N) with Sway Velocity (v)

compared with values of 0.72 and 0.73 determined numerically using $k - \epsilon$ and SST models respectively.

Discussion

For both sets of experiments the sway force is very well captured by the numerical experiments with negligible variation between the $k - \epsilon$ and SST turbulence models, for the drift case the predicted values lie within the experimental uncertainty associated with $\pm$ yaw angles.

The trends in yaw moment(N') variation with angle of incidence are well predicted by the SST model which correctly predicts the reduction in the gradient $\frac{\partial Y'}{\partial v'}$ at higher sway velocities. Both turbulence models over predict the magnitude of the yaw moment by approximately 20%.

The induced drag is also over predicted by the CFD simulations. It is believed that the discrepancies in the experimental and numerical predictions of the yaw moments and induced drag lies in the influence of hull and tip vortices on the flow. The AUV's rudders experiencing three-dimensional flow has very different characteristics than a foil experiencing two-dimensional flow. The flow will tend to spill over the rudder ends
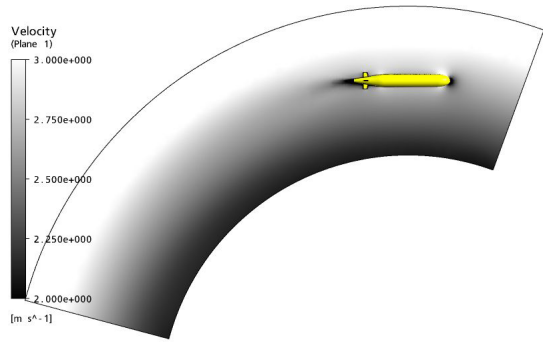
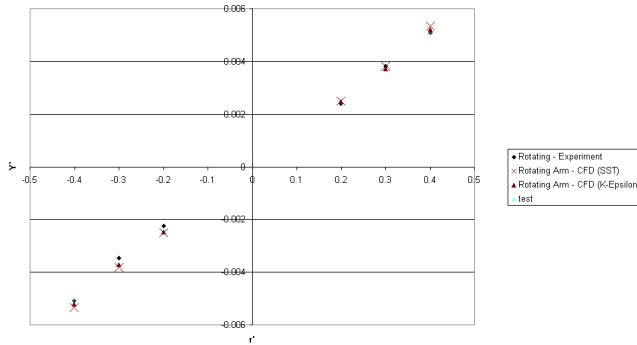Figure 9: Velocity Profile - Rotating Arm Radius 17.328m

Figure 11: Rotating Arm - Variation of Yaw moment(N) with Yaw Velocity (v)

Figure 10: Rotating Arm - Variation of Sway Force with Yaw Velocity

Table 1: Comparison of Experimental and CFD Values for the Hydrodynamic Derivatives all values are non-dimensional and x1000

Derivative	Experimental	CFD (K-epsilon)	CFD (SST)
Y'_v	-28.45	-27.28	-26.57
N'_v	-4.5	-5.90	-5.50
Y'_r	12.64	12.35	12.50
N'_r	-5.35	-6.59	-6.64

from the positive pressure side to the negative pressure side resulting in a tip vortex. Such a flow removes the pressure difference at the tips of the foil and decreases it over the entire span of the rudder. If insufficient elements are correctly positioned to correctly capture the radius of the vortex core, then the low pressure within the vortex will be poorly predicted.

Insufficient elements to resolve the vortex core results in diffused vortices which rapidly decay as seen in figure 12.

Capturing the vortex core requires a much finer mesh than the surrounding potential flow. Increasing the mesh density of the entire fluid domain is impractical. The use of courser meshes with finer elements elements clustered in the vicinity of the vortices is more practical but requires knowledge of the vortex location prior to simulation or the use of adaptive meshing techniques to move the mesh [8].

The numerical predictions of Autosub's dynamic stability margin are good.

Two separate automated meshing strategies where used in the creation of the mesh for the yawed drift and rotating arm tests. The structured meshing strategy used for the drift tests required significant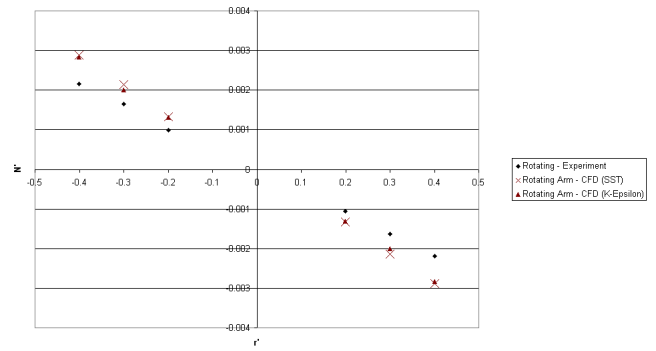 time at the start of the study to automate the blocking procedure to allow for various body orientations, however once defined creation of a new mesh takes less than 5 minutes. The unstructured meshes used for the rotating arm experiments required a much lower initial time investment but take approximately 20 minutes to generate a smoothed mesh. Both mesh strategies produced good quality meshes, which gave good results however for study's of this nature where multiple meshes are required the use of structured mesh with a constant mesh topology results in less uncertainty due to variation in the mesh.

Conclusions

Steady state CFD has been used to successfully replicate yawed towing tank and rotating arm experiments for a torpedo style AUV to derive the steady state hydrodynamic derivatives. Very good agreement was found for the prediction of sway forces, while the induced drag and yaw moments were marginally over predicted.

The dynamic stability margin of Autosub was well predicted by the numerical methods giving close agreement with the experimental value.

Further work

This work forms part of a study to produce a full unsteady hydrodynamic model of the AUV Autosub. Work is ongoing to integrate vortex capture techniques
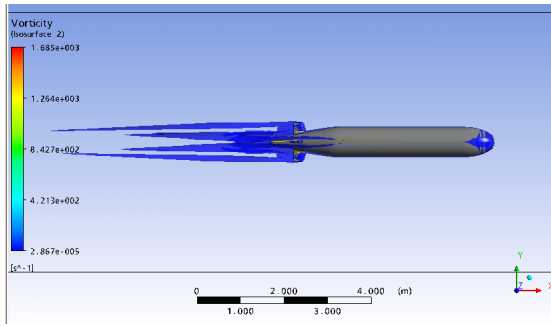
Figure 12: Vortex Structure around Autosub at 10°
Incidence

to better predict the influence of tip vortices on the
flow to enable better prediction of the forces and mo-
ments acting on an AUV.

Acknowledgements

References

[1] Roy Burcher and Louis Rydill. *Concepts in Submarine De-
sign*. Cambridge University Press, 1994.

[2] CFX. Innovative turbulence modeling: Sst model in ansys cfx.
Technical report, ANSYS Ltd, 2006.

[3] Ansys CFX. *ANSYS CFX, Release 10.0*. ANSYS Ltd, 2005.

[4] Jenhwa. Guo and Forng-Chen Chiu. Maneuverability of a flat-
streamlined underwater vehicle. In *Proceedings of the 2001
IEEE International Conference on Robotics and Automa-
tion*. IEEE, 2001.

[5] Joonyoung Kim, Kihun Kim, Hans S Choi, Woojae Seong, and
Kyu-Yeul Lee. Estimation of hydrodynamic coefficients for an
auv using nonlinear observers. *Journal of Oceanic Engineer-
ing*, 27(4), 2002.

[6] N. Kimber and W. Marshfield. Design and testing of control
surfaces for the autosub demonstrator test vehicle. Technical
report, DRA Haslar, 1993.

[7] D. E. Perrault, T. Curtis, N. Bose, S. O'Young, and
C Williams. C-scout manoeuvrability - a study in sensitivity.
In *Oceans 01*. IEEE, 2001.

[8] PEMBERTON RJ, TURNOCK SR, DODD TJ, and ROGERS
E. A novel method for identifying vortical structures. *Journal
of Fluids and Structures*, 2002.

[9] P.J. Statham, D.P. Connelly, C.R. German, T. Brand, J.O.
Overnell, E. Bulukin, N. Millard, S. McPhail, M. Pebody,
J. Perrett, Squire. M, P. Stevenson, and A. Webb. Spa-
tially complex distribution of dissolved manganese in a fjord
as revealed by high-resolution in situ sensing using the au-
tonomous underwater vehicle autosub. *Environmental Science
and Technology*, 2005.

[10] P. Wadhams, J.P. Wilkinson, and S.D. McPhail. A new view of
the underside of arctic sea ice. *Geophysical Research Letters*,
2006.

[11] D. C. Wilcox. *Turbulence Modeling for CFD*. La Cnada, Calif.
: DCW Industries, 1998.

DEVELOPMENT AND VALIDATION OF A SHEET CAVITATION MODEL ON HYDROFOIL AND PROPELLER BLADE

S. PHOEMSAPTHAWEE[*], J.B. LEROUX[*], J.M. LAURENS[*], F. DENISET[**]

[*] *Laboratoire de Mécanique de Structure Navale (MSN), ENSIETA, FRANCE*

[**] *Institut de Recherche de l'Ecole Naval (IRENav), Ecole Navale, FRANCE*

Introduction

The sheet cavitation phenomenon is one of the major problems of marine propellers. Its most adverse effect is the propeller loss of performances. Marine propeller designers try as much as possible to push the limit of cavitation inception to extreme loads only. However, modern larger ships power demand is increasing faster than the available propellers total area because of draft limit. As a consequence, the increase of propeller loads makes apparition of sheet cavitation more difficult to avoid. It is therefore important to study and to understand sheet cavitation in order to assess its effect on marine propellers hydrodynamic forces.

Three important points are discussed when trying to model sheet cavitation in a potential flow code: the criterion used for the cavitation inception point; the additional sub-model used to simulate the sheet cavitation closure; and finally the resolution method.

The first part of reference [1] gives an exhaustive list of the criteria used for the cavitation sheet inception point in various existing models. The most commonly used models for this criterion are the following:

- Brillouin-Villat criterion, used by most (see for instance references [2] and [3]), consists in choosing the point which guarantees the curvature continuity while respecting the slip condition and the steam pressure.

- The laminar boundary layer criterion, introduced by Franc J.P. (reference [4]) stipulates that the cavitation sheet starts after the separation point of laminar boundary layer. This criterion is widely accepted, for instance in references [5], [6] et [7]). Nevertheless, according to the experimental results obtained at the "Laboratoire de Machines Hydrauliques, Ecole Polytechnique Fédérale de Lausanne" (reference [8]), the sheet cavitation phenomenon has been observed without any sign of laminar boundary layer separation.

- The other criteria that are often mentioned are: The minimum pressure and the leading edge. This last model does not comply with physics although it was chosen by the authors of reference [9] who implemented several sophisticated models including several versions of the re-entrant jet.

The authors of reference [1] also present different models for the cavitation sheet closure. The cavitation sheet closures are classified in two categories: open or closed. The definition is given by Rowe A. and Blottiaux O. (reference [10]): a closed model is a model in which the streamline, after it has been deviated by the cavitation sheet, returns and touches the foil surface whereas an open model is a model in which the streamline does not touch the foil surface. Even if the partial cavitation sheet and the closed model are not necessarily identical, the closed model is the most commonly used to simulate partial sheet cavitation (see references [2], [5], [6] and [11]). Although the details of each

model are not the same, the principle is to transform in a continuous manner the vapour pressure condition on the cavitation sheet into the slip condition on the body surface. Open models are used to simulate super-cavitation, see reference [12], but also for partial sheet cavitation of large lengths.

To implement their cavitation model with their potential flow codes, Kinnas S. and Fine N. (reference [2]) as well as Salvatore F. and Esposito P.G. (reference [6]) impose the dipoles strengths distribution on the sheet cavitation using the vapour pressure condition and then compute the sources strengths distribution. In the model proposed by Peallat J.M. and Pellone C. (reference [11]), all dipoles and sources strengths are unknown. The resolution uses an optimisation technique.

In the present study, the goal is also to implement a partial sheet cavitation model within a 3D potential flow code. The code belongs to what Hoeijmakers (reference [13]) refers as second generation potential flow codes. The wet surfaces are discretised into first order panels carrying constant distributions of sources and dipoles. The lifting bodies downstream wakes are modelled by a sheet of first order panels carrying constant dipoles distributions. The wake is generated in a lagrangian manner allowing for unsteady simulations. Thanks to the Dirichlet boundary condition, the sources are directly deduced from the body surface slip condition. Hence, unlike the previously mentioned codes, the only unknowns of the problem are the dipoles. As a consequence, all the methods where the dipoles are imposed from the vapour pressure condition living the sources unknown cannot be applied to this present code without a serious rewriting of the code.

Inspired by a coupling method previously used with the present code to model the boundary layer (reference [14]), the basic idea of the sheet cavitation model presented here is to use transpiration velocities to deviate the flow as to represent the cavitation sheet. These transpiration velocities, v^*, are equivalent to additional sources strengths, σ^*, which are simply added on the part of the surface carrying the cavitation sheet. As a consequence, the implementation in the code is relatively simple since it is only a question to modify the slip condition on the body surface where the cavitation sheet is. The problem is how to determine the additional sources strengths distribution needed to correctly simulate the cavitation sheet. The core of the model is the function used to determine this distribution and it is the topic of the next section.

Physics of the Cavitation Model

The model is based on the existing relationship between the sheet cavitation geometry and the subcavitating pressure distribution. In a previous study, we had tried a model based on this principle which was giving satisfactory results, at least qualitatively (reference [15]). It is only when its results were compared quantitatively with some new available experimental data that it had to be rethought. The new model, presented here in equation (1), is describing the relationship between the transpiration velocity, v^*, and the subcavitating pressure distribution, P.

$$v^* = \frac{2k}{\rho U_\infty l} \int_{s_0}^{s} (P_v - P) \ ds \tag{1}$$

Finally rewriting equation (1) using non-dimensional variables such as the pressure coefficient, C_p, and the cavitation number, σ_v, one obtains equation (2):

$$\bar{v}^* = -k \int_{\bar{s}_0}^{\bar{s}} (C_P + \sigma_v) \ d\bar{s} \qquad (2)$$

The main stages of the general computation procedure are the following:

- Starting from the stagnation point, the algorithm follows the streamline. As long as the subcavitating pressure P is greater than the vapour pressure Pv, the transpiration velocity is set to zero.

- The sheet cavitation inception point corresponds to the first intersection between the subcavitating pressure curve and the pressure vapour threshold.

- Then the sheet cavitation continues to develop and the closure is automatically attained when the integral of transpiration flow becomes insignificantly small. By this way, the sheet cavitation length is intrinsically free and no additional closure model is required.

The only unknown of this model is the adaptive factor, k. Having observed the linear effect of this factor k over the resulting pressure, this factor k is then determined by using the secant method. The criterion is to obtain $P = P_v$ at the maximum cavitation thickness location.

Implementation within a 2D Foil Potential Flow Case and Validation

In this section the present model is implemented and validated within a 2D foil potential flow code. During the study presented in the references [16] and [17], experimental trials have been performed within a cavitation tunnel. These trials have already been used to validate sheet cavitation models; see for instance reference [18]. Furthermore, also in reference [16], it is shown that for this study the effects of confinement and boundary layer are not negligible and must therefore be taken into account. The 2D potential flow code, in which we implemented our model, has been developed within the framework of reference [16]. The code also used the transpiration velocities to simulate the boundary layer. The confinement is modelled by means of the images theory. As already mentioned the same code with these features has been used to implement the sheet cavitation model. It was decided to inhibit the boundary layer model where the sheet cavitation is present.

This is how the computation procedure goes. On the pressure side, the boundary layer is modelled from the stagnation point to the trailing edge. On the cavitating suction side, the transpiration velocities representing the laminar boundary layer are present from the stagnation point to the sheet cavitation inception point. Then from the cavitation inception point to its closure point, the transpiration velocities representing the boundary layer are set to zero. Hence, we consider that the boundary layer has a constant thickness. Once the sheet cavitation has closed itself, the boundary layer computation is resumed in turbulent mode with its current thickness. The method could be improved but it is always preferable to choose the simplest solution. Furthermore, the current procedure allows to model within a same simulation both the boundary layer and the sheet cavitation.

We compare the model results with the experimental results obtained in the framework of reference [16]. For this validation exercise, the results of three trials performed under the same conditions except for the cavitation number was varied. The results of the comparisons between these experimental trials and the model are presented in Figure 1.
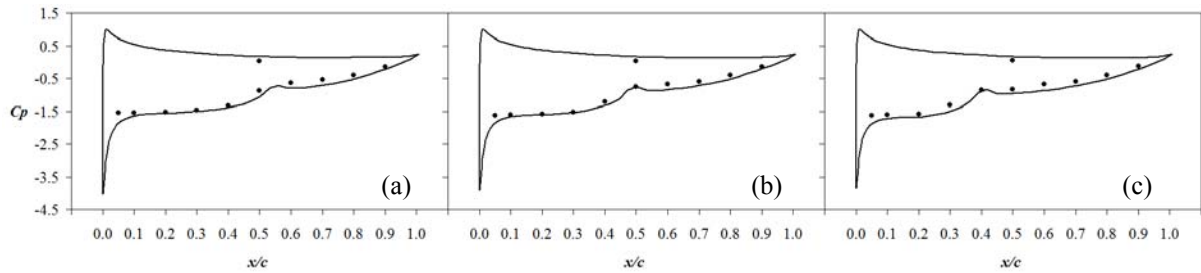
Figure 1. Comparison between the computed and the measured pressure coefficients : section NACA66(mod)–312 a=0.8, $\alpha = 6°$, $Re = 0.75\ 10^6$; Experiments (dots), Simulations (lines); (a) $\sigma_v = 1.495$, (b) $\sigma_v = 1.541$, (c) $\sigma_v = 1.622$.

With the exception of the first measurement point from the leading edge on the suction side, the numerical results are more than reasonably closed from the measurements. In the numerical simulation a peak in the pressure curve, near the leading edge, lower than the vapour pressure is almost always present. In first analysis, we think the peak is mainly due to the inception criterion used $P = P_v$, which imposes a continuous tangent between the profile and the sheet cavitation geometry. A refinement of the criterion, either using a critical pressure $P_c < P_v$, or by imposing the laminar boundary layer separation as an additional condition may improve this behaviour since experimentally the tangent is not observed. Furthermore, the numerical results of Figure 1(c) (i.e. for the smallest length of the sheet cavitation) are slightly less in agreement with the experimental results than the two others. This last remark, no doubt, deserves further investigation such as a complete numerical parameters study. For instance we checked the effect of the number of cells in the computation but there is no special mesh refinement for the sheet cavitation itself.

Implementation within a 3D BEM Code and Validation

Encouraged with the satisfactory results obtained in the 2D hydrofoil case, we also implemented the sheet cavitation model within our 3D BEM (Boundary Elements Method) code already mentioned in the introduction. Although the code is capable of unsteady simulations including when the sheet cavitation is activated, only steady state comparisons against other numerical models and experimental measurements are presented here.

For 3D cases, the determination of the adaptive factor, k, does not appears as simple as for the 2D cases. However, it was decided that k takes a different value per section; the sections correspond to the bands of the structured mesh. The adaptive factor k is then determined independently for each band but iterations on the dipoles to satisfy the Kutta-Joukowski condition ensure the sheet cavitation continuity.

Sheet cavitation lengths have been measured on a three-dimensional hydrofoil at MIT in their hydrodynamic cavitation tunnel. The elliptical hydrofoil is a windsurf fin designed and built by FINTECH. The details of its geometry and the experimental conditions are given in reference [2]. These experimental results have already been used to validate other sheet cavitation models, see references [6] and [11]. Unlike the previous 2D case, the confinement and the boundary layer have not been taken into account. The authors of references [6] and [11] have also ignored these effects since only a qualitative comparison is possible (i.e. no forces nor pressure measurements data are available).

Trials have been conducted for two different cavitation numbers: $\sigma_v = 1.084$ and 1.148. Salvator and Esposito (reference [6]) as well as Peallat and Pellone (reference [11]) also used these experimental results in an attempt to validate their sheet cavitation models. The present results are hence compared not only with the experimental results of reference [2], but also with the numerical results of references [6] and [11]. These comparisons are presented in Figure 2.
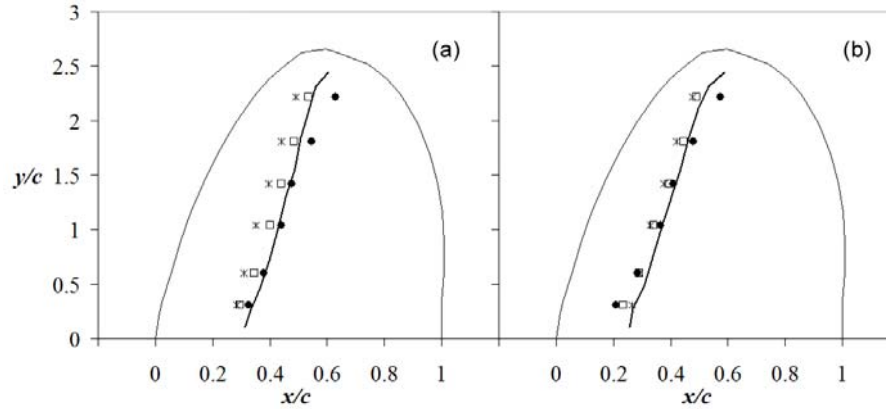

Figure 2.   Sheet cavitation lengths span distribution obtained for the 3D elliptical fin with NACA65a sections: $\alpha = 6.5°$; Experiments (•), Salvator-Esposito (□), Peallat-Pellone (*), Present simulations (—); (a) $\sigma_v = 1.084$, (b) $\sigma_v = 1.148$.

As already mentioned, none of the numerical simulations presented in Figure 2 takes account for the confinement and the boundary layer. The confinement is less important than the previous 2D case but the Reynolds number is about the same. Despite of all the differences in the sheet cavitation models, cavitation inception criterions and additional closure sub-models, all numerical results are reasonably close to the experimental results. This conclusion is only qualitative and trials with accurate measurements of forces and pressures may change it.

Conclusion and Scope for Future Development

A sheet cavitation model has been developed and successfully implemented within a 3D BEM code to estimate the resulting loss of performances and the hydrodynamics effects on a propeller working in an unsteady state mode. A first stage of validation has been completed and presented in this document by comparison with experimental results and other numerical simulations results. Several aspects of the model may be further investigated in the future: the peak of pressure lower than the vapour pressure near the leading edge, the sheet cavitation inception point criterion, and finally an improvement of the algorithm to determine the adaptive factor k in 3D cases would be required.

References

[1]   Pellone C., Maître T., Briançon-Marjollet L., (2000), Partially Cavitating Hydrofoils: Experimental and Numerical Analysis. *Journal of Ship Research*, Vol. 44, pp. 40-58.

[2]   Kinnas S.A., Fine N.E., (1993), A numerical nonlinear analysis of the flow around two- and three- dimensional partially cavitating hydrofoils., *Journal of Fluid Mechanics*, Vol. 254, pp. 151-181.

[3]   Lee H., Kinnas S.A., (2004), Application of a Boundary Element Method in the Prediction of Unsteady Blade Sheet and Developed Tip Vortex Cavitation on Marine Propellers., *Journal of Ship Research*, Vol. 48, pp. 15-30.

[4]   Franc J.P., (1986), Etude Physique d'Ecoulements Cavitants., *Thèse de Docteur d'Etat ès Sciences*, Université de Grenoble.

[5]   Briançon-Marjolet L., Merle L., (1999), Modélisation de la cavitation. *Revue Scientifique et Technique de la Défense*, Bassin d'Essais des Carènes, N°43, pp. 109-114.

[6]   Salvatore F., Esposito P.G., (2001), An improved boundary element analysis of cavitating three-dimensional hydrofoils., *CAV2001 4th International Symposium on Cavitation*, Pasadena, California, June.

[7]   Brewer W.H., Kinnas S.A., (1997), Experiment and Viscous Flow Analysis on a Partially Cavitating Hydrofoil., *Journal of Ship Research*, Vol. 41, pp. 161-171.

[8]   Farhat M., Guennoun F., Avellan F., (2002), The Leading Edge Cavitation Dynamics, *Proceeding of ASME: Fluids Engineering Division Summer Meeting*, Montreal, Quebec, July.

[9]   Vaz G., Bosschers J., DeCampos J.F., (2003), Two-Dimensional Modelling of Partial Cavitation with BEM, Analysis of Several Models., *CAV2003 5th International Symposium on Cavitation*, Osaka, Japan, November.

[10]   Rowe A., Blottiaux O., (1993), Aspects of Modelling Partially Cavitating Flows., *Journal of Ship Research*, Vol. 37, pp. 34-48.

[11]   Peallat J.M., Pellone C., (1996), Experimental validation of two- and three-dimensional numerical analysis of partially cavitating hydrofoils., *Journal of Ship Research*, Vol. 40, pp. 211-223.

[12]   Achkinadze A.S., Krasilnikov V.I., (2001), A Velocity Based Boundary Element Method with Modified Trailing Edge for Prediction of the Partial Cavities on the Wings and Propeller Blades., *CAV2001 4th International Symposium on Cavitation*, Pasadena, California, June.

[13]   Hoeijmakers H.W.M., (1992), Panel Methods for Aerodynamic Analysis and Design. *AGARD Report* 783, pp. 5.1-5.47.

[14]   Laurens J.M., (1993), Couplage code de calcul fluide parfait, code de calcul couche limite 3D, *Rapport DCN/Bassin d'Essais des Carènes*, Etude 2524 pièce 3.

[15]   Laurens J.M., Phoemspatawee S., (2004), Numerical simulation of sheet cavitation effects on foils and propellers hydrodynamic performances, *NuTTs2004 7th Numerical Towing Tank Symposium*, Hamburg, Sept.

[16]   Leroux J.B., (2003), Etude expérimentale en tunnel hydrodynamique des instabilités de la cavitation par poche sur hydrofoil par la mesure spatio-temporelle du champ de pression pariétal., *Thèse de Doctorat*, Ecole Centrale de Nantes et Université de Nantes.

[17]   Leroux J.B., Astolfi J.A., Billard J.Y., (2003), Etude expérimentale des instationnarités et des instabilités des poches de cavitation, *Actes des 9èmes Journées de l'Hydrodynamique*, 10-12 mars, 2003, Poitiers, France.

[18]   Leroux J.B., Coutier-Delgosha O., Astolfi J.A., (2005), A joint experimental and numerical study of mechanisms associated to instability of partial cavitation on two-dimensional hydrofoil, *Physics of Fluids*, Vol. 17, May 2005, pp. 052101 (20 pages, on line issue).

RANS Code Verification Using Method of Manufactured Solution

Daniel Schmode, d.schmode@tu-harburg.de

Thomas Rung

Hamburg University of Technology, M8

1 Introduction

In large software projects quality control is a crucial matter. We will present two verification cases that we use frequently to check the correct implementation of the Navier-Stokes equation in the RANS solver FreSCo. For details on the numerical method in FreSCo see [4].

2 MMS in a Nutshell

2.1 Introduction

The method of manufactured solution (MMS) is a technique to check if differential equations are discretised correctly. It can be adopted to check the complete solution procedure performed by a RANS solver. A good introduction to MMS is given in [3].

2.2 Basic Idea

The basic idea is to specify an analytical solution (AS) which does not necessarily fulfill the differential equation (DE) the solution of which is to be verified. We apply the DE to the AS in an algebraic manner and get residuum which is discretised and added to the DE as a source-term. Solving the DE with this source-term should reproduce the AS. Because the AS we mentioned above does not fulfill the DE we will call it manufactured solution (MS) in the following.

2.3 Simple Example

We present here a simple example MMS given in [3]. We want to verify the implementation of the differential equation

$$\mathcal{L}(u) = u_t + uu_x - \alpha u_{xx} = 0. \qquad (1)$$

We chose a manufactured solution (MS)

$$U(t,x) = A + \sin(x + Ct). \qquad (2)$$

By applying (1) to (2) we get the residuum $\mathcal{L}(U)$:

$$\begin{aligned}
\mathcal{L}(U) &= U_t + UU_x - \alpha U_{xx} \\
&= \quad C\cos(x + Ct) \\
&\quad + [A + \sin(x + Ct)]\cos(x + Ct) \\
&\quad + \alpha\sin(x + Ct) \\
&= Q(x,t)
\end{aligned}$$

Than U is a solution of the following equation:

$$\mathcal{L}(u) = u_t + uu_x - \alpha u_{xx} = Q(x,t). \qquad (3)$$

Solving the correctly implemented discretised equation (3) should reproduce the manufactured solution (2).

2.4 MMS for RANS Equations

MMS can be adopted to the RANS equations in different manners. The common way is to specify several MS for the velocity components, for the pressure and for turbulence quantities. The MS for the velocity component were chosen to fulfill the continuity equation.

3 Smith & Hutton Test Case

3.1 Test Case Description

The case proposed in [5] is a simple test case exercising only the implementation of the convective terms. It is in principle an MMS, but here we specify a AS which fulfills the DE, thus $Q = 0$.

The computational domain is plotted in figure 1.

The assumed velocity field is:

$$u = 2y\left(1 - x^2\right)$$

$$v = -2x\left(1 - y^2\right)$$

We specify the scalar quantity at the inlet as follows:

$$\Phi(x,0) = 1 + \tanh(\alpha * (1 - 2x))$$

where the sharpness of the profile can be controlled by the parameter α, figure 2. The analytical solution in the field reads:

$$\Phi(x,y) = 1 + \tanh(\alpha(1 - 2\sqrt{(x^2 + y^2)})).$$

Figure 3 shows the analytical solution for $\alpha = 100$.

3.2 Grids

We performed computations for a set of seven structured, equidistant, orthogonal grids. The grid characteristics are given in table 1

Table 1: Grid densities for Smith and Hutton test case

	nx	ny	ncells
grid 1	160	80	12800
grid 2	226	113	25600
grid 3	320	160	51200
grid 4	452	226	102152
grid 5	640	320	204800
grid 6	906	453	410418
grid 7	1280	640	819200

3.3 Results

We performed a grid study using three different discretisation schemes. Figure 4 shows the L1-norm of the error in the field

$$E = \frac{1}{ncells} \sum_{ncells} |\phi_{analytic} - \phi_{discrete}|$$

over a reference length h. The numbers attached to the graph are the orders p computed by solving

$$E(h) = ah^p$$

using two subsequent grids. The observed order is approximately 2.4. This is less than the theoretical order of the QUICK scheme which is $p = 3$. This may be due to the computation of the error norm where we use midpoint rule, which is only second order accurate.

Computations using upwind scheme (UDS) are given in Figure 5. The order is $p \approx 1$ as expected. Computations using central differencing (CDS) with 5% UDS are given in Figure 6. The observed order is only $p \approx 1$ which is caused by the 5% UDS. Nevertheless the error is two orders of magnitude lower for CDS than for UDS.

4 Lisbon Test case

4.1 Test Case Description

The case was proposed by Eca level of the for the "2nd Workshop on CFD Uncertainty Analysis" . This MMS mimics an incompressible 2d boundary layer. It verifies the discretisation of convective and diffusive terms, the gradient reconstruction, the pressure correction algorithm and the linear equation system solver.

The computational domain and boundary conditions are shown in Figure 7.

See [1] for a detailed description of the test case. Result presented here were obtained for the MS denoted as "ms2" in [1].

4.2 Grids

4.2.1 Grid Set 1

The first grid set (GS1) is a set of structured grids, which were refined towards the wall. The grid densities are given in table 2. A plot of the coarsest grid is given in figure 8.

Table 2: Grid parameters of grid-set 1 of Lisbon test case

	nx	ny	ncells
grid 1	47	47	2209
grid 2	66	66	4356
grid 3	94	94	9936
grid 4	132	132	17424

4.2.2 Grid Set 2

A second set of unstructured grids (GS2) was provided by Gambo Deng (ECN), (table 3, figure 9). The grids are refined towards wall and have local refinements.

Table 3: Grid parameters of grid-set 2 of Lisbon test case

	ncells
grid 1	2189
grid 2	4601
grid 3	8480
grid 4	16521

4.3 Results

4.3.1 Grid Set 1

Results for GS1 are given in Figure 10 to 12. The plots are similar to those discussed in 3.3. Figure 10 shows the L1 norm of the velocity and pressure errors over the reference length. The observed order is close to the theoretical value $p = 2$.

Figure 11 show the results for a blending of UDS and CDS. The blending is computed depending on the local Peclet number. The results show a much lower order which was anticipated due to the UDS contribution.

Figure 12 show the results for a blending of QUICK and CDS where the blending is computed depending on the local Peclet number. The observed order is close to the theoretical order of $p = 2$.

We conclude that the NS equations are correctly discretised.

4.3.2 Grid Set 2

Results for the locally refined unstructured grids were given in Figure 13 ff. The results are similar to those discussed in 4.3.1. This indicates that our implementation does not suffer from accuracy loss near local grid refinements.

A summary of results obtained for this MMS by other groups is presented in [2].

5   Conclusions

MMS proved to be a reliable tool for code verification. During preparation of the presented exercise we located and fixed several bugs in FreSCo. The test cases presented here were included in the test suite which is computed frequently to verify the implementation after changes of the numerical method. Performing MMS tests is highly recommended to code developers.

Acknowledgment

We thank Luis Eca and Martin Hoekstra for providing the MMS and for organizing the Lisbon workshops. This work was funded by the EU project VIRTUE; thus we thank the EU commission and the project management.

References

[1] L. Eca, editor. *2nd Workshop on CFD Uncertainty Analysis*, 2006.

[2] L. Eca, M. Hoekstra, and P. Roache. Verication of Calculations:an Overview of the 2nd Lisbon Workshop. In *18th AIAA Computational Fluid Dynamics Conference*, pages 4098+, 2007.

[3] D. Pelletier and P Roach. CFD Code Verification and the Method of manufactured Solutions. In *1-th Annual Conference of the CFD Society of Canada*, 2002.

[4] D. Schmode, H. Vorhölter, and T. Rung. RANS-Based Flow Analysis for Propellers and its Benefits. In *7th INTERNATIONAL CONFERENCE ON HYDRODYNAMICS Theory and Applications*.

[5] R.M. Smith and A.G. Hutton. The numerical Treatment of advection: A Performance Comparison of current Methods. *Numer. Heat Tran.* , 5:439–461, 1982.
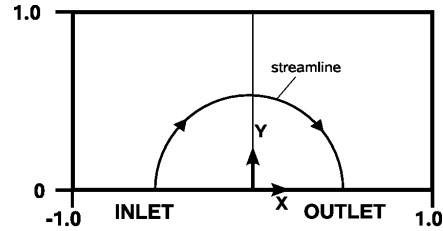
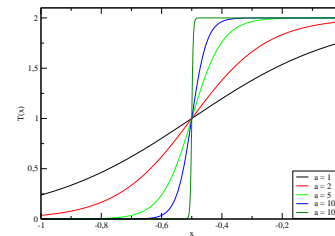Figure 1: Computational domain for Smith and Hutton test case

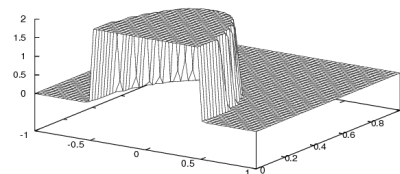Figure 2: Inlet profiles for different α values for Smith and Hutton test case

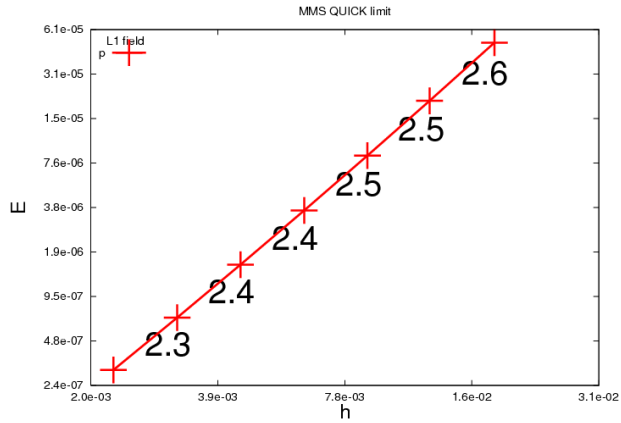Figure 3: Analytical solution for Smith and Hutton test case

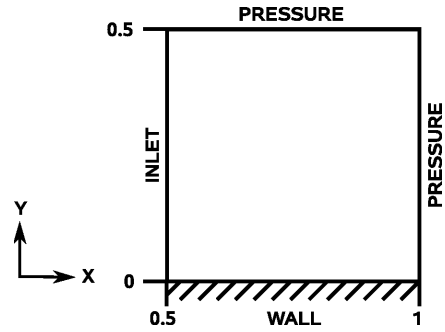Figure 4: Smith and Hutton, limited QUICK

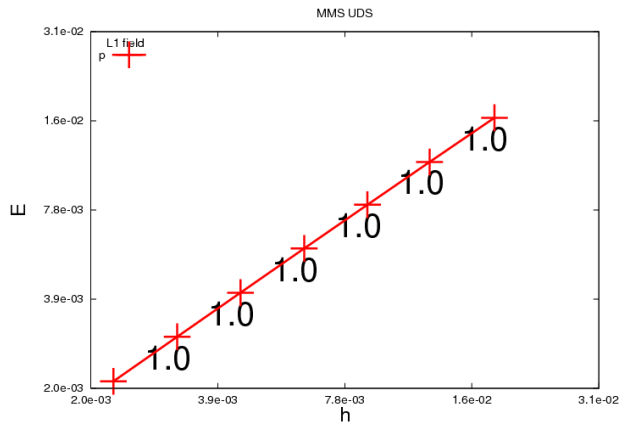Figure 7: Computational domain and boundary conditions for Lisbon test case
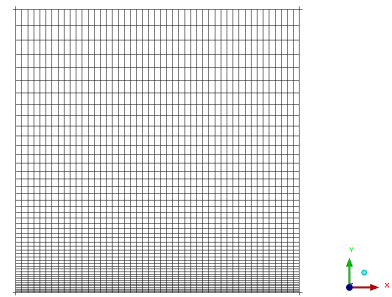

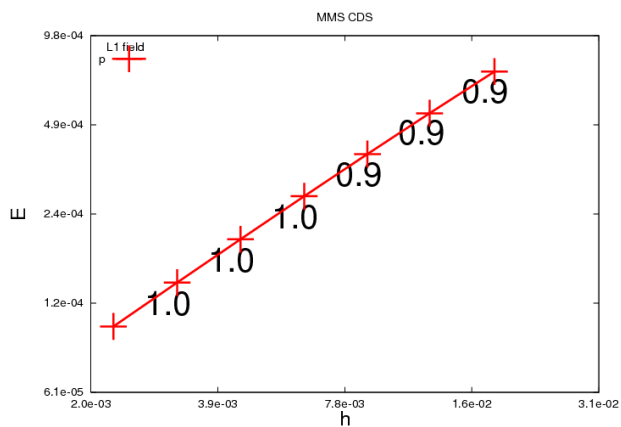Figure 5: Smith and Hutton, UDS

Figure 8: Grid set 1, Lisbon test case

Figure 9: Grid set 2, Lisbon test case
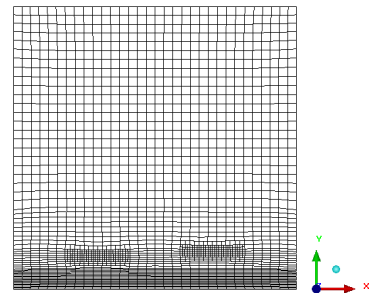

Figure 6: Smith and Hutton, CDS

Figure 10: Lisbon GS1, limited QUICK, left velocity error, rigth pressure error

Figure 11: Lisbon GS1, Peclet number depending UDS CDS blending, left velocity error, rigth pressure error

Figure 12: Lisbon GS1, Peclet number depending QUICK CDS blending, left velocity error, rigth pressure error
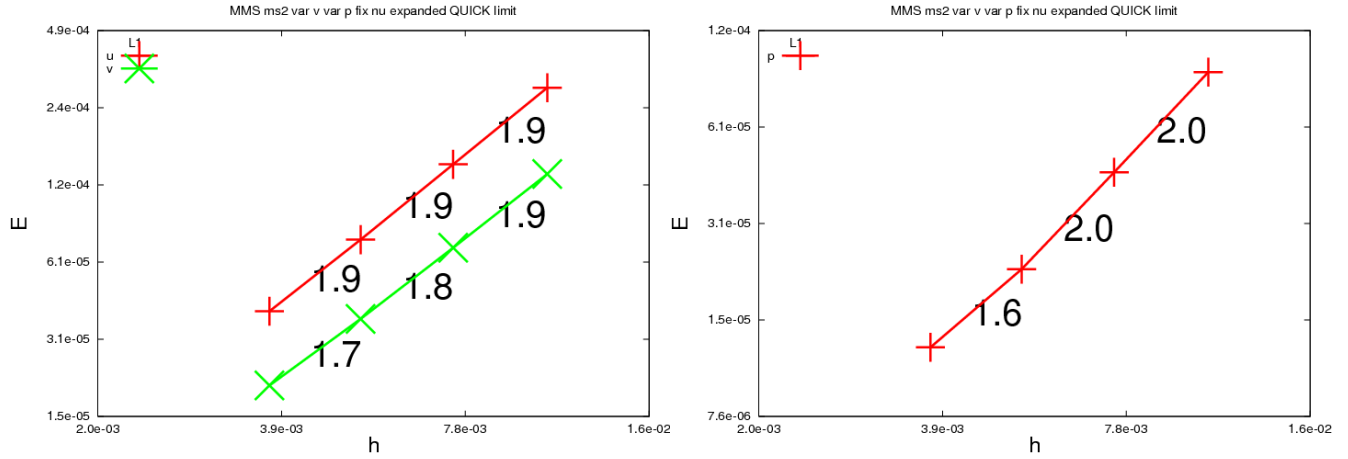
Figure 13: Lisbon GS2, limited QUICK, left velocity error, rigth pressure error
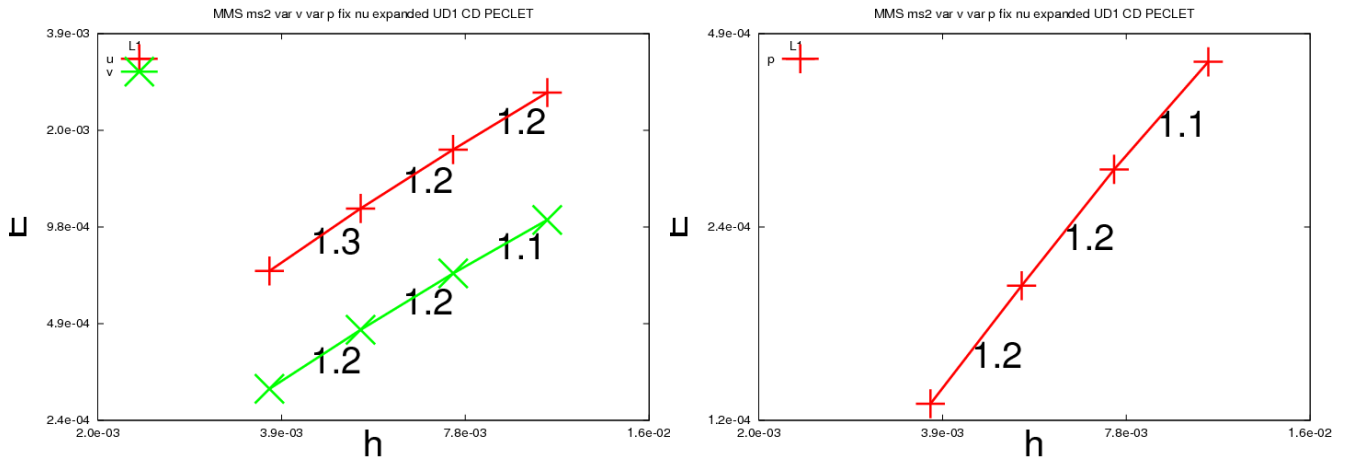

Figure 14: Lisbon GS2, Peclet number depending UDS CDS blending, left velocity error, rigth pressure error
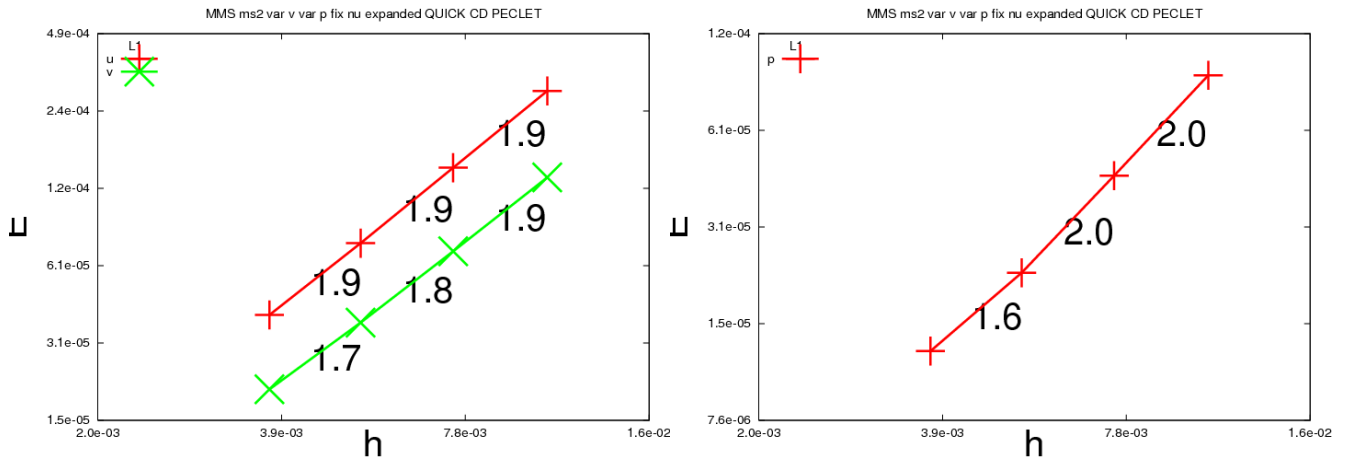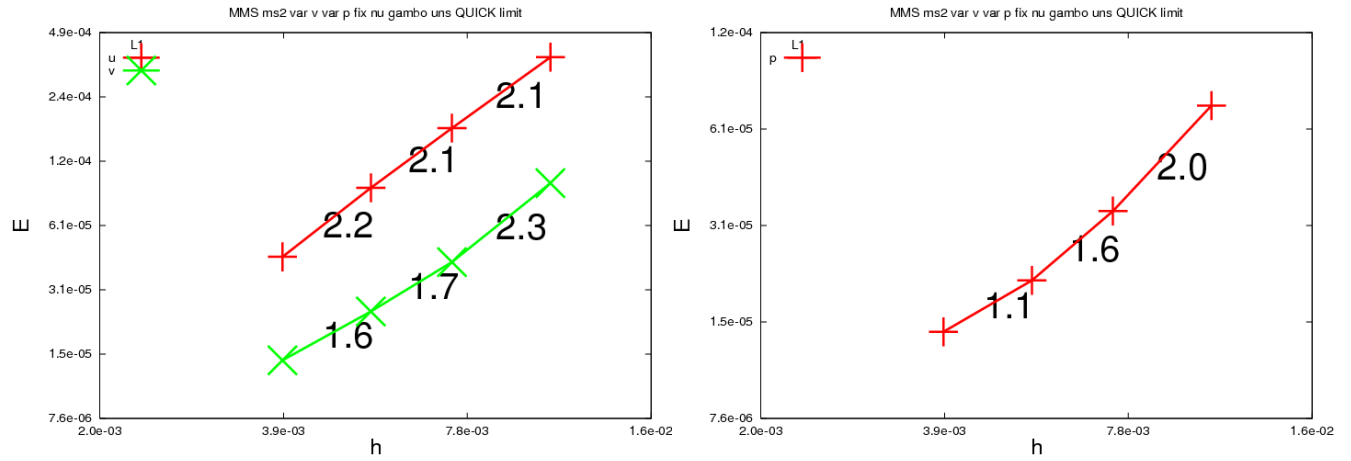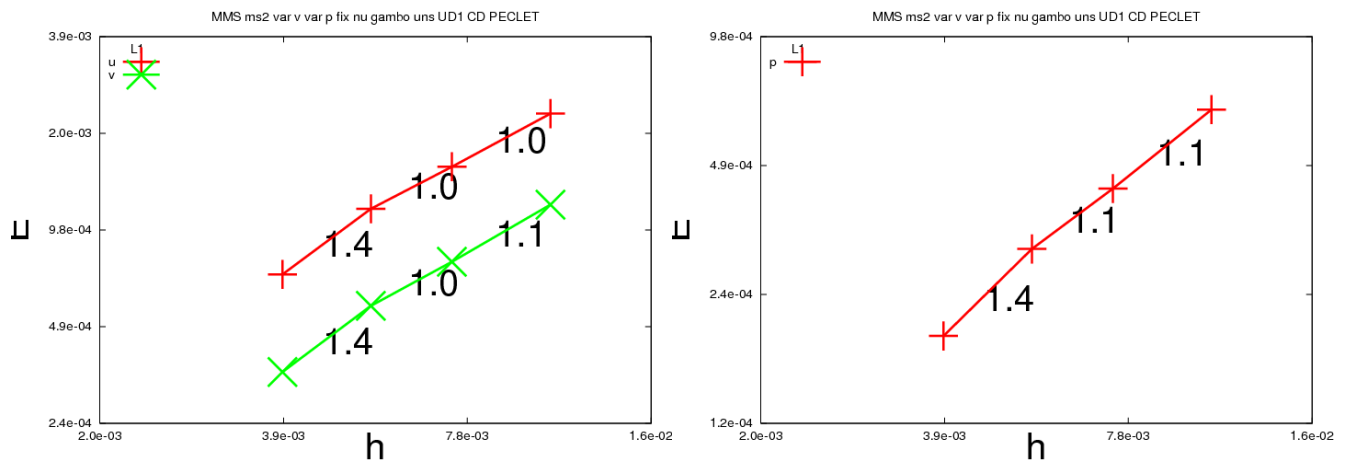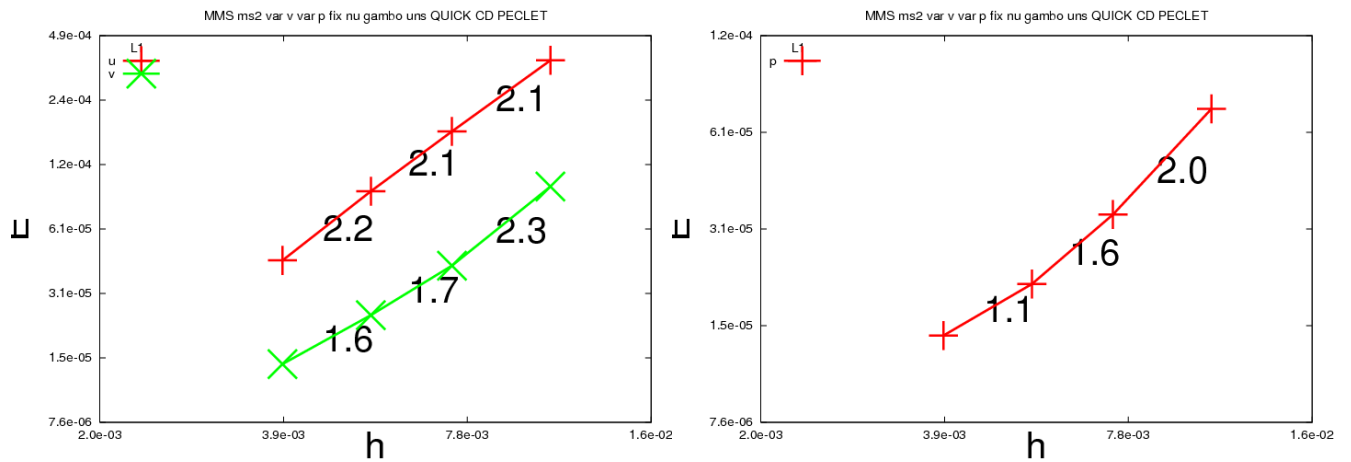

Figure 15: Lisbon GS2, Peclet number depending QUICK CDS blending, left velocity error, rigth pressure error

Free Surface Modelling in FreSCo, Latest Developments

Daniel Schmode , d.schmode@tu-harburg.de

Katja Wöckner,

Thomas Rung

Hamburg University of Technology, M8

1 Introduction

1.1 Free Surface Modelling

In our opinion the free surface (FS) methods presented in literature are not working properly for all kinds of problems encountered in marine applications. Furthermore, many methods require high computational effort that prohibits their application in the design process.

Thus we are working on FS modelling in our RANS solver FreSCo. We present recent results as well as unsolved problems that we would like to discuss with other groups.

We aspire to a robust, efficient and accurate implementation. We think that efficiency can be increased by 1.) gaining accuracy on coarse grids, and 2.) by increasing the time step limit. Thus we present results obtained on grids with grid-spacings appropriate for 3D cases even if they might look coarse for 2D cases. Also we use time steps above the usual Courant number limitations.

1.2 Interface Tracing vs. Capturing

Methods for computing free surface flows in a RANS solver can be classified into *interface capturing methods* (ICM) and *interface tracing methods* (ITM). Both were used in commercial and research codes, and a number of publications discuss the pros and cons. ICM were considered more flexible, in particular for violent sloshing problems where ITM are not applicable. For ship wave resistance computations ITM have been used successfully, but they lack robustness e.g. if wave breaking occurs or behind wetted transoms. ICM have also been used by various authors (e.g. [4]) computing the ship flow. Wave breaking and wetted transom phenomena were captured reasonably, but the computational effort is much higher than for ITM. In FreSCo we apply only on the more flexible ICM which is discussed in more detail below.

1.3 Volume of Fluid Method

The most popular ICM is the volume of fluid (VoF) technique, e.g. [2]. The crucial point is the convection scheme for the concentration transport equation.

Several schemes were proposed e.g. in [7] and [2]. Most of them have a strong time step limitation referring to the local Courant number $Co < 0.3$. These schemes were applied to steady flow problems by performing a transient computation which can become quite expensive. In section 2.1 we propose a scheme which does not have a Courant number limitation.

1.4 Level-Set Method

Another ICM is the Level-Set method (LSM) [6]. It was adopted for free surface flows by various authors. A brief introduction is given in [2]. Here the convective terms of the transport equation are discretised by a high order upwind scheme which itself has no Courant number limitation. Hence it requires less time steps and is more efficient. Some details of our Level-Set implementation are given in section 2.2.

1.5 Sharp Interfaces

In ITM the interface is inherently sharp, while in ICM the sharpness of the interface is a result of the concentration transport equation (CTE). If the interface is smeared over more than one cell height, that causes an error in the momentum equation leading to strong numerical wave damping.

1.6 Influence of the Courant Number

To maintain the sharpness of the interface, special convection schemes for the CTE are required. In [7] the CICSAM scheme is proposed, while in [2] the HRIC scheme is presented. Both produce results that depend on the local Courant number, even if the problem is steady, which is an unpleasant side effect.

2 ICM for large Courant Numbers

2.1 VoF Method

In VoF methods the fluid is considered as homogeneous mixture. The respective concentration of the

air phase is defined by

$$c = \frac{V_{air}}{V} \tag{1}$$

where V_{air} is the cell volume filled with air and V is the cell volume. Accordingly, the density ρ and viscosity μ of the mixture are taken via

$$\rho = \rho_{air}c + \rho_{water}(1-c), \quad \mu = \mu_{air}c + \mu_{water}(1-c) . \tag{2}$$

The transport equation for the concentration c reads

$$\frac{\partial}{\partial t} \int_V c \, dV + \int_S c\mathbf{v} \cdot \mathbf{n} \, dS = 0 \tag{3}$$

where t is the time, V is the volume, S is the surface with the normal vector $\mathbf{n}$ and $\mathbf{v}$ is the velocity,

To maintain a sharp interface, this equations needs to be discretised using special schemes. The scheme outlined in this section is aimed to avoid the time step limitation of other schemes e.g. CICSAM and HRIC. We call it "fast interface capturing scheme" (FICS). It is incorporated into our fully implicit SIM-PLE based finite volume (FV) RANS solver FreSCo. For details of FreSCo see [5]. The scheme that will be

To define the FICS we use the normalized variable diagram (NVD) proposed by Leonard [3].

In the donor-acceptor nomenclature we define acceptor, donor and upstream cell as indicated in figure 1. In unstructured grids the value ϕ_U^* is obtained by extrapolation

$$\phi_U^* = \phi_A + 2 \, \mathbf{grad} \, (\phi)_D \cdot \mathbf{d}_f^*, \tag{4}$$

where $\mathbf{d}_f^*$ is the vector from the acceptor cell centre to the donor cell centre.

For the NVD diagram we normalize variables:

$$\tilde{\phi}_f = \frac{\phi_D - \phi_U^*}{\phi_A - \phi_U^*}. \tag{5}$$

FICS consists basically of two parts: One that is active if the interface is parallel to the face (figure 2a), and the other that is active if the interface is normal to the face (figure 2b). Both parts are blended if the interface is oblique (figure 2c).

The normalised face value for the parallel mode $\tilde{\phi}_p$ is computed

$$\tilde{\phi}_p = \begin{cases} \tilde{\phi}_f & \text{if} \quad \tilde{\phi}_f < 0 \\ \min(10 \, \tilde{\phi}_f, 1) & \text{if } 0 < \tilde{\phi}_f < 1 \\ \tilde{\phi}_f & \text{if } 1 < \tilde{\phi}_f \end{cases} \tag{6}$$

while the part for the normal case $\tilde{\phi}_n$ is simply a CDS with 5% UDS

$$\tilde{\phi}_n = 0.45 + 0.55\tilde{\phi}_f. \tag{7}$$

The blending of $\tilde{\phi}_p$ and $\tilde{\phi}_n$ depends on the angle between the face and the FS. The blending factor γ is computed

$$\gamma = (|\mathbf{grad} \, (\phi)_f| \cdot \mathbf{n})^2 . \tag{8}$$

where $\mathbf{n}$ is the normal vector of the face.

Finally we get the normalised face value

$$\tilde{\phi} = \gamma \tilde{\phi}_p + (1 - \gamma) \tilde{\phi}_n, \tag{9}$$

which is transformed into dimensional values by

$$\phi_f = (1 - \beta)\phi_D + \beta\phi_A, \tag{10}$$

with

$$\beta = \frac{\tilde{\phi} - \tilde{\phi}_D}{1 - \tilde{\phi}_D}. \tag{11}$$

2.2 Level-Set Method

One possibility to overcome the time step limitations is to use a Level-Set approach. We will outline the technique briefly, for more details see [6].

The interface is represented by the zero level of a signed distance function ψ which fulfills the following equation:

$$|\mathbf{grad} \, (\psi)| = 1. \tag{12}$$

We solve a transport equation for ψ:

$$\frac{\partial}{\partial t} \int_V \psi \, dV + \int_S \psi\mathbf{v} \cdot \mathbf{n} \, dS = 0 . \tag{13}$$

where t is the time, V is the volume, S is the surface with the normal vector $\mathbf{n}$ and $\mathbf{v}$ is the velocity,

To compute the effective fluid properties we transform the Level-Set function into a VoF field by

$$c = \frac{1}{2} \left(\tanh \left(\frac{2\psi}{\delta} \right) + 1 \right), \tag{14}$$

where δ is the thickness of the interface. We use (2) to compute the effective density and viscosity.

During iterations the level set function deforms and do no longer fulfill (12). To ensure (12) we must reinitialize the Level-Set function after each time step. We compute the norm of the gradient of ψ and increase (decrease) ψ if $|\mathbf{grad} \, (\psi)$ is ¡1 (¿1):

$$\psi = (\psi + \text{sign}(\psi)(|\mathbf{grad} \, (\psi)| - 1) * \beta_\psi)^{n-1} \tag{15}$$

where $\beta_\psi \approx 10^{-3}$ is an underrelaxation parameter and superscript $n - 1$ denotes values from the preceding iteration.

To assess the quality of the reinitialisation we compute a residual via:

$$r_\psi = \sum (|\mathbf{grad} \, (\psi)| - 1) \tag{16}$$

More sophisticated reinitialisation procedures were proposed; however this one proved to be fast and robust in our applications.

2.3 Test Case: Duncan Foil

To assess the quality of the prediction using the VoF convection schemes and the Level-Set method we compute a submerged hydrofoil in steady 2D flow investigated by Duncan ([1]). The foil is a NACA0012 profile at 5° angle of attack. The chord length is $c = 0.203m$. The dimensions of the computational domain are given in figure 3. We selected the Froude number $Fr = 0.557$, and a submergence of $D = 0.21m$. No wave breaking occurs in this case, thus the flow is steady. Nevertheless we need to perform a transient computation. All results presented below are obtained after a simulation time of $t = 20s$.

The effects of turbulence were neglected. At the outlet we use a pressure boundary condition prescribing hydrostatic pressure, and we use a damping zone to avoid reflections. At the top, bottom and the foil we use slip wall conditions, and at the inflow we define a velocity and the concentration or the Level-Set values, respectively.

Computations were performed on a grid with approximately 20000 cells with a grid-density similar to typical grids for 3D ship wave computations using ICM.

In all plots isolines for concentrations of 0.1, 0.5 and 0.9 are shown. The plots are stretched in vertical direction.

In FreSCo we implemented the CICSAM scheme exactly as described in [7]. Figure 5 shows results obtained with a time step corresponding to $Co \approx 0.7$.

In FreSCo we also implemented the HRIC scheme exactly as described in [2]. Figure 6 shows results obtained with a time step resulting in the Courant number $Co \approx 0.7$.

Results obtained with FICS using the same time step as for CICSAM and HRIC corresponding to $Co \approx 0.7$ are given in figure 7. Results with a much larger time step corresponding to $Co \approx 3.0$ are given in figure 8.

Results using Level-Set technique with a time step resulting in the Courant number $Co \approx 1.5$ are presented in figure 9. Larger Courant numbers can be used by optimising the parameters of the reinitialisation procedure.

2.3.1 Conclusions

At Courant number $Co \approx 0.7$ all three VoF schemes produce similar results in terms of interface sharpness. At Courant number $Co \approx 3.0$ HRIC and CICSAM diverge while FICS produces results similar to those obtained with the same Courant number. We believe that this is an improvement that can cut down the computation time drastically. But we are

also aware that further testing is required to give a final assessment of the performance of this scheme. The best results were obtained using the Level-Set technique.

3 Sharpness of the Interface

3.1 Phenomenological Considerations

Besides the Level-Set results all the computations presented above exhibit a strongly smeared interface. Other test cases, e.g. dam breaks and simple convection tests with fixed velocity fields as proposed in [7], reveal a much sharper interface for all schemes. To understand why the Duncan case is more difficult we look at the FICS outlined above. The FICS uses a angle dependent blending between a parallel and a normal mode. First we look at the parallel mode figure 2a. The water front is moving from left to right. Here the donor cell is donating air as long as air is available. Thus we use downwind differencing (DDS) as long as there is air available. The DDS has a compressive behaviour. Smeared interfaces were sharpened by DDS during simulation. Considering the flow situation indicated in figure 2b where the surface is exactly parallel to the cell face, we can use UDS, CDS or DDS. The result is the same. For the case of figure 2c, using only the parallel mode would firstly remove only air from the donor and produce finally a nonphysical step-shape interface. To avoid this we have to blend ϕ_n and ϕ_p. The larger the angle between interface and face the larger the contribution of the normal mode.

Keeping this in mind and looking at the Duncan case computed on a grid with horizontal and vertical grid-lines (figure 4) we see that the FICS works mostly in normal mode. The normal mode is basically a CDS - UDS blending which introduces numerical diffusion which accumulates during the simulation. The portion of the compressive parallel mode is too small to keep the interface sharp. Considering dam breaks, we see that there is a big portion of the parallel mode that keeps the interface sharp.

The CICSAM and the HRIC scheme are constructed similarly. HRIC uses pure UDS for the normal mode and CICSAM is blended completely to UDS for large Courant numbers. Thus the same is valid for these schemes.

3.2 Sharpening Techniques

Our conclusion is that steady flow cases which allow only a slightly inclined free surface, require special treatment. We are presently developing a sharpening

technique that is redistributing the concentration to maintain the sharp interface. This sharpening correction is constructed such that it disappears in a sharp solution. Thus we believe that it does not spoil the results. At the time of preparing this paper the technique is not tested carefully, thus we do not give details here. Nevertheless an early and encouraging result is given in figure 10.

3.3 Conclusions

We have thoroughly studied the literature and implemented convection schemes as given in e.g. [2]. We get good results for dam breaks and other common test cases, but the Duncan case proved to be very difficult in terms of interface sharpness. Comparison with results obtained with commercial codes (e.g. presented in [2]) reveals that the commercial codes perform better than our implementation of e.g. HRIC. Parameters in these codes not mentioned in the publications give another hint that more sophisticated procedures than presented in the manuals were used. We have started developing a sharpening technique that detects smeared interfaces and redistributes the concentration fully conservatively. This procedure is not active if the interface is sharp. We believe that this is a valid and reliable technique.

In this paper we have omitted comparisons with experiments on purpose. The grid used for the presented computation is rather coarse. A grid study has revealed that a refinement improves the results drastically. But as mentioned earlier, the scope of this paper is to assess the accuracy and efficiency on grids that could be computed with effort affordable for practical 3D applications.

References

[1] J. H. Duncon. The breaking and non-breaking wave resistance of a two-dimensional hydrofoil. *Journal of Fluid Mechanics*, 1983.

[2] J.H. Ferziger and M. Peric. *Computational Methods for Fluid Dynamics*. Springer Verlag, 3rd edition, 2002.

[3] B.P. Leonard. The numerical Treatment of advection: A Performance Comparison of current Methods. *Computer Methods in Applied Mechanics and Engineering*, 19:5998, 1979.

[4] Samir Muzaferija, Milovan Peric, Volker Seidl, and Seung-Deog Yoo. Entwicklung und Anwendung eines Finite-Volumen-Verfahrens fr die Berechnung viskoser Schiffsumströmungen mit freier Oberfläche. Report No 594, Arbeitsbereiche Schiffbau, TUHH, 1998.

[5] D. Schmode, H. Vorhölter, and T. Rung. RANS-Based Flow Analysis for Propellers and its Benefits. In *7th INTERNATIONAL CONFERENCE ON HYDRODYNAMICS Theory and Applications*, Iscia, Italy, oct 2006.

[6] J.A. Sethian. *Level set methods.* Cambridge University Press, 1996.

[7] O. Ubbink. *Numerical prediction of two fluid systems with sharp interfaces.* PhD thesis, Imperial College of Science, Technology and Medicine, 1997.
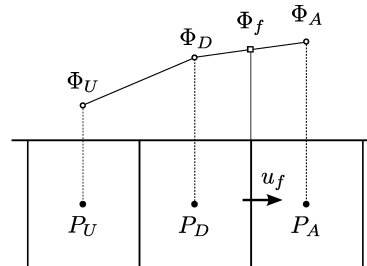
Figure 1: Definition of upwind, donor and acceptor cell.
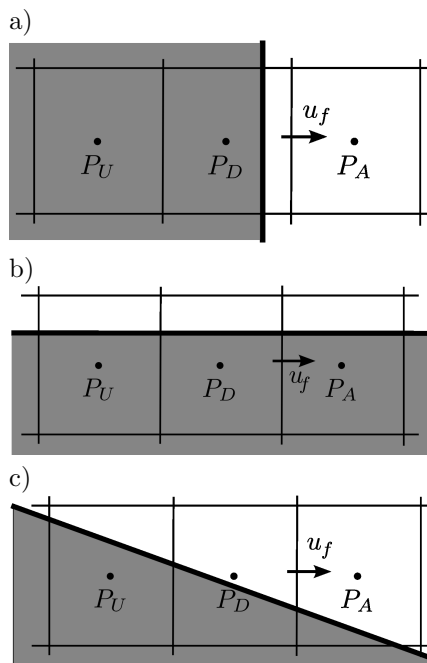

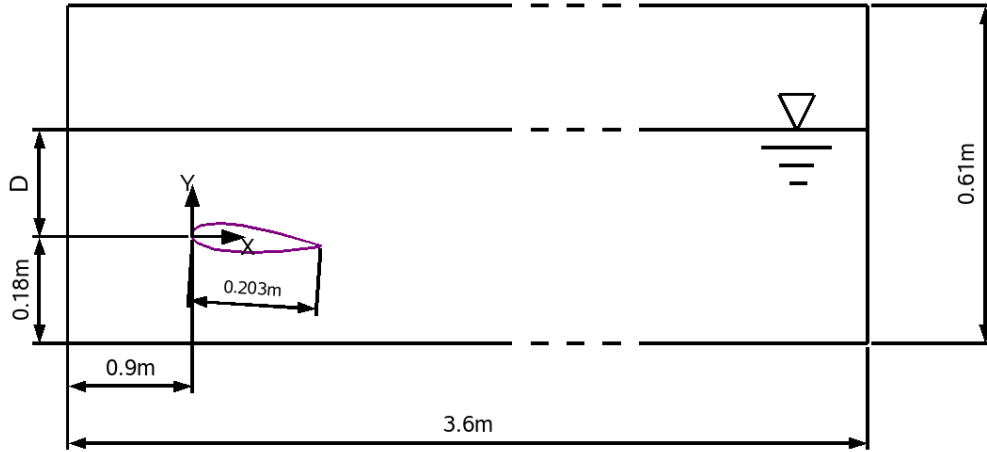Figure 2: The interface is a) parallel , b) normal and c) diagonal to the face.
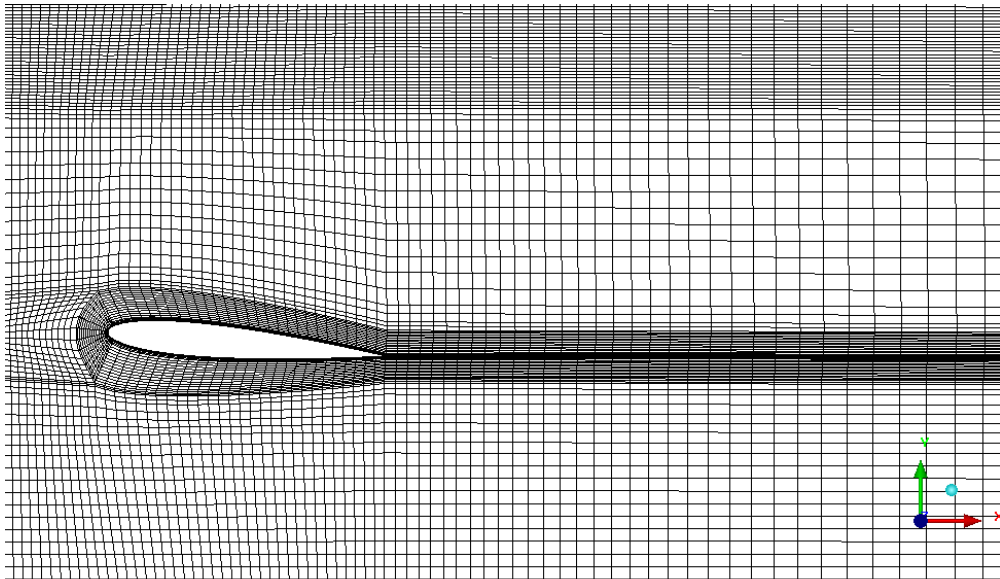
Figure 3: Computational domain.

Figure 4: Detail of the computational grid.

Figure 5: Duncan experiment computed with CIC-SAM, $Co \approx 0.7$, isolines 0.1, 0.5, 0.9.

Figure 8: Duncan experiment computed with FICS, $Co \approx 3$, isolines 0.1, 0.5, 0.9.

Figure 6: Duncan experiment computed with HRIC, $Co \approx 0.7$, isolines 0.1, 0.5, 0.9.

Figure 9: Duncan experiment computed with LS, $Co \approx 1.5$, isolines 0.1, 0.5, 0.9.
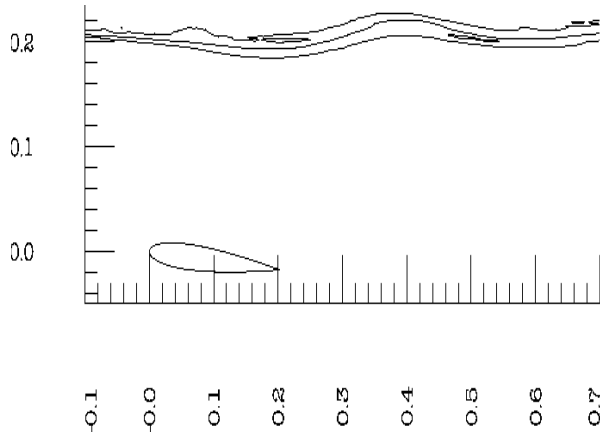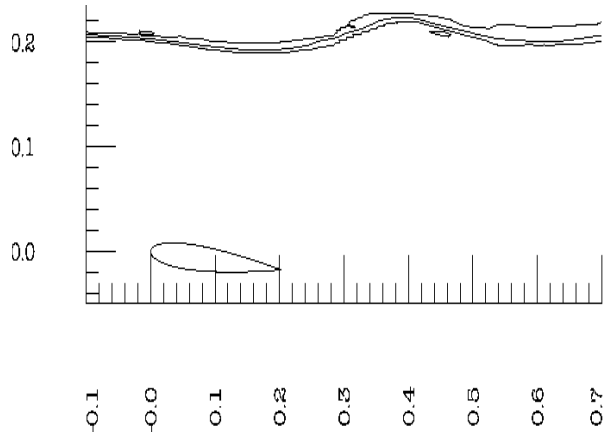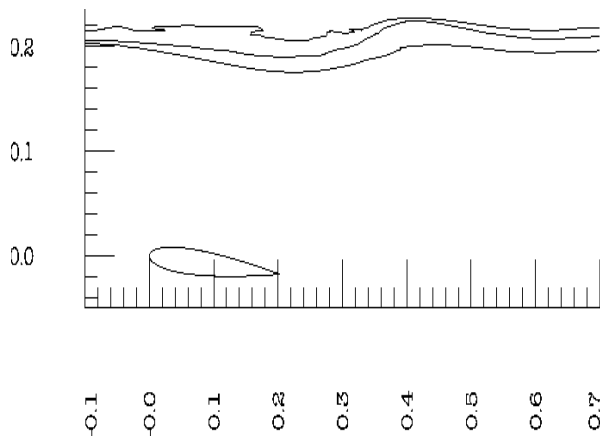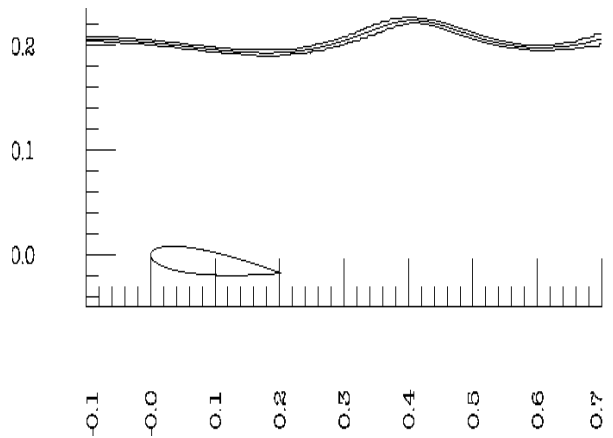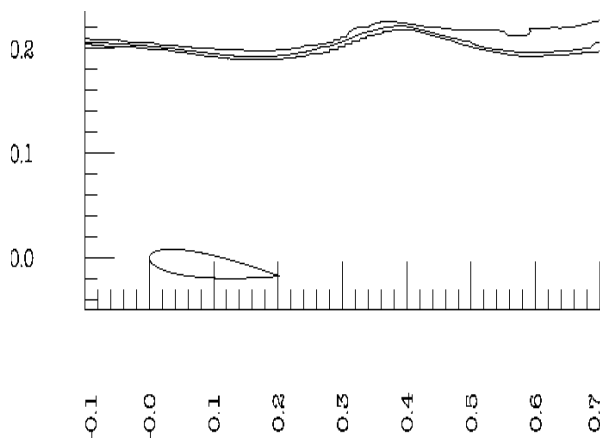

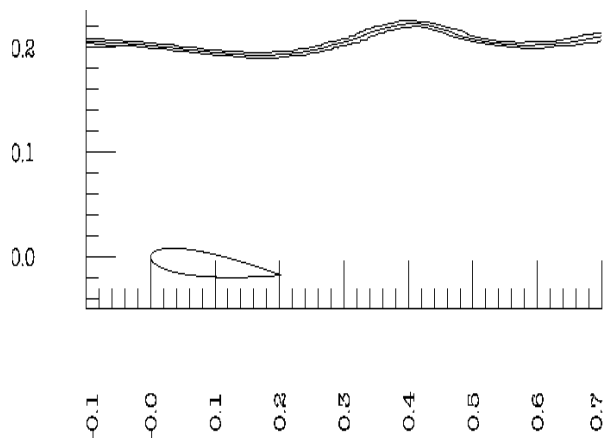Figure 7: Duncan experiment computed with FICS, $Co \approx 0.7$, isolines.1, 0.5, 0.9.

Figure 10: Duncan experiment computed with FICS and sharpening, $Co \approx 3$, isolines 0.1, 0.5, 0.9.

Optimization of Appendages Using RANS-CFD-Methods

Hendrik Vorhoelter, Stefan Krueger, Hamburg University of Technology

Numerical Towing Tank Symposium, Hamburg 2007

There has been a lot of development on RANS-CFD-methods in the past years. The codes are more accurate and faster computers allow computations on finer grids in less time. These new capabilities are widely used in research and development. However, in the practical ship design RANS-CFD-methods are not commonly used. On the contrary it is still perception that the effort for RANS-simulations, i.e. grid generation, computational time and interpretation of the results, is far beyond the benefit.

The following work presents a proposal on how modern RANS-CFD-methods can be used in the early phase of ship design. A process chain is described which combines the CAD-system for ship design E4, the finite volume grid generator HEXPRESS and an arbitrary CFD-code (in this case COMET). The process is presented by the example of a modern ferry design. The ship's wake field is computed for different designs of appendages. The results are compared to model tests. Finally the tool is used for a redesign of the appendages in order to improve the wake field.

1   Motivation

The aspect of vibrations has become more and more important for the design of modern ships during the past years. This has several reasons: On the one hand the comfort standards on board of ships increased significantly. The vessel speed in general has increased and thus the loads on the ship's propeller have also increased. Furthermore, new materials, design techniques and construction methods allow lighter ship structures. Therefore, modern ship structures are more delicate for vibrations. Thus one of the most important issues for ship design is the avoidance, or at least the reduction of vibrations.

The main source for vibrations aboard ships is the propeller. As the propeller is working in an inhomogeneous wake field, the angle of inclination of a single propeller blade varies during one rotation. Especially in the area of reduced inflow velocity around twelve o'clock the angle is increased. This causes higher loads and possible fluctuating cavitation. The loads and cavitation result in a fluctuating pressure field on the ship's hull which in consequence induces vibrations. Hence the aim of a ship design should be to create a homogeneous wake field, as far it is possible. In order to analyse the wake field there exist several criteria. One was developed by Farbach and Krueger (Farbach, 2004). It considers the gradients of the angle of incidence over one turn in the propeller inflow weighted by the radius. It will be used in this work to analyse the wake fields. Concerning twin screw vessels the disturbance of the propeller inflow is rather caused by the appendages i.e. shaft-line, shaft bracket arms and stern tube, than by the hull itself. Therefore, the presented work focuses on the design of the appendages and how it can be improved with the use of RANS-CFD-methods.

2   Common Procedure for the Appendage Design

The common procedure for the appendage design of twin screw vessels is designated by aspects of the machinery design. For instance the diameter and the position of the shaft are determined by the propeller torque and the engine's respectively gear's position. The propeller-shaft needs to be borne in order to compensate the transverse forces and the pitching moment of the propeller. Further bearings are needed as the flat buttocks of modern vessel designs require longer shafts. In addition the section length of the shaft is limited. Thus, couplings outside the hull are necessary. A coupling increases the shaft diameter.

These requirements of the propulsion train lead to

a low priority level for the hydrodynamic optimization of the appendages. Today another problem is that the performance of the appendages of a ship design is not know before the model tests are done. But by the time of the model tests the progress of a project allows only minor modifications of the design. For instance the inclination of the shaft bracket arms can be varied, but a modification of the position of the arms is hardly possible. Another aspect is that the model tests are carried out following Froude's hypotheses. Thus, the boundary layer as well as all other viscous effects are not reproduced correctly.

3   Improving the Design by Using RANS-CFD

The procedure for the design of the appendages can be improved by using RANS-CFD computations. For example, different designs can be tested without time-consuming model modifications and full scale computations are possible. But if RANS-CFD should be used efficiently in a ship design process some special requirements have to be fulfilled. For instance, the European ship builders are known for their large number of prototypes. Most ships are tailor-made designs for the customers and three ships of the same design are already called a series. Thus more designs have to be tested in less time with less budget. Although the normal running time for a project is one and a half years the time-frame for major changes on the design is only four weeks on the beginning of the project because of the leadtime needed for constructional design and component purchase (KRUEGER, 2002).

Therefore, a process chain does not only need a certain accuracy (which is a general requirement), it also has to be fast enough to be used in the time frame of four weeks. On the other hand a CFD-tool which is able to show a good tendency for the behaviour of the fluid flow field would be sufficient during the early ship design process. In the following a process chain for the use of RANS-CFD in ship design is described.

3.1   Description of the process chain

The process chain is divided into four steps preparation of the geometry, grid generation, generation of the CFD-model and computation as well as post processing.

3.1.1   Preparation of the Geometry

The design of the hull form and the appendages is done in the ship design system *E4*. For the generation of the finite volume grid, which is needed for the RANS-computation, the grid generation tool *HEXPRESS* is used. *HEXPRESS* requires a geometry description with an absolutely closed surface. Therefore, the triangulation and clipping of the hull form and the appendages is done in *E4*. In *E4* geometry modifications can be accomplished efficiently and fast. Additionally the hydrostatics, as one main aspect of the ship design, can be tested in each iteration. The creation of the computational domain is done with a new developed tool in *E4*. Thus the accuracy of the geometry description is known and it is possible to create a computational domain with a shaped free surface. Whereas the shape of the free surface is determined with a potential flow solver, which is integrated in *E4*. The possibility of dealing with a shaped free surface allows it to compute vessels with surface piercing bulbous bow or tunnel above the propeller. The geometry is transferred to *HEXPRESS* using the STL-file format.
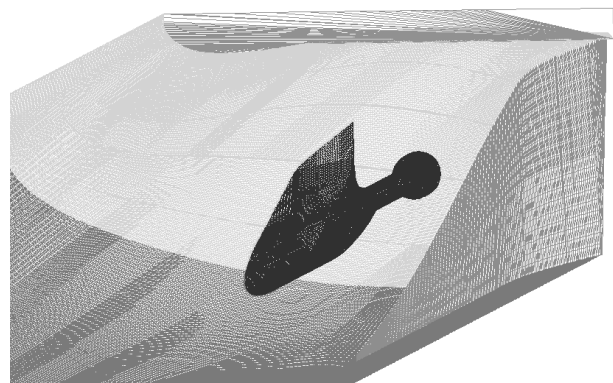
Figure 1: Triangulation of the aft section of a modern ferry design with stern tube housing

The computational domain ranges from one ship length before the hull up to twice the ship length aft of the hull. The vertical and transversal extension is one ship length. In the first step the computations are performed only for one half of the hull, as only the steady straight ahead run is simulated. If the complete hull needs to be meshed, for example for manoeuvring simulations, the mesh can be mirrored. The stern tube housing and the shaft are included in the model as well (see fig. 1). Firstly the shaft bracket arms are not included in the model, as they only have a marginal influence on the wake (see section 4.1).

HENDRIK VORHÖLTER, STEFAN KRÜGER   hendrik.vorhoelter@tu-harburg.de
Hamburg University of Technology

3.1.2 Grid Generation with *HEXPRESS*

The grid generation is done with *HEXPRESS* version 2.3.1, which is an automatic grid generator for finite volume grids. The principle of *HEXPRESS* is that the cells of a coarse initial grid which captures the total computational domain are divided following certain criteria, as there are the distance between parts of the geometry, the curvature of the surface or a certain target cell size at the surface. This step is called "adaption". The cells are intersected in all three dimensions. The result is a mesh with hanging nodes and no cell intersections with the geometry. The following steps are the snapping of the mesh on the surface and the optimization of the grid to avoid degenerated cells. Finally viscous layer cells are inserted along the hull. For further details see the *HEXPRESS* manual (NUMECA, 2005). In the presented work the target cell size criterion was used for the adaption step, because otherwise the mesh is too inhomogeneous for computations with high Reynolds numbers ($Re > 10^7$). The curvature criterion is not applicable for ship hulls as it produces too large cells on plane parts of the body, e.g. the skeg (see fig. 3)

The target cell size is determined on the one hand by the fact that the y^+ value on the boundary, i.e. the nondimensional extend of the first cell layer, should lie between 60 and 100 for the k-ω-SST turbulence model which is used in this work. On the other the aspect ratio of the cells in the viscous boundary layer should not be to big. In this work the maximum is 1:10.

In the first place the computations are done in model scale to reduce the computational effort and also to have the ability to compare the results with measurements from the towing tank.

3.1.3 Generation of the CFD-Model

COMET (version 2.3) is used as CFD-solver. But an arbitrary solver can be used as long as it provides the capabilities for turbulence modelling and dealing with meshes with hanging nodes. The boundary conditions are non-slip walls with wall functions on the ship hull, symmetry condition on the free surface and on the symmetry plane. Upstream an inlet condition is used and downstream an outlet condition. The other boundaries of the computational domain are slip walls. The computations are performed with the k-ω-SST turbulence model. The k-ω-SST model is a combination of the k-ω and the k-ε model (see ICCM, 2001). The model is considered the best two-equations-model for the capturing of the wake field (see SVENNBERG, 2000). Alternatively Reynolds-Stress-Modelling could be used. But this would increase the computational effort which counteracts the intention of a fast design tool. The computations are steady in time. The outer iteration is considered converged if the residuum is less than 10^{-5} according to COMET's convention. The whole fluid domain is initialised with the inflow velocity but with a ten times higher viscosity than at the inlet in order to accelerate the convergence.

3.1.4 Post processing

For the analysis of the flow field, the data is read out in several planes orthogonal to the shaft line in the aft section. This data is used for the design modification of the appendages. Additionally the velocity of the fluid flow is computed on several radii from 35% up to 120% of the half propeller diameter in the propeller plane. 72 angular positions are considered. The angles are measured from the six o'clock position positive to the outer side. The velocity is transformed into a cylindrical coordinate system. In the following this field is called the wake. The transformation is done for two reasons. The wake field can be directly compared with the measurements and it can be analysed by the tools already existing in *E4*.

4 Results

The described process chain has been applied for the analysis of several ships, both single and twin screw vessels. Below the results for the design of a modern ferry with a length of approx. 150m and a service speed of approx. 20kn are presented. The preparation of the geometry, grid generation, fluid computation and post precessing for one design took one day working time. The grid generation and computations were done on a PC with a double-core pentium CPU with 2.8GHz and 1GB RAM.

Following the results of the fluid flow computations are shown. The computations are done on a model scale of approx 1:18.5 and on meshes with approx. 1 million cells. The domain and a closeup showing details of the grid in the aft section are shown in figure 2.

4.1   Comparison to towing tank measurements

Firstly the CFD-results are compared to towing tank measurements. Figure 4 shows the wake field as lines of constant velocity. The view is from the aft the port side. The measured wake is shown on the left, the computed on the right side. The arrows show the velocities in the propeller plane, i.e. transversal and radial component. The area of reduced axial velocity from 135° to 180° is captured good in the computation. This area is the shadow of the stern tube housing. The smaller shadow at 200° is also visible in the computational result but on slightly modified position. The smaller shadow origins from a line separation resulting from the shaft line. The imprint of the bracket arms are barely visible in the measured wake. Thus, it is feasible not to model the bracket arms in the first instance. Figure 5 shows the same wake as curves of the axial, radial and tangential velocity components over the angle of the propeller blade. The velocity is made nondimensional with the velocity of incidence. Each curve represents one radius.

It can be seen that the coincidence of results is sufficient. Greater deviations are only seen on the inner radii and for the tangential component on the inner angles (180° to 360°). The reason for deviations on the inner radii has to be seen in the boundary layer modelling. But this is acceptable as the inner radii are not important with respect to vibrations. The upstream along the hull on the inner side is much stronger in the computation than in the towing tank, which leads to the deviation of the tangential component. The reason for this is not known till now. Modifications of the trim and the depth of the vessel had only minor influence on the wake.

The quality analysis of the wake with the Krueger-Fahrbach-criterion yields to 0.062 for the computed and 0.096 for the measured wake. The criterion yields to quality grade which would be 1. for a homogeneous wake.

4.2   Improving the Wake Field

The CFD-result is used to redesign the stern tube housing for the ferry. The wake field plot for the new design is shown figure 7. The disturbance of the inflow caused by the stern tube housing has been reduced significantly. In addition the area of decelerate velocity is moved to 220°. Therefore, not only the magnitude of the pressure pulses on the propeller blade is reduced but the blade is also farer away from the hull. The analysis with the Krueger-Fahrbach-criterion yields to 0.267, which an enormous improvement to the original design.

4.3   Importance of the Mesh Quality

Figure shows the wake field which is computed on mesh with one cell of bad quality (angular check in *HEXPRESS* says 10°). Although the computation converges similar to the computation on the better grid, the result is poor compared to figure 4.

5   Conclusion

A process chain for the use of RANS-CFD in ship design process has been developed. The tool has been tested on different ships and it has been approved for the use in the practical ship design.

It has to be discussed how the process can be improved so that the results become more accurate without to much additional expenditure of time. For instance it would be possible to test the design after several iterations with computations in full scale using RSM-turbulence models.

6   Bibliography

Farbach, Mark (2004): Bewertung der Güte von Nachstromfeldern. Hamburg. Technische Universität Hamburg-Harburg. Diplomarbeit

ICCM (2001): Comet Version 2.00 - User Manual. Hamburg. ICCM

Krueger, Stefan (2002): Made in Germany: The Route to Real Competitive Advantage. Luebeck. in Proceedings RoRo 2002

Numeca (2005): HEXPRESS User Manual version 2.2c. Brussels. NUMECA International

Svennberg, S. U. (2000): A Test of Turbulence Models for Steady Flows Around Ships. Gothenburg. Proc. Gothenburg 2000 A Workshop on Num. Ship Hydro.
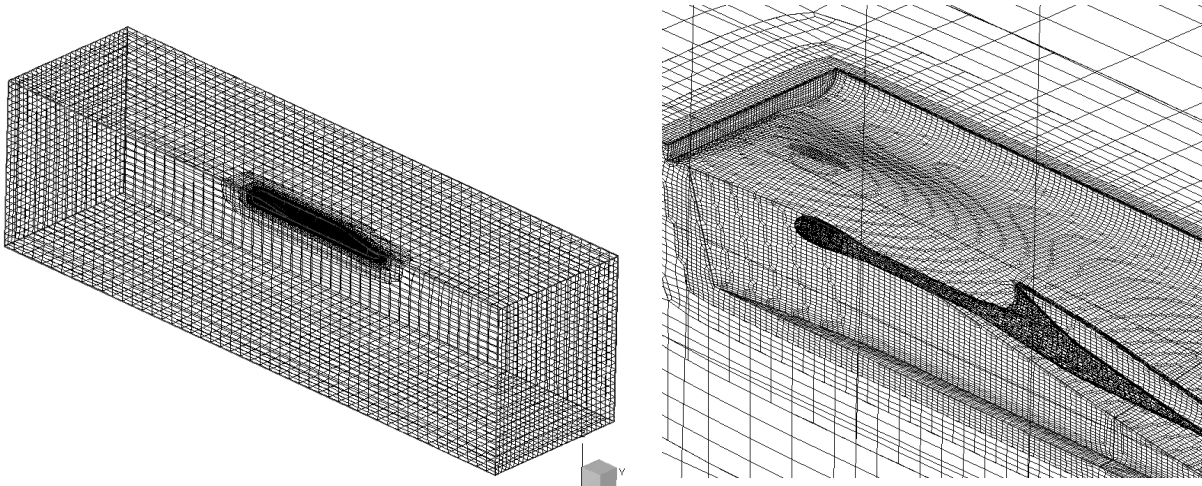
7   Annex

Figure 2: Meshed domain and closeup of mesh details at the aft end
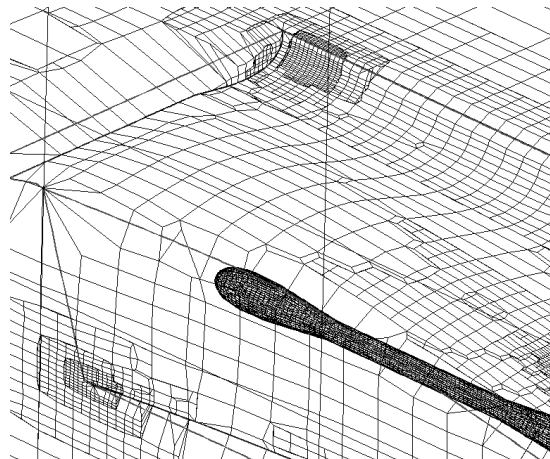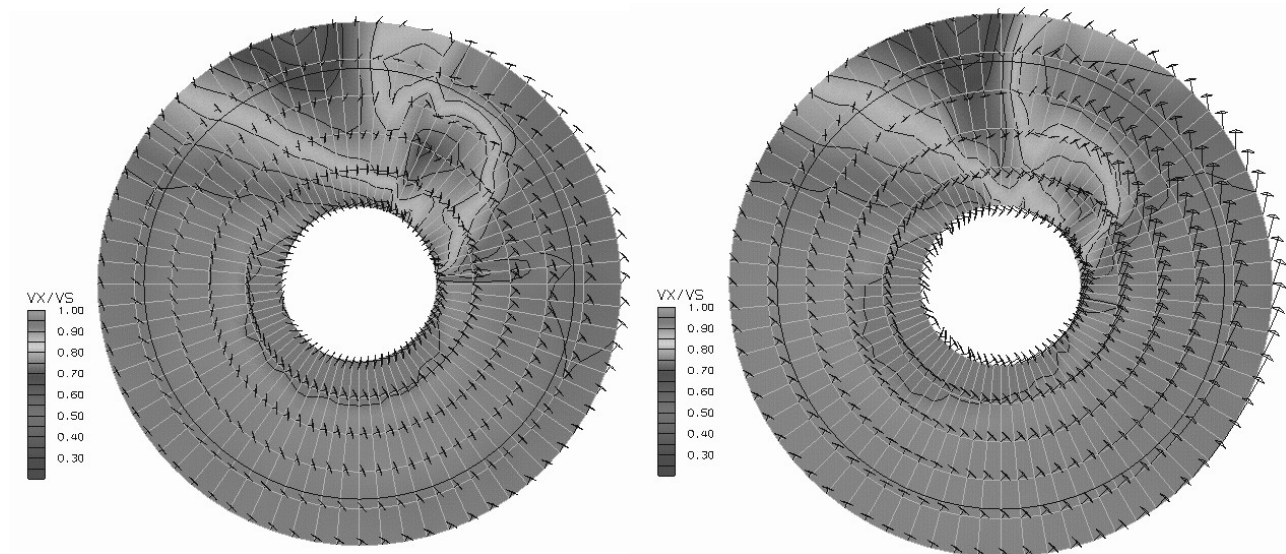

Figure 3: Inhomogeneous mesh

*Figure 4: Lines of constant velocity for measured wake
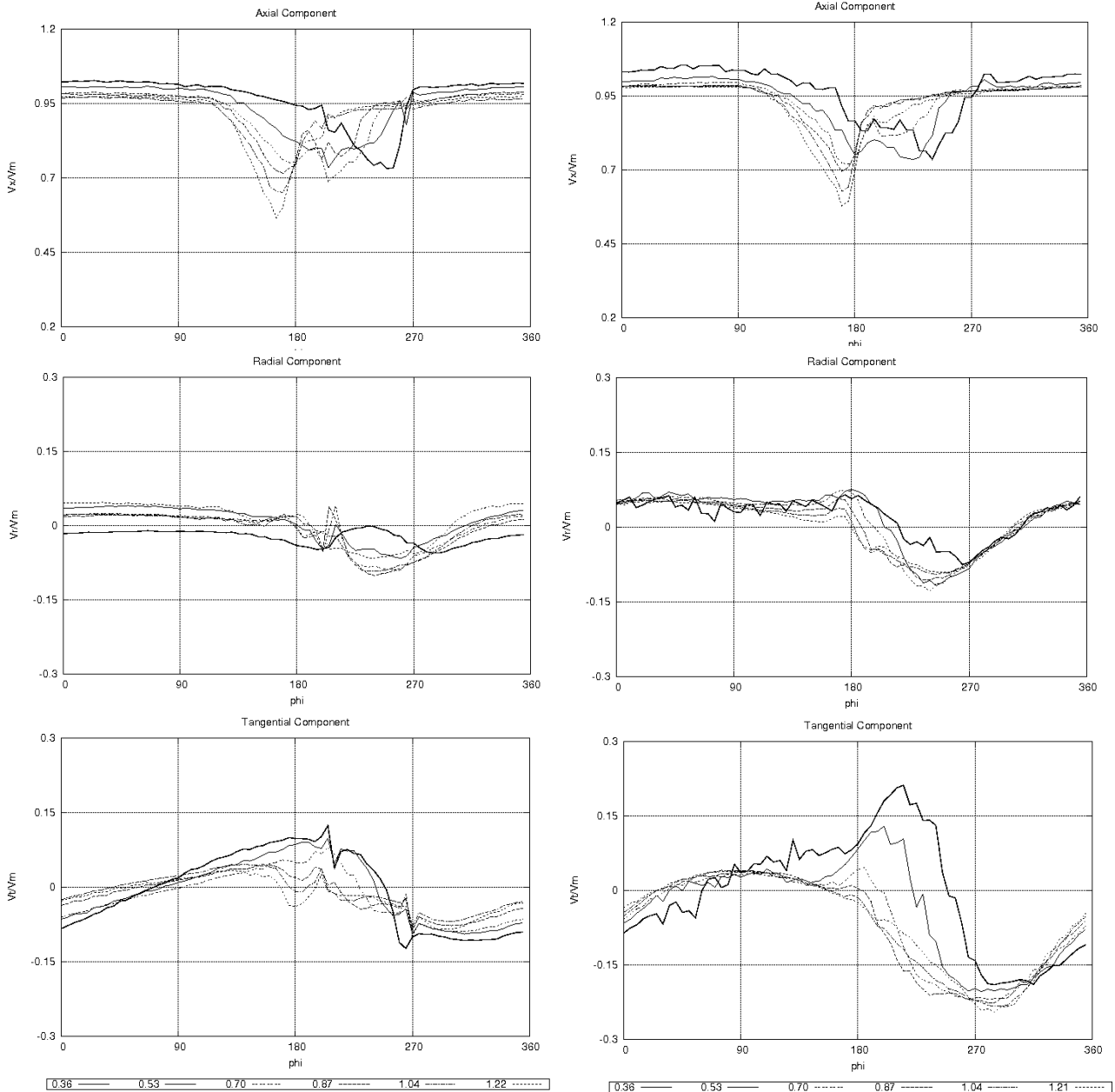(left) and computed wake*

Figure 5: Dimensionless axial, tangential and radial velocity components for measured (left) and computed wake over a full turn for six different radii
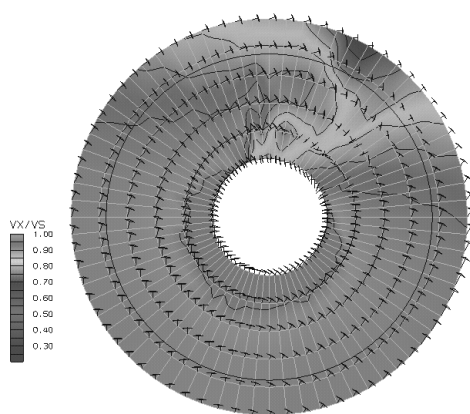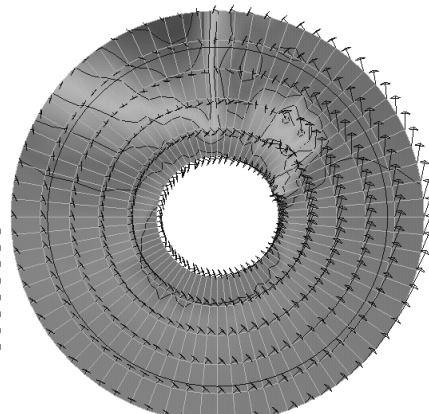

Figure 7: Wake of the improved design

Figure 6: Wake computed on mesh with bad quality

Comparison of Free Surface Wave Simulations using STAR CCM+ and CFX

Jan Westphalen (j.westphalen@bath.ac.uk), Deborah Greaves and Chris Williams
Department of Architecture and Civil Engineering, University of Bath, BA2 7AY, UK

1. Introduction

Wave modelling is a central subject in the area of coastal and offshore engineering. Whether the engineer wants to build an oil rig, a wave energy device or harbour protection, all kinds of coastal and offshore structures have to be tested against wave impact. In this context the software packages by Ansys and CD-Adapco, CFX and STAR CCM+, become more important in the design process and can be used to model waves and wave–structure interaction.

In this paper the application of the two codes to modelling waves is discussed. Regular waves are simulated by using identical conditions in both software packages and the waves are produced by implementing the velocity components along the vertical wavemaker wall boundary rather than imposing piston motions.

2. Model Setup

All test cases are calculated in a 3 dimensional rectangular domain, representing a wave tank. For first convergence tests the domain length is 35m and a 100m tank is used for the later simulations. The tank width and height are 3m and the problem is set up as a free surface flow with a water depth of 1.5m and air as second fluid. The material properties are the same in STAR CCM+ and CFX, i.e. density of water, $\rho_w = 997$ kg/m^3 and of air, $\rho_a = 1.184$ kg/m^3, viscosity of water, $\mu_w = 8.9 \times 10^{-4}$ Pa s and of air, $\mu_a = 1.9 \times 10^{-5}$ Pa s. Depending on the tank length the simulated time varies between 8.4s and 36s, each with a time step length of 0.02 s. Every second time step a results file is written. For time dependent results this gives a frequency of 25 Hz. Both software packages use the Reynolds Averaged Navier Stokes Equations (RANSE) to solve the governing equations of continuity and momentum. For modelling the free surface the Volume of Fluid model (VOF) is implemented, which will be described in detail for both solvers later in this paper.

The boundary conditions are the same in STAR CCM+ and CFX. The left and right boundaries are symmetry planes, the top one is an open pressure boundary, where air is allowed to leave or enter the domain. The bottom and far vertical boundary are walls. The remaining boundary is an inlet, where the waves are generated by defining the vertical and horizontal wave velocity components given by linear wave theory. The formulae are shown in the following equations, where u and w are velocities in x and z direction, A is the wave amplitude, g the gravity, k the wave number, h the mean water level and σ the angular frequency.

$$u = \frac{Agk}{\sigma} \cdot \frac{\cosh k(z+h)}{\cosh kh} \cdot \sin(kx - \sigma t) \, , \, w = -\frac{Agk}{\sigma} \cdot \frac{\sinh k(z+h)}{\cosh kh} \cdot \cos(kx - \sigma t)$$

According to linear theory the simulated waves have an amplitude A of 0.15m, a wavelength of 15.19m and a wave period of 4.2s.
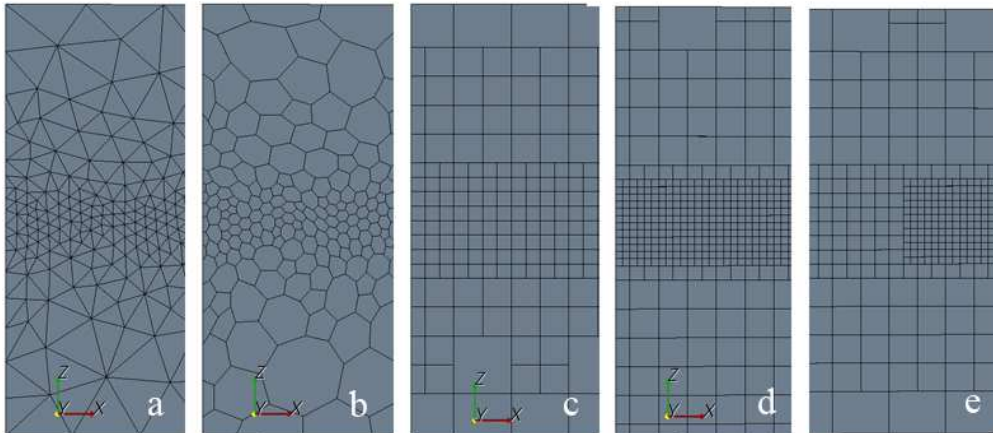

Fig 1: STAR CCM+ Meshes

STAR CCM+ is able to cope with several types of meshes. In this study 5 different meshes are used, a small portion of each shown in Fig.1. The problem is set up on a coarse arbitrary tetrahedral (a) and polyhedral (b) mesh and on regular hexahedral meshes, one coarse (c) and one fine (d). Furthermore one case with a partly refined hexahedral mesh (e) around $x = 10$m is used.

The first step in STAR CCM+ when producing a mesh is generating the surface mesh of the domain. Independent of the volume mesh used later the surface mesh is always tetrahedral shaped. Afterwards the volume mesh is generated according to the user setting. The general surface settings for all meshes are the same. The minimum and maximum cell sizes are 0.2m and 0.5m. Along the free surface a refined region between $z = 1.3$m and $z = 1.7$m is defined. For all three coarse meshes (a,b,c) the maximum cell size is limited to 0.1m in this region. The fine hexahedral mesh (d) is refined to 0.05m in this region. The partly refined hexahedral mesh (e) has the same settings as the coarse mesh, whereas the area around $x = 10$m is refined to 0.05m matching the fine mesh. The properties of all STAR CCM+ meshes used in this study are described in Table 1.

|	Mesh	L/W/H	Cells	Cells/m	vertical no of cells
STAR	Fine Hexahedral	35/3/3	543,021	15,515	12 hex + 14 hex ref
	Coarse Hexahedral	35/3/3	100,663	2,876	10 hex + 8 hex ref
	Polyhedral	35/3/3	99,087	2,831	16 poly
	Tetrahedral	35/3/3	596,124	17,032	27 tet
	Partl.-Ref Hexahedral	35/3/3	145,280		12 hex + 14 hex ref
	Coarse Hexahedral	100/3/3	286,804	2,868	10 hex + 8 hex ref
CFX	Finest	35/3/3	1,534,058	43,830	2x9 tet/ 20 prism
	Fine	35/3/3	636,386	18,182	2x8 tet/ 16 prism
	Coarse	35/3/3	150,480	4,299	2x4 tet / 8 prism
	Fine	100/3/3	1,818,200	18,182	2x8 tet/ 16 prism

Table 1: Properties of all meshes
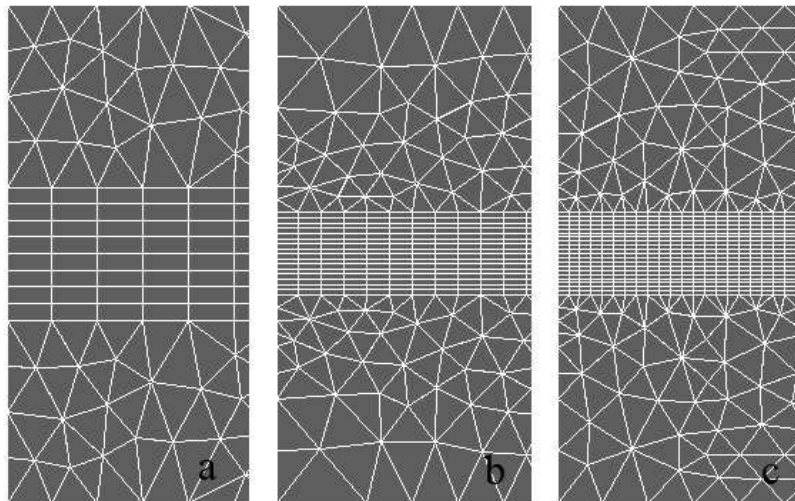
Fig 2: CFX Meshes

In CFX three meshes of different levels of refinement as shown in Fig.2 are used, a coarse (a), a finer (b) and the finest one (c). All three meshes contain tetrahedral shaped elements at the bottom and top of the domain and around the free surface the elements are extruded to generate a prism element to ensure horizontal and vertical element edges.

To achieve a working mesh in CFX a slightly different procedure compared with STAR CCM+ had to be done. At first a domain of half the height of the entire domain was built. After that the degree of refinement for the surface mesh, the volume mesh and the refined region near the free surface had to be chosen. Along the top boundary of this first part the surface elements were extruded to generate the prism layers. As in STAR CCM+ a surface mesh is generated first and from this the volume mesh is developed.

To mesh the entire domain with a similar structure as that used in STAR CCM+ the first mesh part was mirrored along the top boundary and both parts were combined. Table 1 summarises the data for each of the CFX meshes used.

3. Numerical Models & Discretisation

3.1 STAR CCM+

STAR CCM+ solves the Navier Stokes Equation with a segregated, algebraic multigrid solver using the Rhie-Chow interpolation for pressure- velocity coupling. Furthermore the SIMPLE algorithm is applied to control the overall solution [CD-Adapco (2007)].

Rhie- Chow´s [Rhie, Chow (1983)] interpolation is applied to overcome the "checkerboard" effect on collocated (unstaggered) grids. The SIMPLE [Patankar (1980)] algorithm is a guess- and- correct procedure to calculate the pressure and velocity field. Beginning from the boundary conditions the velocity and pressure gradients are calculated and the discretised momentum equations are solved. That gives the intermediate velocity field which is used to calculate the uncorrected mass fluxes at the cell faces. After correcting the pressure field and the boundary pressures the mass fluxes across the cell faces can be corrected. After that the cell velocities can be updated.

STAR CCM+ uses the well known Volume of Fluid (VOF) approach with a High Resolution Interface Capturing Scheme (HRIC) based on the Compressive Interface Capturing Scheme for Arbitrary Meshes (CISCAM) introduced by Ubbink (1997) and enhanced by Peric and Muzaferija (1999). The numerical model can be applied to any structured and unstructured grid with arbitrarily shaped control volumes (CV).

With the conservation equations an additional variable c for the volume fraction of each fluid is solved. Values for c lie between 0 and 1, where 1 stands for a filled CV of one fluid in which at the same time the volume fraction of the other fluid has to be 0 to achieve unity. In this approach both fluids are treated as a single fluid which changes its properties, i.e. density and viscosity, according to the volume fraction.
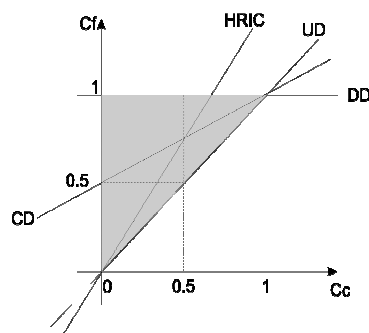

To reproduce the free surface sharply the convective flux along the cell faces is treated specially. There must not be more fluid leaving a cell than is contained within it and the CV cannot accept more fluid from a donor cell than there is space inside the acceptor cell. To control the cell face values and compute the interface orientation correctly, the approximation of the cell face value is managed by using a kind of a weighted upwind/downwind scheme which also depends on the local Courant number. The boundedness of this scheme is described in the Normalized Variable Diagram (NVD) shown in Fig.3 [Muzaferija, Peric (1999)].

Fig 3: NVD

3.2 CFX

In CFX a Finite Volume approach with parts of the Finite Element Method is implemented. By doing this a higher degree of geometric flexibility as typical for FE- approaches together with the strict mass conservation of FV- methods is achieved. The Navier- Stokes equations are discretised in an unstaggered, collocated way and solved by an algebraic multigrid solver [Zwart et al. (2003)]. To avoid pressure- velocity decoupling, Rhie-Chow interpolation is used. Instead of using a solution algorithm like SIMPLE as STAR CCM+ does, CFX solves all conservation equations in one linear equation system, with all equations being fully coupled [Ansys (2004)].

The fluxes are discretised at integration points, which are the subfaces between two control volumes within a particular element. These fluxes are calculated by using FE shape functions to obtain nodal values for pressure and velocity gradients. Advected variables, such as volume fractions, are solved using upwind- biased discretisation [Zwart (2005)]. Reconstruction of the free surface starts from an accurate volume fraction calculation. For time dependent simulations CFX uses a high- order transient scheme, which is similar to that described by Barth and Jesperson (1989). It can be described as a multi dimensional linear reconstruction of cell averaged data with a combination of upwind and downwind differencing depending on the local volume fraction gradient.

4. Results

The grid convergence tests were carried out in the 35m wave tank. At first the initial surfaces given by all meshes were viewed. Only those meshes with horizontal and vertical element edges give smooth initial

conditions. Hence only the hexahedral meshes for STAR CCM+ and all prism layer meshes of CFX were used for the convergence tests. Initial investigations for a very small wave, amplitude 0.01m in 1.5m water depth and 15.19m wavelength, found that large errors in the wave profile for both codes are inevitable unless the wave height is at least three cells high. Results presented here are for a wave amplitude, $A = 0.15$m, and the coarsest meshes used have maximum cell sizes at the free surface equal to 0.1m.

Fig.4 shows the results of the convergence tests for the two codes at x=10m behind the inlet as a time history plot. For STAR CCM+ the simulations are already converged at the first attempt using the fine and the coarse grid. Hence the coarse grid is used for the further studies. Furthermore the partly refined mesh gives smooth results with no unexpected steps. In CFX a not negligible difference especially near the wave crest and trough is seen when comparing results calculated using the coarse and the fine mesh. The maximum difference is 2.2cm. Compared to the wave amplitude of about 15cm this value is significant. Thus the coarse mesh is not converged. The difference in the solution between the fine and finest meshes reduces to 0.5cm, which is equal to 0.033% of the wave amplitude and these meshes are considered to be converged. Each of the CFX simulations exhibits an unexpected step in the wave profile, which will be investigated further through the 100m wave tank results.
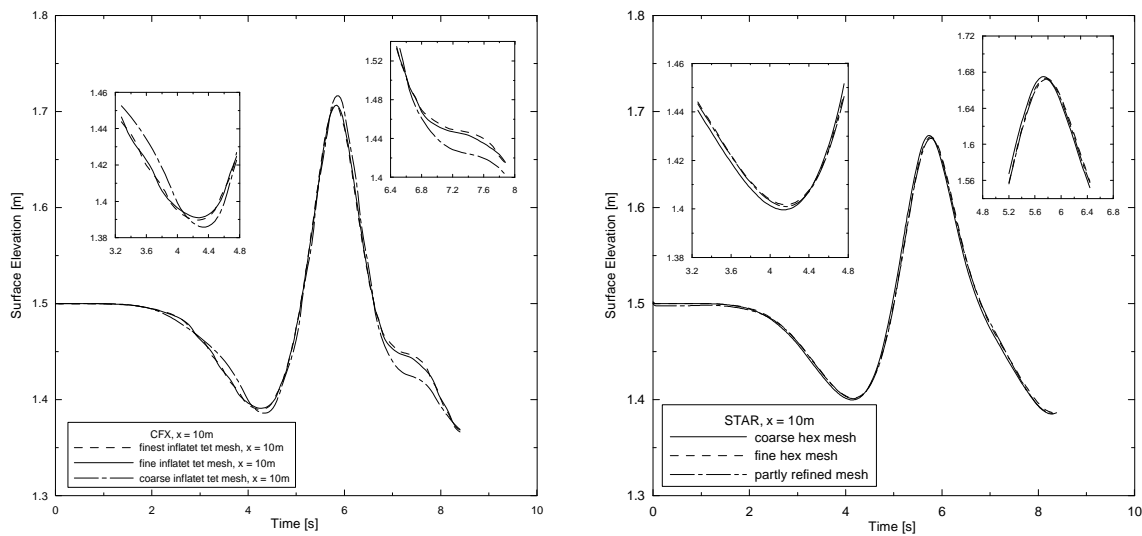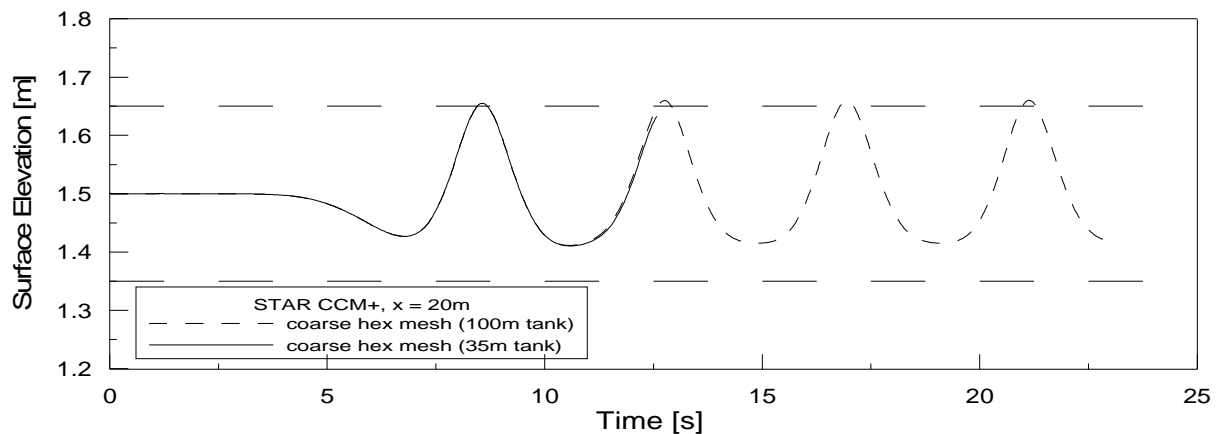

Fig 4: Time-history plot of water level for CFX (left) and STAR CCM+ at position 10m behind inlet

The results for the 100m STAR CCM+ simulation are shown in Fig.5 and Fig.6. The time-history plots of the water level at position x=10m and x=20m behind the inlet are shown. For better orientation the 15cm amplitude levels are added. The 35m tank results are also plotted and match the 100m tank results exactly at $x = 10$m, but small differences are seen at $x = 20$ after 10s, which indicates that some effect from the right hand wall boundary is being felt.

When travelling along the tank the wave changes its shape from asymmetric at $x = 10$m to vertically symmetric further down the tank at $x = 20$m. Close to the inlet the wave front is steep compared to the back. After a while the crests become higher and steeper, the troughs shallower and wider and the wave height decreases.
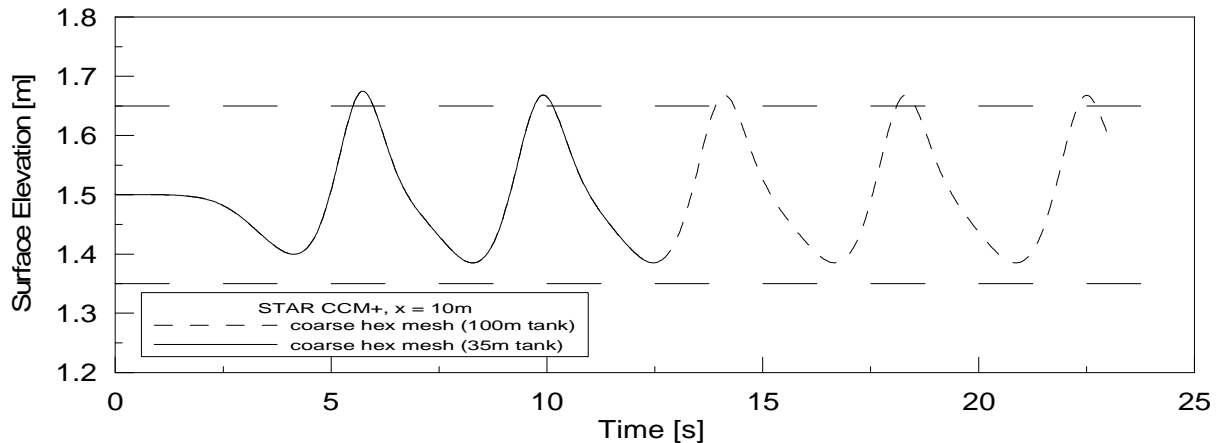
Fig 5: Time–history plot of water level for STAR CCM+ 100m domain at x=10m

Fig 6: Time–history plot of water level for STAR CCM+ 100m domain at *x*=20m

5. Conclusions

During the wave studies with CFX and STAR CCM+ both codes performed well, though differently. The most obvious fact in the difference between the codes is the calculation time needed for a converged solution. All simulations were run on a modern desktop PC with Intel Duo Core processor (each 2.4 GHz) and 2 GB RAM. The STAR CCM+ 100m run was done in 2 days, whereas the equivalent CFX simulation was still running at the time of submitting this paper. The estimated time for that run is about 40 days. The limiting factor for CFX was the provided memory during the run. Windows allocates a maximum of 2 GB for one particular application, which was not enough for a CFX mesh much larger than 2,000,000 cells. The CFX results will be presented at the conference.

Especially when simulating very small waves, i.e. deep water waves, the level of refinement for an accurate reconstruction of the free surface quickly reaches the computational limits of a serial desktop processor. When setting up the simulation in parallel mode the computational resources are optimised, the meshing process itself stays serial though. These limits were hit by STAR CCM+ quicker.

The results presented so far agree with the expected behaviour of travelling waves. The wave height damps out, the crest is higher and pointier than the trough is deep and wide. However, even these regular wave simulations are at the limit of capability of a modern desktop PC and the aims of this work, to consider superposition of waves and the generation of focussed wave groups, will require higher performance computing.

References

Ansys (2004), CFX-5 Documentation, Ansys Canada Ltd., 2004

Barth, T. J.; Jesperson, (1989), D.C., The design and application of upwind schemes on unstructured meshes, AIAA Paper 89-0366

CD-Adapco (2007), STAR CCM+ Documentation, CD-Adapco Group, 2007

Muzaferija, S., Peric, M., Computation of free surface flows using interface-tracking and interface-capturing methods, Chap.2 in O. Mahrenholtz and M. Markiewicz (eds.), Nonlinear Water Wave Interaction, Computational Mechanics Publication, WIT Press, Southampton, 1999.

Patankar, S.V., (1980), Numerical heat transfer and fluid flow. New York: McGraw-Hill.

Raw, M. (1996), Robustness of coupled algebraic multigrid for the Navier-Stokes equations, AIAA Paper 96-0297

Rhie, C.M., Chow, W.L.(1983), A numerical study of the turbulent flow past an isolated airfoil with trailing edge separation. AIAA Journal, Vol. 21, p. 1525-1532.

Ubbink, O. (1997), Numerical prediction of two fluid systems with sharp interfaces, PhD thesis, University of London

Zwart, P. J. (2005), Numerical modelling of free surface flows, VKI Lecture Series

Zwart, P. J., Scheuerer, M., Bogner, M. (2003), Free surface modelling of an impinging jet, ASTAR International Workshop on Advanced Numerical Methods for Multidimensional Simulation of two-phase Flow, Sep. 15.-16. 2003, GRS Garching, Germany

Boundary Conditions for free Surface flow

September 6, 2007

Katja Wöckner katja.woeckner@tu-harburg.de
Peter Soukup peter.soukup@tu-harburg.de
Thomas Rung thomas.rung@tu-harburg.de

Introduction

In this paper we illustrate the impact of different outlet boundary conditions for RANS calculations with free surface waves. The computations are done with the solver Comet, which applies a Volume-of-Fluid method to simulate the free surface. Further information about the solver can be found in [4], more details about the VoF method are given in [2] and [3]. The challenge of such computations is to avoid wave reflections at the outlet whilst maintaining the accuracy at low computational effort and high geometrical flexibility. A common way to do this is a method called "numerical beach" in which the waves are damped with the aid of numerical diffusion obtained from an appropriate gridding before they reach the outlet. A large disadvantage of this method is that we have to adapt the grid for each wave-direction. Another possibility is to idealize the outlet with boundary conditions, that are permeable for waves. Here we present three kinds of such boundary conditions.

Our ultimate goal for this investigation is to simulate ships manouvring in waves using the moving domain technology. This method is necessary to compute arbitrary ship motions. Especially in case of large yaw angles the waves enter (and leave) the computational domain in all directions. Thus the numerical beach isn't suitable.

Numerical model for the 2D cases

We start with computations in 2D, using two different grids and different combinations of boundary conditions. The dimensions of the domains and the position of the initial free surface can be taken from figure 1.

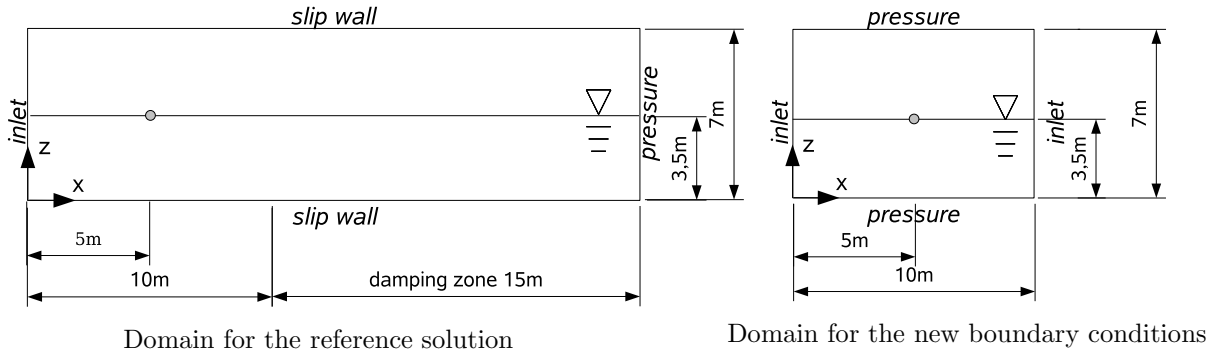Domain for the reference solution   Domain for the new boundary conditions

Figure 1: Computational domains for the 2D cases for waves moving from left to right.

As shown above we use the numerical beach and a pressure condition at the outlet as reference solution. Contrary to this we use an inlet condition, i.e. we have to prescribe the velocity and void fraction values also at the wave outlet for our new boundary conditions. Thus the pressure boundaries are specified at the top and bottom of the domain to achieve conservation of mass. Further details for the inlet condition at the outlet region are given later.

To generate the waves at the inlet conditions (left boundary) we have to prescribe the values of velocities and void fraction. To distinguish between water and air we need the position of the free surface. Using the linear Airy theory [1] to define the waves, the time dependent height of the free surface is:

$$\zeta = \hat{\zeta} cos(\omega t - kx) \qquad (1)$$

Above this surface the void fraction is $c = 0$, which indicates air. Below the interface the domain is filled with water ($c = 1$). The velocity components are:

$$v_x = v_s + \frac{\partial \phi}{\partial x} = v_s + \omega \hat{\zeta} e^{-k(|z-z_{SW}|)} cos(\omega t - kx) \qquad (2)$$

and

$$v_z = \frac{\partial \phi}{\partial z} = -\omega\hat{\zeta}e^{-k(|z-z_{SW}|)}sin(\omega t - kx) \, . \tag{3}$$

In this equations ω is the wave frequency, $k = \frac{2\pi}{\lambda}$ denotes the wave number and $\hat{\zeta}$ represents the wave amplitude. The velocity v_s is a superimposed velocity. This simulates that the whole domain is moving with a constant velocity. The equations are valid for deep water waves with $\frac{\lambda}{2} \leq water\ depth$. For our domain this results in wave length smaller than $\lambda = 7m$.

The use of an inlet condition at the outlet as shown in fig.1, requires values for the variables v_i and c. Three options have been tested, described in the remainder of this section. The first approach is to use equation (1-3) also to determine the values of velocities and void fraction at the outlet, which results in Airy waves at the inlet and outlet. This method is called 2inlet-method in the following sections.

Another possibility is to use a convective boundary condition, known as Non-Reflecting-Boundary-Condition (NRBC) in [5], [6], [7] and [8]. For an arbitrary scalar quantity ϕ this condition reads:

$$\frac{\partial \phi}{\partial t} + C^* \cdot \frac{\partial \phi}{\partial x} = 0. \tag{4}$$

A discretized variant of this equation is used to calculate the values for the variables at the outlet. The convective term is approximated with an upwind scheme. For the momentum equation we substitute ϕ with the cartesian velocities v_i. In the VoF equation ϕ denotes the void fraction c. The difficulty in this approach is to determine the convective velocity C^*. For our calculations we take the phase velocity of the undisturbed wave. Alternative approaches to determine C^* can be found in [5] and [6]. They reveal high order formulations for NRBC's with high accuracy at the expense of high computational complexity.

The third approach is to manipulate the equation system to modify the calculated solution. The aim of this modification, is to blend the calculated wave into a prescibed solution, e.g. the Airy wave. The linear equation system for a unknown scaler ϕ reads:

$$A_P \cdot \phi_P + \sum_{NB} A_{NB} \cdot \phi_{NB} = Q \tag{5}$$

With the manipulation the linear equation system becomes:

$$(A_P + \Delta \cdot \alpha) \cdot \phi_P + \sum_{NB} A_{NB} \cdot \phi_{NB} = Q + \Delta \cdot \alpha \cdot \phi_{Airy} \tag{6}$$

Here A_P is the central coefficient, $\sum_{NB} A_{NB} \cdot \phi_{NB}$ indicates the part of the neighbor cells and Q is the source term. The coefficient Δ is a fixed value, which has to be large enough to dominate the equation. Employing the shape function $\alpha = \alpha(\vec{x})$ this manipulation is applied only locally in the vicinity near the lateral boundaries. This shape function is a cosinus with a wave length of 40% of the total length of the computational domain. For large values of Δ we can neglect all other terms and we get the desired solution for the central coefficient ϕ_P:

$$\phi_P = \phi_{Airy}, \tag{7}$$

where ϕ corresponds to the cartesian velocity coordinate v_i (determined with eq. 2 and 3) or the void fraction c. The height of the free surface for the desired solution is determined with eq.1. Thus the wave near the outlet is known and eq.(1-3) is then used again to determine the wave elevation and the velocities at the outlet. In general any prescribed solution can be blended into the equation system. The most simple examples refer to calm water condition (retrieving a numerical beach variant) and Airy wave fields.

Results for the 2D case

The first example refers to 2D calculations without an obstacle. The results are obtained from the model bassins shown in figure 1. The left one is used for the computations with the numerical beach, while the other model is used for the new approaches. In figure 2 the computational grid and a detail of the refined mesh near the free surface is shown. The whole grid is used for the computations with the numerical beach, while the grid marked with the dashed lines is used for the three new approaches. The wave parameters for these calculations are wave length ($\lambda = 5m$) and wave amplitude ($\hat{\zeta} = 0.1m$). This corresponds to a grid resolution of 20 cells per wave length and approximately 12 cells per wave amplitude. The first computations are done with a
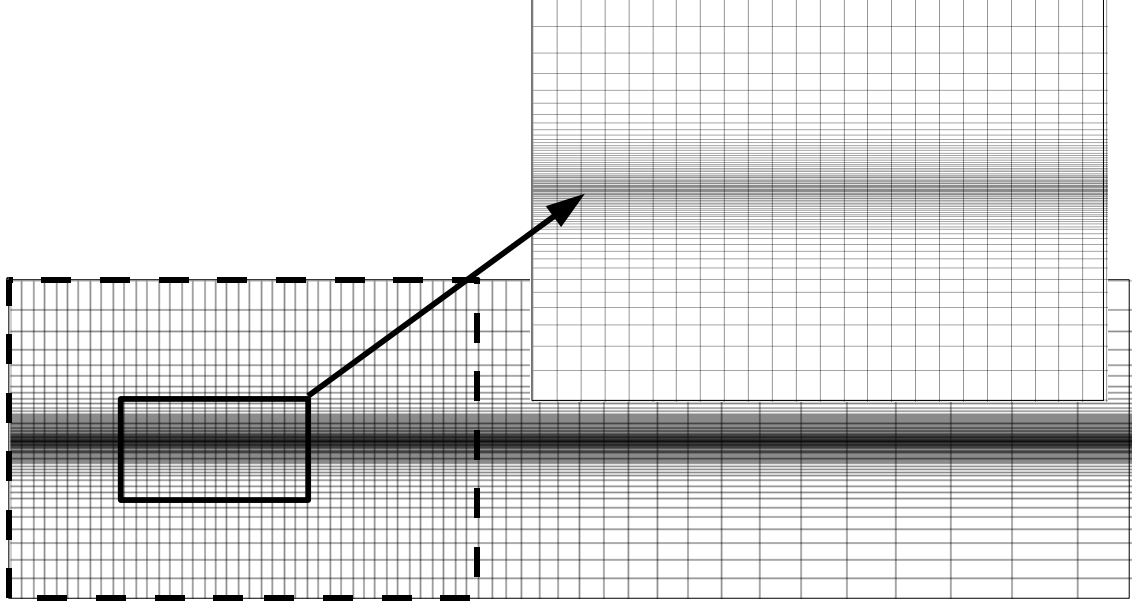
Figure 2: Computational grid

velocity of $v_s = 1\frac{m}{s}$. Thus the encounter frequency at a arbitrary point in the computational domain becomes $\omega_e = \omega + v_s \cdot k$.

To evaluate the performance of the different boundary conditions we compare the position of the free surface for a sensor location at $x = 5m$ (fig.1) against the wave elevation determined from the Airy theory (eq.1). Figure 3 displays the respective results for the different methods for this test case.
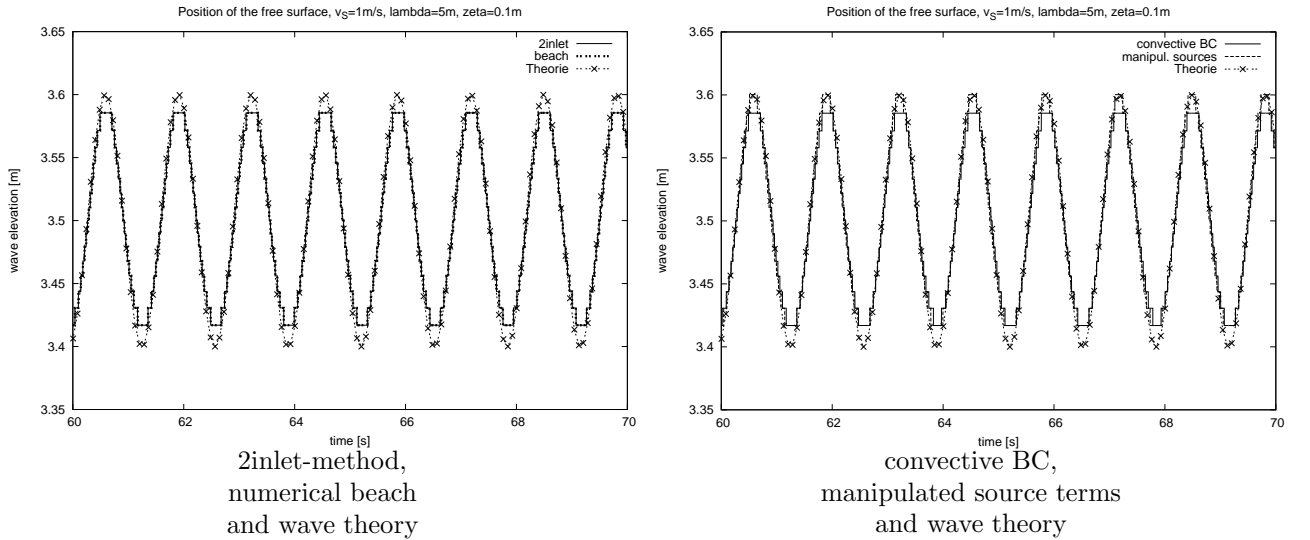

2inlet-method,
numerical beach
and wave theory

convective BC,
manipulated source terms
and wave theory

Figure 3: Wave elevation for the case $v_s = 1\frac{m}{s}, \lambda = 5m, \hat{\zeta} = 0.1m$.

Overall the time series show good agreement with each other. The solutions for the numerical beach, the 2inlet-method and for the convective boundary condition are almost identical and fit well to the theory. Only a small damping occurs because of the finite grid resolution. The results for the method with manipulated source terms show a perfect agreement with the theoretical values. Due to the forcing of the solution (eq.7) near the boundaries, the effectively length of the computational domain is reduced and the accumulated numerical damping is smaller.

Next the calculations without a superimposed velocity $(v_s = 0\frac{m}{s})$ are compared. As indicated by fig.4 the calculations with the 2inlet-method show results that are significantly different from the expected values. The

amplitude is bigger than the theoretical value and we can see a clear phase shift between the computed 2inlet solution and the solution calculated with the Airy theory. This is a result of upstream travelling reflected waves and an interaction of these waves with the incoming waves at the sensor point. The waves reflect at the outflow because the numerically computed wave deviates from the prescribed Airy wave. The results of the other approaches are in good agreement with the theoretical values.
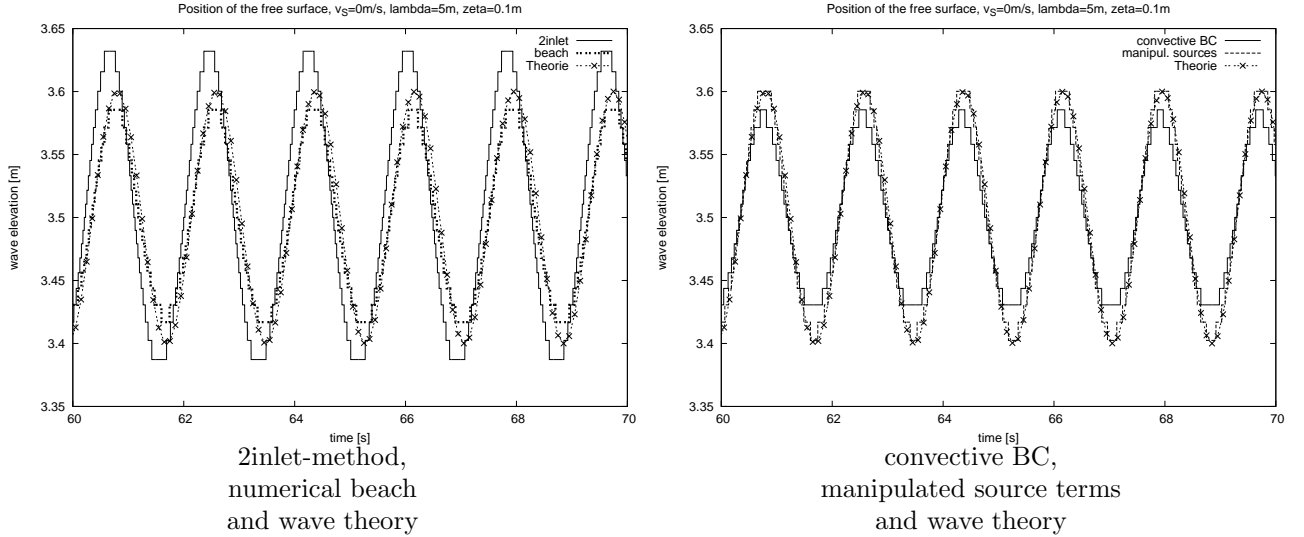

2inlet-method,
numerical beach
and wave theory

convective BC,
manipulated source terms
and wave theory

Figure 4: Wave elevation for the case $v_s = 0\frac{m}{s}, \lambda = 5m, \hat{\zeta} = 0.1m$.

Additionally we investigate simulations with $v_s = -1\frac{m}{s}$. In contrary to the first test case the encounter frequency in the computational domain is $\omega_e = \omega - v_s \cdot k$. The results of these computations are shown in figure 5. This case shows differences between the computed solutions and the values, calculated with the Airy theory. The results of the 2inlet-method, the numerical beach and especially the method using the convective boundary condition show a phase shift and a smaller amplitude. The damping of the amplitudes is larger in this case, because of the reduced wave velocity. The largest phase shift occurs, if we use the method with the convective boundary condition. It can be shown in further computations (described in [9]) that these error always occurs if the phase velocity is contrary to the superimposed velociyt v_s. Only the method with manipulated source terms comes closer to the theoretical results. The damping of the amplitudes is smaller and no phase shift occurs.
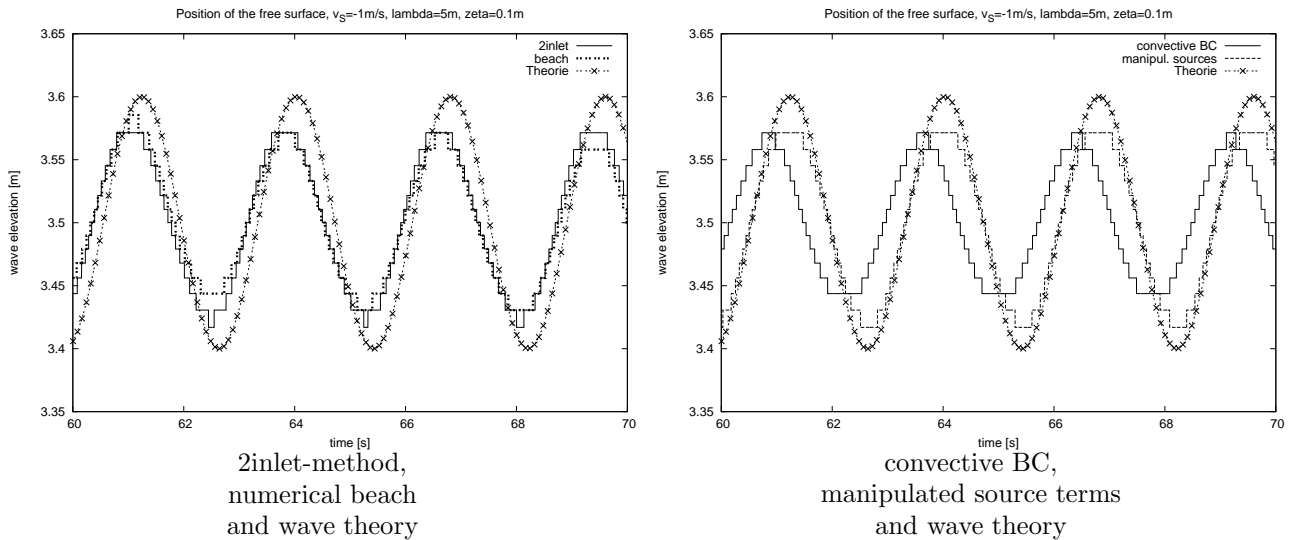

2inlet-method,
numerical beach
and wave theory

convective BC,
manipulated source terms
and wave theory

Figure 5: Wave elevation for the case $v_s = -1\frac{m}{s}, \lambda = 5m, \hat{\zeta} = 0.1m$.

4

3D results with a simple body

Furthermore we made some 3D calculations with and without a fixed obstacle. The dimensions of the corresponding computational domain and the cuboid can be seen in fig.6. This is used for the three new boundary conditions. In these cases all lateral sides are inlet boundaries and the top and bottom faces are idealized with pressure boundaries. The domain for the numerical beach has an additional damping zone behind the cuboid and a pressure condition is used at the outlet. The boundaries at the cuboid are assigned to noslip walls.
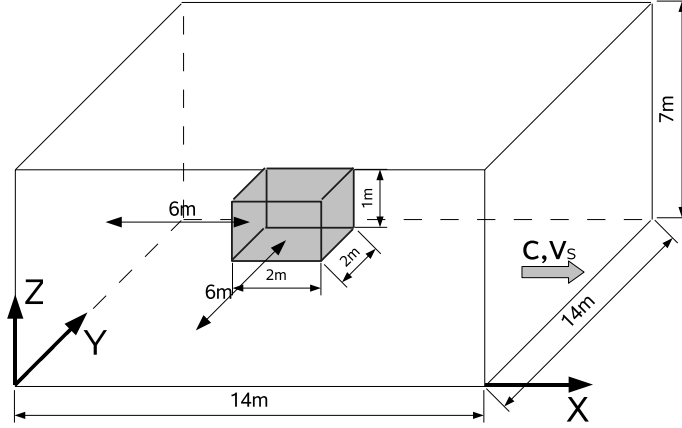

Figure 6: Computational domain for the 3D case with body.

For the shown computations we have an inflow velocity of $v_s = 1\frac{m}{s}$. The angle between v_s and the phase velocity is $\mu = 0°$, which simulates a ship in head waves.

The different approaches are compared by the means of the predicted forces on the front- and backside of the body. Since no analytical solution exists for this case, we take the numerical beach as reference solution. The results for this case are shown in fig.7, using nondimensional force coefficients:

$$c_x = \frac{F_x}{\frac{\rho}{2}(\omega\hat\zeta)^2 A},\tag{8}$$

where F_x is a calculated force in x-direction, ω is the wave frequency, $\hat\zeta$ the wave amplitude and A is the area of the front side of the body.
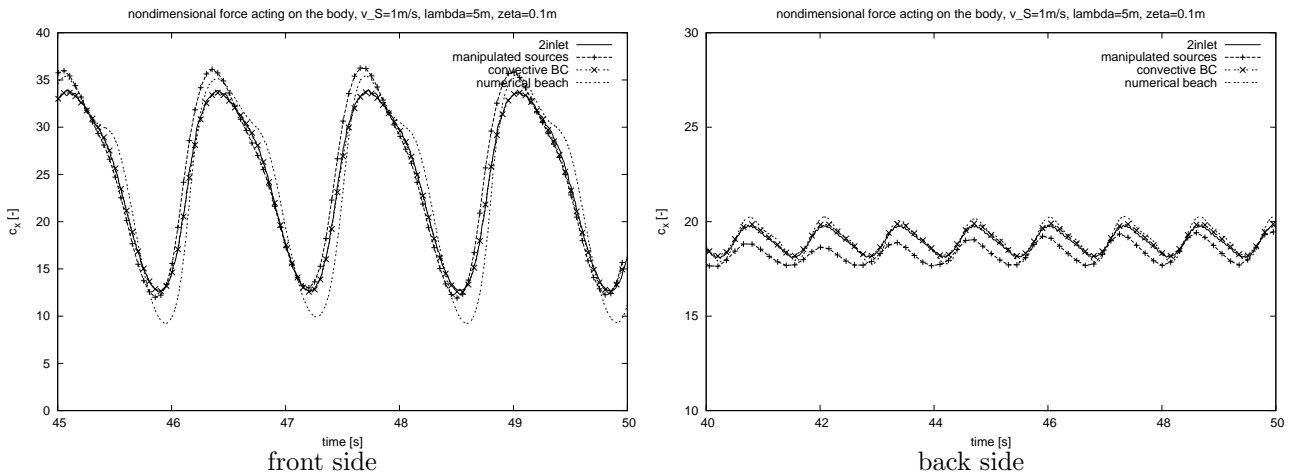

Figure 7: Forces in x-direction acting on the body $v_s = 1\frac{m}{s}, \lambda = 5m, \hat\zeta = 0.1m$.

In the left part of fig.7 the forces acting on the front side are shown. Although we have the same boundary conditions at this side of the computational domain, we saw some differences. The amplitudes for the 2inlet-method and for the method using a convective boundary condition are quite similar, but they are smaller than

the values for the numerical beach. While the calculation with manipulated source terms results in larger maximums.

The results at the backside are quite similar for the 2inlet-method, the numerical beach and the convective boundary condition. Only the results for the method with manipulated source terms are different. This demonstrates that this kind of boundary condition affects the solution in the domain. Further computations show that these problems occur at the transition between calculated and prescibed wave in case of large differences between these solutions.

Conclusion

The results show that none of the investigated boundary conditions is suitable for all applications. The convective boundary condition is inappropriate in following seas. While using the 2inlet-method wave reflections occur, if the superimposed velocity is small ($v_s \leq \omega \cdot \hat{\zeta}$). For the method with manipulated source terms and a body in waves we get problems with reflections in case of large differences between the calculated wave and the prescribed Airy wave.

In view of our final aim, the calculation of a ship manouvring in waves, only the 2inlet-method and the method with manipulated source terms seem to be suitable, because it is not possible to distinguish between inlet and outlet in this cases. These application has to be investigated in following computations. Additionally we can try to improve the method with manipulated source terms. For example we can use a solution computed with a potencial code instead of the Airy theory to determine the prescribed solution.

References

[1] Söding, Heinrich: *Bewegungen und Belastungen von Schiffen im Seegang*, 1982, TU Hamburg-Harburg, Vorlesungsmanuskript

[2] Perić, Milovan; Ferziger J.H.: *Computational Fluid Dynamics*

[3] Perić, Milovan; Muzaferija: *Computation of free-surface flows using interface-tracking and interface-capturing methods*, Artikel aus *Nonlinear Water Wave Interaction*;
Herausgeber: Marenholtz, O. und Markiewicz, M., WIT Press 1999

[4] ICCM Institute of Computational Continuum Mechanics GmbH: *COMET User Manual*, 2001

[5] Givoli, Dan; Neta, Beny: *High-Order Non-Reflecting Boundary-Conditions for Dispersive Waves*, 2002

[6] Durran D.R.: *Open Boundary Conditions Fact and Fiction*

[7] Ransau, Samul R.: *Solution Methods for Incompressible Viscous Free Surface Flows: A Literature Review*, 2002

[8] Clement, A.: *Coupling of Two Absorbing Boundary Conditions for 2D Time-Domain Simulations of free Surface Gravity Waves*, 1995

[9] Wöckner, Katja: *Untersuchung von verschiedenen Randbedingungen für RANSE-Berechnungen bei Strömungen mit freien Oberflächen*, 2007, TU Hamburg-Harburg, Diplomarbeit

CALL FOR PAPERS

11th Numerical Towing Tank Symposium (NuTTS'07)

Brest, France, 7.-9.9.2008

Topics:

- Nonlinear flows around marine structures (LES, RANSE, Euler with or w/o free surface)
- Free-surface flows around marine structures (3-d ship seakeeping, free-surface viscous flows)
- Related topics (validation experiments, numerical techniques, grid generation, etc)

Deadlines:	Early feedback (optional):	30 April 2008
	Extended Abstracts received :	15 July 2008

You are invited to participate in the above event. The objective of the event is to provide a forum for informal discussions among experts in the field and to disseminate latest results. Younger workers and Ph.D. students are especially encouraged to participate. The event will be held at the Centre de la Mer in Aberwrac'h and at Ensieta in Brest. All participants stay and have meals together to maximize interaction and discussion.

The extended abstracts of the proposed talk will be directly reproduced in the proceedings. Proceedings will be in black and white. Work in progress, encountered problems, etc. should be discussed in an open, informal atmosphere (no ties!) among colleagues. The first page of the extended abstract should be headed with the title and authors' names and address (incl. email) in a compact form to economize on space. Academic titles and page numbers shall be omitted. The extended abstract shall neither contain an abstract of the abstract, nor keywords, nor further headers. Font size shall not be less than 10pt Times New Roman. Extended abstracts should be limited to 6 pages in A4 format with 2.5 cm margin. An early reply will help us in organizing the event better. For the early feedback, a tentative title or topic will suffice.

Following the tradition of previous NuTTS events, the fees will be kept low to allow a maximum number of scientists to attend. The fees including accommodation (2 nights) and meals during the symposium will be :

275 Euro PhD candidates and students (expected to share double)
350 Euro authors (in single room)
400 Euro others (in single room)
150 Euro day participation only (excl breakfast, dinner and accommodation)

50 Euro surcharge for updates after 15 July 2008

Contacts:
Volker Bertram, **volker.bertram@ensieta.fr**

Sponsors: To be announced